GaN/AlN nanowires : nucleation, polarity and quantum heterostructures

Thomas Auzelle

UNIVERSITÉ GRENOBLE ALPES

THÈSE

Pour obtenir le grade de

DOCTEUR DE L'UNIVERSITÉ DE GRENOBLE

Spécialité : **Science des nanomatériaux**

Arrêté ministérial : 7 Août 2006

Présentée par

Thomas AUZELLE

Thèse dirigée par **Bruno DAUDIN**
et coencadrée par **Bruno GAYRAL**

préparée au sein du **CEA Grenoble**
et de **l'école doctorale de physique de Grenoble**

Nanofils de GaN/AlN

Nucleation, polarité et hétérostructures quantiques

Thèse soutenue publiquement le **11 Décembre 2015**,
devant le jury composé de :

Hubert Renevier
Grenoble INP, LMGP, Grenoble, France, Président
Henning Riechert
Paul-Drude-Institut, Berlin, Allemagne, Rapporteur
Mathieu Leroux
CNRS, CRHEA, Valbonne, France, Rapporteur
Ludovic Largeau
LPN, Marcoussis, France, Examinateur
Sergey Ivanov
Ioffe institute, Saint Pétersbourg, Russie, Examinateur
Bruno Daudin
CEA, Grenoble, France, Directeur de thèse

Ceci n'est pas une pipe.

Magritte

Remerciements

En premier lieu, je tiens à remercier les membres de mon jury de soutenance de thèse pour avoir pris le temps de se plonger dans les menus détails des nanofils de GaN et pour leurs chaleureux encouragements.

Merci à Bruno Daudin et Bruno Gayral pour avoir sauvegardé cet espace de liberté que fut ma thèse. Vous m'avez donné les moyens matériels et intellectuels pour tracer mon chemin. J'ai essayé d'en tirer profit au maximum et d'y marcher aussi droit que possible. Je suis aussi redevable à l'excellent travail de Yoann Curé et des autres techniciens de l'équipe, Yann Genuist, Didier Boilot et Jean Dussault qui ont su mettre chaque matin le régiment de MBE et autres assemblages occultes au garde à vous. Merci à ceux qui m'ont fait confiance et m'ont suivis dans la jungle des nanofils. J'ai particulièrement apprécié les images résolues au poil d'électron de Benedikt Haas, Jean-Luc Rouvière, Nicolas Mollard ou bien de Catherine Bougerol, les images tout en relief d'Albert Minj et Ana Cros, les images à moultes dimensions de Sophie Meuret, Luiz Tizei et Mathieu Kociak, les jolies gravures de Martien den Hertog, les leçons de diffusion de Gilles Nogues, les forêts de pics de Xavier Biquard, Hubert Renevier, Hervé Roussel et Edith Bellet-Amalric, et les implantations de Katharina Lorenz.

Il y a aussi ceux avec qui j'ai partagé le terrain de jeu : Xin Zhang qui a distillé un peu de sagesse orientale dans le bureau, Zhihua Fang qui a fait résonner sa bonne humeur plus fort que les cliquetis mécaniques et Matthias Belloeil qui a adopté sous son aile le MEB. Merci aux anciens qui m'ont initié aux bonnes méthodes, Aurélie Pierret, Karine Hestroffer et Diane Sam-Giao.

Une petite pensée pour les magiciens des papiers aux noms de Carmelo et Cécile.

Le NPSC fut pour moi un joli théâtre de science, merci à ceux qui l'entretiennent ainsi. Il fut de plus un lieu de vie fort agréable, peuplé de personnalités que j'ai apprécié rencontrer et côtoyer mais que je n'arriverai à citer exhaustivement ici. Il en va de même pour Grenoble et ses surprises, les Copains, les Copines, les amateurs de bonsaï et de pente raide.

Contents

Introduction

0.1 A brief history of nitride and GaN nanowires

GaN nanowires (NWs) are first the result of several decades of research in nitride materials. Since the middle of the 20^{th} century, scientists have strived to improve growth methods and characterization techniques so that high quality nitride crystals could be reproducibly synthesized today on a variety of substrates and even as bulk. To be schematic, one can cite two noticeable breakthroughs in the history of nitrides: (i) the report by Amano *et al.* [1] in 1986 of the use of AlN layers to buffer the GaN from its lattice-mismatched substrate, which increases GaN crystallographic quality and (ii) the successful $p-$doping of GaN by Mg also reported by Amano *et al.* [2] in 1989. Both discoveries paved the way for the growth of efficient light emitting devices (LEDs) based on nitride materials[1]. Hence, Akasaki *et al.* [4] in 1992 and Nakamura *et al.* [5] in 1994, have both reported the synthesis of blue LEDs, which led few years later to the *Blu-ray-disk* technology. Today, at the end of this year 2015, nitride-based LEDs with a white spectrum are available in any retailers and, last but not least, Akasaki, Nakamura and Amano, three of the great scientists in the field of nitrides, have been awarded by the 2014 Nobel prize in physics, which acknowledges the tremendous development undergone in this field.

NWs came as a side product of the systematic studies aiming at optimizing the growth of GaN thin films on sapphire. In 1997 and 1998, two competing research groups, respectively led by Kishino in Japan [6] and Calleja in Spain [7], have reported the spontaneous growth of GaN nanocolumns by molecular beam epitaxy (MBE), if using a specific set of growth conditions. The interest in those bottom-up nanostructures were (i) the absence of crystallographic extended defects although they are grown on highly mismatched materials and (ii) the relative versatility of their growth which would allow to tune their size, density and structure with an accuracy hardly reachable with conventional top-down approaches [8]. The large interest that has been raised by those promising nanostructures could be emphasized by the development of NW-like growth modes with a variety of other growth techniques, including the vapor phase epitaxy [9, 10], which would allow large scale production.

From the application point of view, NWs have been already bet as challengers of conventional thin films in order to push further the efficiency of LEDs or, at least,

[1] the interested reader looking for a more detailed story about the genesis of nitride-based LEDs can read the *History of GaN-Based LEDs for illumination* by Nakamura and Krames [3]

to reduce the production costs. One example is the spin-off Aledia [11], aiming at synthesizing highly efficient white LEDs on silicon substrates, thanks to GaN microwires. Other fields than optoelectronic are envisaged as well, albeit on a longer term, with for instance opto-chemical transducers [12] or piezo-electronic generators [13].

0.2 Motivations of the research

Although this brief overview of the nitride field indicates that a significant part of the researcher community is focusing its efforts at elaborating devices, there is still a large interest shared by several research groups in understanding the basic properties of nitride materials. The research group of Bruno Daudin and Bruno Gayral where my PhD has been carried on is one of them.

Hence, it is not surprising that the course of my experimental research has been initially impulsed with two basic questions concerning nitride NWs:

- what is the nucleation scenario of GaN NWs on AlN buffer layer?
- what are the growth modes of GaN on top of an AlN NW?

From the technological point of view, answering those two fundamental questions is also aimed at (1) increasing the reproducibility of NW nucleation on AlN buffers, especially in terms of NW polarity and density, and at (2) synthesizing a robust GaN/AlN heterostructure which would efficiently confined electron-hole pairs up to room temperature for light emission purpose.

In addition, a few of the synthesized samples has been reused for side studies, usually involving collaborations. Among the obtained results, only the one concerning the general understanding of nitride NWs properties will be presented in this manuscript. They are (1) the detailed characterization of inversion domain boundaries in GaN NWs and (2) the investigation of charge carriers diffusion in NWs.

0.3 Collaborations

The two assets of the research team where my PhD has been carried on are (1) the material growth by MBE and (2) their optical characterization by photoluminescence. In addition, few basic characterization tools are available in the laboratory. Therefore, in order to push further our understanding of the physics of nitride NWs, collaborations have been required for deeper characterization of the material and setting up novel experiments. Those collaborators are:

- Jean-Luc Rouvière and Benedikt Haas for TEM and STEM investigations (CEA, Grenoble, France)
- Catherine Bougerol and Martien den Hertog for TEM investigations and synthesis of specific substrates (Néel institute, Grenoble, France)

- Gilles Nogues for cathodoluminescence observations and synthesis of specific substrates (Néel institute, Grenoble, France)
- Mathieu Kociak, Luiz Tizei and Sophie Meuret for correlated STEM/CL observations (LPS, Orsay, France)
- Anas Cros and Albert Minj for KPFM observations (Institute of material science, Valencia, Spain)
- Katharina Lorenz for rare-earth implantation in NWs (IPFN, Lisbon, Portugal)
- Xavier Biquard, François Rieutord and Samuel Tardiff for X-rays analysis at the european synchrotron radiation facility (CEA, Grenoble, France)

0.4 Organization of the manuscript

Chapter 1 As previously discussed, nitride NWs have been under scrutiny for almost two decades, hence the first chapter is aimed at briefly introducing this specific system as well to provide some generalities on nitrides and characterization techniques, which will be used in the subsequent chapters.

Chapter 2 The diameter of NWs is a parameter which is desirable to freely tune, in order to explore different growth modes (chapter 5) or simply as a trick to ease specific measurements (chapter 3). Therefore, the second chapter of this manuscript is aimed at describing the different growth routes that have been developed to enlarge or reduce NWs diameters. Meanwhile, the growth mechanisms leading to the spontaneous one dimensional growth of NWs are introduced.

Chapter 3 Based on the observation of inconsistencies in literature about the nucleation scenario and the polarity of GaN NWs on AlN buffer layers, the self-organized nucleation of NWs is re-investigated in the third chapter. In addition to an updated nucleation model, a noticeable output of this study is the evidence of the existence of inversion domains (IDs) in a small ratio of GaN NWs, which will be further characterized in chapter 4.

Chapter 4 Thanks to the advantageous NW geometry and benefiting from the quasi-systematic presence of IDs in specific NW assemblies, a systematic structural and optical investigation of IDBs has been performed and is depicted in the fourth chapter. Noticeably, the inversion domain boundary (IDB) optical signature has been identified and is subsequently used to tentatively infer the presence of IDs in other NW assemblies.

Chapter 5 In the fifth chapter, GaN NWs are used as a quasi-substrate for the growth of GaN/AlN heterostructures. First, a critical analysis of the structural and optical properties of GaN quantum disks (QDisks) spontaneously grown on top of AlN NWs is performed. Next, the ability to obtain a 3D growth mode of GaN on top of AlN NWs is evidenced, which allows the synthesis of a novel type of GaN/AlN NW heterostructures.

Chapter 6 At last, in the sixth chapter, the NW one dimensional geometry and the ability to grow GaN/AlN heterostructures are used to perform diffusion experiments of charge carriers. It allows to get an insight in the optoelectronic properties of GaN and AlN NWs and to evidence the possible presence of built-in electric fields and non-radiative defects.

Chapter 1

The basics of GaN nanowires

This chapter is aimed at giving generalities concerning molecular beam epitaxy, nitride materials (III-N), nitride nanowires (NWs) and to briefly introduce the different characterization techniques that are used throughout the manuscript.

Contents

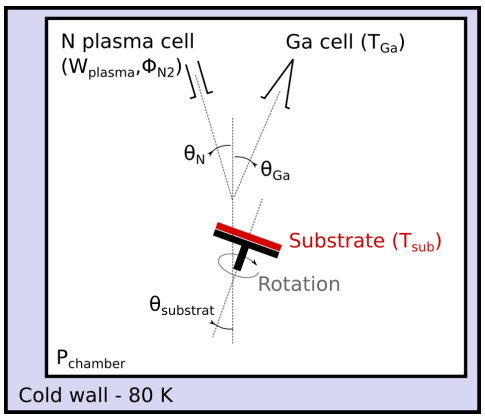

(a) Conceptual sketch of the MBE setup

θ_{Ga}	θ_{Al}	θ_N	$\theta_{substrate}$)
28°	28°	20°	0° (except if mentioned)

(b) Angles of the different atomic beams and of the substrate normal relative to the main axis of the MBE chamber

Figure 1.1: Molecular beam epitaxy

1.1 Growth techniques

All the samples synthesized during this experimental work have been grown in a plasma-assisted molecular beam epitaxy (PA-MBE) from the company MECA2000. A conceptual sketch of the setup is given in Figure 1.1a and its working principle could be schematically described as follow:

1. a substrate is introduced in a close chamber where all the atoms of the atmosphere have been previously removed by intensive pumping (an ultra vacuum of $\sim 10^{-10}$ mbar is reached in the chamber)

2. atomic beams with very low fluxes ($\sim 10^{14}$ at.cm^{-2}.s^{-1}) are generated by specific cells and directed toward the substrate surface.

3. the sample is grown out of the adatoms that have been deposited on the substrate surface. The main free parameters are the substrate temperature and the flux of each atomic beams.

From the technical point of view, metal atomic beams (Al and Ga) are provided by conventional effusion cells for which the atomic flux is dependent on the cell temperature. The N atomic beam is provided by a plasma cell, which dissociates N_2 molecules. In this case, both the flux of the incoming stream of N_2 molecules and the electrical power injected in the plasma are parameters to tune the atomic flux. MBE equipped with such cell are referred as plasma-assisted MBE (PA-MBE), in opposition to NH_3-MBE where the N atoms are provided thanks to the thermal decomposition of NH_3 molecules on the substrate surface. In addition, the chamber is equipped with cold walls, which are cooled down by liquid nitrogen. It performs a cryo-pumping, which allows to keep a low pressure in the chamber.

During the growth, the chamber pressure is at 10^{-5} mBar[1], *i.e.* in a ballistic regime, which means that the atomic species traveling in the chamber have linear trajectories.

1.1.1 Substrate temperature

In order to tailor the diffusion of adatoms that have just impinged and physisorbed on the sample surface, one can regulate the temperature of the substrate thanks to an heater placed at the substrate backside. Due to the high vacuum of the chamber, the temperature of the substrate and its environment are not homogeneous. It noticeably makes the accurate temperature measurement of the sample surface not trivial. In this work, three parameters have been used in order to estimate this temperature:

- the electrical power injected in the heater filament. Units: Watts. Error sources: the thermal inertia of the substrate holder and the steady reduction of the filament diameter along with its use[2], which increases its resistance, hence its efficiency.
- the temperature measured by a thermocouple placed at the backside of the substrate. Units: Celsius degree. Error sources: the dependence of the measurement on the environment geometry, which imply significant variations of the measured temperature as function of the used molybloc (substrate holder) or the exact position of the thermocouple.
- a characteristic time for the desorption of Ga or In adatoms on the bare Si(111) surface *in situ* probed by reflection high energy electron diffraction (RHEED). A typical example for such desorption experiment is shown in Figure 1.2a. Units: seconds. Error sources: the temperature inhomogeneities over the substrate surface and the dependence on the surface roughness.

A plot of the Ga and In desorption times and of the heater electrical power as function of the thermocouple temperature is given in Figure 1.2.

The use of the characteristic desorption time to estimate temperature has been considered as the most reliable method, especially if comparing growth runs performed on different molyblocs. Hence, calibration of the substrate temperature as function of the desorption time has been systematically performed prior to each growth. In the following chapters, for practicality, only substrate temperatures will be given but the associated desorption time could be directly retrieved by using the abacus of Figure 1.2. For all the cases, the estimated accuracy of the temperature is ± 10 °C. In comparison to reports on nanowires (NWs) growth published by other laboratories, this temperature seems to be, on average, overestimated by ~ 30 °C, which likely stems from the peculiar geometry of the thermocouple environment. At last, an *in situ* temperature calibration by monitoring the fusion of an Al ribbon is described in chapter 3, where a more accurate estimation of the temperature in the $600 \sim 700$ °C range was needed.

[1] the base pressure of the MBE chamber is $\sim 10^{-10}$ mBar but during growth the pressure increases up to $\sim 10^{-5}$ mBar due to the stream of N_2 molecules passing through the plasma cell

[2] this aging is on a time scale of several months

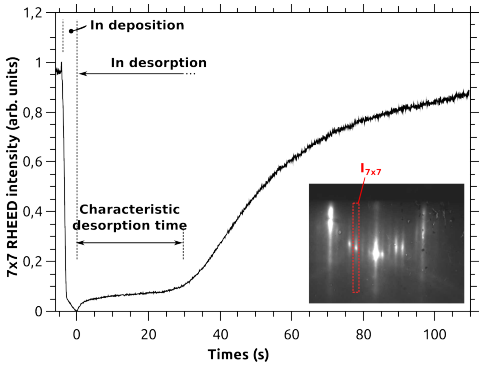

(a) RHEED intensity of the 7x7-Si(111) surface reconstruction as function of time during In deposition and subsequent desorption – inset: RHEED spectra of the 7x7-Si(111) reconstruction, the dashed rectangle represents the area where the 7x7 intensity is measured – more details on the measurement technique could be found in Ref [14]

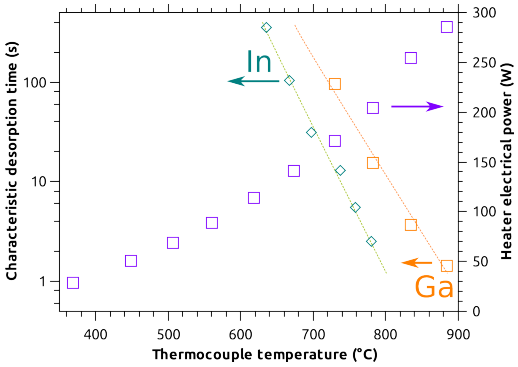

(b) In and Ga characteristic desorption times and heater electrical power as function of the thermocouple temperature – dashed lines are guide for the eyes

Figure 1.2: Temperature measurement of the substrate surface

In addition, the temperature is not homogeneous over the whole substrate surface. Due to the heater geometry and the use of substrate rotation during growth, a monotonous decrease of the temperature from the center to the edge of the substrate is obtained. Such temperature difference, estimated at ~ 40 °C will be advantageously used in chapter 3 and 5 to explore different growth conditions on a single substrate.

1.1.2 Atomic fluxes

An estimation of the Ga, Al and N atomic fluxes is routinely performed through the observation of RHEED oscillations when growing GaN or AlN 2D layers [15].

The principle is based on the monitoring of the specular RHEED spot intensity during the growth of a 2D layer in a ML by ML mode. When a ML is completed, the roughness of the surface is reaching a minimum, implying its larger reflectance, hence, the specular RHEED spot intensity reaches a local maximum. When a ML is half completed, the several islands constituting the uncompleted ML are increasing the surface roughness, implying a more pronounced scattering of the impinging electrons, which results in a loss of intensity for the specular RHEED spot. Therefore, during one oscillation of the specular RHEED spot intensity, a ML has been grown. Such calibration method allows to determine a growth speed in units of ML per seconds. An example of RHEED oscillations observed during the growth of AlN is shown in Figure 1.3a.

For growth of diatomic compounds such as nitrides, the protocol used to estimate the atomic fluxes density from RHEED oscillations is as follows. One of the atomic flux is kept constant, usually the N beam, whereas the other one, usually the metal

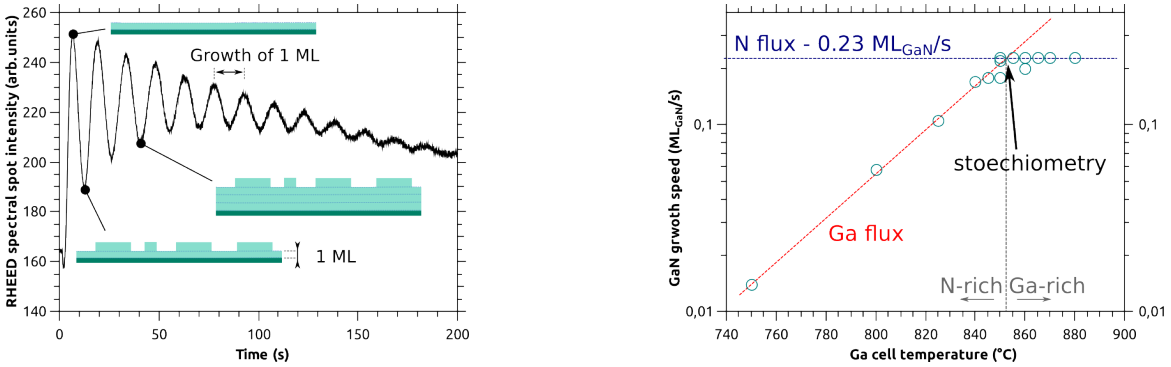

(a) RHEED oscillations during AlN 2D layer growth

(b) GaN growth speed abacus

Figure 1.3: Calibration of the atomic fluxes densities

beam, is tuned in a wide range. If the growth speed is increasing when increasing the metal flux, hence the metal is the limiting reactant, *i.e.* the N-flux is larger than the metal flux and the growth is in the so-called N-rich regime. In this case, the material growth speed is equal to the effective metal flux. If the growth speed is not increasing when increasing the metal flux, hence N is the limiting reactant, *i.e.* the metal flux is larger than the N-flux and the growth is in the so-called metal-rich regime. In this case, the material growth speed is equal to the N-flux. An example of the calibration curve obtained through this method is shown in Figure 1.3b. The measured fluxes are said "effective" because such calibration only measures the ratio of atoms taking part in the growth and neglects the possible ratio of atoms desorbing from the surface. Those calibrations have been typically done every 4 months. During this period, fluctuations in the atomic fluxes in a range of 10% could be expected, hence, the accuracy of the fluxes given in the next chapters is 10%.

One has to note that the surface density of atoms within a ML of GaN or AlN is different, as indicated in Figure 1.1. Therefore, in the following chapters, a subscript will be systematically added to precise the chemical nature of a ML. For instance a deposition of 1 ML_{AlN} of Al atoms corresponds to an Al deposition amounting to the number of Al atoms in 1 ML of AlN, *i.e.* 5.962×10^{14} at.cm^{-2}.

In addition, assuming a constant and collimated atomic beam flux leaving a cell (Φ), the effective atomic flux received by a surface depends on the beam incident angle on the surface itself (θ) and is equal to $\Phi cos(\theta)$. Therefore, and as discussed in the chapter 2, the incident angles of the different beams are gathered in Figure 1.1b. The substrate can be also tilted away from the main axis of the MBE chamber in order to change the incident angle of the atomic beams, however, in the general case, this tilt angle is set to 0°.

1.1.3 Other growth techniques

Direct comparison between MBE and other growth techniques are not straightforward as each has its own working principle and set of peculiarities. Nevertheless, one can mention the two usual drawbacks of MBE: (i) the ultra-high-vacuum required for MBE operation as it obliges the use of specific tools and of complex protocols and (ii) the lower growth speed compared to vapor phase epitaxy (VPE)[3] although the development of a new generation of N-plasma cell might improve this issue. On the other side, *in situ* monitoring tools such as RHEED and a very pure atmosphere allowing the growth of material with high quality, at a rather low temperature and with a significant control constitute the main advantages of the MBE growth technique.

1.2 Nitride properties

A few of the general properties of nitride materials as well as of Si, Al and Si_3N_4 are gathered in Table 1.1[4] .

1.2.1 Lattice properties

The two usual crystal structures of nitride materials are the cubic-face-centered and the hexagonal lattices, with a III-N dumbbell[5] at each nodes of the lattices. They are more commonly referred as, respectively, the zinc-blende and the wurtzite structures, which are depicted in Figure 1.4. However, one has to note that the wurtzite structure of nitrides departs from the ideal case where $u = 3c/8$ and $c/a = 1.633$.

A common feature between the two structures is the existence of a basal plane, *i.e.* a plane where III-N dumbbells are organized along the same hexagonal pattern. Hence, both lattices can be described through a specific stacking sequence of a primitive ML_{III-N} parallel to the basal plane. In a wurtzite cell, the stacking sequence has an $..ABAB..$ pattern, whereas in the zinc-blende cell, the stacking sequence has an $...ABCABC..$ pattern, where A, B and C refer to different in-plane positions of the III-N dumbbells in the ML_{III-N}. A transformation between the ML_{III-N}s A, B and C can be obtained through translations into the basal plane by a vector $1/3(1\bar{1}00)$ in the hexagonal lattice coordinates and $1/6(11\bar{2})$ in the cubic-face-centered lattice coordinates.

In the wurtzite structure, specific directions have been labeled by letters instead of the regular Miller index coordinates. Hence, the normal to the basal plane corresponds to the (0001) direction but is also called c axis or out-of-plane axis. Similarly, a axis and m axis respectively correspond to $(1\bar{1}00)$ and $(11\bar{2}0)$ directions.

For nitrides, the wurtzite phase is thermodynamically more stable than the zinc-blende phase, with an energy difference per atom indicated in Table 1.1. However, the

[3] MBE growth speed: $\sim 0.3\ \mu.h^{-1}$, hidride vapor phase epitaxy (HVPE) growth speed: $\sim 100\ \mu.h^{-1}$ [10]

[4] more material characteristics could be find on the web database $http://www.ioffe.ru/SVA/$

[5] a metal atom chemically bonded to a N atom with a bond length equal to u – see red dotted rectangles in Figure 1.4

	AlN	GaN	InN	Si	Al	Si_3N_4
Lattice parameters – 300 K (see Figure 1.4 for the meaning of a, c and u) Hexa: Hexagonal, cfc.: Cubic faced centered, Wurt: Wurtzite, z-b: Zinc-blende						
Hexa - a	3.112 Å	3.189 Å	3.548 Å			7.595 Å
Hexa - c	4.982 Å	5.185 Å	5.760 Å			~ 3 Å
Hexa - c/a	1.601	1.626	1.609			
Hexa (wurt) - u	1.903 Å	1.955 Å	2.171 Å			
cfc - a				5.43088 Å	4.05 Å	
cfc (z-b) - u				2.35164 Å		
Thermodynamic energy difference between the zinc-blende and wurtzite phases –units: $meV.at^{-1}$						
	18.4	9.9	11.4			
Atomic surface densities in a single ML – units: 10^{14} $at.cm^{-2}$						
(0001) – N	5.962	5.677	4.586			4.004
(0001) – metal	5.962	5.677	4.586	3.915	7.058	3.003
$(1\bar{1}00)$ – N	6.450	6.048	4.893			
$(1\bar{1}00)$ – metal	6.450	6.048	4.893			
Polarization along the c axis for the wurtzite lattice – units: $C.m^{-2}$						
Spontaneous	−0.081	−0.029	−0.032			
Piezo - e_{33}	1.46	0.73	0.97			
Piezo - e_{31}	−0.60	−0.49	−0.57			
Band edge luminescence						
0 K	6.12 eV	3.47 eV	0.62 eV			
300 K	5.96 eV	3.39 eV	0.66 eV			

Table 1.1: A few of the properties of AlN, GaN, InN, Si, Al and Si_3N_4 – references and additional properties could be find on the web database: *http* : *//www.ioffe.ru/SVA/* – polarization coefficients are from [16]

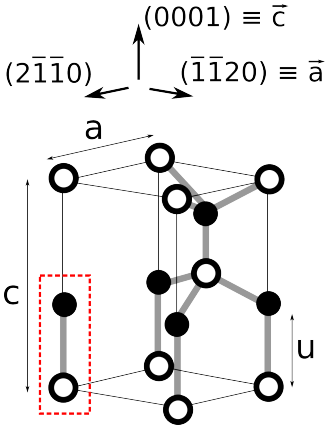

(a) Wurtzite structure

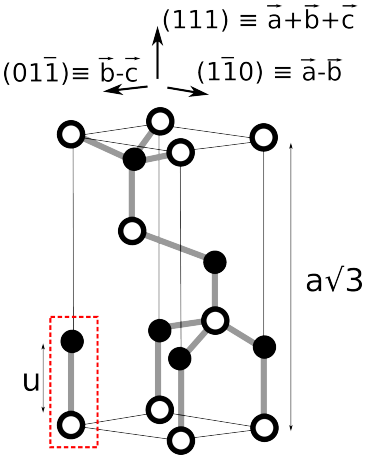

(b) Zinc-blende structure

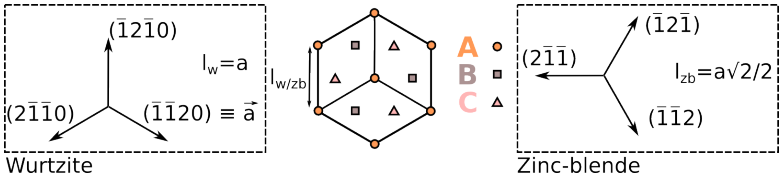

(c) Projection of the atomic positions in the wurtzite and zinc-blende structures on the basal plane

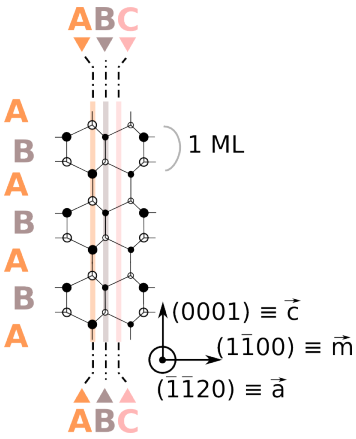

(d) Wurtzite atomic positions projected on a prismatic plane – the ..*ABAB*.. stacking sequence is emphasized

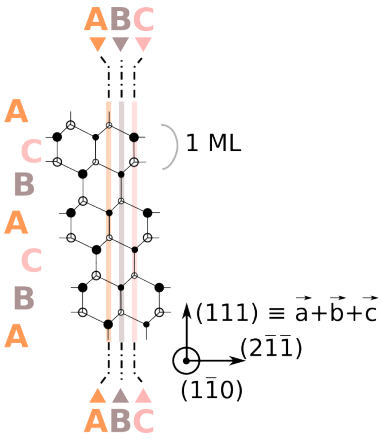

(e) Zinc-blende atomic positions projected on a prismatic plane – the ...*ABCABC*.. stacking sequence is emphasized

Figure 1.4: wurtzite and zinc-blende structures – III-N dumbbells are emphasized by red dotted rectangles– open (filled) circles are cations (N atoms) – letters A, B and C denotes ML_{III-N} with different position of the III-N dumbbells – the basal plane is defined as the plane where atoms are organized with an hexagonal pattern, the prismatic plane is normal to the basal plane

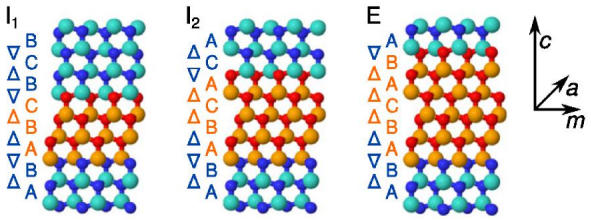

Figure 1.5: Stacking sequences for different types of basal SFs, namely I_1, I_2 and E, which are represented in a ball and stick model – from [18]

inclusion of small sections of zinc-blende material in the wurtzite phase may occur and is usually referred as a stacking fault (SF). Different types of SFs have been labeled and are represented in Figure 1.5. The most common is the I_1 basal SFs, which is regularly observed in GaN NWs and will be specifically used in the chapter 6. A significant interest in such planar defect is its ability to confine electron-hole (e-h) pairs as in the case of a quantum well (QW) [17].

1.2.2 Polarization

The wurtzite structure has piezoelectric and spontaneous polarizations due to its low symmetry [19], with unusually large values (given in Table 1.1) compared to other III-V materials. In the general case, it results in surface charges, which will build-up significant electric fields within the crystal [20]. The electric fields can be deduced from the relation:

$$div(\vec{P} + \epsilon\vec{E}) = \rho \tag{1.1}$$

where $\vec{P}$ is the sum of the spontaneous and piezoelectric polarizations, ϵ the static dielectric constant, $\vec{E}$ the electric field and ρ the free electric charges. As later shown in chapter 5 and 6, the presence of these electric fields will play a major role in the optoelectronic properties of nitride NWs.

In addition, in relation to these electric fields, which are mostly along the c axis, facets (000l) will be referred as polar facets, facets (hkil) with $l \neq 0$ will be referred as semi-polar facets and facets (hki0) will be referred as non-polar facets.

1.2.3 Polarity

The polarity is describing the asymmetry of a material, which results in different properties between the (hkil) facets and the (hki$\bar{l}$) facets. For nitrides, facets with $l > 0$ will be referred as metal-polar, whereas facets with $l < 0$ will be referred as N-polar. By extension, the polarity of a crystal such as a NWs or a 2D layer is defined by the polarity of the main facet, *i.e.* the facet where growth occurs (the top one in case of NWs).

The asymmetric properties of the (hkil) facets and the (hki$\bar{l}$) facets are stemming from different atomic configurations of the surfaces, as well as from the polarization induced electric fields previously introduced. Hence, polarity has several consequences on growth (e.g. incorporation rate of extra atoms for doping and alloying [21], incorporation of defects [22, 23, 24], adatom mobility [25]) and band engineering [26, 27, 28].

The determination of a material polarity, especially in small objects, is not trivial. One can cite several techniques, namely anomalous X-ray diffraction [29], KOH selective

etching [29], KELVIN PROBE FORCE MICROSCOPY (KPFM) [30], convergent beam electron diffraction (CBED) [31], low energy electron diffraction (LEED) [32], electron energy loss spectroscopy (EELS) [33] and X-ray photo-electron diffraction (XPD) [34], which have all been used to characterize single GaN NWs or assemblies. Actually, this topic will be further discussed in the chapters 3 and 4.

1.3 Nanowires

1.3.1 Definition

Due to the widespread use of the prefix "nano", numerous wires are referred as NWs throughout the literature, although they might be synthesized by different techniques and hold different dimensions. Hence, one proposes here a non-exhaustive nomenclature, which will be used in this manuscript for differentiating three types of wires pictured in Figure 1.6:

- NW: it refers to columnar crystallites which are grown by PA-MBE[6] with a self-organized nucleation. It is those NWs that are under the scrutiny of this study. In the case of GaN NWs, an aspect ratio between 10 $\sim$ 40 and a diameter between 30 $\sim$ 150 nm can be expected. However, later events in the growth (coalescence or heterostructuring) might lead to a loss of the NW-like geometry, but for practicality those objects will be still referred as NWs. Additionally, one has to note that the radial confinement of *e-h* pairs within a conventional NW is negligible [35], meaning that NWs are not a 1D system from the optoelectronic point of view, although their name would suggest it.

- pillars: it refers to columnar crystallites which are grown by MBE on a 2D layer of GaN with the help of a mask. Such pillars usually have a larger diameter than NWs, mostly due to the difficulty to etch holes smaller than 100 nm in a mask.

- micro-wires: it refers to the wires grown by VPE techniques. Those wires are either catalyzed or grown thanks to a mask and usually exhibit larger sizes than NWs.

1.3.2 Growth diagram

Systematic studies of the growth of GaN has shown that the nucleation of GaN NWs is occurring for high substrate temperature, *i.e.* where the desorption and decomposition of GaN become significant [38], and in N-rich conditions. The growth diagram reported by Fernández-Garrido *et al.* [39] and shown in Figure 1.7a is a sum-up of those conditions. For practicality, in the following chapters, instead of the absolute values of the atomic beams fluxes, only the flux ratio (referred as the III/V ratio) will be given. From the

[6] note that self-organized NWs obtained by NH3-MBE will be referred as pillars

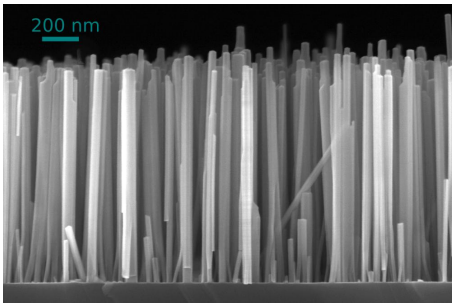

(a) GaN NWs grown by PA-MBE

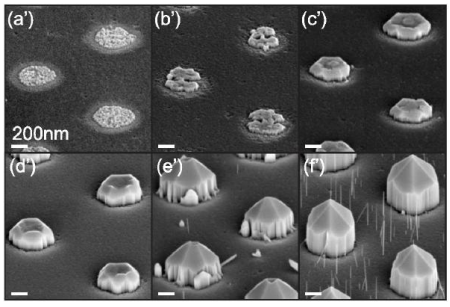

(b) GaN pillars grown by PA-MBE on Ga-polar GaN with a Mo mask – from [36]

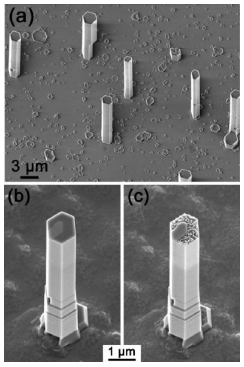

(c) GaN micro-wires grown by metal organic vapor phase epitaxy – from [37]

Figure 1.6: scanning electron microscopy (SEM) images of NWs, pillars and micro-wires named in accordance with the nomenclature used in this manuscript

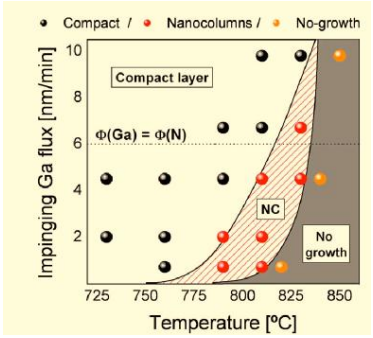

(a) Growth diagram for the self-organized nucleation of GaN NWs on Si(111) (referred here as nano-columns - NCs) – from [39]

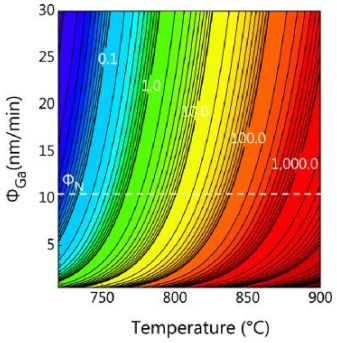

(b) Incubation time for GaN NWs nucleation on Si(111) as function of the Ga flux (Φ_{Ga} and for a N flux of $\Phi_N = 10nm.min^{-1}$ – from [41]

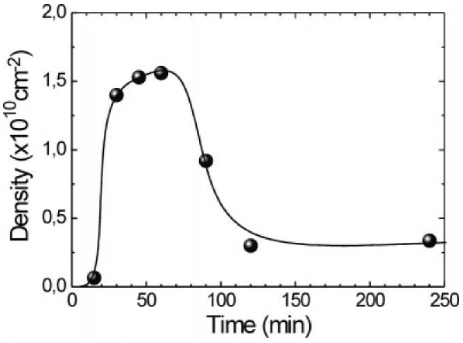

(c) GaN NWs density on Si(111) substrates, as function of growth duration – from [42]

Figure 1.7: Growth phase diagram and density evolution of self-organized GaN NWs

growth diagram, one can see that nucleation of NWs requires III/V ratio lower than 1 at low temperature, in order to obtain the N-rich growth conditions. However, at higher temperature, due to the significant desorption of Ga adatoms, NWs could be readily grown with a III/V ratio above 1 [40].

If grown on bare Si(111), higher substrate temperature leads to lower NW density [43]. It can be explained in terms of incubation time for each NW nucleation as the latter increases with temperature (see Figure 1.7b) and decreases with larger III-V ratio [41]. In addition, later in the growth, coalescence events between neighboring NWs will also reduce the NW density, as shown by Calarco *et al.* [42] in Figure 1.7c. Those

results observed for GaN NWs nucleated on Si(111) could be extrapolated for growth on other types of substrates. However, if nucleated on AlN buffers, *i.e.* on an AlN thin film deposited on Si(111) or sapphire, the structure of the AlN has been observed to influence as well the NW density [44, 45]. It is such dependence on the NW nucleation on the AlN buffer that will be in the scrutiny of the chapter 3.

1.3.3 The interest in GaN nanowires

NWs exhibit excellent crystalline quality, even if grown on highly mismatched materials, noticeably thanks to their ability to bend dislocations toward the side facets [36] and to release the strain through elastic surface deformation [46, 47, 48]. In addition, their self-organized growth has been reported on a variety of substrates including Si(111) [49], Si(100) [49], sapphire [6, 7], SiO_2 [50], SiC (with an AlN buffer) [51], diamond [52] or graphite [53], which indicates a robust nucleation mechanism.

Their photoluminescence (PL) spectra is usually free of luminescence in the gap and might feature band-edge excitonic recombinations with energy line-widths comparable to the state-of-the-art GaN [40].

Although this list is not exhaustive, GaN NWs appear as a well controlled material synthesized through a robust growth method. In comparison, the nucleation of both InN NWs [54] and AlN NWs [55] have been reported and could be readily used for NW heterostructuring. However, AlN NWs need very high substrate temperatures for nucleation, which cannot be reached in the actual MBE setup and InN NWs would probably decompose at the growth temperature of GaN/AlN heterostructures. Hence, in this study and as a general trend observed in the literature, the preference goes to GaN NWs in order to initiate a NW growth, which can be subsequently switched to other materials.

1.4 Conventional characterization techniques

Throughout the manuscript, several characterization methods have been systematically used to probe NWs. Their brief description will be given in the following section.

1.4.1 Reflection high energy electron diffraction

The RHEED is the only tool available in our MBE for *in situ* characterization. It allows to get a live picture of the reciprocal space lattice of the sample surface.

It consists of an electron beam that is focused on the sample surface with a grazing incidence ($\sim 3°$) and an energy of 32 keV, so that the penetration length of the electrons in the sample is limited to the first few MLs. The electrons which are either diffracted or reflected on the sample surface are imaged on a phosphor screen. The obtained diffraction pattern could be analyzed with similar models than for X-rays diffraction although one needs to take into account the energy dispersion and small divergence of the impinging electrons.

In the following chapters, the RHEED has been mostly used to measure lattice parameters and to observe the adsorption or desorption of adatoms. In addition, based on the shape of the Bragg spots, one can infer the roughness of the surface. A streaky RHEED pattern indicates a very smooth surface, whereas a spotty RHEED pattern indicates the existence of small 3D features on the surface. At last, the RHEED pattern is used to emphasize surface reconstructions.

1.4.2 Photoluminescence

Photoluminescence is used in order to probe the lower states of the electronic potential landscape of a material. The technique consists in generating high energy *e*-*h* pairs in a material thanks to a laser excitation and to measure their radiative desexcitation in the material.

In the setup used to acquire the spectra shown in this manuscript, a continuous-wave laser at 244 nm (5.1 eV) is focused on the sample, whose temperature can be set between 5 and 300 K. In the macro-PL configuration, the laser spot shines a sample area of ~ 1 mm^2 whereas in the μ-PL setup, the laser is focused so that it shines a sample area of ~ 1 μm^2 only. In the latter case, it allows to probe single objects if they have a density smaller than 1 μm^{-2}. The collected light from the sample is directed toward a Jobin-Yvon Triaxe550 monochromator equipped with different gratings (600, 1200 and 1800 grooves.mm^{-1}) and an ultraviolet-enhanced charge-coupled device cooled down by liquid nitrogen. In addition, in the μ-PL configuration, a CCD camera is used to image the sample surface.

1.4.3 Electron microscopy

SEM and scanning transmission electron microscopy (STEM) imaging (electron energy: $10 \sim 30$ kV) have been used for structural characterization of the NWs. The spatial resolution is in the order of few nm for the SEM and of 1 nm for the STEM. The intensity of the signal is also dependent on the electron density of the probed material, which gives access to a qualitative chemical analysis. For a more quantitative chemical analysis, an X-ray detector placed in the microscope chamber allows to measure the luminescence spectra in the keV range of atoms excited by the electron beam (energy-dispersive X-ray spectrocopy (EDXS)). Hence, based on tabulated elemental spectra, one can retrieve the chemical composition of the probed area with a moderate accuracy[7]. Note that in the EDXS mode, the spatial resolution of the SEM is reduced.

High resolution STEM imaging of NWs has also been done through collaborations with Catherine Bougerol, Martien den Hertog (Néel Institute, Grenoble, France), Jean-Luc Rouvière and Benedikt Haas (CEA, Grenoble, France).

[7] more precise measurements can be obtained if using proper calibrations steps, but they were considered useless in our studies

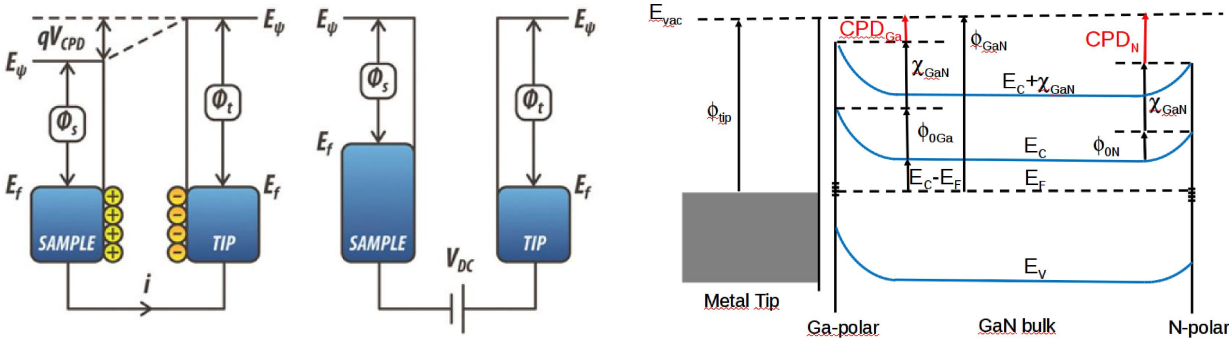

(a) Sketch of the tip-sample contact potential difference

(b) Sketch of the contact potential in a GaN slab

Figure 1.8: KPFM for polarity determination

1.4.4 Atomic force microscopy

Basic structural investigation of surfaces but also of NWs has been done with a commercial atomic force microscopy (AFM).

In addition, KPFM has been done through a collaboration with Ana Cros and Albert Minj (Institute of material science, Valencia, Spain). This technique allows to measure the contact potential difference (V_{CPD}) between a surface and an AFM tip, as depicted in Figure 1.8a. Such potential difference can be use in order to infer the polarity of a crystal by taking advantage of the different surface potentials of the (0001) and ($000\bar{1}$) facets (see Figure 1.8b). It will be the main use of KPFM through this manuscript.

1.4.5 Chemical etching

In thin films, polarity determination used to be done by selective etching with KOH solutions [56, 57]. Such type of characterization has been intended for GaN NWs in the chapters 2 and 3.

The N-polar facets of a material are etched by KOH, leading to the formation of pyramidal structures as shown in Figure 1.9, whereas the metal-polar facets of a material are leaved unchanged. Non-polar facets might be partly etched as well if they feature N-polar terrace edges [58]. At last, KOH is also etching dislocations that are emerging on the sample surface [59].

According to Li *et al.* [60], the etching reaction is as follow:

$$2GaN + 3H_2O = Ga_2O_3 + 2NH_3 \tag{1.2}$$

where OH^- is a catalyst. According to the model of the authors, the etching reaction is effective only if the OH^- molecule can reach Ga atoms, which is favored on N-polar facets but not on Ga-polar ones. It is attributed to a larger density of N-dangling bonds on the Ga-polar facets, which are repulsing the OH^- radicals due to their negative electronic charge.

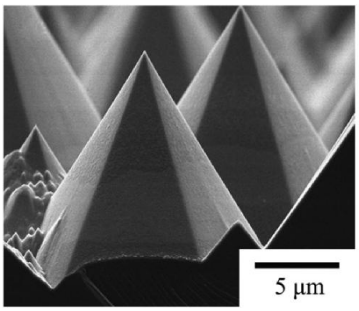

Figure 1.9: N-polar GaN surface after KOH etching – from [57]

1.4.6 Cathodoluminescence

The basic principle is to generate high energy *e-h* pairs in a material by electron excitation and to measure the radiative desexcitation of these *e-h* pairs in the material. Hence, CL is very similar to PL and has the supplementary ability to generate *e-h* pairs in desired areas by moving the electron beam.

Cathodo-luminescence (CL) experiments have been done through collaborations with Gilles Nogues (Néel Institute, Grenoble, France), Matthieu Kociak, Luiz Tizei and Sophie Meuret (LPS, Orsay, France). Such experiments will be further discussed in the chapter 6.

At last, a novel method to measure the lifetime of *e-h* pairs by CL has been developed by the group of Matthieu Kociak and will be referred as time correlated cathodoluminescence (TC-CL) (see sketch in Figure 1.10). Its basic principle is to focus a STEM electron beam on a material so that small bunches of *e-h* pairs are generated [61] with large time intervals between each bunches. Next the collected CL signal stemming from the radiative recombination of the *e-h* pairs bunches is injected in an Hanbury Brown and Twiss setup in order to measure the second order correlation function ($g^{(2)}(\tau)$) of this signal. As exemplified in Figure 1.10b, the $g^{(2)}(\tau)$ function features a maximum at $\tau = 0$, with exponential decays for $\tau \to \pm\infty$ and the time constant of those decays corresponds to the lifetime of the *e-h* pairs in the material. Such novel technique will be used in the chapter 5 but the full demonstration of its principle will not be done as it falls out of the scope of this manuscript[8].

[8] the technique should be published soon and for further details, one can look at the PhD work of Sophie Meuret (LPS, Orsay, France, 2015)

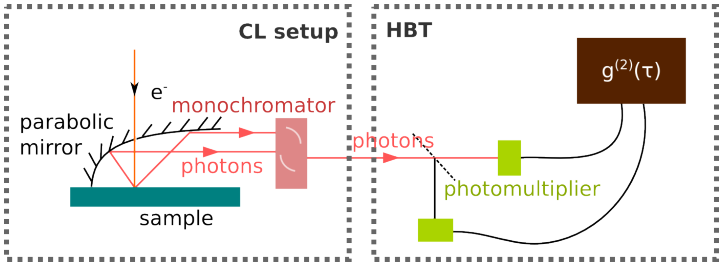

(a) Sketch of the TC-CL setup

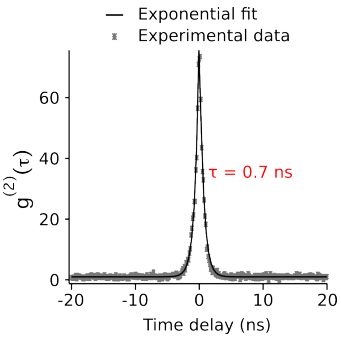

(b) Example of a $g^{(2)}(\tau)$ function measured by TC-CL

Figure 1.10: Basic principle of the TC-CL measurement used to measure e-h pairs lifetime by CL

Chapter 2

Tailoring the one dimensional growth of nanowires

Nanowires (NWs) are defined by their specific quasi-one dimensional growth. Starting from a self-organized nucleation by plasma-assisted molecular beam epitaxy (PA-MBE), NWs exhibit a 50 ± 30 *nm large diameter, independently of the used substrate, for length ranging from* 100 *to* 1500 *nm. As the NW diameter is directly related to the strain in heterostructures, the mastering of growth techniques allowing to get NWs with diameters departing from the usual* 50 *nm are desirable.*
In this chapter, kinetic and thermodynamic mechanisms explaining the one dimensional growth of NWs have been reviewed and illustrated by In/InN growth on GaN NWs. Based on those mechanisms, the NW diameter dependence to the III/V ratio and to the growth temperature have been explored, resulting in the development of a practical growth route for the enlargement of GaN NWs. The AlN growth on GaN NWs has been shown to increase as well the NW diameter but is usually accompanied by a loss of the columnar geometry, which decreases its interest.
At last, reduction of GaN NW diameter has been evidenced through thermal decomposition of GaN.
The different growth routes developed in this chapter will be reused throughout this manuscript in order to eased specific measurements (chapter 3) or to induce different growth modes (chapter 5).

Contents

2.1 Issues at stake

Independently of the substrate, the diameter of self-organized GaN nanowires (NWs) grown by plasma-assisted molecular beam epitaxy (PA-MBE) uses to lie in the 50±30 nm range. At such scale, the elastic relaxation mechanism taking advantage of the available free surface is non-negligible and may have strong influence on growth. For instance, critical radius [46, 47], heterostructure islanding [62] and segregation in ternary allows [63, 64, 65] are directly related to strain, thereby, to the NW diameter. In addition, for diameters lower than 10 nm, radial confinement in the NW is expected to occur [35]. Therefore, it would be desirable to precisely control the NW diameter, in a range between 5 and 150 nm.

A dependence between the diameter of NWs grown on GaN by selective area growth (SAG) and the size of the mask openings has been reported [66], thereby, it could constitute a first step toward diameter engineering. However, such process requires the use of GaN substrates, which somehow denies the intrinsic advantage of NWs to nucleate on cheaper substrates such as Si. SAG growth of GaN on Si has been reported as well, but in such a case, NWs are initially nucleating with their usual small diameter before coalescing with their neighbors [67]. Therefore, the enlargement is provided by coalescence, which might generate additional defects such as stacking faults (SFs) [68] or "zipper" defects [69]. In addition, the minimum opening size of the mask is usually about 50 nm, which *a priori* sets the lower limit for NW diameter to 50 nm. Hence, SAG constitutes an existing interesting solution for diameter engineering of NWs, but it will be disregarded in this chapter.

GaN NWs catalyst-directed growth by Ni-droplets has been reported [70], meaning that by modifyng the droplets diameter and density, one should be able to tune the diameter and density of NWs. However, a non-negligible incorporation of Ni inside the NW so as a large density of SFs has been reported as well, which highly decreases the interest in such growth route. Ga droplets epitaxy to seed the NW nucleation have been tried as well but without any success [71]. Hence, those techniques will be disregarded as well.

In this Chapter, one proposes to explore several other growth routes in order to tune the diameter of NWs after their nucleation.

2.2 The one dimensional growth of nanowires

NWs could be defined through their quasi one-dimensional growth, *i.e.* a larger axial growth (along the *c* axis) compared to the radial growth (perpendicular to the *c* axis). Both Sanchez-Garcia *et al.* [7] and Yoshizawa *et al.* [6] have shown that the growth parameters window resulting to NWs is rather narrow and defined by $T_{substrate}$ above 780 ℃ and strong N-rich conditions. Within this growth window, several phenomenons could account for the growth anisotropy of NWs:

- surface energies

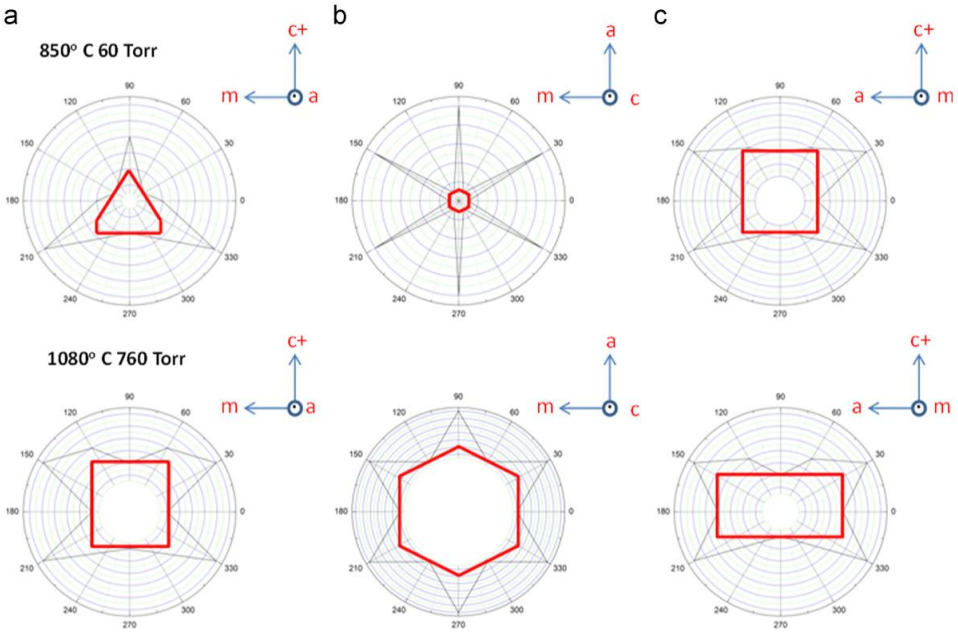

Figure 2.1: Kinetic Wulff plots for GaN grown by HVPE at 60 Torr, 850 ℃ and 760 Torr, 1080 ℃ – (a) *mc* plane, (b) *ma* plane and (c) *ac* plane – from [73]

- diffusion barriers
- geometry of the growth chamber

2.2.1 The role of surface energies

In relation to their wurtzite structure, GaN NWs top facets are $-c$ plane and side facets are m planes [72]. Hence, the atomic configurations of the NW top and side facets are different and should result in different stabilities, *i.e.* formation energies. Those relative surface energies can be estimated experimentally, for instance, by measuring the relative growth speed of the different GaN crystal facets in order to build a so-called kinetic Wulff plot, as shown in Figure 2.1. Such Wulff plot has been reported for GaN hidride vapor phase epitaxy (HVPE) growth [73] and GaN metalorganic vapor phase epitaxy (MOVPE) growth [74, 75] but both do not emphasize a significant difference between $-c$ and m facets growth speed.

In contrast, in a recent report, Li *et al.* [76] have succeeded to build a thermodynamic Wulff plot for GaN based on *ab initio* calculations. Results for different chemical potentials are shown in Figure 2.2. It features the same stable facets than the kinetic Wulff plots obtained by MOVPE and HVPE. However, for stronger N-rich conditions, likely corresponding to the MBE growth conditions of NWs, the stability of polar and semi-polar facets is lower than for non-polar facets, leading to a columnar morphology of the crystal in its thermodynamic equilibrium. Still, the obtained aspect ratio is lower than for NWs, suggesting that additional kinetic mechanisms must play a role in the quasi one dimensional growth of NWs.

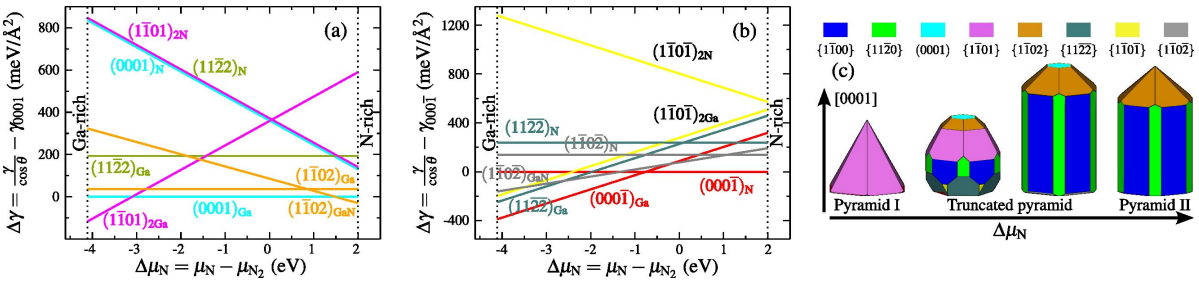

Figure 2.2: Surface energies of different GaN facets relative to (a) the (0001) facet energu or (b) the (000$\bar{1}$) facet energy for different chemical potentials. (c) GaN crystals under thermodynamic equilibrium conditions. The shape varies continuously from Ga-rich conditions (left) to N-rich conditions (right). The underlying label - pyramid I, truncated pyramid, and pyramid II - refers to the top shape. – from [76]

2.2.2 Kinetic mechanisms

By contrast to MOVPE or HVPE, MBE growths are performed in high vacuum, which prevents molecular beams to interact between each other, on their way to the substrate. Hence, chemical reactions can only occur once atoms are physisorbed on the substrate surface, which sets up kinetic barriers for the effective GaN growth. Atomic diffusion on the substrate surfaces and non-uniform adatom densities, due to the shadowing effects, are accounting for those kinetic mechanisms.

Diffusion barriers Once Ga and N adatoms are physisorbed, two different chemical reactions are competing:

$$Ga \quad + \quad N \quad \rightleftharpoons \quad GaN \tag{2.1}$$

and

$$N \quad + \quad N \quad \rightleftharpoons \quad N_2 \quad \Rightarrow N_2^{gaz} \tag{2.2}$$

Despite GaN has a rather high cohesive energy (2.2 eV/bond [77]), the reaction 2.1 is an equilibrium as thermal dissociation of GaN may occur [38], especially if the GaN germ has not reached a critical radius. Conversely, for the competing reaction 2.2, the high stability of the N_2 molecule (binding energy of about 5 eV) prevents its dissociation and allows its quick desorption from the substrate. This reaction is critical as it constitutes a leak channel for N atoms that would hinder GaN growth.

The probability of having one of the two reactions is directly related to the probability for a N adatom to meet first a Ga adatom or another N adatom, meaning that the relative diffusion lengths between Ga and N adatoms is a key parameter.

On polar facets, Zywietz *et al.* [25], have *ab initio* calculated diffusion barriers for Ga and N adatoms, which were found to be significantly higher for N adatoms on both c and $-c$ facets (see Figure 2.3). By contrast, Lymperakis *et al.* [78], have calculated an intrinsic instability of N adatoms on non-polar facets (a and m planes). More exactly, their calculations predict that a N adatoms would quickly desorb as an N_2 molecule by bonding to another N atom included in the GaN matrix, which once extracted,

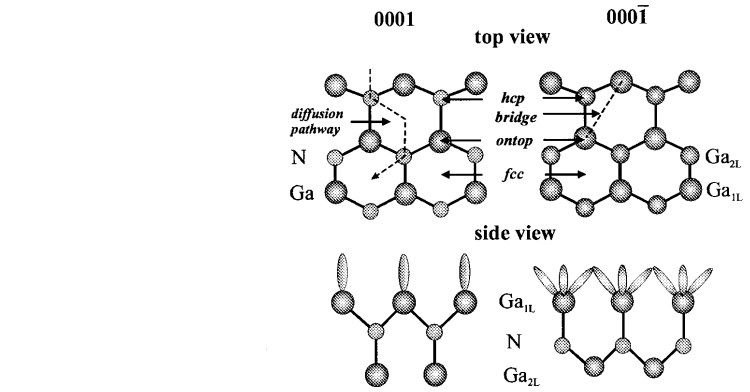

(a) Diffusion paths

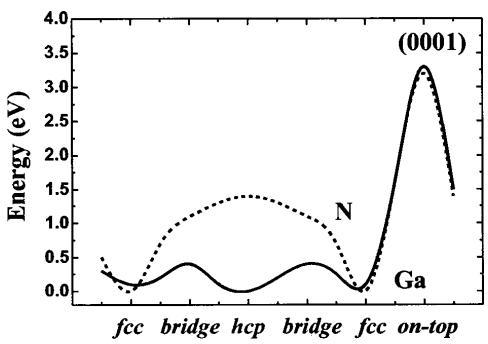

(b) (0001) facet

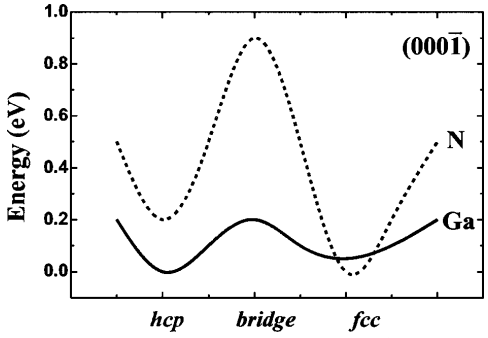

(c) (000$\bar{1}$) facet

Figure 2.3: Total energy (in eV) for Ga adatom (solid line) and N-adatom (dashed line) diffusing on the two polar facets – the energy zero corresponds to the energetically lowest adsorption site – from [25]

leaves a vacancy. This mechanism would suggest that NWs are unstable under N flux, which is not experimentally observed[1]. Nevertheless, it suggests a short lifetime for N adatoms physisorbed on non-polar NW facets, which corroborates with molecular dynamic calculations [79].

Therefore, in comparison to Ga adatoms, N adatoms are kinetically stabilized on polar facets, whereas their low stability on non-polar facets suggests their quick desorption. It means that the probability for an N adatom sitting on a polar facet to meet another N adatom is lower than the probability to meet a Ga adatom, thereby, GaN growth should be prominent over N_2 formation. On the contrary, the low stability of N adatoms compared to Ga adatoms on non-polar facets, prevents the chance for the N adatoms to meet a Ga adatom, thereby, GaN growth is hindered. It is this striking opposite behavior for N adatoms on polar and non polar facets that should constitute the main driving force for preferential incorporation of GaN on the polar facet, hence promoting the axial growth of NWs.

[1]The average NW diameter has been qualitatively observed to be unchanged after exposition for few hours and at 840 °C to the N flux (experiment not shown here)

However, the absence of Ga incorporation on NW side facets (*i.e.* non polar facets) should induce a local Ga accumulation. Those adatoms might either desorb[2], or diffuse. Despite the existence of rather high diffusion barriers along the c axis on NW side facets [78], those Ga adatoms have been reported to reach the NW top surface. It generates an additional Ga flux that contributes to the axial growth of the NW [81].

If diffusion and desorption rates are not fast enough, the Ga concentration on the side facets should significantly increase, resulting in an increased probability for GaN growth, in accordance to the principle of Le Chatelier. Hence, Ga adatom density on NW side facets should be directly related to the radial growth speed of NWs. Knowing that Ga adatom density on side facets is dependent on diffusion and desorption processes, which are both thermally activated, it appears that the substrate temperature could be used to drive the radial growth rate.

Atomic beam geometry Due to the low pressure of the MBE chamber ($\sim 10^{-5}$ mBar), the mean free path for atoms is reaching several meters, implying straight trajectories for impinging atoms. Therefore, the effective atomic flux received by a facet is dependent on its relative orientation compared to the atomic beam, and can be drastically lowered in case of shadowing effect by neighboring nano-structures. In addition, surface atomic densities are dissimilar on non equivalent facets, which would account for different growth speeds under similar atomic pressure (*i.e.* similar effective atomic flux). Both Foxon *et al.* [82] and Hestroffer *et al.* [83] have build geometrical models in order to account for the variations in the effective flux received by facets having different orientations (*i.e.* NW top and radial facets).

For GaN growth, the effective atomic flux impinging on the a facet (hkl), expressed in ML.s^{-1}, is:

$$\nu_{at,(hkl)} = \frac{\Phi_{at} cos(\theta_{at,(hkl)})}{\sigma_{\text{at.,(hkl)}}} \tag{2.3}$$

with $\Phi_{at.}$ the nominal atomic flux leaving the cell expressed in at.cm^{-2}.s^{-1}, $\theta_{at,(hkl)}$ the angle between the facet normal and the atomic flux direction, and $\sigma_{\text{at.,(hkl)}}$ the atomic density of the specific atom on the facet (hkl) expressed in at.cm^{-2}. In the case of our MBE, those values are given in Table 2.4a.

One can evaluate now the effective flux ratio between the NW top and side facets:

$$\frac{\nu_{Ga,(000\bar{1})}}{\nu_{Ga,(1\bar{1}00)}} = 4.01 \quad \text{and} \quad \frac{\nu_{N,(000\bar{1})}}{\nu_{N,(1\bar{1}00)}} = 5.86 \tag{2.4}$$

Neglecting diffusion, desorption and the competitive formation of N_2, it means that when 1 ML (1 nm) of GaN have been grown on the NW side facet, about 4 ML (4.26 nm) of GaN have been grown on the NW top facet.

This geometric model exhibits the importance of the relative position of the N and Ga cells in comparison to the NW top and side facets. It has been experimentally

[2]note that for geometrical reason, a non-negligible part of the desorbing adatoms will impinge on neighboring NWs and might still contribute to GaN growth [80], meaning that desorption in a NW assembly might not constitute an efficient leak channel

Facet	$\sigma_{\mathrm{at,(hkl)}}$		$\theta_{at,(hkl)}$	
	Ga (at.cm^{-2})	N (at.cm^{-2})	Ga	N
$(000\bar{1})$	5.677×10^{14}	5.677×10^{14}	28°	20°
$(1\bar{1}00)$	12.10×10^{14}	12.10×10^{14}	62°	70°

(a) Surface atomic density and cell atomic flux orientation relative to top and side facets of NWs

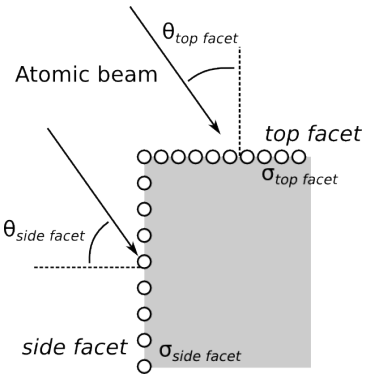

(b) Sketch of the geometry of the incoming beam on NW

Figure 2.4: Effective atomic flux for each facet

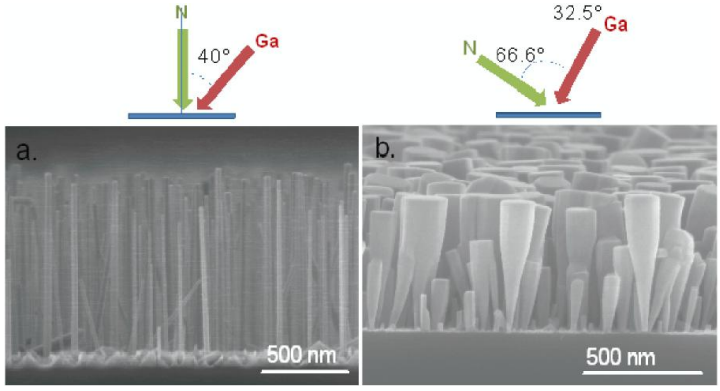

Figure 2.5: Lateral scanning electron microscopy (SEM) observation of GaN NWs (a) with the N plasma cell normal to the substrate and (b) with the N plasma cell at a grazing angle of 66.6 ℃ relative to the substrate – from [84]

emphasized by Galopin *et al.* [84] (see Figure 2.5), who have shown that shifting the N cell toward grazing incidence provokes a large increase in the radial growth of the NWs. Hence, increasing N adatoms density of side facets also foster radial growth.

2.2.3 Case study with InN

The In/InN is a convenient system for SEM observations. First, In is observed to dewet the GaN at low temperature, forming small droplets that are visible by SEM. Second, the InN appears with a different contrast on SEM images and grows with a specific shape that allows to differentiate it from the surrounding GaN. Therefore, the deposition/growth of In/InN on GaN NWs, pictured by SEM and shown in Figure 2.6, could be use to illustrate the mechanisms previously described. One has to note that epitaxial strain between GaN and InN will be neglected here, which constitutes a crude approximation.

In atoms deposited at low temperature ($\sim$ 100 ℃) are observed (Figure 2.6a) to remain close to the NW top. It is assigned to the shadowing effect of neighboring NWs that prevents to deposit In at the bottom of the NWs, and to the low temperature that has hindered In diffusion. Indeed, if deposited at higher temperature ($\sim$ 400 ℃), In is

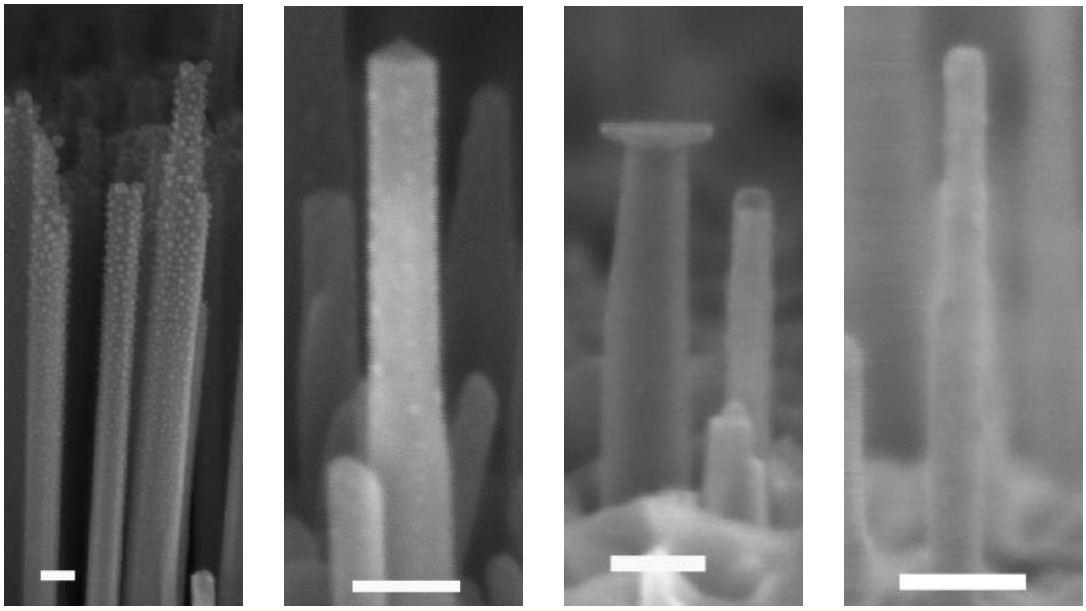

(a) In deposited at low temperature on GaN NWs – N1960

(b) In deposited at high temperature on GaN NWs – N2033

(c) InN grown on GaN NWs – N2044

(d) InN grown on GaN NWs after annealing – N2047

Figure 2.6: SEM side view of In/InN deposited/grown on GaN NWs – scale bar: 50 nm

observed to diffuse all along the NW length (see Figure 2.6b). Noticeably, the In droplets seems to be preferentially located on the corners of the NW. This position minimizes the contact angle with the GaN and the In droplet, suggesting a strong dewetting of In on GaN.

For deposition of In at high temperature, if N atoms are provided at the same time, InN is grown on top but not on the side facets of the GaN NW (see Figure 2.6c). It clearly demonstrates the ability for In adatoms located on the side facets to diffuse and contribute to the InN growth on top of the NW. If the grown InN is then dissociated by annealing, the released In will diffuse again along the NW side walls (see droplets on Figure 2.6d).

2.2.4 The model of Fernández-Garrido *et al.*

As a conclusion, the quasi one dimensional growth of GaN NWs should be the result of three contributions: (i) the higher stability of non-polar facets relative to polar facets, (ii) the kinetic stabilization of N adatoms on polar facet compared to non-polar facets and (iii) the geometry of the incident atomic beams, which all contribute to limit the growth on non-polar facets.

However, NW nucleus radius have been measured to be lower than 16 nm, whereas well developed NW assembly have larger diameters [43], emphasizing a non-negligible NW radial growth, especially at the beginning of the growth. Similarly, SEM images shown in Figure 2.5 suggest the existence of a maximum diameter for NWs, above which

radial growth is quenched. Actually, by taking into account the kinetic mechanisms previously introduced, those startling observations can be fully explained through the growth model developed by Fernández-Garrido *et al.* [85].

During steady state NW growth, the Ga adatom density on top of the NWs (n_{Ga}) is expected to be constant, meaning that the sum of the Ga fluxes converging to the NW top facet (Φ_{Ga}) should be zero. Hence, one can write:

$$\frac{\partial n_{Ga}}{\partial t} = 0 = \Phi^{o}_{Ga} + \Phi^{diff}_{Ga} - \Phi^{desorp}_{Ga} - \Phi^{GaN}_{Ga} \tag{2.5}$$

with Φ^{o}_{Ga} being the flux of Ga atoms impinging directly on the NW top facet, Φ^{diff}_{Ga} being the flux of Ga adatoms coming from the NW side facets, Φ^{desorp}_{Ga} the flux of desorbing Ga adatoms and Φ^{GaN}_{Ga} being the flux of Ga incorporated in the NW. As the growth of NWs is usually performed in N-rich conditions and at high temperature, one has $(\Phi^{o}_{Ga} - \Phi^{desorp}_{Ga}) < \Phi^{o}_{N}$, with Φ^{o}_{N} being the flux of N atoms impinging directly on NW top facet. It means that the expected density of Ga adatoms on the NW top facet should be low, so that considering a diffusion flux of Ga adatoms from the side facets toward the top facet, based on the Fick's law[3], is reasonable.

GaN incorporation requires both Ga and N atoms, so that $\Phi^{GaN}_{Ga} = min(\Phi^{o}_{N}, \Phi^{o}_{Ga} + \Phi^{diff}_{Ga} - \Phi^{desorp}_{Ga})$. If for any reasons (lower growth temperature, increase Ga flux, etc.), the total Ga flux reaching the top facet is increased above Φ^{o}_{N}, one should expect a local Ga accumulation. In such a case, as the Ga density on the top and on the side facets are in equilibrium through the diffusion process, Ga accumulation on the side facets should occur as well, thereby, enhancing radial growth. It will result in an increase of the NW radius r.

Now, if looking at the dependence of the atomic fluxes reaching the NW top facet to r, one can see that Φ^{o}_{Ga}, Φ^{GaN}_{Ga}, Φ^{desorp}_{Ga} and Φ^{o}_{N} are proportional to r^2 (those fluxes scale with the NW top facet area), whereas Φ^{diff}_{Ga} is proportional to r (this flux scales with the areas of NW side facets projected on the plane normal to the Ga impinging flux). Hence, an increase of the NW radius provokes a relative decrease of the contribution of Φ^{diff}_{Ga} on the top facet, which will decrease the local accumulation of Ga-adatoms, hence quenching the radial growth.

This scenario demonstrates that the NW radius is actually self-regulated. If the axial growth speed of the NW already saturates due to the limited N flux, an increase of the incoming Ga flux will result in the enlargement of the NW until a new equilibrium is obtained. Hence, Ga flux could be used to conveniently increase the NW diameter. Conversely, a decrease in Ga flux does not induce a decrease of the NW diameter.

2.2.5 Discussion

Based on the growth mechanism of NWs, few parameters could be *a priori* used to tune the radial growth speed of NWs:

[3] *i.e.* the diffusion scales with the surface density gradient of Ga adatoms

- changing surface relative energies, which can be attempted by changing the local chemical potential or by directly switching material
- changing temperature in order to play with the diffusion and desorption of adatoms on the side facet.
- changing the metal flux, or the cells position, in order to play with the metal density on the side facets

The results given by each of those routes will be discussed in the next sections of this Chapter.

2.3 Enlarging GaN nanowires

Enhanced radial growth for NWs is expected to occur if one succeeds in increasing the Ga or N adatom density on the side facets. In this section, the N beam flux (0.3 $ML_{GaN}.s^{-1}$) and direction relative to the NWs have been kept constant, so that only the influence of growth temperature and of the Ga flux on NW diameter are in the focus.

2.3.1 Growth routes

First, regular GaN NWs assemblies[4] have been grown on Si ($\frac{\Phi_{Ga}}{\Phi_N} = 0.3$ and $T_{substrate} =$ 840 ℃), with the help of an AlN buffer[5]. The latter is aimed at obtaining NWs with a low density ($\sim 10^9$ cm^{-2}) expected to minimize shadowing effects and with a reduced tilt dispersion to minimize their coalescence. NWs were grown for few hours in order to obtain lengths over 400 nm, so that for the subsequent growth steps, the 2D layer[6] will be partially shadowed by the NWs, which efficiently slows down its parasitic growth. Next, GaN was grown on top of the NWs, for 1 hour, with $T_{substrate} \leqslant 840$ ℃ and $\frac{\Phi_{Ga}}{\Phi_N} \geqslant 0.3$. In addition, during this growth step, the rotation of the substrate holder has been turned off, which is expected to slow down the parasitic GaN 2D layer growth. Indeed, due to the shadowing effect and the different orientations of the N and Ga beams, the absence of rotation should minimize the overlapping between areas exposed to the direct Ga flux and areas exposed to the direct N flux, on the 2D layer surface.

2.3.2 Structural characteristics

As shown in Figure 2.7, after a Ga rich and low temperature growth, the average diameter of NWs has been increased compared to conventional N rich growth, especially in their top section. It indicates that shadowing effect coupled with a finite adatom diffusion length are likely preventing the growth of GaN at the bottom of the NW. For the rest of the study, the diameter of enlarged NWs will refer only to the diameter on its top part.

[4] samples: N2062, N2063, N2064, N2068, N2069, N2072, N2075, N2085, N2098
[5] either Al- or N-first AlN buffer (see Chapter 3 for further details
[6] The 2D layer refers to the parasitic growth of Ga-polar GaN at the NW base (see the chapter 3).

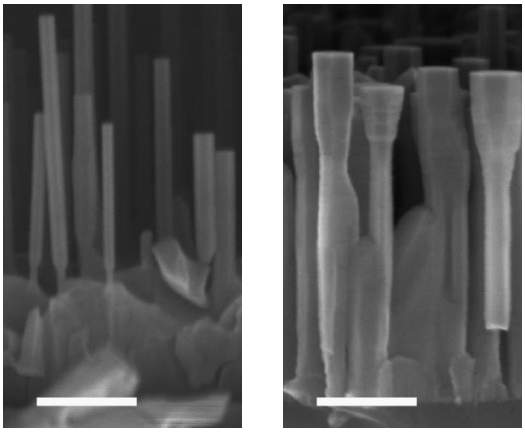

(a) ($T_{substrate}$ = 762 °C, $\frac{\Phi_{Ga}}{\Phi_N}$ = 0.31) – N2069

(b) ($T_{substrate}$ = 718 °C, $\frac{\Phi_{Ga}}{\Phi_N}$ = 0.44) – N2075

Figure 2.7: SEM side views of enlarged NWs – scale bar: 200 nm

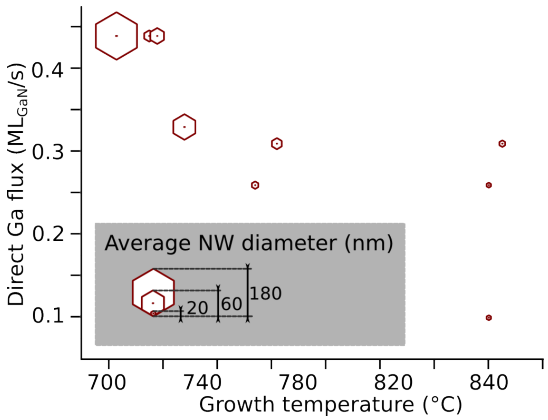

Figure 2.8: Average enlarged NW diameter as function of ($T_{substrate}$, $\frac{\Phi_{Ga}}{\Phi_N}$) – N flux is 0.3 $ML_{GaN}.s^{-1}$

The average diameter of NWs, as function of ($T_{substrate}$, $\frac{\Phi_{Ga}}{\Phi_N}$) parameters, is plotted in Figure 2.8. It clearly emphasizes that increasing Ga flux and lowering the growth temperature is efficient to foster radial growth. It also exhibits the importance of Ga desorption as at 840 °C, increasing the incoming Ga flux by 300% did not implied a significant enlargement of the NWs average diameter.

2.3.3 Ga desorption monitored by reflection high energy electron diffraction

In addition to the enlargement of the top diameter, the Ga rich growth provokes a smoothing of the NW facets. Hence, streaks attributed to diffraction of electron on the NW side and top facets are observable on the reflection high energy electron diffraction (RHEED) pattern, as shown in Figure 2.9a.

Horizontal streaks (green rectangle) corresponds to the NW side facets and vertical streaks (red rectangle) to the NW top facets only. Indeed, the 2D layer, as seen by SEM, exhibits a rough surface and the NW density is high enough to prevent the electron beam (e-beam) to reach the 2D layer[7].

The streak intensity could be directly related to the amount of adsorbed adatoms on the related facets. Therefore, an intensity monitoring could be used to measure the dynamic of Ga adatom desorption and incorporation both on the top and side NW facets at the same time. The obtained intensity transients for Ga desorption and incorporation

[7]NWs are 600 nm long above the 2D layer surface and the e-beam incidence angle is 87°, hence an electron has to travel about 20 μm in the NW layer in order to probe the 2D layer surface. Despite their random position, the probability for an electron to impinge on one NW along his trajectory is close to 100%.

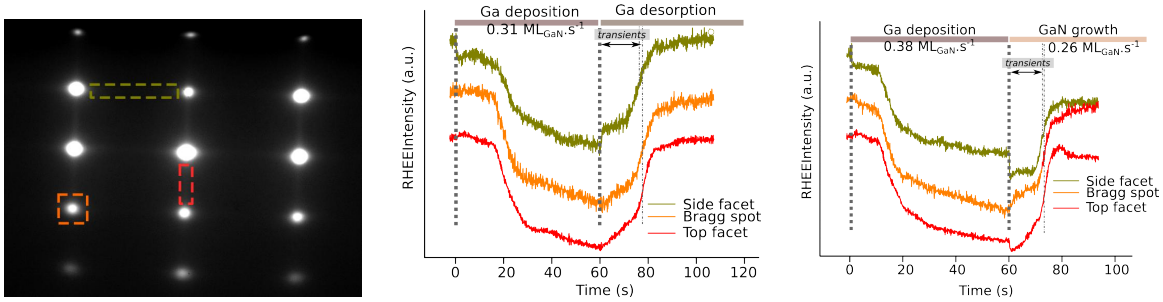

(a) RHEED spectra of enlarged NWs

(b) RHEED intensity transient for Ga deposition and desorption

(c) RHEED intensity transient for Ga deposition and consumption by N

Figure 2.9: RHEED monitoring of desorption and incorporation of Ga on enlarged NWs at 760 ℃ (N2069) – SEM pictures of the NWs are shown in Figure 2.7a

on GaN NWs, at 760 ℃ are shown in Figure 2.9. It exhibits very similar transients, which indicates that the Ga adatom density on all the facets are at the equilibrium. This result correlates well with the kinetic growth model of Fernández-Garrido *et al.*.

2.3.4 Diameter dispersion

The radial growth is not uniform from NW to NW, as exhibited by the top view SEM images of Figure 2.10. The distribution of NW top diameter after enlargement is plotted in Figure 2.11. A large spread is observed while decreasing temperature and increasing the Ga flux.

According to the model of Fernández-Garrido *et al.* [85], the self-regulation of the NW diameter should imply a lower radial growth speed for NWs already having a larger diameter, thereby, reducing the NW diameter dispersion. By contrast, the observed large dispersion suggests that the self-regulation mechanism is not anymore operating, probably because the NW diameter that would allow to reach the equilibrium exceeds by far the distance between two neighboring NWs.

The Ga rich growth is observed to smooth the different facets of the NWs, which is clearly observed by the appearance of RHEED streaks corresponding to the diffraction on NW top and lateral facets (see Figure 2.9a). It indicates that a quasi thermodynamic equilibrium is reached during the growth, expectantly provided by the enhanced diffusion of N adatoms in Ga-rich conditions [86].

One can observe on Figure 2.12 that the top part of the NWs exhibits both polar and semi-polar facets. Based on the theoretical Wulff plot calculated by Li *et al.* [76] (see Figure 2.2), and knowing the probable existence of inversion domains (IDs) in NWs (see the chapters 3 and 4), such different structures for the top facets could be assigned to different polarities. Indeed, due to different surface energies, Ga-polar material is expected to be capped by semi-polar facets, whereas N-polar one is expected to be capped by a polar facet.

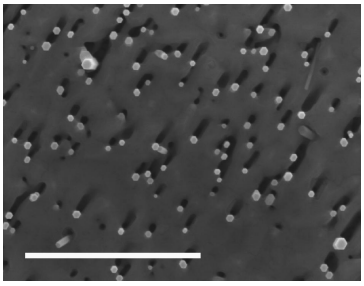

(a) ($T_{substrate}$ = 762 °C, $\frac{\Phi_{Ga}}{\Phi_N}$ = 0.31)

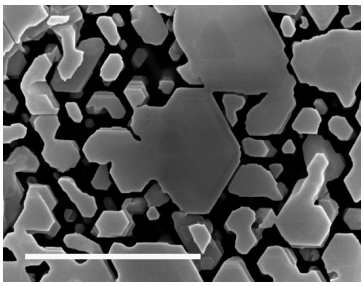

(b) ($T_{substrate}$ = 703 °C, $\frac{\Phi_{Ga}}{\Phi_N}$ = 0.44)

Figure 2.10: SEM top views of enlarged NWs – scale bar: 1 μm

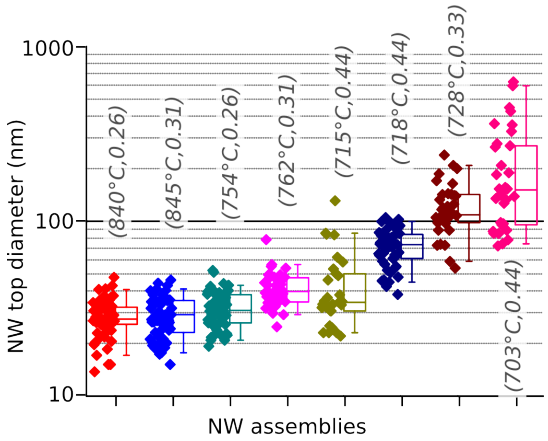

Figure 2.11: NW top diameter for samples grown with different ($T_{substrate}$, $\frac{\Phi_{Ga}}{\Phi_N}$) values – N flux is 0.3 $ML_{GaN}.s^{-1}$ – each dot refers to one measurement – boxes and whiskers respectively enclose $25-75\%$ and $5-95\%$ of the distribution; the mean value is indicated by the line, inside the box.

The presence of different polarities could also account for the observed large dispersion in NWs top facet area. Indeed, Adelmann *et al.* [88] have shown that on a (0001) GaN facet, a Ga bilayer could be stabilized at high temperature and under a small Ga flux, whereas for the $(000\bar{1})$ GaN facet, no such phase exists [87] (see Figure 2.14). Therefore, Ga-polar NWs would be expected to accumulate Ga, *i.e.* foster radial growth, for a lower Ga flux or at least for a different one than N-polar NWs, leading to two distinct behaviors.

At last, hillocks are observed for enlarged NWs having a top diameter above 150 nm (see Figure 2.13), suggesting the occurrence of a Villain-instability[8]. It should be assigned to the low diffusion length of adatoms at the growth temperature used for the enlargement and to a decrease in the Ga flux diffusing from the side facets, which was responsible for providing atoms from the bottom side of the terraces.

2.3.5 Adatom diffusion

For a sample grown with the following parameters, ($T_{substrate}$ = 762 °C, $\frac{\Phi_{Ga}}{\Phi_N}$ = 0.31), an hole in the 2D layer, located beside each NW could be observed by SEM, as shown in Figure 2.15.

[8] the Schwöbel barriers are limiting the diffusion of adatoms across step edges, leading to an increase density of step edges

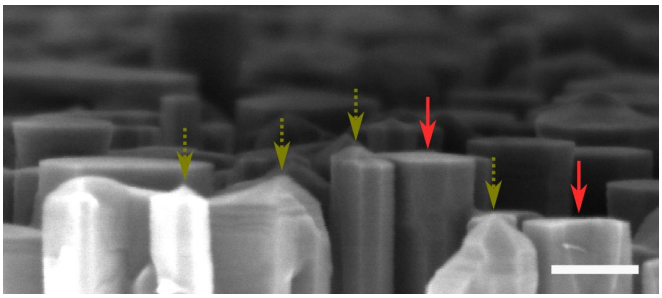

Figure 2.12: SEM side view of enlarged NWs with ($T_{substrate}$ = 718 °C, $\frac{\Phi_{Ga}}{\Phi_N}$ = 0.44) – scale bar: 100 nm – in the foreground, dotted green arrows point toward NWs exhibiting semi-polar top facets whereas the continuous red arrows point toward NWs exhibiting polar top facets

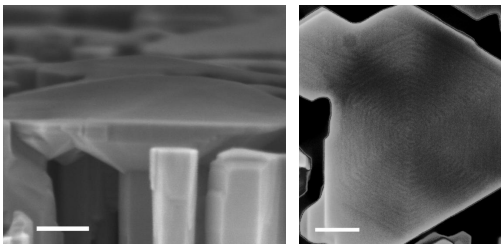

(a) SEM side view – scale bar: 100 nm

(b) SEM top view – scale bar: 100 nm

Figure 2.13: SEM views of the top facet of enlarged NWs where hillocks are observed

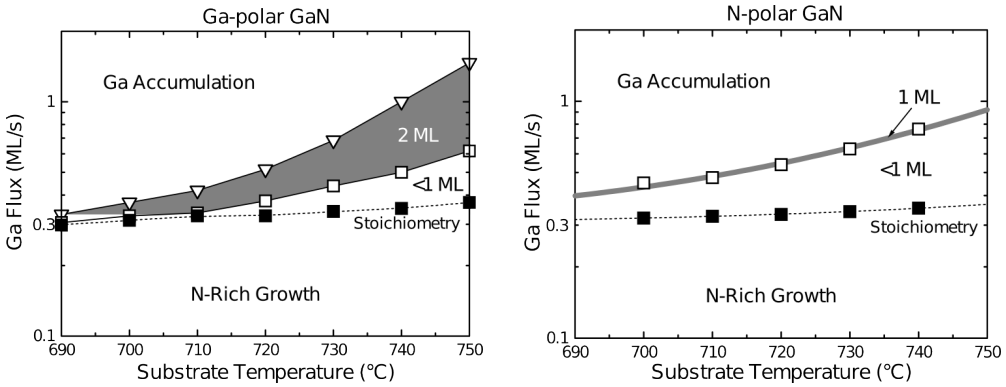

(a) (0001) GaN

(b) (000$\bar{1}$) GaN

Figure 2.14: GaN growth diagram – from [87]

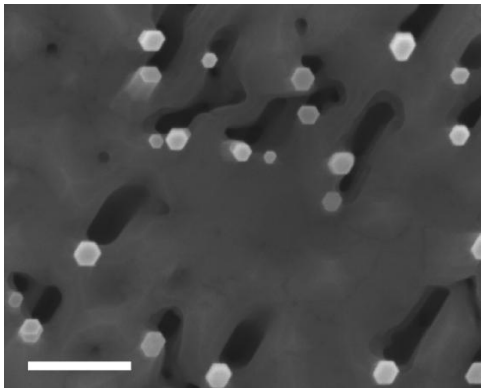

Figure 2.15: SEM top view of enlarged GaN NWs – ($T_{substrate}$ = 762 °C, $\frac{\Phi_{Ga}}{\Phi_N}$ = 0.31) – scale bar: 200 nm

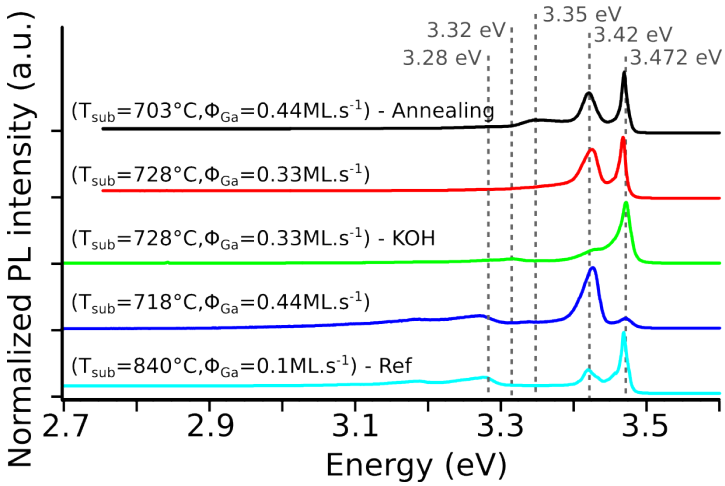

Figure 2.16: 10 K PL spectra of enlarged NWs – annealing has been done at $\sim$ 900 °C for 40 min – KOH etching has been done until the full removal of the NW enlarged top part

This hole is assigned to a shadowing effect, arousing from the absence of sample holder rotation. It should be the result of the low diffusion of N or Ga adatoms on the 2D layer. However, such low diffusion is not observed at all if looking at the shape of the enlarged NW, that have a regular 6 fold symmetry. Even for NWs grown at lower substrate temperature, the enlarged part has never been observed to be preferentially elongated in a specific direction. Those observations would indicate that efficient diffusion channels are existing for Ga and N adatoms on NW side walls, compared to the 2D layer. Lymperakis *et al.* have already calculated a favorable diffusion channel for Ga adatoms on $(1\bar{1}00)$ facets, in a direction perpendicular to the c axis, which would fit our observation. But according to Neugebauer *et al.* [86], the formation of the Ga contracted bilayer on (0001) GaN, which is expected in the present Ga-rich conditions, should also enhance the diffusion of N atoms on the 2D layer. In our case, it seems that the diffusion was high enough to obtain a rather smooth 2D layer top surface, but not high enough to fill the holes beside the NW, suggesting a diffusion length for N or Ga adatoms lower than 20 nm. By contrast, a diffusion of N or Ga-adatoms on NW side facets as long as 50 nm should have been expected.

2.3.6 Optical signature

The Ga rich growth conditions used during the enlargement step of the NWs is expected to produce large GaN crystallites, free of strain and of extended defects, hence having excellent optical properties [89]. In the extreme case, the top part of the NWs can be enlarged until coalescence, producing a low defective 2D film [90]. This technique is referred as epitaxy lateral over growth (ELOG) and is envisaged for growth of high quality GaN on highly mismatch substrates.

Photoluminescence (PL) spectra of assemblies of GaN enlarged NWs are shown in Figure 2.16.

They exhibit the regular features for GaN NWs, no matter the scale of the enlargement:

- exciton bound to donors at 3.472 ± 0.002 eV and referred as the band edge
- exciton bound to several types of SFs at 3.42 and 3.35 eV
- recombination of donor-acceptor pair (DAP) and phonon replica for energies lower than 3.28 eV

The enlargement of the NWs seems not to have influenced dopants incorporation as the relative intensities between the band edge and the DAP band are unchanged. Only, an intensity increase of the 3.42 eV peak, is observed to correlate with the enlargement of NWs. This peak remains unchanged after annealing at 900 °C for 40 min but its intensity is drastically reduced after KOH etching of the NW, which has implied the removal of the NW enlarged top part.

Therefore, the 3.42 eV contribution is attributed to an high density of SFs included in the enlarged part of the NWs. Similar observations have been reported by Lähnemann *et al.* [18], who have observed an increased density of SFs where NW side facets are oblique. Actually, SFs seems to be a regular defect for ELOG GaN grown by MOVPE [91] or HVPE [92] as well. Hence, it suggests a close relation between radial growth and SFs.

However, there is yet no direct explanation for the nucleation of SFs in GaN NWs. From the thermodynamic point of view, Chisholm and Bristowe [93] have *ab initio* calculated a decrease in the SF formation energy while increasing the amount of Si dopants (and in a less extent for Mg dopants). They have correlated this SF formation energy decrease to an increase of the c/a ratio and to a decrease in the ionicity of the atomic bonds in the crystal, both resulting from the doping. Similar trends were observed while comparing the SF formation energy between AlN, GaN, InN and BeO [94]. Based on these considerations, the increased amount of SFs observed in GaN NWs while increasing growth temperature has been assigned to Si doping coming from the melt-back etching[9] of the substrate by Ga [40]. In our case, the Si substrate is fully covered by a thick GaN 2D layer, which should prevent any melt-back etching, although the Ga-rich conditions would favor it. Only the low growth temperature could have accounted for an higher incorporation of impurities from the MBE chamber (O for examples) and the formation of point defects, likely decreasing the SF formation energy. In addition, from the kinetic point of view, the low growth temperature should lower the diffusion length of adatoms, hence increasing the chance of growing a faulted plane.

As a conclusion, enlargement of the NWs can be obtained by lowering the growth temperature and increasing the Ga flux. It is driven by an increased density of Ga adatoms on the side facets. This procedure allows to obtain NWs with top diameter as large as 180 nm, noticeably due to coalescence. Drawbacks of this growth route are the appearance of numerous SFs in the enlarged section of the NW and a loss in uniformity within the NW assembly.

[9] it consists in the etching of the Si substrate by dissolution of Si in Ga droplets due to the existence of a Si/Ga eutectic at 302.8 K [95]

2.4 Diameter evolution with heterostructures

Neglecting the MBE chamber geometry, the one dimensional growth of NWs relies on the asymmetric properties between polar and non-polar facets, which are material dependent. Hence, growing heterostructures should likely result in a growth mode change, with different growth speed ratio between polar and non-polar facets.

A striking example is the growth of InGaN on top of GaN NWs, which for high In content results in a complete loss of the preferential axial growth of the NWs [96]. However, the study of In incorporation falls out of this study and will not be addressed here. In addition, InGaN growth has not been chosen for NW diameter engineering, mostly for two reasons: (i) its growth lacks uniformity from NW to NW, (ii) InGaN is unstable at high temperature, which would prevent the subsequent growth of AlN for instance.

2.4.1 Growth of AlN on GaN nanowires

Two growth steps could be differentiated: (1) the initial deposition of a conformal AlN ML and (2) the "regular" growth of AlN.

Initial conformal growth For very short AlN growth on GaN NWs, a conformal film of AlN is deposited on all the NW facets [97]. In the thin film case, a deposition of Al on GaN quantum dots (QDs) or quantum wells (QWs) has been demonstrated to result in an exchange between the top most Ga atoms and Al atoms, leading to the formation of an AlN ML, at the expense of a GaN ML [98]. A similar mechanism could be assumed in order to explain the AlN conformal growth on GaN NWs. Such growth is isotropic, hence the axial over radial growth speed ratio for AlN is equal to ~ 1 for the first ML.

Regular growth Further growth of AlN leads to the formation of an AlN shell around the NW[10], meaning that radial growth becomes non-negligible all along the initial NW length. SEM and scanning transmission electron microscopy (STEM) micrographs of typical GaN NWs embedded in an AlN shell are shown in Figure 2.17. The shell formation has been assigned to the low diffusion length of Al adatoms on the NW side facets at the usual growth temperature, hence, Hestroffer and Daudin [83] have directly related its thickness to the MBE chamber geometry (*i.e.* the direction of the atomic fluxes).

A consequence of the shell growth is the enlargement of the NW top diameter. Indeed, depending on growth conditions for the shell, NWs with a top diameter reaching 100 nm could be obtained, as recorded in Figure 2.18. However, the shell thickness is usually not uniform due to its dependence on shadowing effect, on the direction of the incoming flux and on the epitaxial strain relaxation. For instance, abrupt variations in the AlN shell thickness are emphasized by black arrows in the NW of Figure 2.17b. It is expected to generate an inhomogeneous epitaxial strain of the shell over the GaN core that would be responsible for the observed bending of the NW. At the scale of the NW assembly, the

[10] N2042, N2178

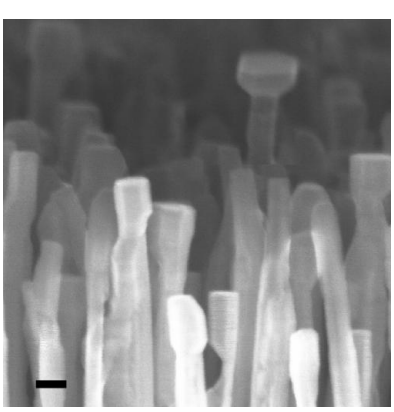

(a) SEM side view of GaN NWs with an AlN shell on top – scale bar: 100 nm

(b) annular dark field (ADF) STEM view of a dispersed NW – scale bar: 100 nm

Figure 2.17: GaN NWs with an AlN shell grown for 32 min, at 860 °C, with a III/V ratio of 1 and without any rotation of the sample holder – in Figure 2.17b, arrows emphasize abrupt variations in the AlN shell thickness

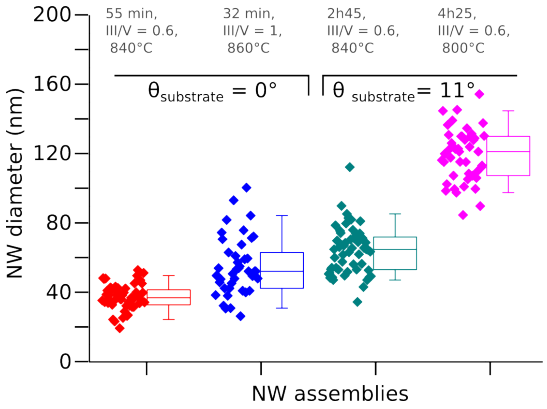

Figure 2.18: NW top diameter for samples grown with an AlN shell and with substrate rotation for different durations, III/V ratio, substrate temperature and $\theta_{substrate}$ – $\theta_{substrate}$ is the angle of the substrate holder in the MBE (see Figure 1.1a, page 10) – N flux is 0.3 $ML_{GaN}.s^{-1}$ – each dot refers to one NW within the assembly – boxes and whiskers respectively enclose $25-75\%$ and $5-95\%$ of the distribution; the mean value is indicated by the line, inside the box.

non-uniform deposition of the AlN shell when rotating the substrate holder provokes a bending of the NWs toward random directions, implying a loss of the RHEED contrast.

By contrast, if the rotation of the substrate holder is turned off during the AlN growth, all the NWs are observed to bend toward the same direction. An *in situ* monitoring performed by measuring the rotation of the NW reciprocal space lattice (RSL) observed by RHEED is shown in Figure 2.19. The in-plane shift of a $000l$ AlN Bragg spot along a direction normal to a side facet of the NW, monitored by RHEED, is reported as function of the deposited amount of AlN. In this case, the in-plane direction has been later shown by SEM observations not to be parallel to the bending direction (about 30° off). Nevertheless, a linear dependence between the average NW tilt, *i.e.* bending, and the amount of grown AlN is observed, with an amplitude of $0.018°.ML_{AlN}^{-1}$. Taking into account the 30° misalignment of the RHEED azimuth, the amplitude of the NW bending should be $0.021°.ML_{AlN}^{-1}$. NWs are bending toward the N and Al cells (which are roughly in the same direction), emphasizing again the prominent role of the MBE chamber geometry. However, the dispersion in NW tilt within the assembly is observed to increase as well while depositing AlN, which leads after ~ 100 ML_{AlN} of deposited AlN to a loss of the RHEED contrast. Hence, stopping the sample holder rotation during AlN growth allows to delay but not to prevent the loss of the RHEED contrast, stemming from the

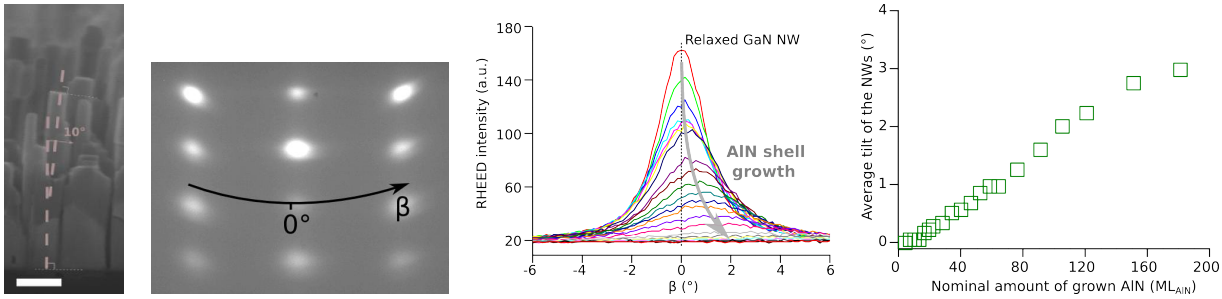

(a) SEM side view of the NW assembly – scale bar: 100 nm

(b) RHEED spectra of the AlN grown on the GaN NW assembly – 60 ML_{AlN} have been nominally grown

(c) RHEED intensity profile along the β direction of a 000l spot

(d) Average bending of the NWs as function of the deposited amount of AlN

Figure 2.19: *In situ* monitoring of the NW bending during AlN growth – N2133

increased tilt dispersion of the NWs.

Interestingly, the AlN NWs are observed to feature semi-polar facets in the opposite direction of the NW bending. Based on the thermodynamic Wulff plot of GaN [76], it suggests a difference of chemical potential between the two sides of the NWs, leading to different stabilities for the facets. Assuming similar facets energy for GaN and AlN, the growth of semi-polar facets would be favored for less prononced N-rich conditions, which would fit with a lower diffusion length for N adatoms compared to Al adatoms on AlN NWs.

2.4.2 Enhancing radial growth

According to the geometric model of Hestroffer and Daudin [83], the radial growth of AlN can be enhanced by moving the N and/or Al cell toward grazing incidence. More exactly, it is not the cells that are physically moved but the sample holder, through the angle $\theta_{substrate}$ indicated in the MBE sketch of Figure 1.1a (at page 10 in chapter 1), in order to expose the side facets of the NWs to the direct Al and N flux. A drawback of this technique is that the sample is shifted out of the convergence point of all the cells, thereby, RHEED cannot be used anymore, so as the atomic flux values measured from previous calibrations.

Two AlN shells on GaN NWs[11] have been grown along the route proposed by Hestroffer and Daudin [83]. Usually, thin GaN sections have been added within the AlN shell, but their specific characterization will be only addressed in the chapter 5. Typical SEM side view of the obtained NWs are shown in Figure 2.20, and the obtained NW top diameters are recorded in Figure 2.18.

[11] N1950 and N1958

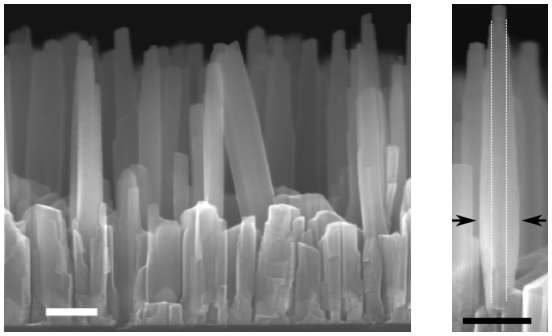

(a) (b)

Figure 2.20: SEM side view of AlN grown on GaN NWs with $\theta_{substrate} = 11°$ – N1950 – scale bar: 200 nm

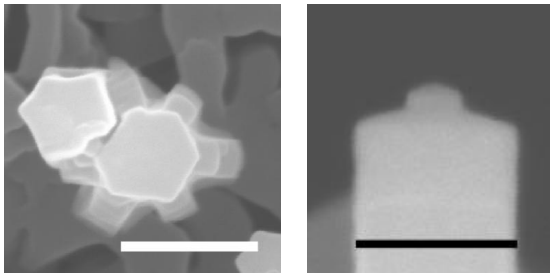

(a) scale bar: 200 nm (b) scale bar: 100 nm

Figure 2.21: SEM top view of AlN grown on GaN NWs – N1958

The method is observed to be efficient in order to increase the diameter of NWs, up to 120 nm at their top, although the larger diameter increase actually occurred at the NW bottom or mid-height. In addition, the NW top facet is usually not flat, and there are multiple shoulders on the NW side facets, as shown in Figure 2.21. Those shoulders are deforming the NW, ultimately provoking a loss of the regular NW geometry.

An appreciable consequence of AlN growth is the enlargement of the NW top diameter thanks to the radial growth of the AlN. However, the formation of an AlN shell around the initial GaN NWs, which is not uniform, generates an inhomogeneous epitaxial strain along the NWs length leading to their bending. It provokes a loss in the NW uniformity within the assembly, which can hamper the ability to perform a proper RHEED *in situ* monitoring of the growth. In addition, the low diffusion of the Al adatoms on the NW side facets might deform the NWs, which are loosing their columnar geometry. Hence, those drawbacks are limiting the relevance of AlN heterostructuring for a diameter engineering purpose.

2.5 Thinning nanowires

The typical diameter for self-organized growth of GaN on Si is 50 ± 30 nm, but NW nuclei were observed with diameters as small as 10 nm [43]. It demonstrates that a non-negligible radial growth is occurring at the beginning of the NW growth. It should be attributed to the self-regulation of the NW diameter, due to a large diffusing flux of Ga adatoms reaching the NW. In order to hinder this initial radial growth, high temperature and low Ga flux should be used. However, it leads to extensive incubation times before the effective NW nucleation [41], which sets up a practical upper limit for nucleation temperature and fluxes, thereby, a lower bound for NW diameter. In addition, the self-regulation mechanism of the NW diameter only lead to diameter increase, hence forbids

an eventual thinning procedure only by playing with temperature or flux ratio during GaN growth.

The route intended here is to perform an annealing of the NW, in the MBE chamber, right after their growth. The *in situ* annealing is aimed at preventing the possible formation of natural oxide on the NW facets if they are exposed to air, which would add another free parameter in the system.

2.5.1 GaN decomposition

There are various reports tackling GaN thermal dissociation.

According to the work of Fernández-Garrido *et al.* [38], GaN decomposition in vacuum is a thermally activated process, already operating at 750 ℃ (for the (0001) GaN facet). It is in accordance with the observation of Groh *et al.* [99], who measured an increase of the N_2 overpressure for GaN thermally annealed in vacuum at 700 ℃ and above.

Lin *et al.* [100] have used low temperature PL in order to monitor GaN properties after thermal annealing in N_2 atmosphere (at ambient pressure) at either 700 or 900 ℃. The overall PL intensity was increased after the treatment at 700 ℃ but decreased after the treatment at 900 ℃. However, this PL intensity drop cannot be directly related to thermal dissociation, as diffusion and coalescence of point defects might also account for the generation of non-radiative defects. Instead, Raman could be used to probe the crystal structure modification along with thermal annealing in N_2 atmosphere. Kuball *et al.* [101] observed a small evolution of Raman spectra for annealing between 900 and 1000 ℃ and large modification for annealing above 1000 ℃. Hence, they have inferred a strong thermal dissociation of GaN only above 1000 ℃.

The reported temperature threshold for thermal annealing in vacuum are much lower than in the N_2 atmosphere (at ambient pressure). Although temperature measurements are less accurate in vacuum, this difference should be assigned to the prominent role of surface in the GaN dissociation process, whose stabilities are tailored by the gaseous environment. Vartoli *et al.* [102] have annealed GaN in N_2 atmosphere and monitored the surface evolution. Starting from a resistive GaN crystal, they have observed an increased conductivity after annealing below 900 ℃ that has been assigned to the formation of N vacancies in the vicinity of the surface.

As a conclusion, GaN decomposition in vacuum should be favored at low temperature (lower than 900 ℃) and expectantly without a strong degradation of the GaN "bulk", *i.e.* for GaN far from the surfaces. However, the properties of NWs are largely dominated by their surface, which would suggest an high degradation of their optical properties after high temperature annealing.

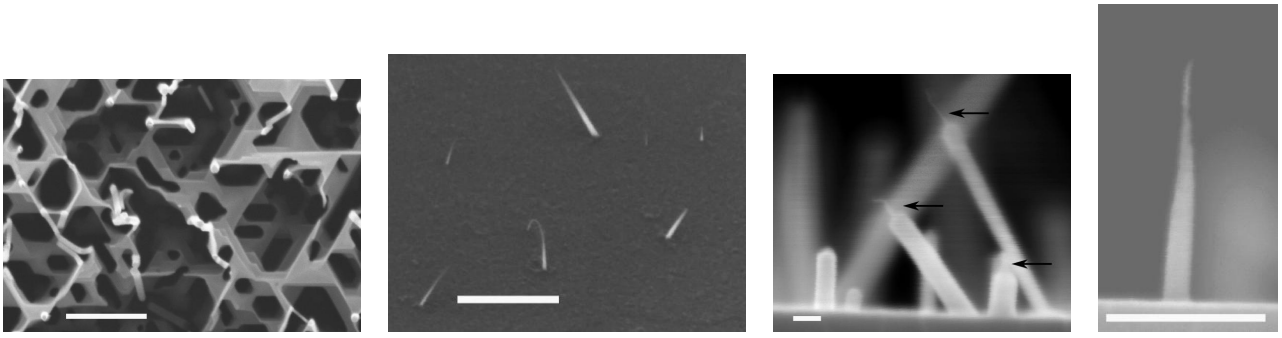

(a) Top view SEM image – Annealing: ∼ 900 °C; 1 hour – AlN buffer – scale bar: 200 nm

(b) Top view SEM image – Annealing: ∼ 900 °C; 1 hour – no AlN buffer – scale bar: 200 nm

(c) Side view SEM image – Annealing: ∼ 900 °C; 30 min – no AlN buffer – scale bar: 20 nm

(d) Side view SEM image – Annealing: ∼ 900 °C; 30 min – no AlN buffer – scale bar: 100 nm

Figure 2.22: SEM micrographs of annealed GaN NWs

2.5.2 Structural characteristics

A regular assembly of GaN NWs have been grown on Si with an AlN buffer for 5 hours (III/V ratio of 0.3 and $T_{substrate} = 840$ °C)[12]. The growth has been ended by an annealing at ∼ 900 °C (Ga desorption time on Si of ∼ 1 s) for one hour. An SEM top view image of the sample is given on Figure 2.22a.

The minimum NW diameter is 10 nm according to the SEM images, which is thinner than for usual NW assemblies. A rough estimation would give a decomposition speed on the side facets of 5 ± 3 nm.h^{-1}. A striking feature is the structure of the 2D layer that exhibits a similar structure than after a KOH etching, *i.e.* deep hexagonal holes. It suggests a preferential decomposition for GaN in areas that are also prone to be etched by KOH, *i.e.* extended defects and N-polar IDs. Actually, Mastro *et al.* [103] have reported an increased thermal stability of Ga-polar surface compared to N-polar surfaces. This different behavior is assigned by the authors to the inability to accumulate Ga droplets on Ga-polar GaN, which would act as a catalyst for the GaN decomposition[13], and to the low density of grain boundaries in their Ga-polar GaN. In our case, the 2D layer is highly defective compared to the NWs and expectantly free of N-polar IDs (see the chapter 3), therefore, it presumes grain boundaries and extended defects as favored dissociation sites for GaN in the 2D layer.

Two additional NW assemblies[14] have been grown directly on Si at high temperature ($T_{substrate} \sim 860$ °C with a III/V ratio of 0.3) to obtain already thin NWs (about 20 nm in diameter). Next, the two assemblies have been annealed at ∼ 900 °C for respectively 60

[12] N1912

[13] It is expected to lower the activation energy of GaN decomposition by dissolving the freshly dissociated Ga and N atoms.

[14] N1953 and N1956

and 30 min. Typical SEM images are shown in Figure 2.22b and 2.22c. After 60 min of annealing, the NWs exhibit a needle like shape. At their top, the diameter is lower than 10 nm, which suggests a radial decomposition speed of 5 ± 3 nm.h^{-1}, in accordance to the previous sample. Actually, in this case, the SEM imaging is not anymore suited for the diameter measurement as thin NWs are becoming transparent to electrons. In addition, NWs are electrically charged by the SEM e-beam, leading to their deformation due to electrostatic interactions (see the bended NW in Figure 2.22b that has been deformed "on live" during the SEM imaging).

Within the NWs annealed for 30 min, a few features a thinned top part whereas their bottom part is preserved, with an abrupt transition between both (see arrows in Figure 2.22c and Figure 2.22d). The thin wire, which is emerging from the larger base of the NW is tentatively assigned to Ga-polar IDs. It would corroborate with the preferential decomposition of N-polar GaN compared to Ga-polar GaN observed by Mastro *et al.* [103], leading to the removal of the N-polar shell prior to the Ga-polar core. It is also in accordance to the ID diameter measurements performed by STEM, which used to exhibit diameters lower than 10 nm for IDs. Therefore, GaN dissociation is also dependent on facets, with a preferential decomposition on $(000\bar{1})$ facets compared to side facets and to (0001) facets.

As a conclusion, *in situ* annealing of GaN NWs is efficient to decompose GaN. However, the effective dissociation is not anisotropic and has been shown to depend both on facets and sample geometry. Hence, the NW diameter dependence to annealing time and temperature is not straightforward, which limits the practicality of this technique. Nevertheless, in the case of polar core-shell NWs, the NW diameter could be abruptly reduced down to the Ga-polar ID diameter, thanks to the preferential dissociation of GaN on the $(000\bar{1})$ facet compared to the (0001) one.

2.6 Conclusion

In this Chapter, the focus has been brought on the mechanisms providing the one dimensional growth of NWs. Their understanding has been used to perform a diameter engineering of NWs in the 5 to 180 nm range.

A literature review, corroborated by In/InN deposition/growth has emphasized the dependence of NW steady state growth on three facts:

- a difference between NW facets formation energy,
- a difference in Ga and N adatoms stabilities and mobilities on NW facets,
- the geometry of the incoming atomic flux in the MBE chamber

Hence, for regular growth conditions, NWs with a 50 ± 30 nm diameter are systematically obtained for length varying between 100 and 1500 nm.

Next, a tailoring of those mechanisms have been attempted in order to modify the top diameter of post nucleated NWs. Best results were obtained for NW enlargement by

increasing the Ga flux and lowering the growth temperature. NWs with top diameters up to 180 nm have been obtained although a loss in uniformity within the NW assembly is noticed. Growth of AlN on GaN, especially by shifting the Al cell toward grazing incidence, is also efficient for enlarging the NW diameter. However, a roughening of the facets was observed, ultimately leading to a loss of the NW geometry, and the increase of the NW tilt dispersion within the assembly are limiting the relevance of this technique. At last, thinning of the NWs has been observed upon annealing under vacuum. However, the dependence of the NW diameter to annealing temperature and duration was not straightforward, which makes the technique unpractical. Noticeably, the presence of IDs has been shown to interfere in the GaN decomposition process, leading to the formation of exotic structures.

Enlargement both by AlN growth or Ga rich growth have been carried on to answer the need of studies addressed in this manuscript (see the chapters 3 and 5).

Chapter 3

GaN nanowires self-organized nucleation and polarity

Starting from the observation that reported polarity and tentative nucleation scenarios for self-organized GaN nanowires (NWs) are missing a global coherence, the experimental work gathered in this chapter aims at re-investigating NW nucleation and polarity.
The focus has been first directed to the AlN nucleation film usually grown prior to NW nucleation. Structural characterizations have revealed the existence of specific nano-structures that are breaking the uniformity of the film. A nucleation scenario has been developed for those singularities, relying on the high reactivity of Al and N atoms with the Si substrate. Next, those singularities were observed to interfere in the subsequent nucleation of GaN NWs by playing the role of preferential nucleation sites.
A systematic polarity study has shown that GaN NWs are N-polar whereas the GaN 2D layer is Ga-polar. Hence, it has been deduced that the N-polarity is a requirement for the self-organized nucleation of GaN NWs and that the AlN buffer singularities are actually seeds for N-polar GaN.
At last, the unexpected presence of Ga-polar inversion domains (IDs) has been evidenced in a significant ratio of GaN NWs, whether nucleating on AlN buffers or on bare Si. It brings a first explanation to the large variability of the reported GaN NW polarity. A few consequences of the presence of IDs in NWs will be tackled in the next chapters.

Contents

Experimental data credits

All the scanning transmission electron microscopy (STEM) images shown in this chapter have been acquired by Benedikt Haas (CEA, Grenoble, France), transmission electron microscope (TEM) images coupled to energy-dispersive X-ray spectrocopy (EDXS) have been acquired by Catherine Bougerol (CNRS, Grenoble, France), synchrotron X-ray measurements have been done by François Rieutord and Samuel Tardiff (CEA, Grenoble, France) and all the Kelvin probe microscopy images have been acquired by Ana Cros and Albert Minj (Institute of material science, Valencia, Spain).

Related publication

Part of the results dealing with the polarity and structure of the AlN buffer along with the consequences on GaN nanowire (NW) nucleation have been published by Auzelle *et al.* [104]. In addition, the development of the Kelvin probe force microscopy (KPFM) technique for the determination of NW polarity has been published by Minj *et al.* [30].

3.1 Issues at stake

The robustness of GaN NW self-organized nucleation by plasma-assisted molecular beam epitaxy (PA-MBE) is remarkable. Indeed, using similar growth conditions (*i.e.* temperature higher than 800 °C and $\frac{\Phi_{Ga}}{\Phi_N} \ll 1$), NWs nucleation has been reported on a wide variety of substrates including Si, sapphire, diamond, SiC and graphite with the possible help of AlN buffer layers (for references, see page 20 in chapter 1). It suggests a nucleation mechanism intrinsically based on GaN properties rather than on the substrate surface properties. As soon as a GaN nucleus has formed non-polar facets, the mechanisms leading to the one dimensional growth of NWs are expected to start operating (see the chapter 2). Hence, a key element in NW nucleation resides in the formation of m facets.

Strain as a driving force Among the ingredients ruling the nucleation of GaN and potentially triggering the formation of m facets in the initial germs, strain is usually highlighted in the literature. Two types of strain are identified:

- a surface strain, also referred as a Laplace-pressure induced strain, stemming from the perturbed atomic arrangement in the vicinity of the surface [105, 106]. Such strain becomes prominent in the case of very small GaN crystallites for which the surface over volume ratio is high.
- an epitaxial strain if nucleation is occurring on a crystallized surface

A typical example is the epitaxial strain of GaN grown on AlN, which infers the formation of GaN quantum dots (QDs) through the Stranski Krastanov (SK) growth mechanism [107]. Its specificity is to switch the growth mode from 2D to 3D in order to efficiently

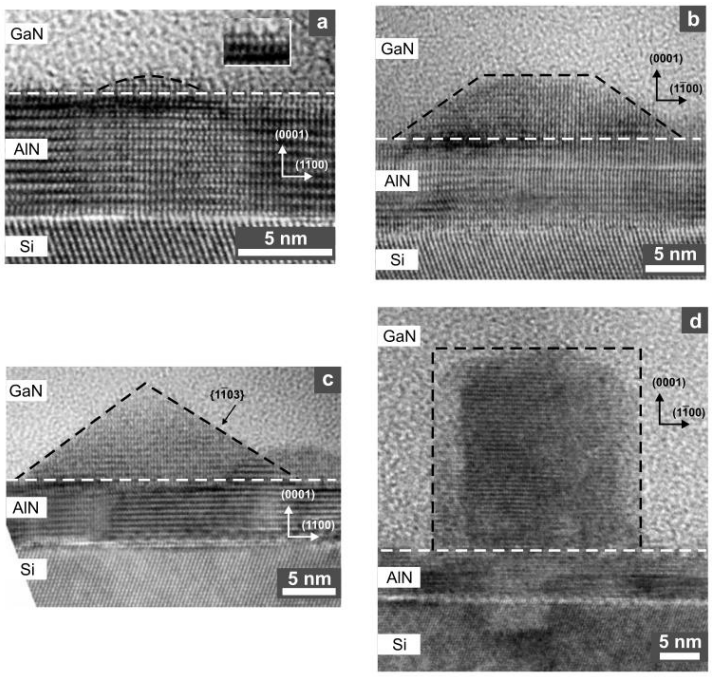

Figure 3.1: TEM micrographs of the successive shapes of GaN nucleus along growth, according to the model of Consonni *et al.* [109] – (a) the spherical capped island, (b) the truncated pyramid, (c) the full pyramid and (d) the NW nucleus

release the accumulated strain through elastic deformation of the 3D islands. It results in the singularization of tiny areas over the surface, *i.e.* the SK QDs, which will be preferential incorporation sites for further GaN growth.

The nucleation of NWs also corresponds to a singularization of tiny areas over the surface, thereby, recalling SK QDs nucleation. However, NW nucleus have been measured to be fully relaxed, whereas SK QDs are still strained [108], which suggests that it is actually the strain relaxation process that would form m facets, thereby, triggering NW nucleation.

The nucleation model of Consonni *et al.* Consonni *et al.* [109] have observed by TEM the shape evolution of GaN crystallites from the first deposited nuclei to the NWs formation (see Figure 3.1). It revealed that the growth proceeds along a Volmer-Weber mechanism[1]. First, GaN crystallites have a spherical capped shape that evolves toward a truncated pyramid shape and next a full pyramid.

This shape evolution is specifically optimizing the relaxation of the epitaxial elastic energy accumulated in the crystallite, meaning that a similar driving force than for SK QDs nucleation is operating. Then, Consonni *et al.* observed that NW nucleus, identified as crystallites laterally enclosed by m facets, are plastically relaxed. Indeed, a

[1]similar to the SK growth mechanism as it is strained induced, except that no GaN wetting layer is formed in between the 3D islands

threading dislocation is systematically observable at their bottom. As a consequence, it was concluded that the shape transition from the full pyramid toward the NW nucleus is driven by the plastic relaxation of the pyramid. Once free of strain, the shape of this crystallite becomes driven by surface energies, compelling the formation of m facets. To strengthen this hypothesis, they additionally mentioned that the GaN NW nucleus radius grown on AlN was in the range of the critical radius for which the plastic relaxation of GaN on AlN becomes energetically favored.

This mechanism has been further strengthened by a strain relaxation monitoring of the initial GaN nucleus [110] and by a thermodynamic modeling of the growth [111]. It is this mechanism, based on the observation of GaN NW nucleation on AlN, that is usually invoked to explain the NW growth on all other crystalline substrates. However, we do notice some remaining puzzling facts.

The density of GaN SK QDs grown on AlN is never lower than 10^{10} cm^{-2} whereas NW density can be lowered down to 10^{9} cm^{-2}. It implies that only a fraction of the pyramids assembly should ripen into NWs. Additionally, the growth of GaN NWs on AlN is always accompanied by the formation of a rough GaN 2D layer located at the foot of the NWs. It suggests that two different growth modes are achievable for the GaN pyramids: the NW one or the 2D layer one.

What would be the driving force leading to either of those two growth modes?

NW nucleation on AlN buffers No 2D layer is observed in ensemble of NWs grown on bare Si, whereas one is observed if depositing a thin AlN nucleation film, called AlN buffer, prior to NW nucleation. It suggests, that AlN is a main contributor in the growth of the 2D layer. Thus, in this chapter, the focus will be mainly brought to NWs grown on an AlN buffer.

One can note a remarkable variability in the reported polarity of NWs nucleated on Si (see Table 3.1). Neglecting possible inversion domains, which will be discussed later, NW polarity has to be set at the NW nucleation step, depending of the chemical interface between the substrate and the GaN nucleus. The polarity variability hence suggests non-negligible variations in the AlN buffer growth performed in different laboratories and/or MBE chambers.

Actually, a few reports precisely details the AlN buffer structure prior to GaN NW nucleation. Brubaker *et al.* [114] first noticed that depending on the growth conditions, the AlN could feature nano-structures, so-called “columnar protrusions“, presumably acting as nucleation centers for GaN NWs. It would mean that strain relaxation of the initial GaN nucleus is not sufficient to trigger the NW nucleation, but that an additional seeding by nano-structures in the AlN is required. The synthesized NWs on this AlN buffer were determined Ga-polar. Largeau *et al.* [31] have reported the growth of similar nano-structures in their AlN buffer, namely ”AlN pedestals”. However, they only obtained N-polar NWs. This dissimilarity should likely stem from a reversed polarity of the underneath AlN, probably due to different growth conditions. At last, Fernández-Garrido *et al.* [51] have reported the absence of NW nucleation on high quality metal polar AlN, at the exception of few N-polar NWs, which suggests the impossibility to

Author	Nucleation film	GaN NWs polarity	Measurement	Remarks
		Silicon 111 substrate		
Hestroffer *et al.* [29]	(SiN)	N-polar	KOH attack and X-ray measurements	-
Kong *et al.* [33]	(SiN)	N-polar	EELS (50 NWs)	-
Carnevale *et al.* [26]	(SiN)	90% N - 10% Ga	PINLED	-
Furtmayr *et al.* [112]	(SiN)	Ga-polar	CBED (20 NWs)	-
Armitage *et al.* [113]	(SiN)	Ga-polar	KOH	InGaN NWs
Romanyuk *et al.* [32]	(SiN)	N-polar	LEED and XPD	-
Largeau *et al.* [31]	Al-first AlN film	N-polar	CBED and KOH	-
Brubaker *et al.* [114]	Al-first AlN film	Ga-polar	CBED	-
Kong *et al.* [33]	Al-first AlN film	Ga-polar	EELS	AlGaN NWs
Alloing *et al.* [37]	N-first AlN film	90% Ga - 10% N	CBED	NH3-MBE
		Polar substrates: SiC(0001) and SiC(000$\bar{1}$)		
Fernández-Garrido *et al.* [51]	AlN film	N-polar	CBED and EELS	for Si- and C-polar SiC

Table 3.1: Reported results on the polarity of self-organized GaN NWs grown by MBE – CBED stands for convergent beam electron diffraction, EELS for electron energy loss spectroscopy, PINLED for p-i-n light emitting device, LEED for low energy electron diffraction, XPD for X-ray photoelectron diffraction

nucleate Ga-polar NWs.

Those antagonist results are far from giving a clear picture of the NW nucleation process. Nevertheless, it emphasizes the fact that both polarity and nano-structures in the AlN buffer have to be taken into account if one wants to fully understand the nucleation mechanism. As a consequence, an in-depth study of the AlN buffer, including polarity and nano-structures, becomes a necessary step prior to the study of the GaN NW nucleation.

3.2 AlN buffers

3.2.1 AlN buffer growth routes

The AlN buffer routes reported in the literature are usually poorly detailed. Nevertheless, two main schemes can be identified:

- the Si surface is wet by Al prior to nitridation [115, 116, 117, 118, 119]. This predeposition of Al is aimed at saturating the Si dangling bonds, which is empirically expected to prevent the formation of Si_xN_y during the nitridation. Indeed, Si_xN_y is known to quickly become amorphous under exposition to N, which would ruin the epitaxial relationship between Si and AlN [120]. However, this approach has been shown to be unable to fully prevent Si_xN_y appearance, except if Al is continuously provided during the nitridation [121]. This is due to the fact that the full coverage of the Si surface is obtained after the deposition of 0.68 ML_{Si} of Al, through the formation of the so called γ-Al/Si phase. After nitridation, the 0.68

ML_{Si} of Al are transformed into 0.45 ML_{AlN} meaning that up to 55% of the Si surface is uncovered and, thereby, exposed to the N flux. This AlN buffer growth route is the only one used for GaN NW nucleation reported in the literature.

- the Si surface is first exposed to the N flux, leading to the formation of Si_xN_y. Then, Al only is deposited on the surface and reduces the Si_xN_y into AlN [122, 123]. The obtained AlN is well crystallized, meaning that the pre-existence of amorphous Si_xN_y has not been deleterious to the preservation of the epitaxial relationship between the substrate and the AlN.

Both cases are usually followed by the growth of few more AlN ML in metal rich conditions, aiming at increasing the surface smoothness and decreasing defects density [124]. Noticeably, thickening the AlN film allows to decrease the in-plane rotation of the grains [125]. Hence, thick AlN buffer interfacing Si and GaN NWs are preferred in order to improve the relative orientation of the overgrown GaN [126]; it is actually the main technological use for AlN buffers. On the other hand, too thick AlN buffers were reported to prevent NW nucleation [44, 45], suggesting that nucleation centers for NWs reside in the few first ML only. At last, a report states that AlN polarity can be reversed after the growth of few first ML of AlN [116].

As a consequence, to keep things simple, the AlN buffers synthesized in this study have been reduced to a minimum amount of steps. Two different growth routes have been used:

i. predeposition of 10 ± 1 ML_{Al} of Al on Si at 670 ℃ followed by a nitridation for 2 min at a temperature T_N. It results in 12 ± 1 ML_{AlN} of AlN, which is about 3 nm thick. This recipe will be referred as Al-first.

ii. exposure of the Si substrate to the N flux for 2 min at 840 ℃. Next, the N flux is shut down and Al is deposited on the surface, at a temperature T_{Al}, until the clear appearance of the AlN streaks on the reflection high energy electron diffraction (RHEED) pattern. This occurs after the deposition of 6.7 ± 0.8 ML_{Al} of Al resulting in 8 ± 1.0 ML_{AlN} of AlN. A last nitridation step is performed to ensure that all the deposited Al is transformed into AlN. This recipe will be referred as N-first.

For both cases, no supplementary growth of AlN have been done and T_N or T_{Al} were set between 670 and 840 ℃. The amount of pre-deposited Al in the case of Al-first buffers and the duration of the Si nitridation in the case of N-first buffers were intentionally chosen large, with the expectation of enlarging the eventually generated AlN nanostructures. Hence, scanning electron microscopy (SEM) or atomic force microscopy (AFM) observations tools would be sufficient to identify and collect valuable information on those objects.

3.2.2 Al-first AlN growth

Nano-structures observation

A set of Al-first AlN buffers[2] have been grown for nitridation temperature (T_N) ranging from 670 to 840 °C. In these conditions, the deposited Al was liquid and the 840 °C, set as the upper bound of the series, is the typical temperature used for GaN NWs nucleation.

Despite a metal rich growth expected to guarantee a smooth AlN film growth [124] and a relaxation of the AlN indicated by the RHEED, both AFM and SEM observations, shown in Figure 3.2, reveal very perturbed AlN surfaces, independently of the chosen nitridation temperature.

Focusing at the buffer grown with T_N = 670 °C, two types of nano-structures are identified:

- Dark areas. They are almost round shaped areas that appeared in SEM images with a darker contrast than the surrounding AlN (one is circled in Figure 3.3a). Their density is about 10^9 cm^{-2} and their diameter about 100 nm. Their average altitude, measured by AFM and shown in Figure 3.4a is under the average altitude of the AlN film, meaning that they are holes.

- Pedestals. They are AlN islands with an hexagonal shape that protrude over the average AlN surface and are located on the edge or inside dark areas (see the arrow in Figure 3.3a). Those islands are exactly the AlN pedestals first described by Largeau *et al.* [31] and are named accordingly.

Those nano-structures cover up to 50% of the surface and the AlN film in-between exhibit a smoother surface, with an average root mean square (RMS) of 0.8 nm.

While increasing T_N, the nano-structures were not vanishing, but their shape and density have been observed to smoothly evolve. SEM and AFM images of dark areas obtained at different T_N are shown in Figure 3.3 and 3.4. It means that the nano-structures observed at T_N = 840 °C and at T_N = 670 °C, despite being shaped differently, must share a common origin and a common growth mechanism.

For T_N > 670 °C, the density of dark areas remains constant at about 10^9 cm^{-2}. However, within one buffer, their dimensions and overall aspect within a sample are increasingly loosing uniformity with increasing T_N. It means that looking at a single dark area is not anymore sufficient to characterize a whole population on a buffer, and that distributions and average values are now required.

Dark areas average height, measured by AFM and gathered in Figure 3.5a, was observed to gradually increase with T_N, being negative at T_N = 670 °C but positive at T_N = 840 °C. Additionally, from T_N = 670 °C to T_N = 800 °C, dark areas areal distribution, extracted from SEM images and displayed in Figure 3.5b, was measured to shift toward larger areas. As a consequence, at T_N = 800 °C, few dark areas with diameters up to 300 nm could be spotted. For T_N above 800 °C, the trend was reversed

[2] N1965, N1966, N1967, N1968 and N1969

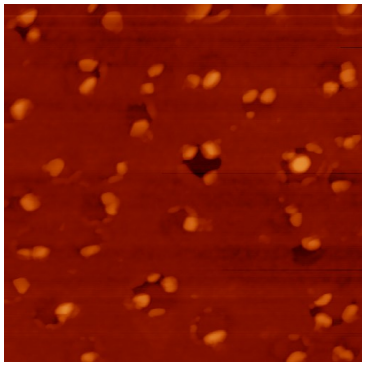

(a) 1×1 µm^2 AFM image

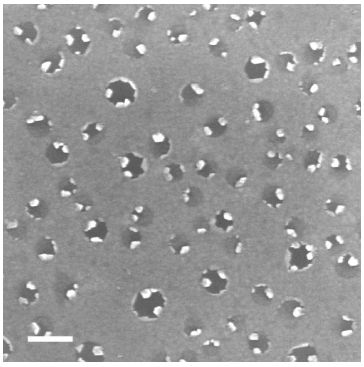

(b) SEM top view – scale bar: 200 nm

$T_N = 670$ ℃

(c) Nitridation temperature

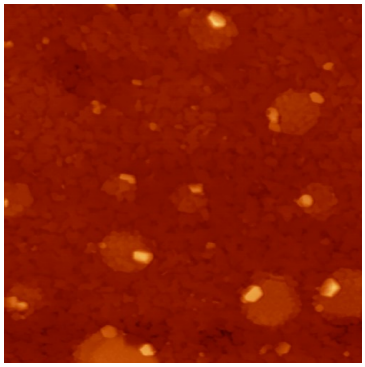

(d) 1×1 µm^2 AFM image

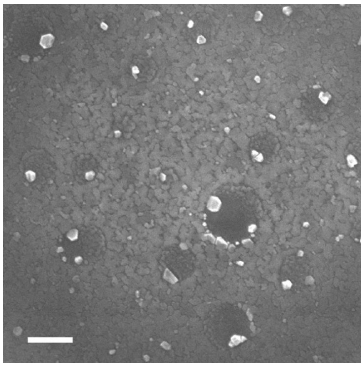

(e) SEM top view – scale bar: 200 nm

$T_N = 840$ ℃

(f) Nitridation temperature

Figure 3.2: Tapping mode AFM images and SEM images of Al-first AlN buffers

and the average dark areas areal was observed to decrease. At last, dark areas total surface coverage, shown in Figure 3.5c, was observed to decrease from 50% at 670 ℃ down to 20% at 840 ℃. It correlates well with the observation of the RHEED spectra that became more streaky while increasing T_N.

Higher T_N also implied an increase of the pedestals size and an apparent randomization of their localization over the surface. However, their nucleation in the vicinity of tiny dark areas, becoming hardly identifiable by SEM due to an observed contrast loss at high T_N, cannot be ruled out. Hence, a common origin between dark areas and pedestals, even for high T_N, seems still reasonable.

At $T_N = 670$ ℃, a growth mechanism for dark areas and AlN pedestals has been been proposed by Largeau *et al.* [31]. It invokes the formation of Al/Si droplets during the prior wetting of the Si surface by Al. To challenge this hypothesis, Al deposition on Si will be next under scrutiny.

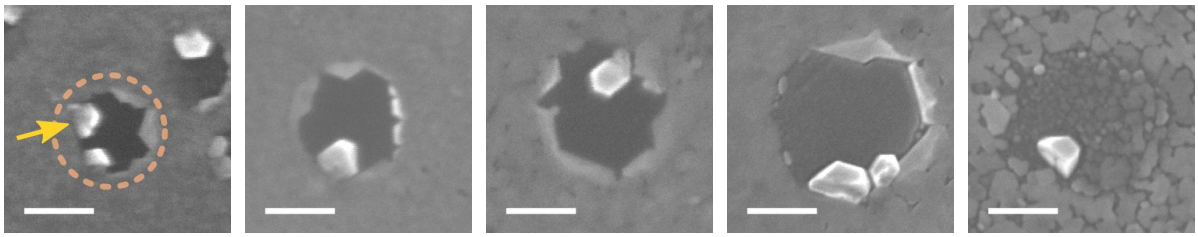

(a) $T_N = 670$ °C (b) $T_N = 700$ °C (c) $T_N = 750$ °C (d) $T_N = 800$ °C (e) $T_N = 840$ °C

Figure 3.3: SEM images of dark areas and their surrounding AlN pedestals – scale bar: 100 nm - a dark area is circled and a pedestal pointed by an arrow in the image (a)

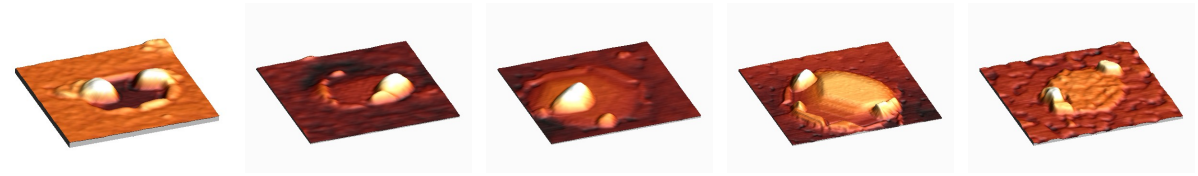

(a) $T_N = 670$ °C - $208 \times 208 \times 17$ nm^3 (b) $T_N = 700$ °C - $222 \times 222 \times 23$ nm^3 (c) $T_N = 750$ °C - $500 \times 500 \times 38$ nm^3 (d) $T_N = 800$ °C - $500 \times 500 \times 38$ nm^3 (e) $T_N = 840$ °C - $276 \times 276 \times 14$ nm^3

Figure 3.4: AFM images of dark areas and their surrounding AlN pedestals

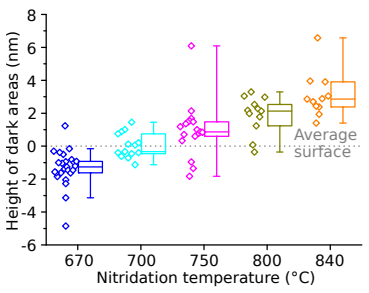

(a) Height of dark areas extracted from AFM – each dot referred to one measurement – boxes and whiskers respectively enclose $25-75\%$ and $5-95\%$ of the distribution; the mean value is indicated by the line, inside the box.

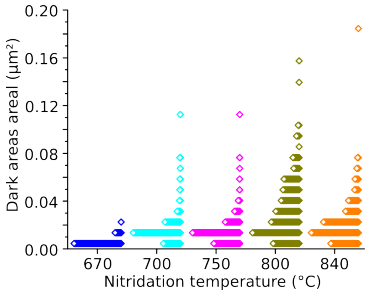

(b) Areal distribution of dark areas extracted from SEM images

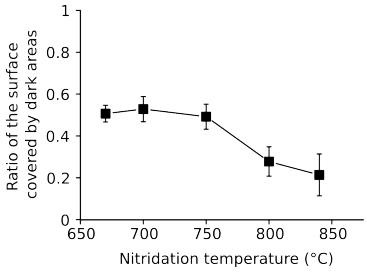

(c) Ratio of the Al-first AlN buffer surface covered by dark areas

Figure 3.5: Evolution of dark areas characteristics as function of nitridation temperature

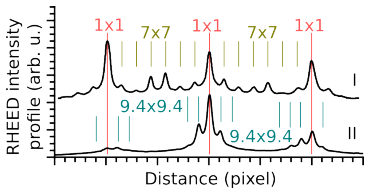

(a) RHEED intensity profile of the 7×7 Si and 9.4×9.4 Si observed at I and II

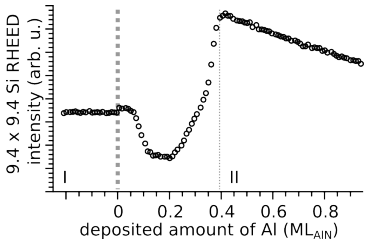

(b) Evolution of the RHEED intensity of the 9.4×9.4 Si during Al deposition on Si (111)

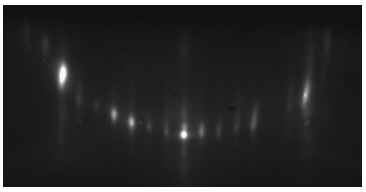

(c) I - RHEED spectra of the 7×7 Si

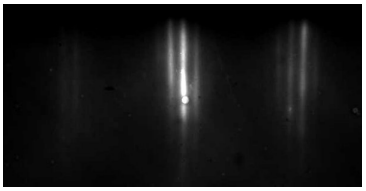

(d) II - RHEED spectra of the 9.4×9.4 Si

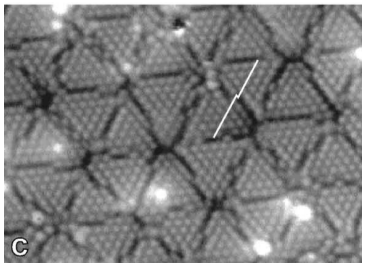

(e) STM image of the γ-Al/Si phase - extracted from [127]

Figure 3.6: RHEED monitoring of the Al deposition on Si (111).

Al deposition on Si

γ-Al/Si phase Al deposition on Si (111), performed with different fluxes and substrate temperature has been *in situ* monitored by RHEED[3]. Independently of the used flux, the Al deposition at 670 °C has provoked the disappearance of the 7×7 Si reconstruction and has been followed by the appearance, on the RHEED screen, of transient satellites rods around the 1×1 Si (see Figure 3.6). Their spacing, extracted from a RHEED intensity profile, indicates a 9.4×9.4 Si pattern. The plot of the RHEED intensity of the 9.4×9.4 Si rods as a function of the amount of deposited AlN is shown in Figure 3.6b. The initial intensity is not zero due to a spatial overlapping of the 7×7 Si rods and the 9.4×9.4 Si rods on the RHEED screen. After less than 0.1 ML$_{AlN}$ of deposited Al, the 7×7 Si has faded out. The 9.4×9.4 Si RHEED pattern has popped up after 0.2 ML$_{AlN}$ of deposited Al and reached its maximum for 0.4 ± 0.05 ML$_{AlN}$ of deposited Al. For extra deposition of Al, the 9.4×9.4 Si progressively dimmed. It suggests that the atomic pattern responsible for the 9.4×9.4 Si RHEED signature is not destroyed by an Al accumulation but only buried.

This reconstruction is attributed to the presence of the γ-Al/Si phase. Previous STM observations [127] have shown that this phase is composed of one bilayer made of Al/Si with approximately 1 ML$_{Si}$ of Si and 0.7 ML$_{Si}$ (*i.e.* 0.45 ML$_{AlN}$) of Al. The extra Al atoms, which are not included in the phase, were reported to cluster into islands.

According to the phase diagram of Al on Si (111) [128], those accumulated Al atoms on top of the γ-Al/Si phase are desorbing beyond 700 °C, and the γ-Al/Si phase decomposes beyond 770 °C. However, the specific 9.4×9.4 Si RHEED pattern was still

[3] N2016

observed for temperatures higher than 770 ℃ when the Si (111) surface was exposed to an Al flux, meaning that the γ-Al/Si phase is dynamically stabilized under Al exposure. Therefore, the γ-Al/Si phase could be used as a surface state reference in the full range of temperature explored in this study (670 $\sim$ 840 ℃).

Al desorption Once the γ-Al/Si phase has been formed, the 9.4×9.4 Si RHEED rods were observed to dim while accumulating Al. However, for a temperature higher than 700 ℃, if the exposure to Al was stopped after accumulation, the rods intensity was observed to recover almost to its initial value, and eventually to dim again and vanish (see Figure 3.7a). It suggests that Al atoms accumulated on top of the γ-Al/Si phase are desorbing before the γ-Al/Si decomposes [129]. Taking advantage of this specific transient, a typical desorption time $\tau_{n_0,T}$ for an accumulated amount n_0 of Al on the γ-Al/Si phase at a temperature T can be extracted (see Figure 3.7a). Independently of n_0 and T, the residual amount of Al on the γ-Al/Si phase, $n(t)$, at $t = \tau_{n_0,T}$, should be the same and close to zero:

$$n(t = \tau_{n_0,T}) = n_\tau \approx 0 \mathrm{ML}_{AlN} \quad \text{and} \quad \left(\frac{\mathrm{d}n_\tau}{\mathrm{d}\tau_{n_0,T}}\right)_T = 0 \tag{3.1}$$

One can write as well:

$$n_\tau = n_0 - \int_0^{\tau_{n_0,T}} \Phi_{desorp}(n(t), T)\mathrm{d}t \tag{3.2}$$

$\Phi_{desorp}(n(t), T)$ being the desorbing flux of Al.

$\tau_{n_0,T}$ values measured for different T and n_0 are plotted in Figure 3.7b. An affine dependence between $\tau_{n_0,T}$ and n_0, for $n_0 > 0.5$ ML_{AlN}[4], is observed, suggesting that for $n(t) > 0.5$ ML_{AlN}, the desorption flux is independent of the Al coverage.

$$\Phi_{desorp}(n(t) > 0.5, T) = \Phi^o_{desorp}(T) \tag{3.3}$$

Therefore, the derivative of equation 3.2, for $n_\tau > 0.5$ ML_{AlN}, can be expressed as:

$$\left(\frac{\mathrm{d}n_\tau}{\mathrm{d}\tau_{n_0,T}}\right)_T = 0 = \left(\frac{\mathrm{d}n_0}{\mathrm{d}\tau_{n_0,T}}\right)_T - \Phi^o_{desorp}(T) \tag{3.4}$$

$\left(\frac{\mathrm{d}n_0}{\mathrm{d}\tau_{n_0,T}}\right)_T$ values are extracted from the affine fits in 3.7b, allowing to plot in Figure 3.7c, with the help of equation 3.4, the Al desorption speed as function of T. As a first approximation, an Arrhenius law is used to fit the desorption speed dependence to temperature. It is expressed as:

$$\Phi^o_{desorp}(T) = A\mathrm{e}^{-\frac{E^o_{desorp}}{k_B T}} \tag{3.5}$$

[4]the non linear dependence observed for $n_0 < 0.5$ ML_{AlN} is tentatively attributed to a change in the surface roughness along the desorption experiment, due to a partial etching of the Si surface by Al

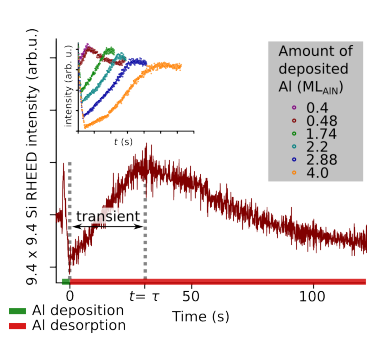

(a) γ-Al/Si RHEED intensity transient during Al desorption - inset: transient observed for different amount of deposited Al

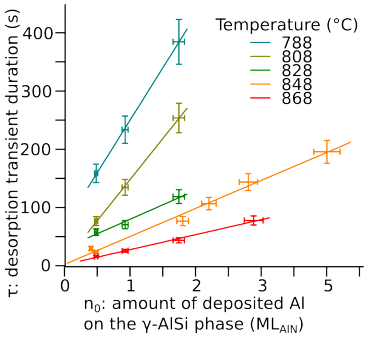

(b) Al desorption transient duration as function of the initial amount of deposited Al on the γ-Al/Si phase

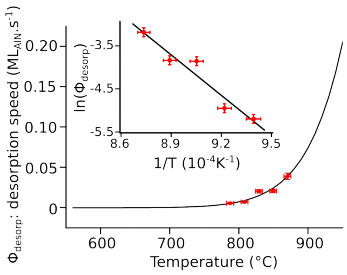

(c) Al on the γ-Al/Si phase (more than 0.5 ML$_{AlN}$ accumulated) desorption speed versus temperature - inset: linear fit of the desorption speed logarithm versus the temperature inverse

Figure 3.7: Measurement of the desorption speed of Al accumulated on the γ-Al/Si phase

A being a constant and E^o_{desorp} denoting the activation energy of the desorption, which can be related to the bonding energy of the Al atoms to their environment, prior to desorption. The fit gives $E^o_{desorp} = 2.36$ eV, and $A = 4.5 \times 9$ ML.s^{-1}. Using those coefficients, the desorption speed of more than 0.5 ML$_{AlN}$ of Al accumulated on the γ-Al/Si phase is plotted in Figure 3.7c.

$E^o_{desorp} = 2.36$ eV is slightly lower than the bonding energy of the bulk Al which is 2.75 eV [130] but this 0.4 eV difference is almost the estimated accuracy of this measurement. However, as observed by STM [127], the Al adatoms on top of the γ-Al/Si phase are observed to cluster. It will be later confirmed by the observation of the formation of Al droplets. This dewetting suggests that the Al-Al bond is stronger than the anchoring bond of an Al adatom on the γ-Al/Si phase, meaning that the surface in-between the Al droplets should be the main desorption channel. This is in accordance with $E^o_{desorp} < E_{Al-Al}$.

Therefore, the pathway for desorption should be (1) diffusion of an atom out of a droplet and (2) desorption from the γ-Al/Si bare surface. Thus two energy barriers accounting for (1) and (2) should be considered instead of one. In such a case, the diffusion speed of Al atoms out of the droplets is expected to be proportional to the droplets perimeter, *i.e.* proportional to the amount of deposited Al elevated to the power 1/3:

$$\Phi_{diffusion} \propto \text{Droplet perimeter} \propto (\text{Droplet volume})^{\frac{1}{3}} \propto [n(t)]^{\frac{1}{3}} \tag{3.6}$$

As, this behavior is not observed, it suggests that the barrier to the diffusion out of the droplets is negligible compared to desorption energy of Al adatoms on the γ-Al/Si surface.

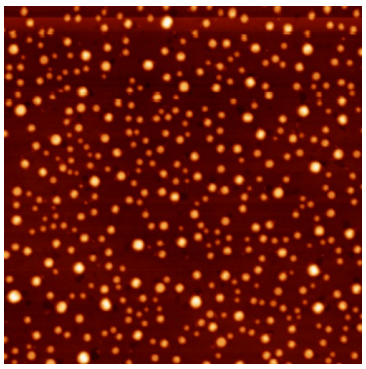

(a) AFM image - 5×5 μm^2 - z scale span from 0 to 66 nm

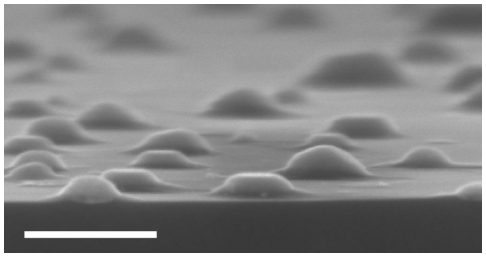

(b) SEM side view image - scale bar: 200 nm

Figure 3.8: Al droplets on Si (111) – N1989

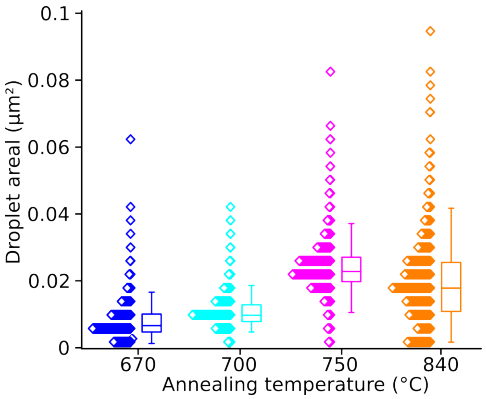

Figure 3.9: Areal distribution of droplets annealed at temperatures spanning from 670 °C to 840 °C

Nevertheless, Al desorption is occurring and is not negligible for temperatures up to 840 °C, which should be taken into account for the growth of the AlN buffers. Noticeably, it indicates a large increase in Al adatoms mobility on the γ-Al/Si phase, between 670 and 840 °C.

Al/Si droplets 12 ML_{AlN} of Al were deposited on Si at 670 °C[5], in the exact same conditions than for Al deposition aiming at growing an Al-first AlN buffer at T_N = 670 °C. Next, the Al was rested under vacuum for 2 min and quickly cooled down to room temperature, implying its solidification. SEM and AFM observations of the sample, shown in Figure 3.8, reveal the presence of droplet-like structures (termed droplets from now on). On average, those droplets are 25 nm high, have a diameter of 100 nm and a density in the order of 10^9 cm^{-2}.

Three similar samples[6] with Al deposited on Si were prepared. For each, the Al have been annealed for few seconds to one of the following temperature: 700, 750 or 840 °C and next quickly cooled down to room temperature. AFM observations confirmed the presence of droplets. Their areal distributions extracted from the AFM observations, are plotted as function of the annealing temperature, in Figure 3.9. The droplets average areal is increasing with annealing temperature, reaching a maximum

[5] N2009
[6] N2123, N2115, N1989

for $T_{annealing}$ = 750 ℃, and decreasing for further annealing. However, the areal distribution is continuously spreading while increasing the annealing temperature from 670 to 840 ℃. The average areal decrease for high temperature annealing is assigned to the partial desorption of Al, which has been previously measured above 700 ℃. The droplets areal distribution dependence on the annealing temperature demonstrates that their formation occurred when Al was liquid and not during their solidification or later events. Additionally, this observed dewetting of Al on Si is in accordance with STM studies where Al atoms are observed to cluster in small islands as soon as the γ-Al/Si phase is completed [127].

The evolution of Al droplets density and distribution as function of the annealing temperature follows a trend very similar to the one of dark areas as function of the nitridation temperature. It highly suggests that both are correlated.

An additional sample[7] with 12 ML_{AlN} of Al deposited at 500 ℃ on Si has been grown. The deposited Al is solid and a pattern on the RHEED screen corresponding to a cfc[8] reciprocal space lattice (RSL) is observed (Figure 3.10a). Next, the Al was annealed up to 690 ℃ leading to its liquefaction as demonstrated by the disappearance on the RHEED screen of the cfc RSL (see Figure 3.10c). In order to extract the liquefaction temperature, a prior calibration of the temperature measurement apparatus has been performed.

In the MBE, the temperature measurement is obtained thanks to a thermocouple put in contact with the rear side of the Si substrates. Due to the high vacuum of the chamber, heat transfer occurs through diffusion (in solid bodies) and radiation only, hence, a poor contact between the thermocouple and the substrate might lead to a systematic measurement error. To prevent such artifact measurement, a calibration of the thermocouple has been done by observing the melting temperature of bulk Al, which occurs at 660 ℃ [95][9]. For this purpose, an Al ribbon has been glued to the substrate with indium to ensure an optimal heat transfer between both. Next, the ribbon was annealed to 700 ℃ and in the mean time, its shadow was monitored on the RHEED screen, by defocalizing the electron beam. When the Al ribbon shadow collapsed and formed a large droplet-like profile, the Al was deduced to be melted. It inferred a measurement error of +15 ℃ for the thermocouple, meaning that the substrate surface was cooler than the thermocouple itself. It correlates well with the overall geometry of the setup.

By including this systematic error of the thermocouple, a liquefaction temperature of 580 ℃ have been measured for the 12 ML_{AlN} of Al deposited on Si (111), which is 80 ℃ lower than the 660 ℃ of the bulk Al melting [95]. Next, the Al has been cooled down and by using the same experimental method, a freezing temperature of 530 ℃ have been measured. Those melting and freezing temperatures, gathered in Figure 3.10e, remained identical even after repetitive melting and freezing cycles.

The 580 ℃ melting temperature of Al droplets on Si is attributed to the diffusion of

[7] N2225
[8] cubic-face-centered
[9] N2380 and N2381

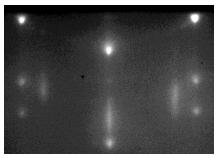

(a) I - RHEED spectra of solid Al deposited on Si (111)

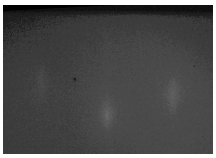

(b) II - RHEED spectra of liquid Al deposited on Si (111)

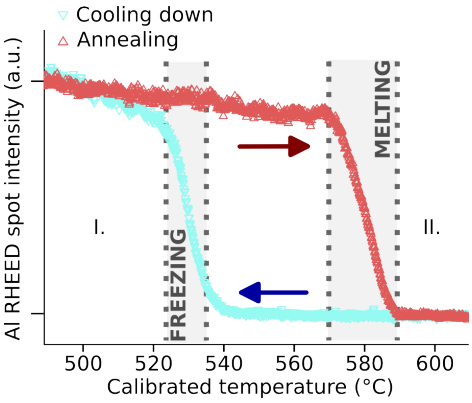

(c) 10 ML_{Al} of Al on Si (111) RHEED spots intensity for cooling down or annealing

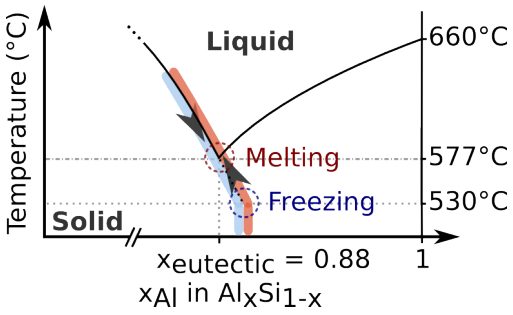

(d) Expected pathway of the Al/Si droplet system reported on the bulk $Al_xSi_{(1-x)}$ phase diagram

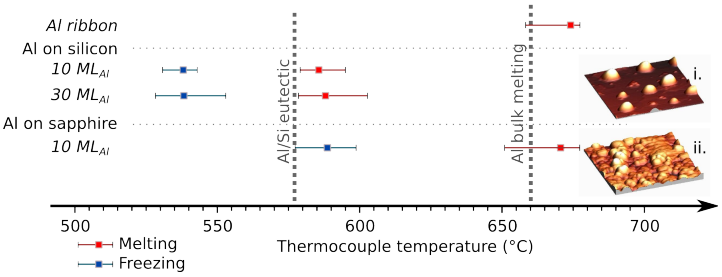

(e) Melting and freezing temperature of assemblies of Al droplet depending of the substrate. (i-ii) insets are 3D display of AFM images of Al deposited on, respectively, Si and sapphire.

Figure 3.10: Melting and freezing temperatures of Al droplets monitored by RHEED.

Si inside the droplets, leading to their melting at the Al/Si eutectic temperature, which is 577 °C [95]. To strengthen this hypothesis, the melting and freezing temperatures of 12 ML_{AlN} of Al deposited on sapphire was measured using the same experimental procedure. On this substrate free of Si, the Al was measured to melt at 655 °C and to freeze at 575 °C. It confirms that Si is required to shift down to 580 °C the melting temperature of Al droplets.

The observed hysteresis between the melting and freezing temperatures of Al deposited either on Si or on sapphire, also observed for 30 ML_{AlN} of Al deposited on Si (see Figure 3.10e), is attributed to a size effect. Indeed, in the similar Au-Si system, which has been studied in details, a similar phenomenon is reported. Au deposited on Si (111) has been shown to dewet the surface and forms droplets once a Au-Si intermetallic phase is formed and Si is dissolved as well in the Au droplets [131, 132]. Additionally, such Au/Si droplets were reported to melt at the Au/Si eutectic but to freeze at much lower temperature. This supercooling phenomenon was attributed to the ordering of the liquid Au-Si atoms in the vicinity of the substrate, in a symmetry that differs from the one of solid Au, generating a barrier to the crystallization [133]. Such local ordering has been already reported for Al on sapphire [134].

Hence, taking into account Si dissolution in the Al and supercooling phenomenon

likely stemming from local ordering, Al droplets deposited on Si are expected to follow the pathway indicated in Figure 3.10d, which is reported on the bulk Al/Si diagram. It is this reactivity of Al with Si which is incriminated for the formation of the nanostructures observed in the synthesized AlN buffers.

Growth mechanism

All the experimental results collected so far are consistent with the initial model of Largeau *et al.* [31], which can now be further extended to higher temperatures and detailed. The following growth scenario for the Al-first AlN buffer, sketched in Figure 3.11, is proposed.

The first 0.4 ML_{Al} of Al deposited on bare Si imply the formation of the so called γ-Al/Si phase and the last 9.4 ML_{Al} of deposited Al dewet the surface and reorganize into droplets. Considering the substrate as an infinite reservoir of Si in equilibrium with the Al droplets, this system has to satisfy the Al/Si phase diagram [95]. Thus, Si diffuses into the Al droplets with a concentration ranging from 12% at the temperature of the Al/Si eutectic to more than 30% at 840 °C. During the nitridation step, Al atoms are drained out of the droplets as they are consumed by the N atoms that impinge all over the surface. Si substitutional incorporation in AlN is limited by a maximum miscibility measured to be 12% in $(AlN)_{1-x}(SiN)_x$ [135, 136]. Thus, for temperatures higher than 577°C, where more than 12% of Si dissolved in the Al/Si droplets, the release of Al atoms from the droplet, due to nitridation, is provoking an increase of the Si concentration above its maximum miscibility, leading to the Si precipitation at the location of the droplet. As soon as all the Al is consumed, the precipitated Si will react with the impinging N and form Si_xN_y. The chemical contrast of these large Si_xN_y patches allows their observation by SEM, appearing as the dark areas. By increasing the nitridation temperature, a larger amount of Si is dissolved in the droplets. It leads, after Si precipitation, to the observed increase of the areal and height of the dark areas (Figures 3.5b and 3.5a). The decrease in dark areal size for high nitridation temperature can be assigned to a partial Al desorption that led to smaller Al/Si droplets.

Part of the dissolved Si is likely interfering in the AlN growth. Indeed, high Si doping, due to a surfactant effect of Si atoms, has been reported to imply an increase of the average AlN crystallite lateral size [137, 138, 139], which suggests that AlN pedestals and AlN crystallites surrounding the Si_xN_y patches are the result of a Si-rich growth. For kinetic reasons, an high amount of Si might have been incorporated in the AlN pedestals and surrounding crystallites. Due to its thermodynamic instability [140], phase decomposition responsible for defects formation and polytypism [141, 142] might have occurred. Additionally, the eventual presence of oxygen impurities[10], coming from residual SiO_2 for instance, could have stabilized those defects [142, 144]. Therefore, the crystalline struc-

[10]Harris *et al.* [143] have shown that above a threshold of 0.75% of oxygen in AlN, defects such as basal inversion domain boundarys (IDBs) are formed. Actually, the $(Si_3N_4)(SiO_2)(AlN)(Al_2O_3)$ system, so-called Sialons, have been extensively studied since the 70's because of ceramic synthesis with excellent mechanical, thermal, chemical and electrical properties.

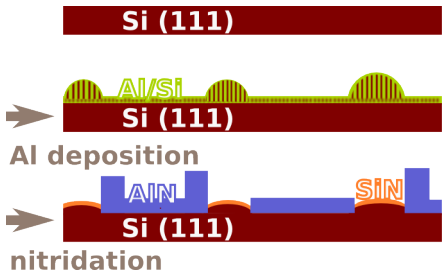

Figure 3.11: Schematic Al-first AlN buffer growth mechanism.

ture of the AlN grown in Si-rich conditions is expectantly defective and most probably different from the rest of the AlN grown far from the transient Al/Si droplets.

From the developed nucleation mechanism, it is clear that the formation of the AlN pedestals and the concomitant local Si-rich growth is related to the Al-predeposition. What would happen in the case of the N-first AlN buffer?

3.2.3 N-first AlN growth

Nano-structures observation

Samples have been grown according to the N-first AlN buffer route[11].

Nitridation of the Si is done at 840 ℃. It implies the formation of a $8/3 \times 8/3$ Si RHEED pattern (visible on the RHEED spectra of Figure 3.14c), which is attributed to the growth of a crystalline Si_3N_4 film. The maximum intensity of this reconstruction is obtained for ~ 3.5 ML_{AlN} of deposited N atoms. Longer exposition of the surface to N atoms leads to a dim of the $8/3 \times 8/3$ Si RHEED pattern, which is attributed to an amorphisation of the Si_3N_4 into Si_xN_y [145]. For the next samples, the nitridation time was set to more than 2 min, which allows to obtain an amorphous Si_xN_y whose thickness is self-limited (as discussed later), thereby, expectantly increasing the reproducibility of the growth.

Reduction of the Si_xN_y by Al is done for T_{Al} ranging from 670 ℃ to 840 ℃.

SEM and AFM observations of the sample reduced at $T_{Al} = 700$ ℃, shown in Figure 3.12, revealed a smooth AlN film surface disturbed by the presence of nano-structures (Figure 3.13). They are identified as dark areas decorated by large AlN crystallites, which resemble the nano-structures already observed on the Al-first AlN buffer. The dark areas density ($\sim 7 \times 10^8$ cm^{-2}) and diameter (~ 150 nm) are almost similar to the one observed for the Al-first AlN buffer nitridated at 700 ℃.

Conversely, by increasing the reduction temperature to 840 ℃, the density of dark areas is reduced down to 1×10^8 cm^{-2} and their diameter is increased up to 300 nm, which deviates from the Al-first AlN buffer nitridated at 840 ℃. The AlN film in between the nano-structures is extremely smooth with a RMS down to 0.7 nm. It is such observations that led first Le Louarn *et al.* [122] and later Hu *et al.* [123] to conclude that optimal

[11] N2299 and N1999

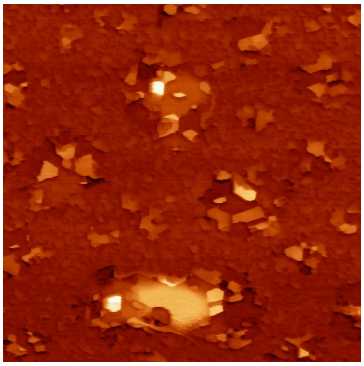

(a) 1×1 µm^2 AFM image

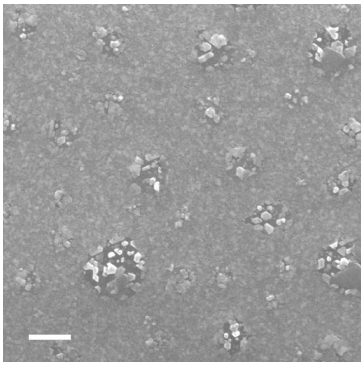

(b) SEM top view - scale bar: 200 nm

$T_{Al} = 700$ ℃

(c) Reduction temperature

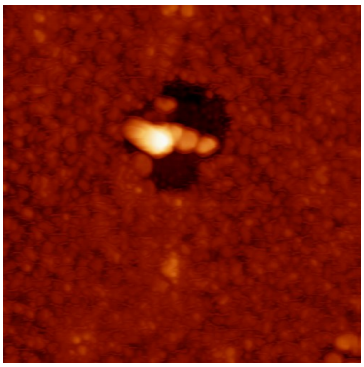

(d) 1×1 µm^2 AFM image

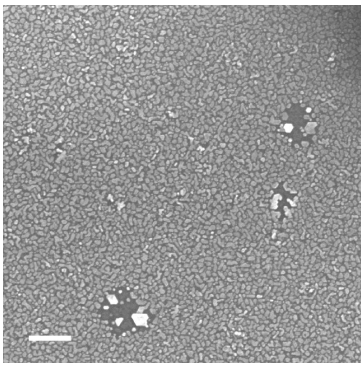

(e) SEM top view - scale bar: 200 nm

$T_{Al} = 840$ ℃

(f) Reduction temperature

Figure 3.12: Tapping mode AFM images and SEM images of N-first AlN buffers

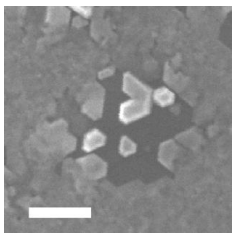

(a) $T_{Al} = 700$ ℃

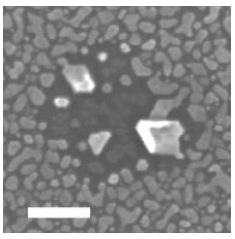

(b) $T_{Al} = 840$ ℃

Figure 3.13: SEM micrographs of dark areas and their surrounding AlN pedestals - scale bar: 100 nm

Si/AlN interfaces could be obtained by a prior nitridation instead of first wetting the Si surface by Al.

The AlN film in between the nano-structures (visible around the dark area of Figure 3.13b) is composed of adjacent but disconnected platelets, which is attributed to the reduction process. Indeed, considering the following reduction equation,

$$Si_3N_4 + 4Al \rightleftharpoons 4AlN + 3Si \tag{3.7}$$

the primitive lattice cell of Si_3N_4, which has an in-plane parameter of 0.76 nm, should be reduced into four primitive lattice cells of AlN, which corresponds to a total in-plane lattice cell of 0.62 nm. It means that a contraction of the Si_xN_y layer is occurring during its reduction, leading to the observed platelet structure. Using the contrast of SEM micrographs, the surface coverage of AlN platelets is measured to be 60%, which correlates well with the 66% expected theoretically from the lattice parameter analysis and neglecting a vertical reorganization of the film.

A comparison of the formation energy of Si_3N_4 and AlN at 850 °C have led Nikishin *et al.* [118] to estimate a larger bond energy for AlN (0.8 eV) than for SiN (0.65 eV), which would be the driving force of the reduction reaction.

During the Si_xN_y reduction, the Al is deposited until the appearance of the AlN related rods on the RHEED screen, which happens after a deposition of 7 ± 1 ML_{AlN} (see Figure 3.14b and 3.14e). To prevent a possible residual overage of deposited Al, a last nitridation step is performed. However, if neglecting this last step, large droplets sitting on few dark areas, are observable by SEM (not shown here), suggesting that 7 ML_{AlN} of deposited Al is already too much.

The thickness of Si_xN_y grown on Si by nitridation, using a N_2-plasma source cell, has been reported to be self-limited [112], saturating at $2 \sim 3$ nm on average by looking at various TEM pictures displayed in literature [71, 115, 146]. It corroborates the observation that the energy required to form Si_3N_4 is mainly provided by the kinetic energy of the impinging N atoms coming from the plasma cell, instead of the thermal energy of the substrate [147]. Hence, as soon as a conformal few nm thick Si_xN_y film is formed, the further available Si atoms are buried under the Si_xN_y itself and isolated from the energetic N atoms, which is expected to hinder the reaction. If so, the dependence of the Si_xN_y film properties (crystalline quality and thickness) to the growth temperature should be minimal.

Therefore, considering a 3 nm thick Si_xN_y with the average lattice parameters of Si_3N_4, only 6 ML_{AlN} of deposited Al would be required to fully reduce it, whereas the RHEED monitoring suggest that 7 ML_{AlN} are necessary. Actually, the increase in the AlN rods RHEED intensity seems correlated to the intensity decrease of observed transient RHEED spots (plotted in Figure 3.14a), rather than the amount of deposited Al. Are the AlN rods transiently screened by an additional compound?

Released Si

The RHEED monitoring of the Si_xN_y reduction performed at $T_{Al} = 840$ °C (Figure 3.14) has exhibited the transient appearance of supplementary diffraction spots, shown

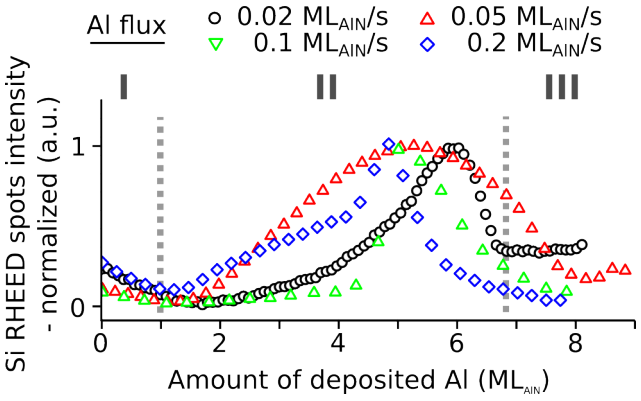

(a) Si RHEED spot intensity during the reduction of the Si_xN_y by Al.

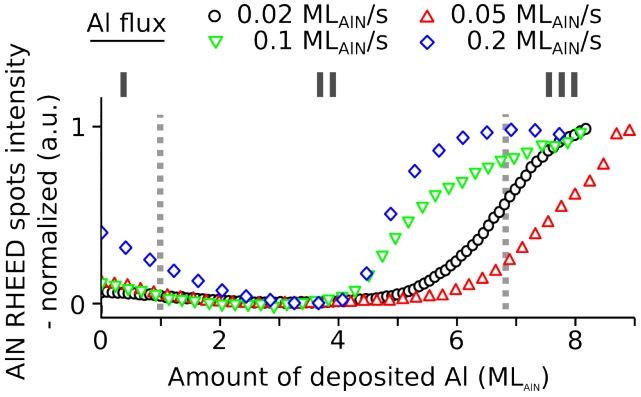

(b) AlN RHEED spot intensity during the reduction of the Si_xN_y by Al.

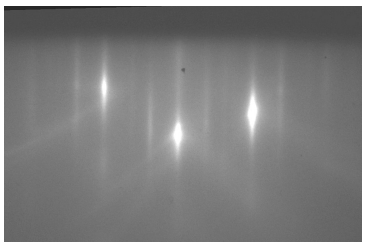

(c) Initial RHEED spectra - corresponding to I

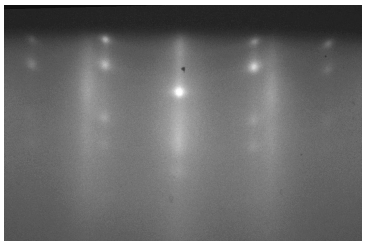

(d) RHEED spectra for 5 ML_{AlN} of deposited Al - corresponding to II

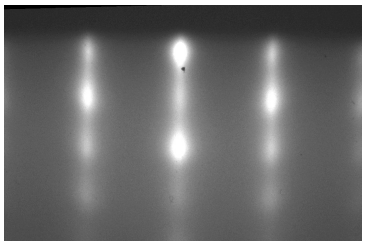

(e) RHEED spectra for 8 ML_{AlN} of deposited Al - corresponding to III

Figure 3.14: RHEED spectra and intensity evolution of Si and AlN spots during the reduction. RHEED spectra were acquired in the $[11\bar{2}0]_{AlN} \equiv [1\bar{1}0]_{Si}$ azimuth

in Figure 3.14d. Those are perfectly fitted by two patterns of a porous Si[12] RHEED spectra, which are 60^o rotated each other around the [111] direction, as depitcted in Figure 3.15. The maximum intensity was reached at 5.6 ± 0.7 ML_{AlN} of deposited Al.

Four N-first AlN buffers[13] were grown with varying the Al impinging flux, from 0.02 to 0.2 $ML_{AlN}.s^{-1}$. For all the samples, the transient appearance of the Si Bragg spots was again observed. The RHEED intensity of the transients dots and of AlN rods are plotted in Figure 3.14 as function of the deposited amount of Al. For the four samples, the maximum intensity of the Si Bragg spots is reached at 5.6 ± 0.7 ML_{AlN} of deposited Al, which would correspond to the full reduction of 2.7 nm thick Si_xN_y by Al.

Therefore, the transient spots are attributed to the growth of epitaxial Si crystallites

[12] the porous Si has been obtained from the courtesy of Dr. Guido Mula
[13] N2085, NN2072, N2124 and N2207

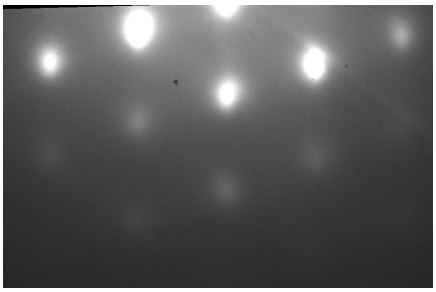

(a) RHEED spectra of porous Si

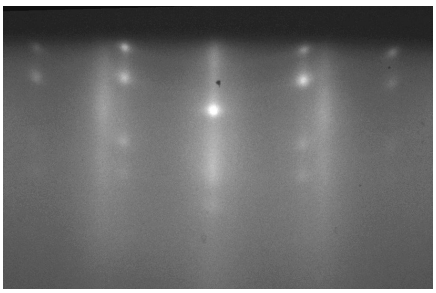

(b) RHEED spectra of the transient spots

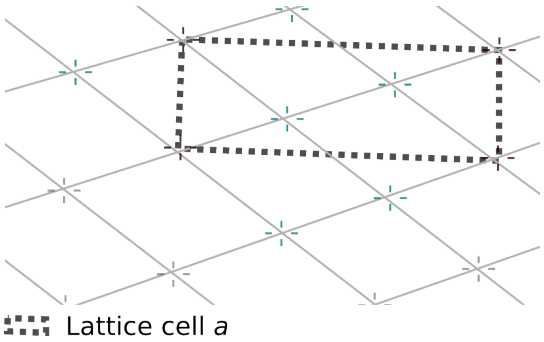

(c) Schematic pattern of the porous Si RHEED spectra

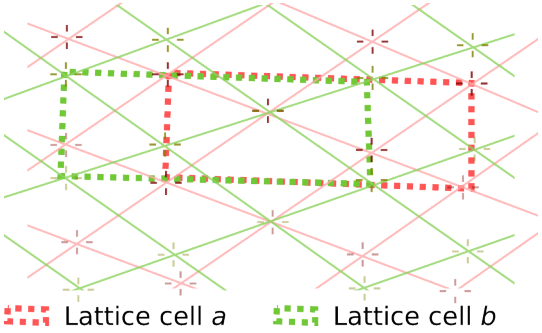

(d) Schematic pattern of the transient RHEED spots observed during Si_xN_y reduction

Figure 3.15: RHEED spectra taken along the Si[1$\bar{1}$0] azimuth of Si and extracted reciprocal space lattices.

out of the Si atoms released during the reduction reaction 3.7. It additionally suggests that the reduction occurs by a switch between Al and Si atoms, instead of a diffusion of the N atoms in the Al film.

From the RHEED spectra, the synthesized AlN is in epitaxial relationship with the underneath Si, with only one orientation: AlN (0001) [11$\bar{2}$0] ≡ Si (111) [02$\bar{2}$], which is similar to high temperature growth of Al-first AlN film on Si [125]. Conversely, the two different orientations of the Si crystallites, transiently observed by RHEED, suggest the existence of a $Si_{substrate}$/AlN/$Si_{crystallites}$ stacking sequence. Indeed, two different orientations are allowed for cubic crystallites (*i.e.* Si) that are epitaxially growing on an hexagonal substrate (*i.e.* AlN) with $[111]_{Si} \equiv [0001]_{AlN}$. It would indicate that the observed islands are Si crystallites epitaxially stacked on AlN, and that two populations differing by their in-plane orientation coexist.

For a deeper characterization of the released Si, a dedicated sample[14] has been grown according to the N-first AlN buffer route with $T_{Al} = 840$ °C, except that the deposited Al amount has been limited to 6 ML_{AlN} and no extra nitridation has been done. Therefore, the sample growth has been exactly stopped when the transient Si dots were reaching their maximum intensity in the RHEED spectra. AFM and SEM micrographs of

[14] N2105

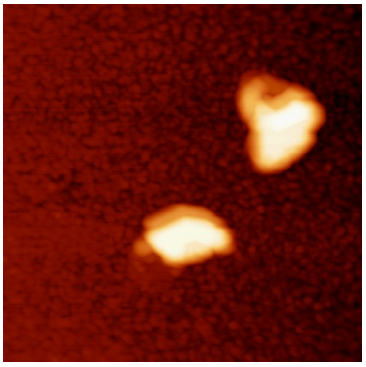

(a) 1×1 μm^2 AFM image - z scale span from 0 to 26 nm.

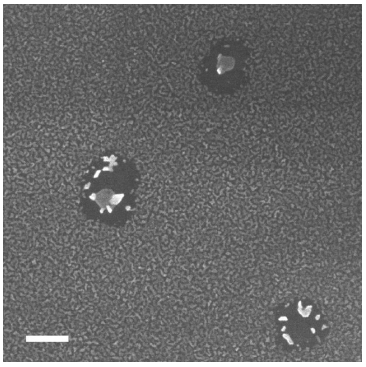

(b) SEM top view - scale bar: 200 nm

$T_{Al} = 840$ °C,
$n_{depositedAl} = 6$ ML_{AlN}

(c) Growth characteristics

Figure 3.16: AFM and SEM images of a N-first AlN buffer obtained by using only 6 ML_{AlN} of Al for the Si_xN_y reduction – N2105

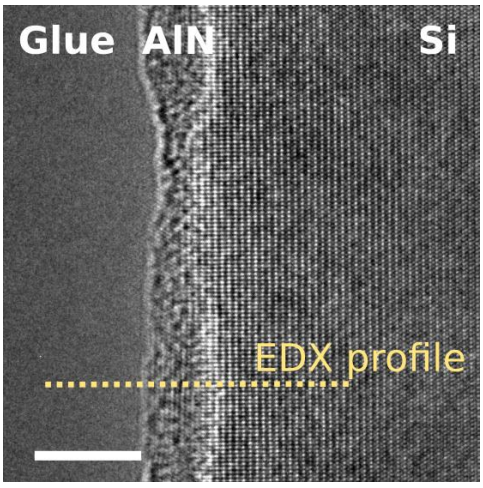

(a) TEM cross section micrographs of the N-first AlN buffer, along the Si $11\bar{2}$ azimuth - scale bar: 5 nm

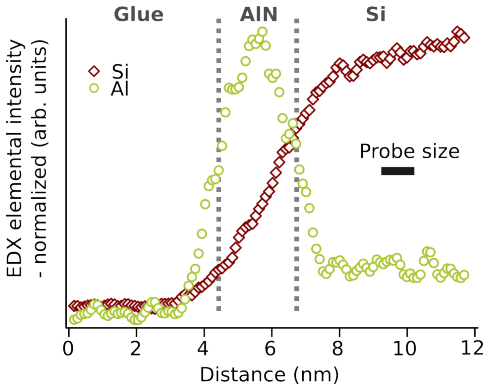

(b) EDXS profile of the Al and Si signal along the dot line indicated in Figure 3.17a

Figure 3.17: TEM and EDXS analysis of a N-first AlN buffer obtained by using only 6 ML_{AlN} of Al for the Si_xN_y reduction – N2105

the sample are shown in Figure 3.16, revealing a very similar structure and contrast compared to the conventional N-first AlN buffer obtained at $T_{Al} = 840$ °C, except the presence of small droplet-like structures on few dark areas (two are visible in the shown SEM images).

A cross-section along the $[11\bar{2}]$ Si azimuth of the sample has been prepared, allowing TEM imaging and the acquisition of a chemical profile by EDXS. Both are presented in Figure 3.17.

The AlN buffer is clearly observed by TEM as a rough film, whose thickness varies between 2 and 3 nm. This is attributed to the probable uneven thickness of the former

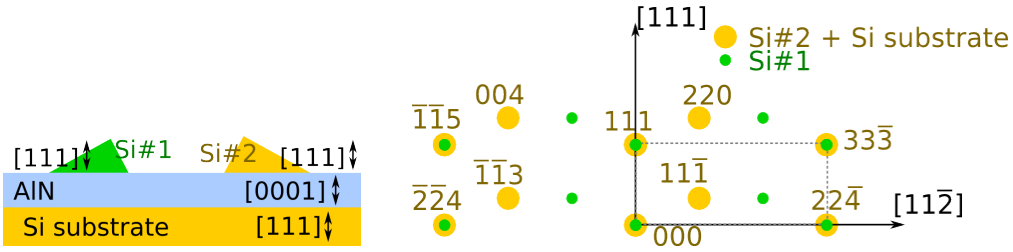

(a) Sketch of the stacking sequence – the two populations of Si crystallites are labeled #1 and #2

(b) Sketch of the diffraction pattern for the Si – only the Bragg spots corresponding to the Si substrate are labeled

Figure 3.18: Sketch of the expected diffraction pattern of the Si substrate and the surface Si crystallites

Si_xN_y. Noticeably, neither Si nor SiO_x stacked on the AlN can be observed. It suggests that the released Si has not reorganized into a conformal film. The spatial resolution of the EDXS scan is estimated to be down to 1 nm by looking at the 1 nm length of the Al signal tail penetrating the Si substrate or the glue. It means that the Si signal tail that is crossing the whole AlN film has to correspond to Si atoms located in the AlN. Such signal might stem from remaining Si_xN_y in the AlN, with a maximum density of 12% [135, 136], and/or from pure Si phases. In the latter case, such phases would correspond to the dark meanders, observed by SEM, between the adjacent AlN platelets (see Figure 3.16b). However, there is no reason that this Si would screen the appearance of AlN rods on the RHEED spectra during the reduction.

A strong limitation to the characterization of the Si crystallites is the close vicinity of the Si substrate whose signal might overlap the one of interest, as in EDXS for instance. However, by taking advantage of the fact that one population of Si crystallites has an in-plane orientation 60° off the one of the Si substrate, a selective X-rays diffraction measurement can be performed by targeting the Si crystallites diffraction spots that are not superimposed to the Si substrate diffraction spots. As sketched in Figure 3.18, for instance, the $11\bar{1}$ spot would fulfill this requirement.

Experiments were carried on using a monochromatic synchrotron beam at 18keV, set in a grazing incidence configuration[15]. Looking at the $11\bar{1}$ spot of the Si RSL anti-parallel to the substrate, its intensity has been plotted as function of the grazing angle, in Figure 3.19a.

For grazing angles lower than 0.08°, the intensity is observed to sharply increase. Knowing that the critical angle for 18 keV photons impinging on Si is theoretically predicted at about 0.1° (Figure 3.19b), it indicates that the probed Si crystallites are located at the surface and not in the bulk of the sample. Indeed, when probing the sample with a grazing incidence lower than the critical angle, the beam is fully reflected at the surface and only an evanescent wave field is penetrating the matter over distance

[15] measurements were carried on at the Eurepean Synchotron Radiation Facility, on the BM32 beam line by Samuel Tardiff and François Rieutord

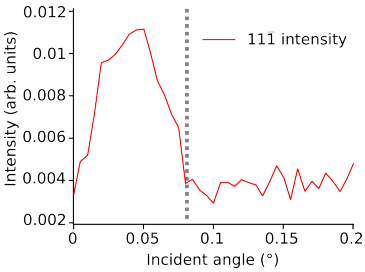

(a) 11$\bar{1}$ intensity as function of the incident angle

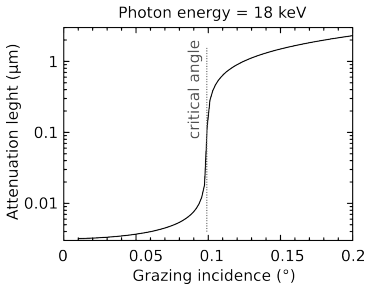

(b) Attenuation length of 18 keV photons impinging in Si, as function of the grazing incidence. Data obtained from *www.cxro.gov*

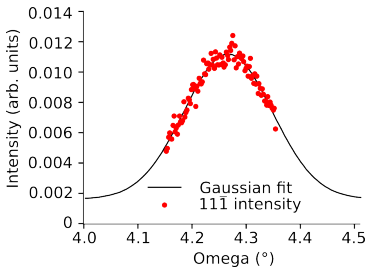

(c) 11$\bar{1}$ intensity as function of ω

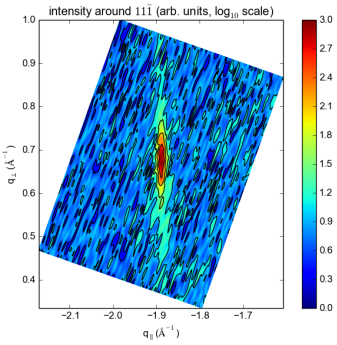

(d) 11$\bar{1}$ cartography in the reciprocal space map

Figure 3.19: X-ray study of the transient Si – N2105

in the order of 10 nm, which maximizes the overlap between the Si crystallites and the beam. An ω scan of the 11$\bar{1}$ Si spots[16], plotted in Figure 3.19c, indicates an in-plane orientation dispersion of the probed crystallites of 0.2°. It strengthened the hypothesis of the localization of the Si crystallites on the AlN film and not on the Si substrate as in such a case, a narrower in-plane dispersion would have been expected.

At last, an high resolution mapping of the 11$\bar{1}$ spot has been acquired and is displayed in Figure 3.19d. The spot is elongated along the out-of-plane direction suggesting a smaller size of the Si crystallites along the out-of-plane direction compared to the in-plane direction. Using the Scherrer equation:

$$\mathrm{d}l = \frac{2\pi}{\mathrm{d}Q} \tag{3.8}$$

with $\mathrm{d}l$ the average size of the crystallite and $\mathrm{d}Q$ the full width half maximum (FWHM) of the diffraction peak, both in the same crystallographic direction, the Si crystallites are expected to be on average 9 nm high and 45 nm large. Additionally considering

[16] ω measure the rotation of the sample around the normal of the surface

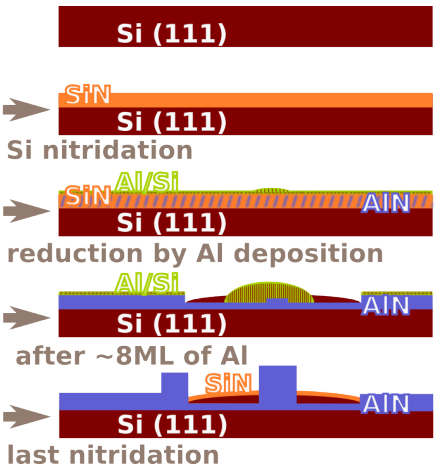

Figure 3.20: Schematic N-first AlN buffer growth mechanism

their probable partial oxidization at the time of the measurement, their initial size was probably slightly larger. Therefore, those Si crystallites should protrude over the AlN surface, which suggests that they are included in the 10^8 cm^{-2} islands observed by AFM and SEM on the sample surface (Figure 3.16).

As a conclusion, it is the release of Si occurring during the reduction of Si_xN_y that has expectantly perturbed the *in situ* monitoring of the AlN growth by RHEED. Furthermore, such massive amount of released Si should have consequences for further growth of AlN or even GaN.

Growth mechanism

Based on the collected experimental results, a growth mechanism, sketched in Figure 3.20, is proposed. A soon as the Si_xN_y is exposed to Al atoms, a reduction reaction is initiated, occurring by switch between the Si of the Si_xN_y matrix and the impinging Al atoms. All the Si_xN_y is reduced as suggested by TEM micrographs and the consumed quantity of Al atoms. The reaction provokes a uniform Si release over the surface, in-situ observed by RHEED. The released Si atoms are not wetting the AlN but clustered into islands. Once the Si_xN_y film has been fully reduced, which should be done after the deposition of ~ 6 ML_{AlN} of Al, the incoming Al is reorganizing in droplets that would dissolve the previously released Si, in a similar manner than for the Al-rich AlN buffer growth. It leads to the intensity decrease of the transient Si RHEED spots. The last nitridation provokes a precipitation of the dissolved Si at the location of the droplets accompanied by the growth of AlN pedestals. The different sizes of the dark areas between N-first and Al-first AlN buffers suggest different contact angles of the transient Al/Si droplets on the surface.

Once again, Al has demonstrated its high reactivity with the substrate, meaning that the N-first route is unable to hamper the formation of AlN pedestals and the concomitant

localized Si-rich growth. In addition, the amount of Si transported during the growth has been even larger in this case than for the Al-rich route.

3.2.4 Thick AlN film grown on Si

A common point between the N- and Al-first AlN buffers growth routes is the precipitation of Si on their surface (resulting from the Si_xN_y reduction and/or the nitridation of Al/Si droplets), which would be turned into Si_xN_y during any nitridation step. Nevertheless, Si_xN_y has been shown not to be stable in presence of Al, leading to the release of Si.

Therefore, it can be proposed that further growth of AlN on both the Al- and the N-first AlN buffers, carried in strong Al-rich conditions, should lead to a perpetual transportation of Si atoms on top of the AlN surface, if neglecting the incorporation of Si in the AlN itself.

In order to verify this proposal, two thick AlN films[17] were grown on Si (111): one on a Al-first AlN buffer (obtained with $T_N = 670$ ℃) and the other one on a N-first AlN buffer (obtained with $T_{Al} = 840$ ℃). For both cases, the AlN was grown at 840 ℃ by alternate deposition of ~ 30 ML_{AlN} of Al followed by its nitridation. A total thickness of 45 nm of AlN has been grown for both samples (measured by *ex situ* SEM cross-section observations).

Structure SEM and AFM micrographs of the AlN top surface are shown in Figure 3.21 and 3.22. For both cases, few dark areas and large AlN islands protruding over the surface are observed, which clearly recall the dark areas and AlN pedestals observed on the bare AlN buffers. However, in this case, protruding AlN islands are not exclusively located in the vicinity of dark areas. Additionally, their measured density, 4×10^8 cm^{-2} on the Al-first AlN film and 3×10^7 cm^{-2} on the N-first AlN film, is lower than the average AlN pedestal density on the corresponding bare AlN buffers.

AFM measurements have shown that dark areas are actually deep holes, few being deeper than 45 nm meaning that they are crossing the full thickness of the AlN film.

Taking advantage of the large thickness of the AlN film, EDXS scans over dark areas have been acquired. Two representative linescans are shown in Figure 3.21c and 3.22c. The Al and N signal is clearly observed to drop over the dark area while the Si signal raise, meaning that dark areas are Si rich areas, not to say pure Si.

Growth mechanism Using similar mechanisms than for AlN buffer growth, the obtained structure for the thick AlN film can be described as follows.

During Al accumulation, the Al atoms have dewetted the surface to form droplets, most probably located on the later observed dark areas. Remaining silicon on the surface and/or from the substrate, was next dissolved into the droplets to satisfy the Al/Si phase diagram. Then, during nitridation, the Al atoms are consumed by the impinging N atoms and the dissolved Si is incorporated in the AlN, up to 12% and/or is precipitated

[17] N2113 and N2114

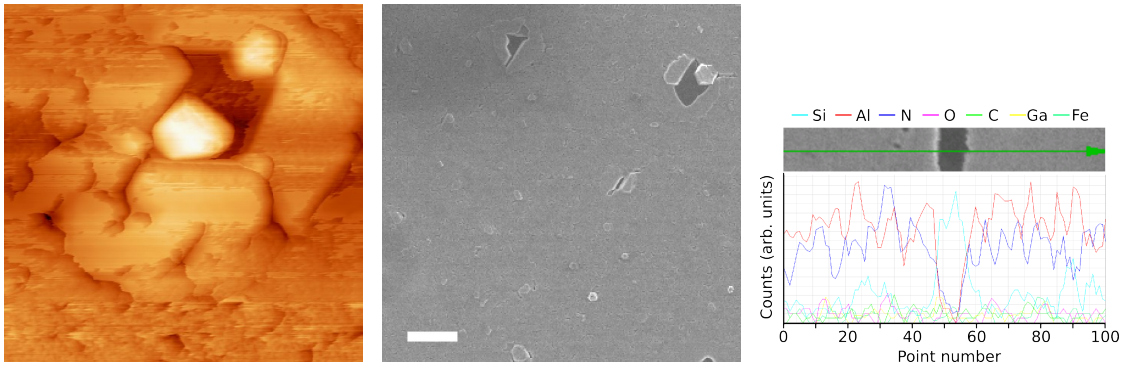

(a) AFM view - 1×1 μm^2 - z scale span from 0 to 91 nm

(b) SEM top view - scale bar: 400 nm

(c) EDXS line scan - incident electron energy: 3 keV

Figure 3.21: 45 nm thick AlN film nucleated on a Al-first AlN buffer and grown in Al-rich conditions – N2113

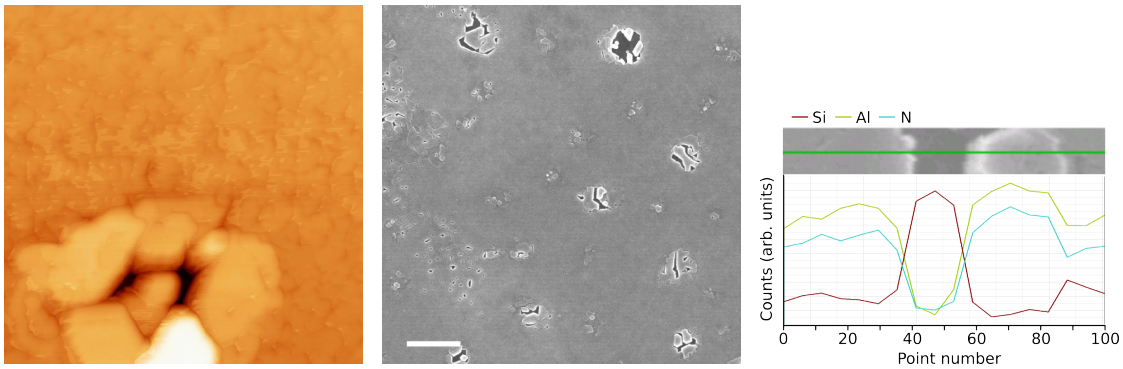

(a) AFM view - 1×1 μm^2 - z scale span from 0 to 82 nm

(b) SEM top view - scale bar: 400 nm

(c) EDX line scan - incident electron energy: 3 keV

Figure 3.22: 45 nm thick AlN film nucleated on a N-first AlN buffer and grown in Al-rich conditions – N2114

underneath the droplet, leading to the formation of the observed dark areas, where no AlN has been grown.

The spread in size of the dark areas observed in the thick AlN film compared to the buffer is attributed to a probable Ostwald ripening of the large Al droplets that have been deposited. In addition, the smooth surface of the crystallites surrounding the dark areas is tentatively attributed to a surfactant effect of the Si coming from the transient Al/Si droplets.

As a conclusion, the growth of thick AlN films, in strongly Al-rich conditions, and initiated on both Al- or N-first AlN buffer, led to the formation of large holes filled by Si, eventually crossing the whole AlN film. Protruding AlN islands, recalling the initial AlN pedestals are also visible.

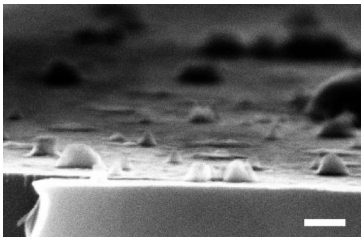

(a) SEM side view Scale bar: 100nm

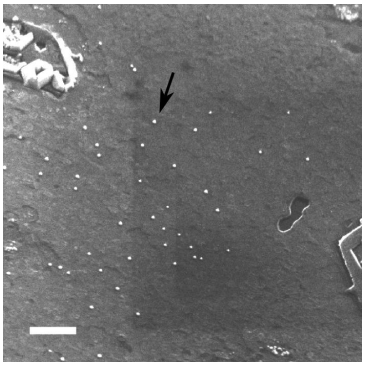

(b) SEM bird eye view, the dark arrow indicates an etched crystallite with a pyramidal shape. Scale bar: 200nm

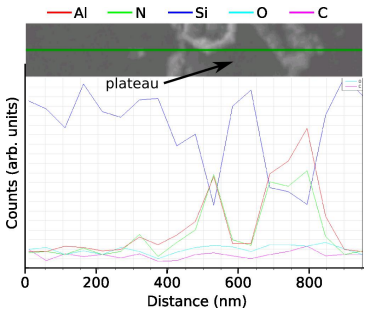

(c) EDXS line scan – incident electron energy: 3keV

Figure 3.23: KOH selective etching of a 45 nm thick AlN film grown on an Al-first AlN buffer – N2113

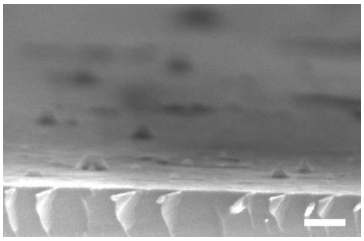

(a) SEM side view. Scale bar: 100 nm

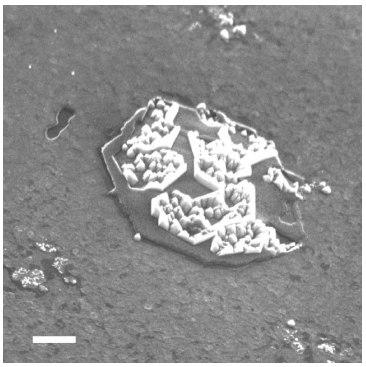

(b) SEM bird eye view. Scale bar: 200 nm

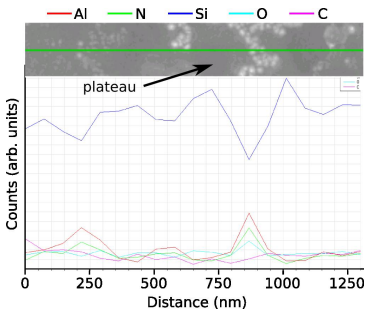

(c) EDXS line scan – incident electron energy: 3keV

Figure 3.24: KOH selective etching of a 45 nm thick AlN film grown on an N-first AlN buffer – N2114

Polarity KOH selective etching has been used to determine the polarity of the two grown AlN thick films. Pieces of the two films were dipped for 1 min in a $5 \sim 6$ M.L^{-1} KOH solutions at about 40 °C. The resulting AlN films are shown in Figure 3.23 and 3.24.

For both samples, the majority of the AlN film has been fully etched, except few protruding bright crystallites, which are the only residual AlN. It suggests an N-polarity to the AlN film, except for few Al-polar inversion domains (IDs). However, it cannot be excluded that the films were highly defective, which would have led to their etching, no matter their polarity.

On the Al-first AlN, the suggested Ga-polar IDs are uniformly dispersed on the

surface and their density is measured to be 1.5×10^9 cm^{-2}, which is similar to the dark areas observed on the bare Al-rich AlN buffer.

On the N-first AlN film, the dispersion of the suggested Ga-polar IDs is not uniform over the surface, fluctuating over distance in the range of 10 μm.

For both case, the removal of the AlN has unveiled dark areas with few appearing as large plateaus, whose chemical nature has been confirmed to be pure Si by EDXS analysis (see Figure 3.23 and 3.24). It confirmed that Si has been transported during the AlN growth, which strengthen the growth mechanism outlined in the previous paragraph. Those plateaus are hosting numerous AlN crystallites, presumably Al-polar, which would suggest that the Si-rich growth induces the nucleation of Al-polar crystallites. Additionally, the Al droplets have probably dug the Si surface, as witnessed by the presence of shallow holes in the bare Si substrate surface, although such structures might have been generated by the KOH etching as well.

Despite the thick AlN films display similar features than their respective AlN buffer, the extrapolation of their polarity to the one of the buffer would not be safe. Indeed, the polarity of AlN is hardly predictable as emphasized by its dependence on growth conditions instead of the initial nucleation step [116, 139]. For instance the two synthesized thick AlN films are N-polar whereas the majority of the GaN (the 2D layer) grown on the same AlN buffers is Ga-polar (see further results), suggesting that the AlN buffers are actually metal-polar. Additionally, as seen later, one AlN pedestal has been observed to be cubic. If large cubic crystallites would remain in the thick AlN film, the polarity determination from KOH etching would be invalid as the selectivity of KOH etching in cubic nitrides has not yet been reported.

3.2.5 Pedestal polarity

As the characterization of the thick AlN films cannot be used to get a relevant insight in the polarity of the AlN pedestals, a direct determination is mandatory. However, very few techniques could be able to assess the pedestal polarity.

The highly defective structure of the AlN and the low density of pedestals considerably lower the probability to observe, in a cross section preparation, a single pedestal by STEM. Actually, only one AlN pedestal, in a N-first AlN buffer[18], has been successfully observed, at the bottom of a GaN NW. The obtained images are shown in Figure 3.25. The power spectrum of the high angle annular dark field (HAADF) HR-STEM view of the pedestal reveals that it has crystallized in a zinc-blende lattice instead of the stable wurtzite structure expected for AlN. The Si/AlN interface is not abrupt, suggesting a large amount of dissolved Si in the pedestal (as expected from their growth mechanism), most probably leading to the observed cubic growth. A template matching routine [148] has been used to average the HAADF contrast of the AlN pedestal. It allows to infer a N-polarity to this pedestal.

[18] N2056

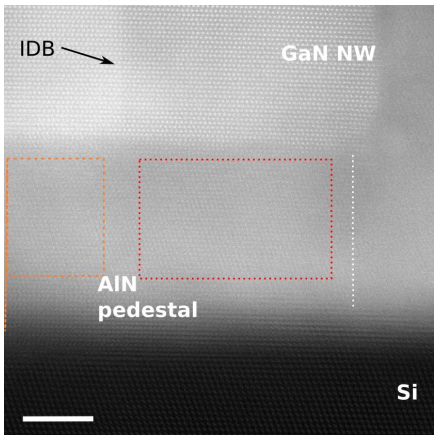

(a) Cross-section HAADF STEM image, taken along the $11\bar{2}0$ zone axis, of the base of a GaN NW anchored on an AlN pedestal, which is part of a N-first AlN buffer. A prismatic IDB, hinted higher up in the NW, is indicated by an arrow. Scale bar: 4 nm

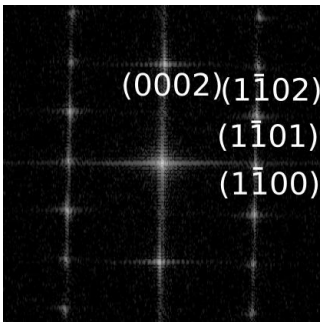

(b) Indexed power spectrum of the AlN pedestal STEM image

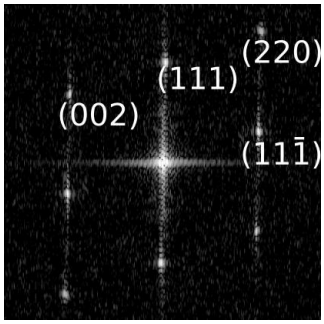

(c) Indexed power spectrum of the AlN pedestal STEM image

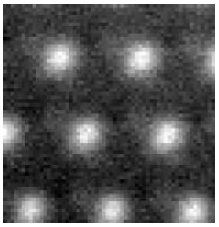

(d) Averaged contrast of the left part of the AlN pedestal (orange rectangle).

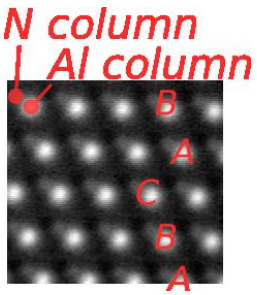

(e) Averaged contrast of the right part of the AlN pedestal (red rectangle).

Figure 3.25: Cross-section HAADF STEM view of a GaN NW hosted by an AlN pedestal of an N-first AlN buffer – N2056

In order to obtain statistically significant results over the polarity of pedestals, KPFM and piezo force microscopy (PFM) [30] analysis of the AlN buffer surface would be relevant techniques. Measurement have been intended but results are preliminary, hence not yet ready to be shown here.

As a conclusion, there has been yet no direct and systematic determination of the pedestals polarity. As shown later, only indirect determination will be done by probing the GaN grown on the pedestals themselves.

3.2.6 Hampering the nucleation of AlN nano-structures

Since AlN nano-structures are now identified and their nucleation scenario elucidated, the next prospect would be to prevent their nucleation or, at least, to tune their density. Only few efforts have been devoted to do so, as this prospect slightly fall apart the scope

of this study, thereby, only preliminary results and suggestions are given and discussed here.

First results were obtained by switching the growth from Al-first to N-first. Indeed, for a reduction performed at 840 ℃, the density of dark areas has been divided by 10 compared to the Al-first AlN buffers. Other routes can be envisaged:

- tuning the initial amount of deposited Al for Al-first AlN buffer
- depositing Al at a lower temperature than the Al/Si eutectic
- burying the AlN buffer

Initial amount of deposited Al The formation of Al/Si droplets during the Al-first AlN buffer growth is due to the initial accumulation of Al. Reducing the pre-deposited Al amount to its minimum, 1 ML_{AlN}, did not allow to decrease the density of the grown nano-structures, as observed in Figure 3.26a. It suggests that as soon as the γ-Al/Si phase is completed, extra deposition of Al leads to the formation of Al/Si droplets with a $\sim 10^9$ cm^{-2} density, independently of the amount of Al. Depositing less than 1 ML_{AlN} of Al will necessarily imply a nitridation of the Si surface, which brings to the N-first AlN buffer growth case. Another idea, suggested by Yasutake *et al.* would be to continuously provide the Al on the Si substrate, but at a sufficiently high temperature to prevent accumulation over the γ-Al/Si phase, *i.e.* the formation of Al/Si droplets. Hence, during the nitridation, meanwhile the γ-Al/Si phase is decomposed by the consumption of Al atoms that are participating in the growth of the AlN, the γ-Al/Si phase is healed by the impinging Al flux. However, such method requires to grow at very high temperature (higher than 900 ℃) and large temperature gradient over the substrate surface should be banned, which is technically difficult to obtain.

Growth at lower temperature than the Al/Si eutectic To prevent the dissolution of Si in the Al droplets, growth at a lower temperature than the Al/Si eutectic can be envisaged.

The reduction of the Si_xN_y by Al has been observed to be quenched at temperatures lower than the Al/Si eutectic. Hence, AlN growth on Si_3N_4 or Si_xN_y[19] might be intended in Al-rich conditions. However, SEM observations of a 100 nm thick Al deposited at 450 ℃ on bare Si (111) (Figure 3.27a and 3.27b) have revealed that the deposited Al film is not conformal. It means that even 100 ℃ lower than the Al/Si eutectic, diffusion of Al atoms occurs, leading to a full reorganization of the solid Al film. A partial covering of the Si substrate would again bring back to the N-first AlN buffer growth case.

Nevertheless, according to Zotov *et al.* [129], in order to obtain a layer by layer Al growth, deposition of the Al has to be done close to room temperature. Such fashion has been recently reported for AlN buffer growth [126] with an initial 1.5 ML_{AlN} Al

[19] however, the epitaxial relationship in the AlN would be loosed if grown on such amorphous film [120]

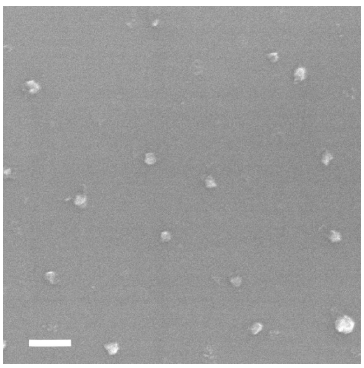

(a) SEM top view - Al-first AlN buffer prepared with only 1 ML_{AlN} of pre-deposited Al. Scale bar: 200 nm – N2002

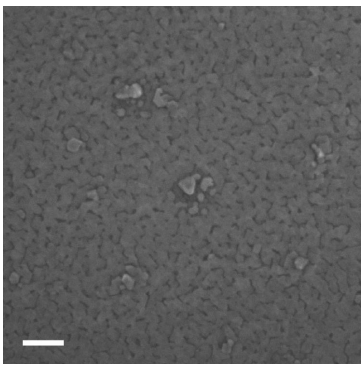

(b) SEM top view - Al-first AlN buffer prepared with 4 repetitive steps, each including 3 ML_{AlN} of Al deposition followed by nitridation. Scale bar: 100 nm – N1971

Figure 3.26: Al-first AlN obtained with different quantity of Al

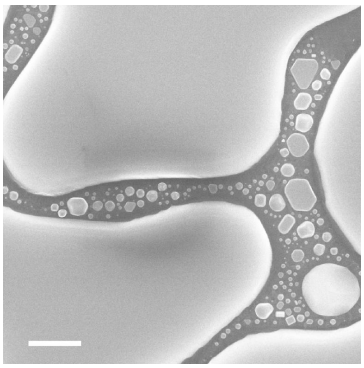

(a) SEM top view - Al deposited at 450 ℃ on Si (111) - scale bar: 1 μm

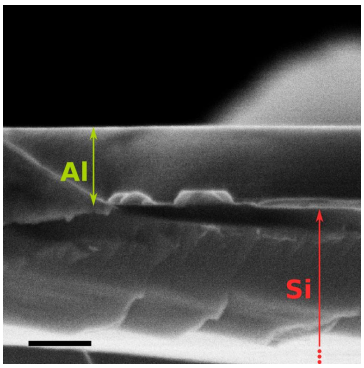

(b) SEM side view - Al deposited at 450 ℃ on Si (111) - scale bar: 200 nm

Figure 3.27: Tentatives to hamper the formation of AlN nano-structures – N2082

deposition at 50 ℃, followed by nitridation and further AlN growth at higher temperature. The obtained AlN is not any more monocrystalline, which probably constitutes the main drawback of this strategy. Additionally, the reported AFM micrographs reveals for one of this AlN buffer the presence of small protruding AlN islands, having a density of 6×10^9 cm^{-2}, which recalls the AlN pedestals. Hence, it is difficult to conclude about the efficiency of this strategy in order to grow AlN film free of nano-structures.

Burying the AlN buffer Subsequent growth of AlN on the initial AlN buffer, with Al-rich conditions, might be expected to heal the AlN by burying the nano-structures.

An AlN buffer has been grown at 840 ℃ using 4 similar steps, with one step consisting in depositing 3 ML_{AlN} of Al and to nitride it. Hence, the total amount of grown AlN is nominally the same than for a regular Al-first AlN buffer. However, SEM (Figure 3.26b) and AFM analysis have revealed that Al pedestals were still observable, so as few dark areas. Similar results were obtained for the growth of very thick AlN film grown in Al-rich conditions (see Figure 3.21 and 3.22).

Considering that the dark areas are the result of Si dissolution in transient Al/Si droplets, growing the AlN in N-rich conditions might be an interesting alternative. However, such strategy should fail to obtain a smooth and regular AlN film [149].

As a conclusion, it is clear that no obvious method would allow to prevent the formation of AlN nano-structures, rather suggesting their systematic growth in AlN on Si.

Discussion

Independently of the chosen growth route, Si has been demonstrated to aggregate or precipitate at the surface due to the transient existence of Al/Si droplets or due to the reduction of Si_xN_y by Al. An observed consequence is the growth of few AlN crystallites in Si-rich conditions (*i.e.* pedestals and surrounding AlN), which are breaking the uniformity of the AlN film. Depending on the growth route, the spatial density of those nano-structures is varying between $10^8 \sim 10^9$ cm^{-2}. Growth of thicker AlN film has been shown to be inefficient to bury them.

The typical density of self-organized GaN NWs grown on Si, with the help of an AlN buffer, is in the order 10^9 cm^{-2}. It means that the nano-structures are likely to play a role in the nucleation of the NWs, as first envisaged by Brubaker *et al.* and Largeau *et al.*.

3.3 GaN nanowires assembly

3.3.1 Growth routes

Assemblies of GaN NWs were nucleated on the previously described AlN buffers, using the typical conditions: $\frac{\phi_{Ga}}{\phi_N} = 0.3$ and $T_{substrate} = 840$ ℃.

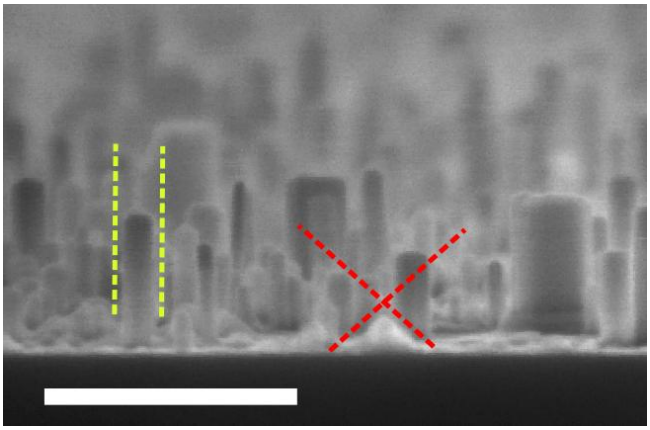

(a) SEM side view – coexistence of pyramids and NW nucleus

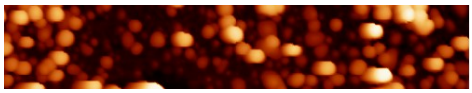

(b) AFM tapping mode - 1.7×2 μm^2 - z span from 0 to 121 nm

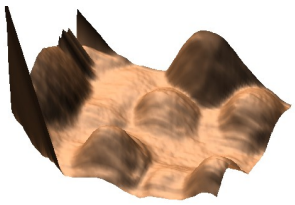

(c) 3D display AFM micrographs - zoom over GaN pyramids - $109 \times 150 \times 36$ nm^3

Figure 3.28: Identification of two types of GaN crystallites – N-first AlN buffer – N2000

For most of the growths, only two AlN buffers were used:

- the Al-first AlN buffer obtained with a nitridation at 670 ℃. It has $\sim 10^9$ cm^{-2} AlN pedestals and the dark areas can be easily identified by SEM.
- the N-first AlN buffer grown at 840 ℃. It has only $\sim 10^8$ cm^{-2} AlN pedestals, thereby, differing from the other buffer.

For the shorter GaN NWs assemblies, growth duration was set down to 30 min so that two types of GaN crystallites can be identified by SEM and AFM (Figure 3.28):

- pyramids: crystallites delimited by polar and semi-polar facets only. SEM observations (Figure 3.28a) allowed their easy identification whereas AFM (Figure 3.28b and 3.28c) lacks spatial resolution to clearly resolve the pyramid facets. Crystallites resulting from the coalescence of pyramids will be still referred as pyramids.
- NW nucleus: crystallites laterally delimited by m facets. Neglecting coalescence events with neighboring crystallites, the presence of m facets ensures an enhanced vertical growth,[20] which defines a NW.

It is not excluded that a pyramid might later evolve toward a NW shape, whereas the reverse is expected to be prohibited thanks to the high stability of m facets.

Additionally, in the MBE chamber, the heater geometry was responsible for a 40 ℃ monotonous temperature drop from the center to the edge of the substrate, with a radial symmetry due to sample rotation. Such temperature variation did not alter AlN growth due to a negligible Al desorption and AlN decomposition in the range of used growth temperatures. Hence, the obtained AlN buffers were homogeneous over the whole substrate surface. Conversely, during GaN NW growth, desorption of Ga and

[20] see chapter 2

GaN decomposition are significant, which has resulted in an increased amount of grown GaN towards the sample edge, where temperature was minimal. Hence, by carefully selecting GaN growth temperature and duration, only scarce GaN crystallites could be grown in the substrate center whereas a fully developed GaN NW assembly featuring 10^9 NW cm^{-2} was grown at the edge. As a first approximation, it provides a chronology of NW nucleation, all on a single wafer.

3.3.2 Nucleation sites and chronology

Grown GaN nucleus have been identified using SEM observations. Indeed, in SEM micrographs, the GaN appears brighter than the AlN thanks to the chemical contrast ($Z_{GaN} > Z_{AlN}$) and to the presence of numerous facets that increase the chance for secondary electrons to be released from the material. AlN pedestals also appeared brighter than the rest of the AlN film due to their lateral facets, but darker than GaN crystallites.

Nucleation on Al-first AlN SEM micrographs taken along the substrate radius (*i.e.* versus growth temperature) of GaN grown on the Al-first AlN buffer[21] are shown in Figure 3.29.

No nucleation of GaN is observed in the substrate center whereas a fully developed GaN assembly, made of NWs with a 2D layer, is visible close to the substrate edges. No GaN growth occurred as well in the dark areas of the AlN buffer, except at very low temperature. This is attributed to the presence of Si_xN_y in the dark areas, acting as an in-situ mask [150]. It allows to localize the AlN nano-structures even after the nucleation of a thick GaN 2D layer.

For high growth temperature, the GaN pyramids distribution is observed not to be uniform over the surface: pyramids density increases while getting closer to dark areas. It suggests the existence of different nucleation probabilities for GaN on AlN buffer as function of the distance to dark areas. As emphasized in Figure 3.30, the meander-like pattern given by the pyramid density variations (observed by SEM) appears to be very similar to the pattern given by height fluctuations of the AlN buffer surface (measured by AFM and neglecting the AlN nano-structures), with low height areas matching low pyramid density areas. Adding the fact that decreasing the AlN buffer thickness from 8 to 4 nm has been reported to increase the incubation time of GaN NW nucleation by Musolino *et al.* [126], the inhomogeneous nucleation of GaN pyramids is thus attributed to AlN thickness variations. The thickness dependence to the distance from the dark areas have probably arisen from the slow diffusion of Al atoms out of the Al/Si droplets during the nitridation step.

Musolino et al [126] have hypothesized that the reduced incubation time of GaN on thicker AlN is correlated with a roughening of the surface, leading to the increase of the amount of adsorption sites. However, in our case no significant variations in the AlN surface RMS as function of the distance to dark areas has been observed on the Al-first

[21] N1982

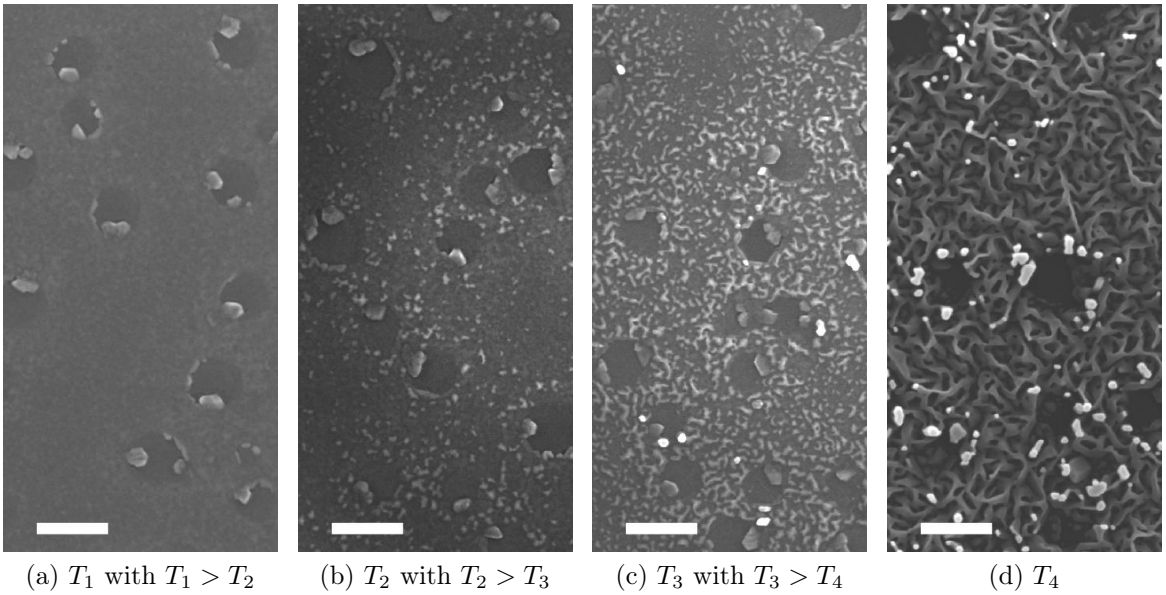

(a) T_1 with $T_1 > T_2$ (b) T_2 with $T_2 > T_3$ (c) T_3 with $T_3 > T_4$ (d) T_4

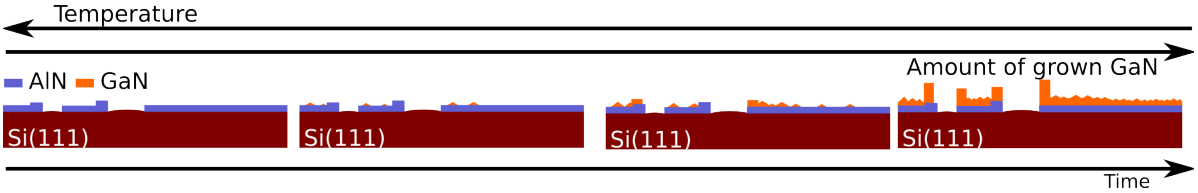

(e) Schematic chronology of the initial GaN growth

Figure 3.29: GaN nucleation on an Al-first AlN buffer – scale bar: 200 nm – N1982

AlN buffer. It suggests the influence of other constraints over GaN nucleation such as AlN texturing or average AlN grain size, which have been reported to evolve in the few first ML of AlN grown on Si [125].

Decreasing the growth temperature led to an increase of the pyramid density (up to $\sim 10^{11}$ cm^{-2}) until the appearance of a continuous 2D layer. In the chronological scheme, it suggests that the 2D layer is the result of the growth of the pyramid assembly until their coalescence, leading to the specific structure of the 2D layer.

NW density reached a maximum in the cooler area of the substrate, with $\sim 10^{10}$ NW.cm^{-2}. This value is below the one of pyramids and above the usual NW density in assembly grown for few hours, meaning that coalescence events between NWs should be expected for longer growth. Additionally, despite pyramids are spread almost all over the substrate, NW nucleation occurs almost exclusively on AlN pedestals and in the close vicinity of dark areas. Therefore, the ripening of a pyramid into a NW nucleus seems not to be the general case and an additional ingredient is most likely required to trigger the NW nucleation. NWs are observed not to exclusively nucleate on AlN pedestals but rather in the close vicinity of the dark areas, where AlN has resulted from the nitridation of Al/Si droplets (*i.e.* it has been grown in Si-rich conditions). Therefore, it is this specific growth mode that is suggested to provide to those AlN crystallites the

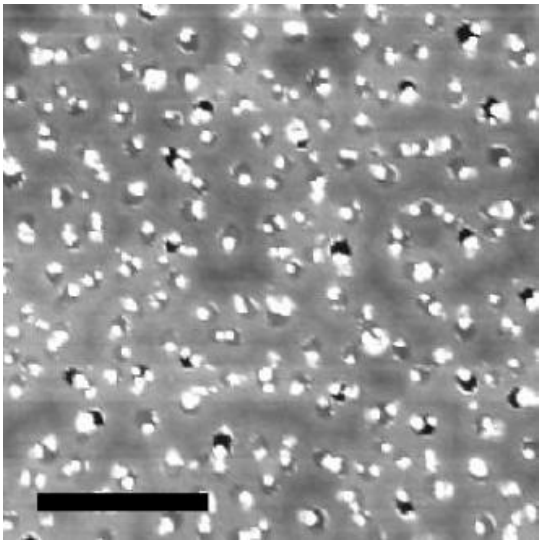

(a) AFM micrographs of an Al-first AlN buffer obtained with T_N = 670 °C – scale bar: 1 μm, z scale span from 0 to 27 nm – N1965

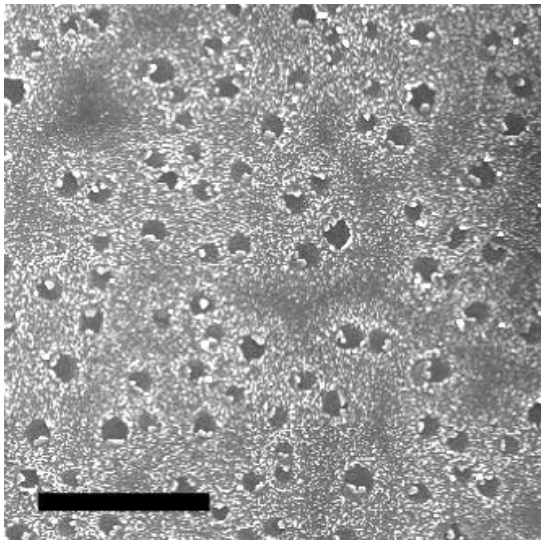

(b) SEM top view of GaN nucleus on an Al-first AlN buffer obtained with T_N = 670 °C – scale bar: 1 μm – N1982

Figure 3.30: Comparison between areas of low density for GaN pyramids and AlN film height. Images have intentionally contrasted in order to emphasize the specific patterns.

ability to trigger GaN NW nucleation, through a specific polarity or surface chemistry or crystalline phase compared to the rest of the AlN film.

Nucleation on N-first AlN SEM micrographs taken along the substrate radius (*i.e.* versus growth temperature) of GaN grown on the N-first AlN buffer[22] are shown in Figure 3.31.

Nucleation of pyramids on the N-first AlN occurred uniformly on the substrate, suggesting the absence of AlN thicknesses variations as function of the distance to dark areas. However, no growth occurred on dark areas, which is still attributed to the presence of Si_xN_y.

GaN NWs were observed to nucleate on AlN pedestals but not exclusively. Once on a pedestal, NWs are observed not to laterally extend until the pedestal edges (see Figure 3.32b). It indicates that NWs are not the mere continuation of AlN pedestals, which probably differs from the case of Al-first AlN buffers where pedestals are smaller (see Figure 3.32a). It clearly emphasizes that NW nucleation does not rely on the columnar morphology of the underneath AlN crystallite, as hypothesized by Brubaker *et al.* [114] or Largeau *et al.* [31]. For a well developed assembly of NWs, reaching $\sim 10^9$ NW.cm^{-2}, only 10% of NWs are hosted by a pedestal, which further indicates that NW density is independent of the pedestal density.

[22] N2000

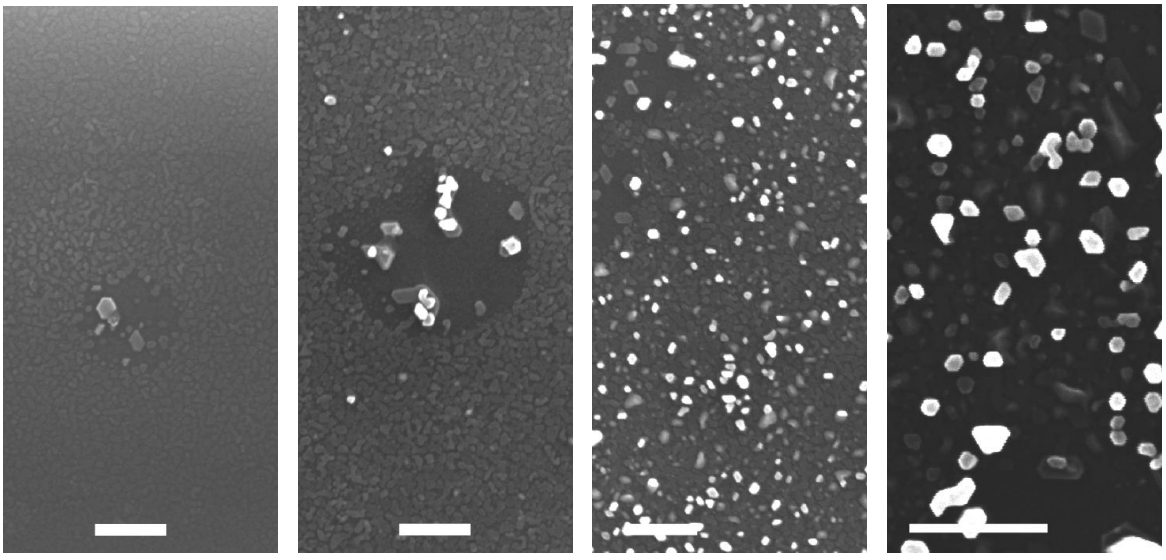

(a) T_1 with $T_1 > T_2$ (b) T_2 with $T_2 > T_3$ (c) T_3 with $T_3 > T_4$ (d) T_4

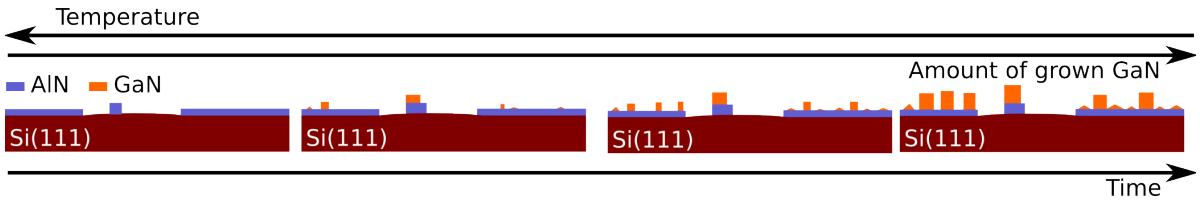

(e) Schematic chronology of the initial GaN growth

Figure 3.31: GaN nucleation on an N-first AlN buffer – scale bar: 200 nm – N2000

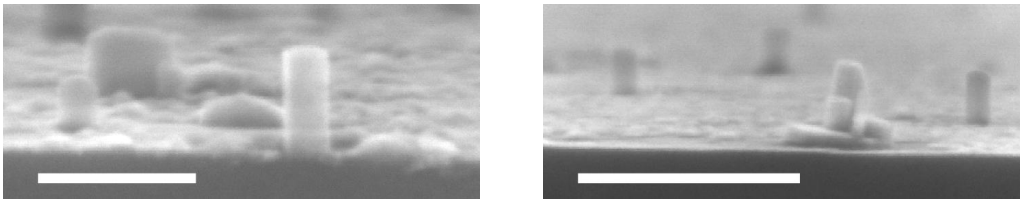

(a) GaN NW on Al-first AlN buffer – scale bar: 100 nm – N1982

(b) GaN NW on N-first AlN buffer – scale bar: 200 nm – N2000

Figure 3.32: SEM side view of GaN NWs sitting on AlN pedestals

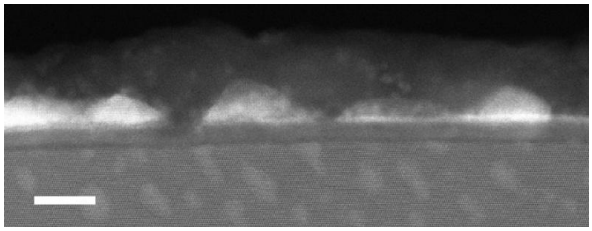

(a) HAADF STEM large view of pyramids – scale bar: 10 nm

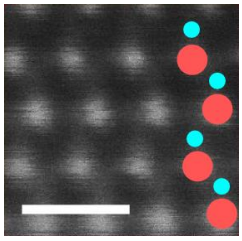

(b) HAADF STEM zoomed view in #1 pyramid lattice – scale bar: 5 Å

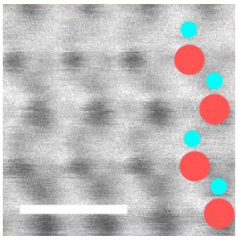

(c) Annular bright field (ABF) STEM zoomed view in #1 pyramid lattice – scale bar: 5 Å

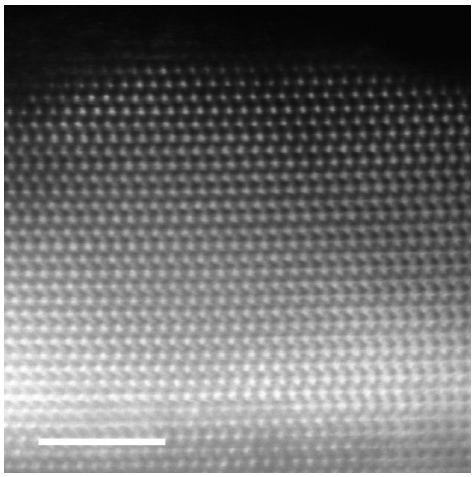

(d) HAADF STEM zoom view of the GaN pyramid #1 – scale bar: 25 Å

Figure 3.33: Polarity determination of a GaN pyramid sitting on a Al-first AlN buffer by STEM observation – N1982

3.3.3 GaN polarity

The observation of different growth modes for GaN crystallites, *i.e.* a pyramidal growth mode for pyramids and a columnar growth mode for NW nucleus, suggests the existence of intrinsic differences such as polarity, between pyramids and NWs. Polarity determination has been intended using different means: HR-STEM allowing fine structural resolution and KPFM or KOH selective etching allowing polarity determination over large scale.

Two types of sample preparation were used for HR-STEM analysis:

- NW dispersion on a carbon grid. In such a case, NWs were grown long and with a small AlN insertions in order to keep track of the growth direction once removed from their substrate.

- NWs still attached to the substrate prepared in cross-sections. In such a case, NWs were grown short so that single pyramids and NWs were observable with a minimal superposition of both.

As emphasized in the cross-section sample of Figure 3.33, pyramids were determined fully Ga-polar when sitting both on the Al- or N-first AlN buffers.

Conversely, NWs were observed to be fully N-polar or hosting "core-shell" IDs, *i.e.* a Ga-polar core laterally enclosed by a complete sleeve of N-polar GaN (see Figure 3.34).

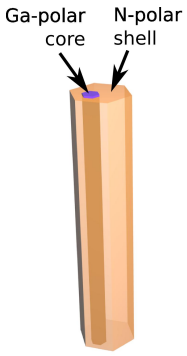

(a) Sketch of a NW hosting a "core-shell" ID

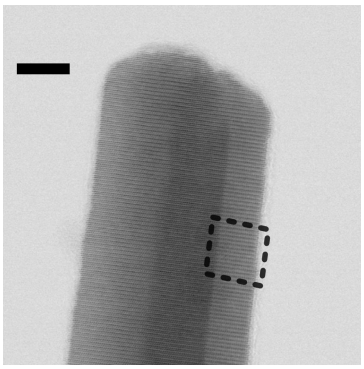

(b) ABF STEM large view of a GaN NW – scale bar: 10 nm

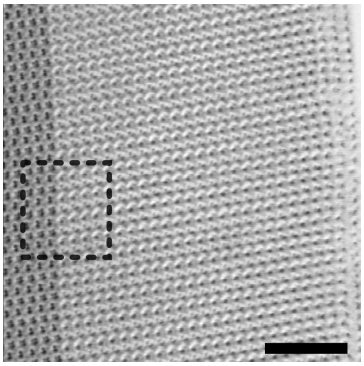

(c) ABF STEM view of the boundary of the dark contrasted area (drift during the micrographs acquisition has slightly deformed the image) – scale bar: 2 nm

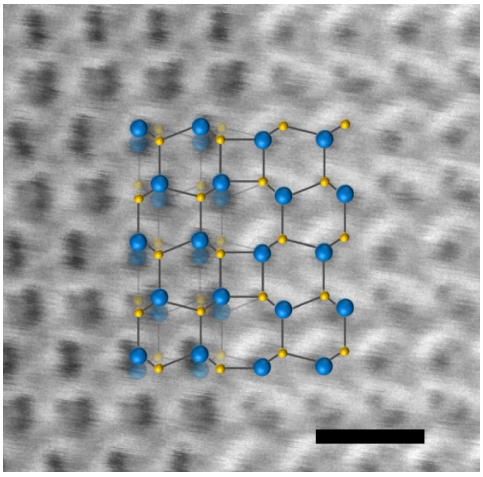

(d) ABF STEM zoomed view of the dark contrasted area – deduced N-columns (small yellow ball) and Ga-column (large blue ball) positions are superimposed over the micrographs, on the left side, the projection through the core-shell structure imply the superposition of Ga and N-columns – scale bar: 5 Å

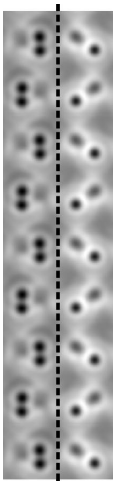

(e) Simulated ABF pattern obtain for a core-shell ID structure on the left and a unipolar material on the right – see chapter 4

Figure 3.34: Polarity determination of a GaN NW nucleated on a Al-first AlN buffer and hosting a "core-shell" IDs – N2183

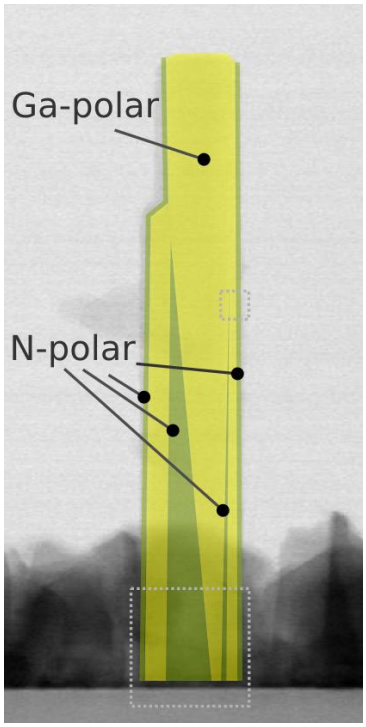

(a) ABF STEM view – IDs location are emphasized by colors

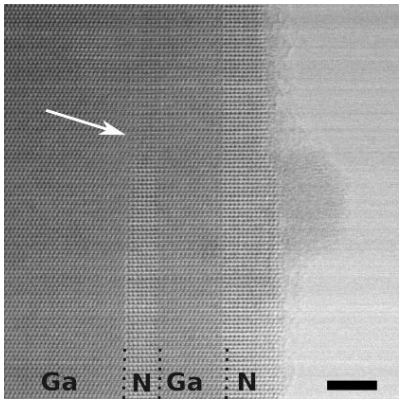

(b) ABF STEM zoomed view over an N-polar ID closing area (indicated by the white arrow) – IDs are delimited based on contrast – scale bar: 4 nm

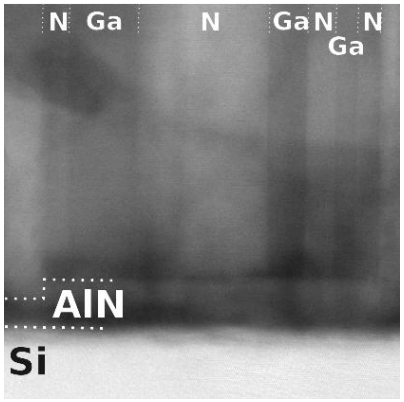

(c) ABF STEM zoomed view at the bottom of the NW – IDs are indicated based on contrast

Figure 3.35: STEM micrographs exhibiting the closing of inner N-polar IDs and the propagation from the bottom to the NW top of the N-polar shell

Inversion domains The process used to identify the presence of IDs is detailed in the chapter 4. In the general case, IDs were observed to propagate from the bottom to the top of the NW, to feature an hexagonal section with a constant diameter along NW length, and to be delimited by prismatic IDBs, parallel to m planes, having the IDB*[23] atomic structure.

In one case, shown in Figure 3.35, N-polar IDs were found in a Ga-polar domain, which was itself surrounded by a N-polar shell. There, the inner N-polar IDs have tapered during growth leading to their closing, whereas the N-polar shell enclosing the Ga-polar core has propagated to the NW top. This particular case demonstrates that IDs[24] can be unstable and might close during growth.

In order to account for the formation of the IDs in the NWs, one has to raise the question of basal IDBs formation, which reverses the polarity along the c axis. In polar materials, the divergence of the spontaneous polarization within the plane of a basal IDB results in surface charge[25], which should drastically increase the formation energy of such

[23] see reference [151]

[24] in that case, N-polar IDs in Ga-polar material

[25] $\pm 0.162 C.m^{-2}$ for AlN, $\pm 0.114 C.m^{-2}$ for ZnO and $\pm 0.058 C.m^{-2}$ for GaN, based on calculated spontaneous polarizations from [16]

defect. Nevertheless, basal IDBs have been theoretically or experimentally reported for GaN, AlN and ZnO:

- in GaN, basal IDBs reversing from Ga-polar to N-polar GaN were reported in the case of high Mg-doping [152, 153]. The defect formation is attributed to the growth of the Mg_3N_2 compound that stabilizes the formation of Ga-Ga bonds [154]. Additionally, saturating a GaN (0001) facet by Si atoms has been theoretically predicted to favor a polarity reversal [155, 156]. However, there is an uncertainty over the experimental ability to grow such structures as emphasized by the work of Markurt *et al.* [157] who had shown that Si deposited on GaN leads to the formation of a $SiGaN_3$ compound acting as an antisurfactant, which would make further GaN growth thermodynamically unstable. Nevertheless, high Si doping of GaN grown on Si (with an SiC buffer) has been reported to invert the GaN polarity from N- to Ga- polar [158]. At last, deposition of few nanometers thick Al_2O_3 on Ga-polar GaN has been also used to reverse polarity [159].

- in AlN, accumulation of exactly 2 ML_{Al} of Al on top of a N-polar AlN has been theoretically predicted to favor a polarity reversal for the overgrown AlN [160]. The same authors have also shown that such Al coating is unstable relative to bulk Al, which forbids their formation in a system close to the thermodynamic equilibrium. Nevertheless, polarity reversal from N- to Al-polar AlN, intended by deposition of an Al interlayer, has been experimentally reported [116] but TEM observations did not revealed the presence of any Al metallic bilayer. One can mention as well the synthesis of AlON compounds by sintering. Beyond 0.75% of incorporated oxygen into AlN, formation of defects such as IDBs have been reported [143, 161, 162, 163]. Si atoms were reported as well to stabilize IDBs and to planarize them [144].

- in ZnO synthesized by sintering, basal IDBs were reported to form due to the deposition of a monolayer of cations (Sn^{4+} or Sb^{5+}) [164]. Similarly, Sb dopants have been observed to accumulate in basal IDBs in ZnO NWs [165].

Neglecting the formation of Al-Al bonds under strong Al-rich conditions, which were never experimentally observed, it can be inferred that basal IDBs growth requires the massive incorporation of ionic impurities or dopants in order to stabilize the concomitant surface charges that appeared. Therefore, their formation in undoped GaN NWs could be reasonably disregarded. In the AlN buffer, only the Si-rich growth of the pedestals and nearby crystallites would gather the required conditions to foster the formation of basal IDBs. Possible residues of SiO_2 might stabilize as well basal IDBs in AlN by providing O atoms.

Disregarding the bulk of AlN or GaN, basal IDBs could nucleate as well at the two interfaces of the system:

- the $Si_{substrate}/AlN_{buffer}$ interface. The Si substrate is non-polar, suggesting that polarity of the overgrown AlN should only depend on the chemistry of the Si/AlN

interface (*i.e.* the relative stability of the Si-N and Si-Al bonds under the different growth conditions). However, the situation is rather more complex as the polarity has been experimentally reported to depend on temperature [166, 139]. And despite improved growth conditions, it seems that growth of perfect unipolar AlN films on Si is not the general case as small columnar IDs are usually observed [167, 125, 168, 169].

- the AlN_{buffer}/GaN interface. Indeed, IDs have been already reported to nucleate in GaN films grown on AlN [168, 170]. Accommodation of step edges has been invoked as a potential driving force for their nucleation [171] but the presence of residual Si at the interface might be envisaged as well, taking into account the demonstrated Si precipitation occurring during the AlN buffer growth. Additionally, in Figure 3.25a, the IDB visible in the GaN NW, is tentatively observed to stem from the AlN pedestal surface[26] bringing an additional experimental clue.

As a conclusion, the formation of columnar IDs in GaN or AlN thin films grown on Si seems rather common and can be assigned to multiple causes, including dopants accumulation or accommodation of step edges. The case seems similar to the growth of GaN or AlN on sapphire [172]. Hence, there is no reason that GaN NWs would be free of IDs. However, two singularities should be noticed: (i) IDs were observed in NWs but never in pyramids and (ii) IDs in NWs are always confined in their core. Both will be further discussed in the section dealing with NW nucleation.

Nevertheless, it is remarkable that such defect in GaN NWs grown by PA-MBE has not been reported so far and it questions the relevance of previous polarity determination, which were performed with tools whom the probe was larger than the potential IDs diameter. Indeed, depending on samples, the shell thickness or the ID diameter could be thinner than 4 nm and so likely ignored during the polarity determination. Therefore, if the presence of IDs in GaN NWs is further generalized, which is agreed in the chapter 4, it would bring a first answer to explain the polarity variability reported for NWs (Table 3.1).

Large scale polarity determination With the purpose of obtaining statistically significant results, additional KPFM measurements were carried on, especially to determine the ratio of NWs hosting IDs.

The principle of the technique is detailed in the the chapter 1, in the section 1.4.4, page 22. It consists in mapping the local potential difference between the substrate and an AFM tip (noted V_{CPD}) while scanning a surface. Thanks to prior calibrations, the V_{CPD} value can be assigned to a specific polarity. Therefore, the V_{CPD} mapping allows to spatially resolve the polarity structure of the probed surface, which is in our case the top facets of a NWs assembly.

NWs grown on the Al- or N-first AlN buffers do not exhibit a density high enough to obtain a substrate surface filling factor higher than few percents. In such a case, AFM

[26] the conclusion is tentative as distortions in the AlN pedestal or its cubic structure might have vanished the contrast related to the presence of the IDB.

probing of as-grown NWs is rather adventurous as each NWs top facets is separated by gaps 100 nm large and hundreds nm deep, which has generally led to the breakage of NWs or of the tip[27]. To overcome this experimental difficulty, a last step in the growth of the NWs, aiming at enlarging the top facets, has been added. It required a transient Ga-rich growth as described in the chapter 2. The obtained NW assembly[28] has a surface filling factor reaching up to 50%, with 200 nm large top facets, providing terraces large enough for AFM scanning (see SEM micrographs in Figure 3.36a and 3.36e).

A force gradient feedback has been used to scan the top of the as-grown NWs, allowing to increase the spatial resolution down to 50 nm for the V_{CPD} mapping, which is smaller than the average size of the NW top facet. Correlated topographic and V_{CPD} mapping are shown in Figure 3.36. Homogeneous V_{CPD} have been measured on top of the NW top facet, which were observed to be very flat. For the NWs grown on the Al-first AlN buffer, the average V_{CPD} value was 0.84 V with a width of 70 mV, which non-ambiguously corresponds to a N-polar material. For the NWs grown on the N-first AlN buffer, most of the NWs exhibited a similar V_{CPD} value to that observed for the NWs grown on the Al-first AlN, except a minority, which were measured with a V_{CPD} of 0.4 V. Those NWs are identified as the NWs hosting a Ga-polar inversion domain. However, the measured V_{CPD} value is slightly higher than the one expected for a pure Ga-polar surface (0.27 V). This shift is attributed to the probable presence of an N-polar shell (which is not resolved by the technique used here) and of the numerous surroundings N-polar NWs. From 5×5 μm^2 scans including on average 250 NWs, the ratio of NWs hosting a Ga-polar core has been observed to fluctuate from 5 to 25%, depending on the localization on substrate.

Those values should be considered as a lower bound for the ratio of NWs nucleating with an IDs. Indeed, STEM observations have already shown that IDs might close in NWs (more exactly N-polar IDs in a Ga-polar domain). Additionally, there is probably a limited sensibility of the KPFM technique to very small IDs. And at last, the consequence of the enlargement of the NW top facet over the growth of the inner IDs are unknown. Nucleation of new IDs should not be expected but the numerous stacking faults (SFs) resulting from the specific growth conditions (see chapter 2, section 2.3.6, page 40) could interfere and close the existing IDs (see chapter 4, section 4.4, page 129 for more details)[29]. Therefore, KPFM ratio should be considered as minimal values.

Aside of KPFM, KOH etching has been used to image the polarity structure of the enlarged GaN NWs grown on the N-first AlN. NWs have been dipped in a $5 \sim 6$ mol.L^{-1} KOH solution at ~ 40 °C. For an etching longer than 10 min, the top part of the NWs has been systematically observed to be fully etched away, independently of its polarity. However, for etching no longer than 2 min, the NW top part is still preserved, as shown in Figure 3.37. In such a case, NWs can be classified in four types:

[27] Actually, the tip is not literally broken but broken NWs agglomerate on it by van der Waals interactions, which makes the tip unstable and non-reliable

[28] N2313 and N2085

[29] actually, STEM imaging of IDs have been intended on enlarged NWs but their large diameter prevents high resolution imaging, which hinders IDs identification

Al-first AlN buffer

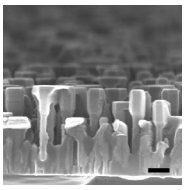

(a) SEM side view – enlarged GaN NWs – scale bar: 200 nm

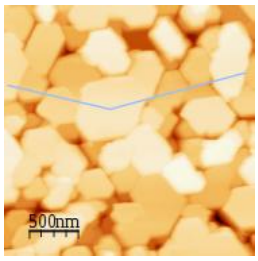

(b) Topographic mapping obtained by AFM

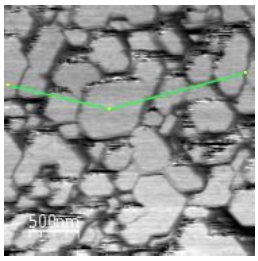

(c) V_{CPD} mapping spanning from 0.3 to 1.1 V

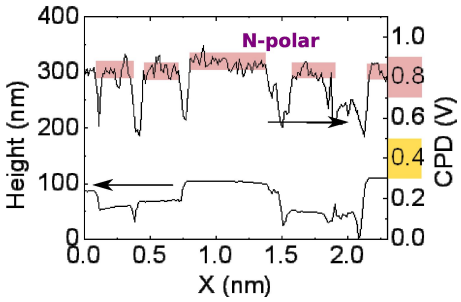

(d) Profile of the altitude and the V_{CPD} along the green line

N-first AlN buffer

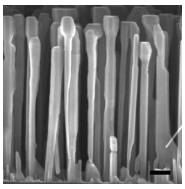

(e) SEM side view - enlarged GaN NWs – scale bar: 200 nm

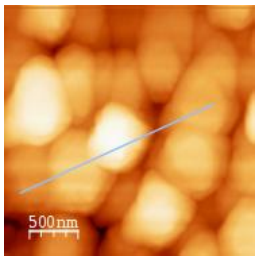

(f) Topographic mapping obtained by AFM

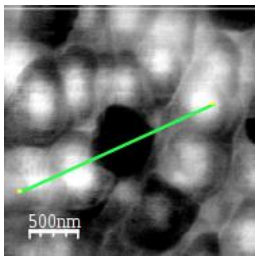

(g) V_{CPD} mapping - spanning from 0.3 to 1.1 V

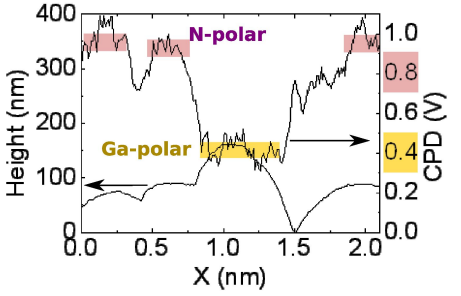

(h) Profile of the altitude and the V_{CPD} along the green line

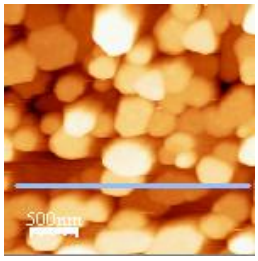

(i) Topographic mapping obtained by AFM

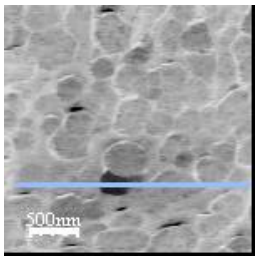

(j) V_{CPD} mapping spanning from 0.3 to 1.1 V

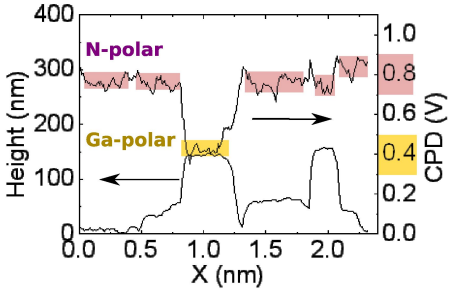

(k) Profile of the altitude and the V_{CPD} along the green line

Figure 3.36: KPFM mapping of the top surface of enlarged as-grown GaN NWs – N2313 and N2085

- fully etched NWs, which exhibit large pyramids. Those NWs are non-ambiguously identified as N-polar.
- smoothly etched NWs, which exhibit a top facet rougher than before the dip in KOH but without large pyramids. Such phenomenon recalls the observations of Urban *et al.* [36] who had observed a smooth etching by KOH of Ga-polar GaN pillars including numerous basal SFs. Therefore, knowing that the enlarged part of the NWs also includes numerous basal SFs, those NWs are tentatively identified as Ga-polar and will be later considered as "non-etched".
- partly etched NWs, which exhibit an area with large pyramids and an untouched area. Those NWs are identified as N-polar with a Ga-polar IDs.
- non-etched NWs, which are free of pyramids and within the resolution of the SEM micrographs seem as smooth as before the KOH bath. Those NWs are identified as Ga-polar.

Similarly than for KPFM, the ability of KOH to resolve small IDs such as the thin N-polar shell observed by STEM and shown in Figure 3.34 is most probably null. Therefore, the presence of supplementary IDs in the presumed Ga-polar NWs cannot be discarded on the base of those results.

Nevertheless, the ratio of each type of NWs has been extracted from the SEM micrographs and plotted as function of the distance from the substrate center (*i.e.* as function of the growth temperature). No specific correlation between a type ratio and its position on the wafer could be drawn, suggesting that the nucleation of those objects does not depend on temperature. The ratio of NWs hosting a Ga-polar part (NWs partly or non-etched) fluctuates between 15 and 35%, which is slightly over the estimation given by the KPFM analysis.

2D layer polarity The GaN 2D layer is a defective film [115], which prevents a clear polarity assessment. HR-STEM imaging hints a Ga-polarity at the top part of the GaN 2D layer, as shown in Figure 3.38. However the bottom part of the 2D layer is thicker and made of superposed grains, which prevent a clear assessment of the polarity by STEM. At last, the STEM technique only provide local insight of the polarity instead of the full picture.

Therefore, large scale techniques such as KPFM or KOH would be required. However, KPFM would require extensive calibration measurements on all the different semi-polar facets that can be found in the rough 2D layer and KOH might loose its selectivity due to the defective nature of the material[30]. Only KOH etching of GaN 2D layers has been attempted and the obtained results are presented in Figure 3.39 and 3.40.

Well developed ensembles of GaN NWs grown on N- and Al-first AlN buffers were dipped in a 5 $\sim$ 6 mol.L^{-1} KOH bath, at $\sim$ 40 °C for 2 min. SEM micrographs of the samples before and after KOH etching are shown in Figure 3.39 and 3.40. For both

[30]KOH is etching dislocations even in Ga-polar surfaces [59]

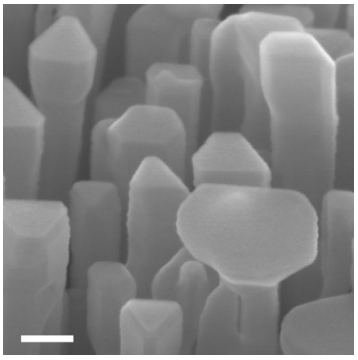

(a) bird eye view SEM micrographs of enlarged GaN NWs grown on an N-first AlN buffer - scale bar: 100 nm

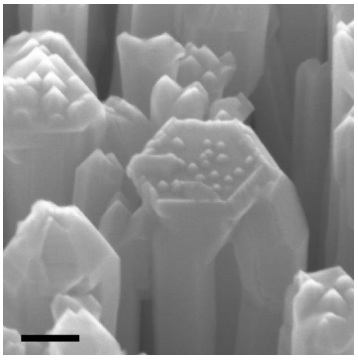

(b) bird eye view SEM micrographs of enlarged GaN NWs grown on an N-first AlN buffer after KOH etching - scale bar: 100 nm

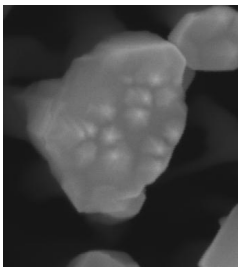

(c) GaN NWs fully etched by KOH

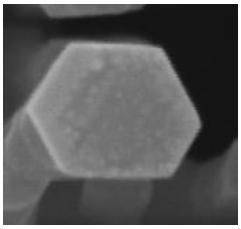

(d) GaN NWs smoothly etched by KOH

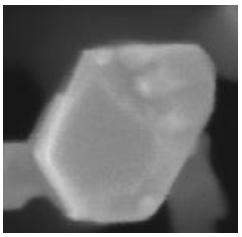

(e) GaN NWs partly etched by KOH

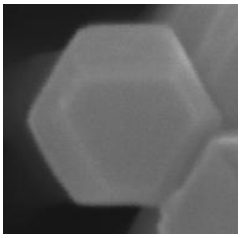

(f) GaN NWs non-etched by KOH

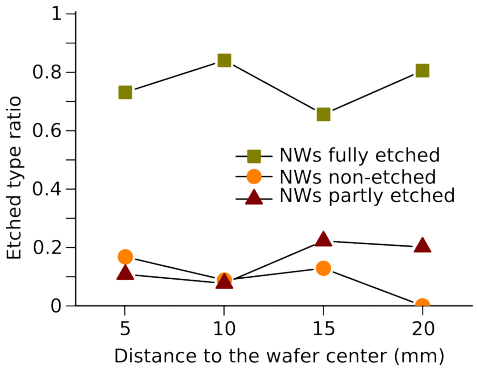

(g) Extracted ratio of KOH etched NWs as function of the position on the wafer

Figure 3.37: KOH etching of enlarged GaN NWs grown on the N-first AlN buffer – N2085

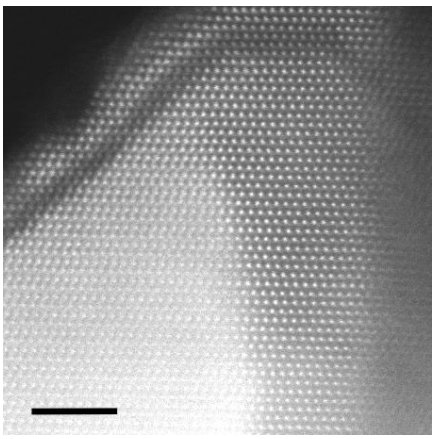

(a) zoomed HAADF STEM image - the darker film correspond to an AlN marker included in the GaN - scale bar: 5 nm

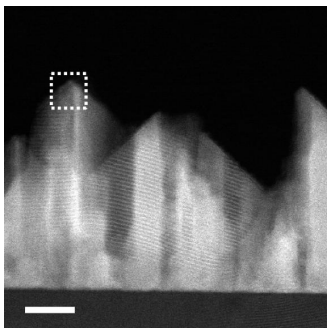

(b) HAADF STEM image - contrast correspond to interferences patterns - scale bar: 20 nm

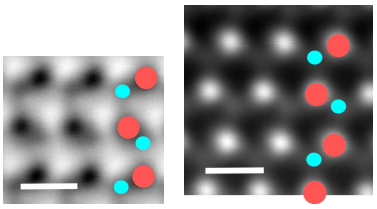

(c) ABF (left) and HAADF (right) average contrast obtained from a template matching routine performed in the middle of the pyramid - large red dots correspond to the Ga-column and small blue dots correspond to the N-column - scale bar: 3 Å

Figure 3.38: Cross-section STEM view of a GaN 2D layer grown on the N-rich AlN buffer – N2056

samples, NWs are almost all etched away and part of the 2D layer as well. Large and small hexagonal holes are observable in both 2D layers which would correspond to the etching of dislocations or of N-polar domains.

In the case of the GaN 2D layer grown on the N-first AlN, the typical pyramidal pattern due to KOH etching of N-polar surfaces is visible underneath the 2D layer (see the black arrow on Figure 3.39c). Coupled with the STEM results, it hints an average Ga-polarity for the 2D GaN layer.

In the case of GaN 2D layer grown on the Al-first AlN buffer, the KOH etching is less conclusive. The 2D layer has been etched in a similar manner than for the GaN 2D layer grown on the N-first AlN buffer, suggesting a Ga-polarity, but no typical pyramidal pattern can be observed underneath the 2D layer. Nevertheless, based on STEM results and on literature [31], the GaN 2D layer is hinted Ga-polar.

As a conclusion, the polarity of grown GaN determined from different techniques is sum-up in the tabular 3.41.

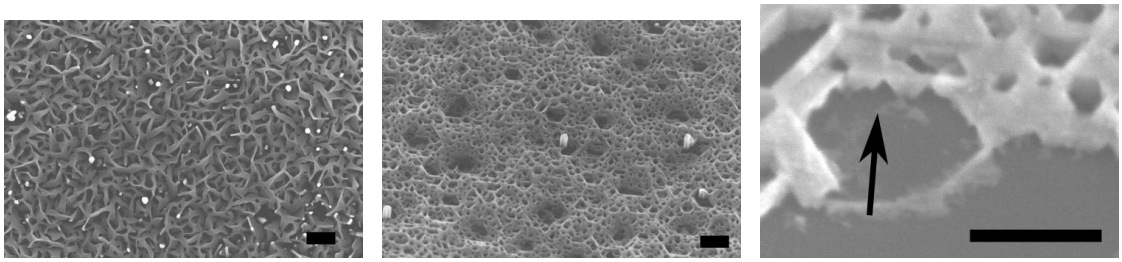

(a) top view SEM micrographs - before KOH - scale bar: 200 nm

(b) bird eye view SEM micrographs - after KOH - scale bar: 200 nm

(c) bird eye view SEM micrographs - after KOH - scale bar: 100 nm

Figure 3.39: KOH etching of GaN 2D layer grown on an N-first AlN buffer – N2000

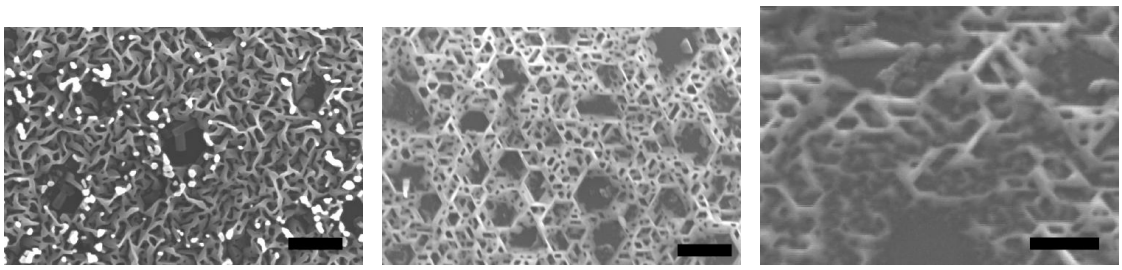

(a) top view SEM micrographs - before KOH - scale bar: 200 nm

(b) top view SEM micrographs - after KOH - scale bar: 200 nm

(c) bird eye view SEM micrographs - after KOH - scale bar: 100 nm

Figure 3.40: KOH etching of GaN 2D layer grown on a Al-first AlN buffer – N1982

Characterization technique	**GaN NW**	**enlarged GaN NW**	**GaN pyramid**	**GaN 2D layer**
		Al-first AlN buffer		
STEM	N-polar or N-polar with a Ga-polar core	-	Ga-polar	Ga-polar
KPFM	-	N-polar	-	-
KOH	-		-	Ga-polar
		N-first AlN buffer		
STEM	N-polar or N-polar with a Ga-polar core	-	Ga-polar	Ga-polar
KPFM	-	$\sim$ 80% N-polar – $\sim$ 20% Ga-polar or N-polar with a Ga-polar core	-	-
KOH	-	$\sim$ 75% N-polar – $\sim$ 15% Ga-polar or N-polar with a Ga-polar core	-	Ga-polar

Figure 3.41: Polarity of GaN measured from different characterization techniques

3.3.4 Nucleation scenario

Based on the collected results on polarity and nucleation sites for GaN NWs and pyramids, a general growth scenario can be now outlined.

GaN 2D layer For growth occurring on N- and Al-first AlN buffers, both GaN pyramids and the 2D layer were hinted Ga-polar, were observed to be terminated by semi-polar facets and to grow at the same localization relative to the dark areas. Therefore, it is concluded that the 2D layer is the result of the growth and coalescence of GaN pyramids.

GaN nanowires nucleation scenario GaN NWs were all[31] observed to be N-polar or to include N-polar material in the case of the polar core-shell NWs. According to the nucleation model of Consonni *et al.* [109], NW nucleation is triggered by the plastic relaxation of GaN pyramids, implying the release of the epitaxial strain. Hence, the shape of the GaN nucleus becomes ruled by the facets energy hierarchy, which was expected by the authors to promote the formation of the m facets that constitute a prerequisite for NW growth. Our experimental observations have shown that a majority (if not all) of the numerous Ga-polar pyramids have failed to ripen into NWs and that all NWs have side facets (*i.e.* m facets) belonging to a N-polar domain. Therefore, it suggests that the formation of m facets, which are the prerequisite to grow GaN NWs, is also dependent on the polarity of the initial nucleus, due to different energy facets hierarchies between the Ga- and the N-polar sides.

Such asymmetry can be tracked in the kinetic Wulff plots obtain from MOCVD growth. They indicate a lower stability of the $(1\bar{1}0\bar{n})$ facets relative to m and $-c$ facets, whereas the $(1\bar{1}0n)$ facets were observed to be more stable, for certain growth conditions, than the m and c facets [74, 75, 73]. For MBE, no such Wulff plot has been reported but the study of Urban *et al.* [36] has shown that Ga-polar pillars grown by means of selective area growth (SAG) exhibit a top part capped by $(1\bar{1}0n)$ facets whereas parasitic N-polar NWs that have succeeded to grow on the mask exhibit a top part capped by a $-c$ facet only. It hints again an asymmetry between the Ga- and N-polar sides. *Ab initio* simulations have been unable to calculate the absolute energies of the polar facets due to the non-centrosymmetric structure of the GaN lattice. However, a recent work done by Li *et al.* [76] succeeded to extract relative facets energies, leading to the calculation of a thermodynamic Wulff plot. Within the range of simulated N chemical potentials, they confirmed a complete asymmetry between Ga- and N-polar sides. On the N-polar side, semi-polar facets were shown to be almost absent whereas, on the Ga-polar side, they were shown to coexist with the m and c facets, becoming prominent for less N-rich.

Back in the growth scenario of Consonni *et al.*, those results suggest that in the case of a newly relaxed Ga-polar pyramid, the semi-polar facets are stable so that the crystallite is expected to grow isotropically, leading to the formation of the 2D layer. Conversely, in the case of a newly relaxed N-polar pyramid, the semi-polar facets are

[31] at least from STEM observations and for non-enlarged NWs

unstable relative to m and $-c$ facets so that further growth of the crystallite is expected to promote m facet formation, which triggers the NW nucleation.

GaN nanowires nucleation sites A direct consequence of the required N polarity to trigger NW nucleation is that nucleation sites should be any area where GaN can nucleate with the N polarity. Therefore, the driving force leading to the nucleation of NWs on AlN pedestals or in the vicinity of dark areas relied on the ability for the GaN to nucleate with the N-polarity.

GaN has been grown at the same time[32] on two different AlN films, exhibiting different polarity states. One AlN film has been grown on Si (111) and the other one on sapphire. Both have been initiated by a derivative of the 840 ℃ Al-first AlN buffer, which leads to a mixed polarity state for the AlN on Si (see KOH results shown in Figure 3.43), and to an Al-polarity for the AlN on sapphire [173, 174][33]. SEM views of the grown GaN are shown in Figure 3.42. No GaN NWs have nucleated on the Al-polar AlN, except on some dust (not shown here), which somehow confirms that the substrate temperature was high enough to promote NW growth. Instead, the grown GaN is shaped as the typical 2D layer previously studied, suggesting its Ga-polarity. On the mixed polar AlN, GaN NWs, or at least GaN crystallites delimited by m facets, have been successfully nucleated. It confirms the requirement of the N-polarity to form the m facets, which is in accordance with the similar experiment performed by Fernández-Garrido *et al.* [51] on Si- and C- polar SiC. GaN NWs are observed not the be uniformly spread over the surface, especially only scarce NWs are observed in the close vicinity of the large dark areas. The AlN in the vicinity of dark areas has been observed to be very smooth (see Figure 3.21), which would account for a reduced amount of favorable nucleation sites for GaN germs or favorable physisorption sites for N or Ga adatoms (*i.e.* no step edges) provoking the local absence of GaN growth.

Inversion domains in GaN nanowires The occurrence of the specific structure of NWs composed of a Ga-polar core and a N-polar shell can be still explained through the previously proposed growth mechanism. In such a case, the initial nucleus is expected to be Ga-polar, hence to be shape as a pyramid. While growing, the nucleus is laterally extending until overflowing on an area with different surface properties, leading to the nucleation of the N-polar shell. Based on the previous energy considerations, m facets are expected to form in the N-polar domain, meaning that the GaN nucleus becomes laterally terminated by m facets and may further evolve as a NW.

This growth scenario relies on the presence of a specific configuration allowing the GaN to nucleate with the Ga-polarity on areas as large as the future Ga-polar core, and to nucleate with the N-polarity all around. Nonetheless, this specific configuration has to exist with a non-negligible density as emphasized by the large amount of NWs hosting IDs. Therefore, the self organized growth of such structure seems unlikely. However,

[32] two different substrates were mounted on a single substrate holder

[33] actually in those reports, only the polarity of the overgrown GaN on AlN has been measured, so in this case, possible nucleation of basal IDBs at the AlN/GaN interface are neglected

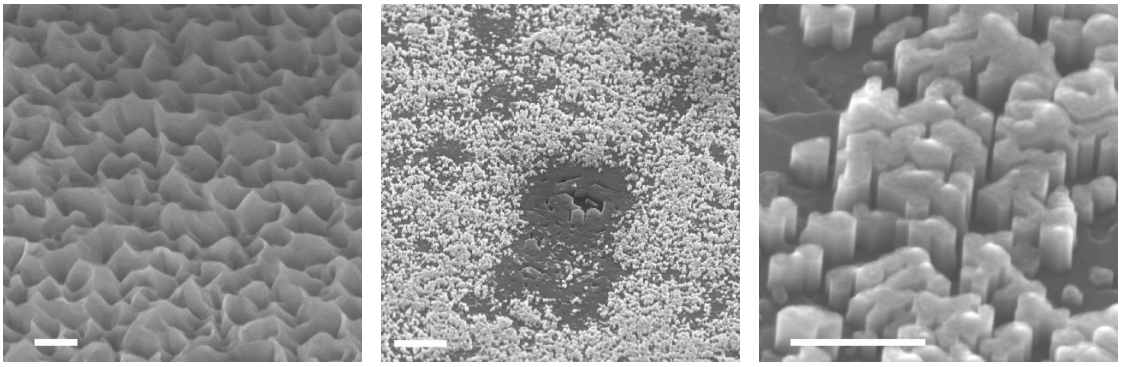

(a) GaN on Al-polar AlN – scale bar: 200 nm

(b) GaN on mixed polarity AlN – scale bar: 1 μm

(c) GaN on mixed polarity AlN – scale bar: 200 nm

Figure 3.42: SEM bird eye view of GaN NWs grown on AlN with different polarity – N2202

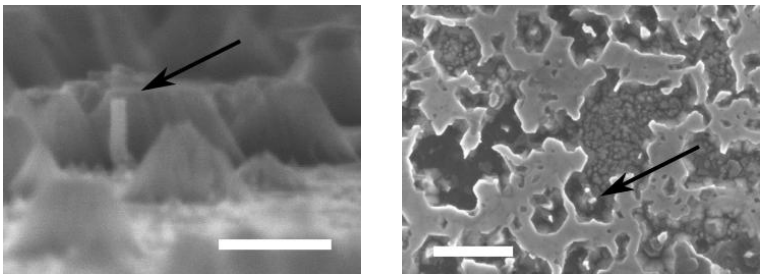

(a) SEM side view - scale bar: 100 nm

(b) SEM top view - scale bar: 200 nm

Figure 3.43: Thick AlN film grown on Si (111) and initiated with a derivative of the 840 ℃ Al-first AlN buffer. The AlN has been dipped in KOH for 1 min. Dark arrows emphasized small columnar Al-polar IDs – N2084

KOH etching of a thick AlN film grown on Si (111), initiated by a derivative of the 840 ℃ Al-first AlN buffer, has revealed the exact required structure within the AlN and with a very high density as pointed by the arrows in Figure 3.43.

At last, a zoom over the NWs synthesized on the thick mixed polarity AlN, shown in Figure 3.42c reveals the presence of dendritic domains delimited by m facets. The central part of the domain almost feature semi-polar facets, suggesting their Ga-polarity, whereas the outer part of the domains systematically feature a flat polar top facet, suggesting an N-polarity. Therefore, the growth of m facets seems again correlated to the presence of N-polar domains and to be independent of the shape of the crystallite. It means that in this case, the shape of the NWs is not anymore ruled by the plastic relaxation of the initial nucleus [109, 110] or by surface energy hierarchy [111] or by the applied flux ratio [85] but ruled by the polarity pattern given by the underneath AlN.

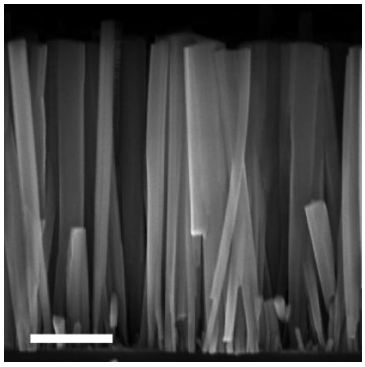

(a) SEM side view – scale bar: 300 nm

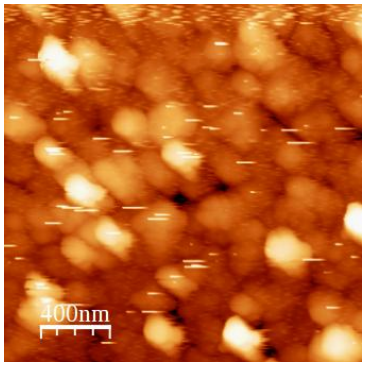

(b) AFM topographic mapping

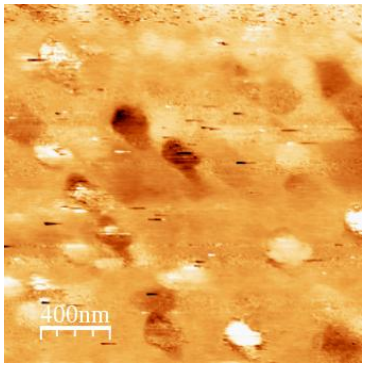

(c) V_{CPD} mapping – values scales from 0 to 1.1 V

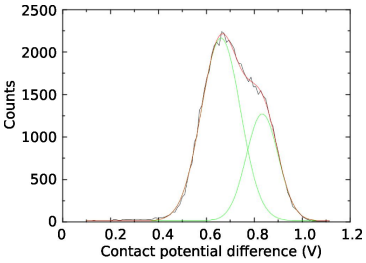

(d) Distribution of V_{CPD} values

Figure 3.44: KPFM measurement on as grown GaN NWs grown on bare Si (111) – N1970

3.4 GaN nanowires grown on bare Si

GaN grown directly on Si has been measured to be N-polar and expectantly free of IDs if the Si is strongly nitridated prior to growth [175], which corresponds to the NW growth case. Therefore, on such substrate, each GaN nucleus is expected to ripen into a NW for further growth. Indeed, if using an high enough growth temperature ($>\sim$ 800 °C), no 2D layer is observed when growing NWs on bare Si (111). However, HR-STEM imaging of the NWs has revealed that a non-negligible fraction are hosting a small Ga-polar IDs in their core, such as for NWs grown on AlN buffers.

An assembly of dense as-grown NWs[34] have been probed by KPFM, in order to extract a ratio of NWs hosting an ID. Results are synthesized in Figure 3.44.

The correlated topographic and V_{CPD} mapping done on the NW assembly reveals that the NWs top facets exhibit different V_{CPD} values. By looking at the distribution of the V_{CPD} values, two main contributions can be identified: one centered at 0.84 V

[34] N1970

and the other one centered at 0.65 V. The line-width of each contribution is larger than 200 mV, which is much higher than the 70 mV line-width obtained while scanning the enlarged NWs. The contribution at 0.84 V is attributed to purely N-polar NWs and its large line-width to the NW top facets that deviates from a perfect $-c$ plane (visible on the SEM pictures in Figure 3.44a) so as to instability of the tip. The contribution at 0.65 V is tentatively attributed to N-polar NWs hosting an ID. In such a case, the higher measured V_{CPD} compared to the expected 0.4 V for a Ga-polar c facet should stand for the specific polar core-shell structure, and the larger line-width compared to the one of N-polar NWs could be assigned to the distribution in size of the IDs.

By considering that all the NWs have the same diameter, the amount of NWs hosting an ID should be proportional to the 0.64 eV contribution, which allows to estimate that only 30% of the NWs are free of IDs.

As the growth mechanism for IDs is not yet resolved, this extracted ratio can be hardly generalized to all GaN NWs grown on Si. But once again, the presence of IDs might account for the polarity variability reported for GaN NWs grown on Si (see Table 3.1).

3.5 Conclusion and discussion

In this chapter, the focus has been brought to the synthesis of AlN buffers on Si and subsequent GaN NWs nucleation and growth.

For all the investigated growth routes used for AlN buffer synthesis, the systematic precipitation of Si on the AlN surface and the growth of few AlN crystallites (including AlN pedestals) in Si-rich conditions has been demonstrated. It has emphasized the high reactivity of Al with Si or Si_xN_y, suggesting that identical growth mechanisms should occur for AlN buffer growth routes deviating from the one used in this study. The Si-rich growth occurring in specific areas of the AlN buffers is responsible for breaking the uniformity of the film, likely resulting in the nucleation of GaN both with N- or Ga-polarity on the same buffer.

The systematic polarity analysis of GaN grown on AlN buffers has shown that NWs are N-polar (possibly with a Ga-polar ID in their core), whereas the 2D layer is Ga-polar. Based on different facets energy hierarchy between the N- and Ga-polar sides, it has been concluded that the N-polarity is a necessary condition for the formation of m facets in self-organized GaN nucleus, which are prerequisite for NW nucleation and growth. Therefore, the spatial localization of NWs on the substrate is dependent on the ability of GaN to nucleate with the N-polarity. It means that NWs on an AlN buffer can only nucleate on N-polar materials or on singularities favoring the formation of basal IDBs leading to the GaN N-polarity, which both depends on the growth history of AlN. Hence, in addition to the flux ratio and the substrate temperature, the polarity pattern of GaN grown on its substrate (including the AlN buffer) is a supplementary constraint to take into account for successfully nucleate self-organized NWs.

At last, the presence of Ga-polar IDs in N-polar NWs was observed and has been also assigned to a specific polarity pattern of the AlN buffer or to singularities favoring

the formation of basal IDBs. The formation of such IDs has been observed as well in GaN NWs grown on bare Si, which promotes them as a recurrent defect in NWs, in a similar manner than for nitride films grown on Si. Therefore, NWs constitute a novel system in order to study the optical and structural properties of prismatic IDBs, which will be in the focus of the chapter 4. The usual observation of IDs only in a fraction of NWs belonging to the same assembly brings a new element in order to explain the dispersion in the NW properties of the same assemblies. It will be further emphasized in chapter 5.

Chapter 4

Inversion domains boundaries

This chapter focuses on structural and optical investigations of inversion domains (IDs) in GaN nanowires (NWs) synthesized by plasma-assisted molecular beam epitaxy (PA-MBE). Taking advantage of the NW small size and their ability to be dispersed, the IDs characterization is pushed further in comparison to previous reports on thin films. Noticeably, NWs exhibit small sizes and straight IDBs, which allows their convenient observation by STEM, possibly without the requirement for cross-section preparations.

Among the various atomic configurations hypothesized for IDBs in GaN, the energetically most stable has been always resolved in NWs. Additionanly, a systematic correlation between the presence of IDs and a photoluminescence (PL) at 3.45 eV is reported. Hence, the 3.45 eV PL is attributed to an excitonic recombination bound on an IDB, which should end up a controversial issue dealing with the origin of this PL band in GaN NWs. Next, if using the presence of the 3.45 eV PL as a probe for the existence IDBs, samples grown in other laboratories on Si(111) but also on Si(100) and sapphire are inferred to host this extended defect as well.

At last, the IDBs are observed to interact with stacking faults (SFs) by generating a linear defect that is likely acting as a non radiative recombination channel. Hence, IDBs could be deleterious to the overall optoelectronic properties of the material, thereby, are not desirable.

Contents

Experimental data credits

All the scanning transmission electron microscopy (STEM) images shown in this chapter have been acquired by Benedikt Haas. The SiN membranes used for the inversion domain boundary (IDB) optical study were synthesized by Martien Den Hertog.

Related publications

The attribution of the optical signature at 3.45 eV to the IDBs has been published by Auzelle *et al.* [176][1]. A publication by Haas *et al.* focused on the structural characterization of IDBs by STEM should be soon announced.

4.1 Issues at stake

One of the inversion domain (ID) specificity resides in their boundaries, delimiting two domains with opposite polarity. Indeed, in the vicinity of such boundary, the local atomic arrangement is highly perturbed in comparison to the bulk, which constitutes an extended defect potentially affecting the optical and electrical properties of the material.

Up to now, IDBs have been experimentally observed in thin films [177, 178, 179, 180, 181, 182] and theoretically studied using *ab initio* calculations [151, 183, 184, 185] with a rather good agreement between both. However, most of the experimental observations were done on non-intentionally grown IDs, which has complicated their study by transmission electron microscope (TEM) due to their random localization within the film. Attempts have been done in order to intentionally synthesize IDBs in GaN by growing on sapphire substrate patterned with a thin AlN buffer [22, 23] or by growing on Ga-polar GaN patterned with an Al_2O_3 film [159]. However, for both cases, the obtaining of sharp IDBs is not systematic, which prevents a precise structural investigation in cross section and makes the system more complex. Additionally, optimized growth of both the N- and Ga-polar domains at the same time is challenging, and has usually led to inhomogeneous optical properties of the IDB area itself.

For all those reasons, nanowires (NWs) constitute an advantageous system. Indeed, their small diameter is adequate for TEM and STEM imaging of the IDBs. Not all the NWs are hosting an ID, which allows to use as a reference the ones free of IDs. At last, the total surface of the IDB in NWs is down to 0.03 μm^2, which increases the chance of having a uniform environment, leading to a reduced spectral broadening.

Finally, GaN NWs feature a typical sub-band gap luminescence at 3.45 eV, whose origin has been debated for long. Since IDs have been observed in several assemblies of GaN NWs (see the chapter 3), IDBs are a good candidate to be at the origin of this photoluminescence (PL) line.

[1] This work has also been awarded at the 28^{th} international conference on defects in semiconductors by the Corbett prize.

4.2 Structural investigation

4.2.1 Scanning transmission electron microscopy characteristics

Different techniques such as KOH etching, piezo force microscopy (PFM) or Kelvin probe force microscopy (KPFM) can be used in order to infer the presence of IDs in GaN NWs[2], but they are either destructive or have a limited spatial resolution. For tiny objects, such as NWs, or for complex polarity structures, the convergent beam electron diffraction (CBED) technique is reaching its limits, due to the difficulty to interpret the produced patterns[3]. Therefore, the HR-STEM technique has been found adequate to both identify the IDs on large scale images, within complex stack, and to resolve the atomic configuration of the IDBs.

The microscope used for this study is a FEI Titan^3 Ultimate working at 300kV and equipped with objective and condenser spherical aberration correctors allowing a maximal resolution of 60 pm. In addition, taking advantage of the crystal periodicity imaged by STEM, a template matching routine could be used in order to spatially average a selected lattice cell [148]. It is the combination of those elements that have allowed to precisely resolve the atomic configuration of structures such as IDs.

Two complementary observation modes have been used with HR-STEM:

- the high angle annular dark field (HAADF) mode. In this case, the majority of the signal is coming from incoherently elastically scattered electrons so that its intensity roughly scales with Z^x with $x = 1.6 \sim 2.2$ and Z being the atomic number of the probed atoms. Therefore, if aligned on a crystal zone axis, an HAADF image could directly reveal the atomic columns positions. Additionally, the signal could be considered linear, meaning that an HAADF image is not dependent on the stacking order of different crystal slabs along the beam direction (*i.e.* considering A and B, two different crystal slabs, imaging the $ABAB$ stack will give similar results than imaging the $AABB$ stack).

- the annular bright field (ABF) mode. In this case, part of the signal is coming from coherently transmitted electrons, so that its intensity is including a contribution from diffraction and interference phenomenons. Therefore, if aligned on a crystal zone axis, an ABF image exhibits a contrast that can be hardly directly interpreted in terms of atomic columns positions. To fully determine the probed atomic structure, ABF images could be simulated from trial atomic structures, until a reasonable matching with the experimental image is reached. The interference contribution of the ABF signal implies a strong non-linearity, meaning that the ABF images will be dependent on the stacking order of different crystal slabs

[2] (see chapter 3, section 3.3, page 90)

[3] for instance, concerning polarity, CBED is an injective characterization technique, meaning that the probed structure cannot be retrieved from the experimental CBED images. Up to now, to retrieve the structure, the CBED images of trial structures is calculated and compared to the experimental one until an agreement is obtained.

along the beam direction (*i.e.* imaging the $ABAB$ stack should not give similar results than imaging the $AABB$ stack).

In addition, NWs dispersed on a grid, or as-grown NWs prepared in a conventional cross section, have been observed by STEM through two different zone axis (see Figure 4.1):

- the $[11\bar{2}0]$ zone axis. In this configuration the in plane periodicity of the atomic column position is proportional to $a\sqrt{3}/2$ and the out of plane periodicity is c (a and c, being respectively, the in plane and out of plane lattice parameter of the wurtzite cell of the considered material).
- the $[1\bar{1}00]$ zone axis. In this configuration, the in plane periodicity of the atomic column position is proportional to $a/2$ and the out of plane periodicity is $c/2$.

The first zone axis is preferred in order to infer the polarity of unipolar GaN as the Ga and N-atomic columns are more spaced, one from each others, which increases the chance to observe the latters as they could be easily overlapped by the "more intense" Ga atomic columns. Additionally, based on thicknesses variations, the $[11\bar{2}0]$ zone axis should be preferred in order to image by STEM the boundary between the N- and Ga-polar domains. Indeed, while scanning transversally the NW, the Ga-polar domain will abruptly appear and disappear, which allows to increase the visibility of the boundary at those two particular points (indicated by two arrows in Figure 4.1c).

One has to note that IDs were always localized in the core of the NW. It means that for the two sets of used zone axis, the STEM imaging of the ID cannot be done without observing the superposed shell, which will constitute the main difficulty of the structural investigation of the IDBs in NWs.

4.2.2 Identification of inversion domains

As shown in Figure 4.2, some of the GaN NWs observed by STEM exhibit an area with a lighter (darker) contrast compared to the rest of the NW, in HAADF (ABF) mode. A zoom over one boundary of the contrasted area, in the $[11\bar{2}0]$ zone axis, is shown in the same figure.

In the ABF mode, a linear boundary emphasized by arrows is clearly observed to separate domains having different patterns. It indicates different atomic arrangements on both side of the boundary that cannot correspond to a thickness effect or to the presence of a facet.

In the HAADF mode, the boundary is less marked but the two domains clearly exhibit different patterns. On the right side, the contrast pattern corresponds to unipolar GaN. The Ga atomic columns (*i.e.* bright spots) are well resolved whereas the N atomic columns are fainter in contrast but still observed above each bright spots. This specific contrast is typical for a pure N-polar domain (further confirmed in the ABF mode images). On the left side, the bright spots attributed to Ga atomic columns exhibit a perturbed shape. They seem to be made of two Gaussian-like spots slightly shifted each

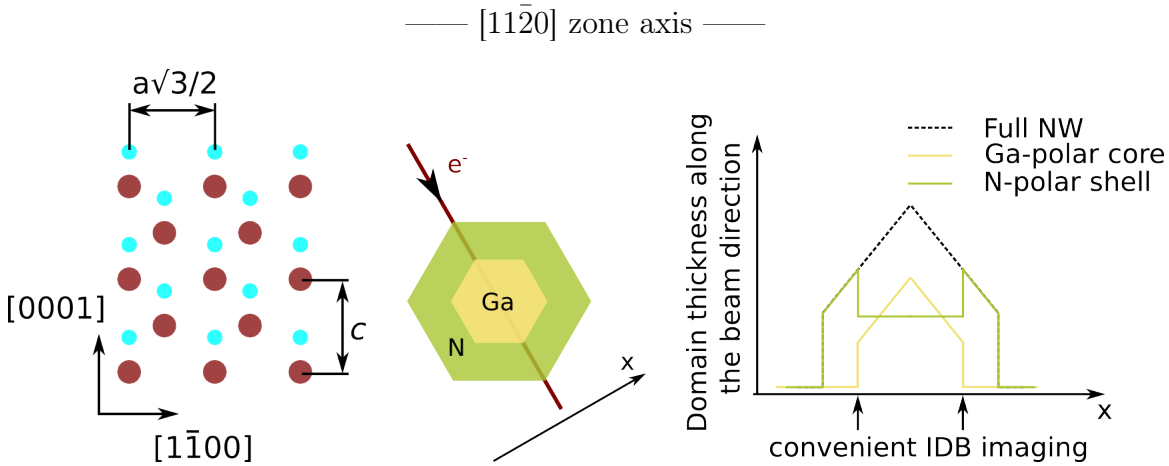

(a) Relative atomic columns positions – blue: N column, red: Ga column

(b) NW orientation versus electron beam (e-beam)

(c) Domain thickness crossed by the e-beam

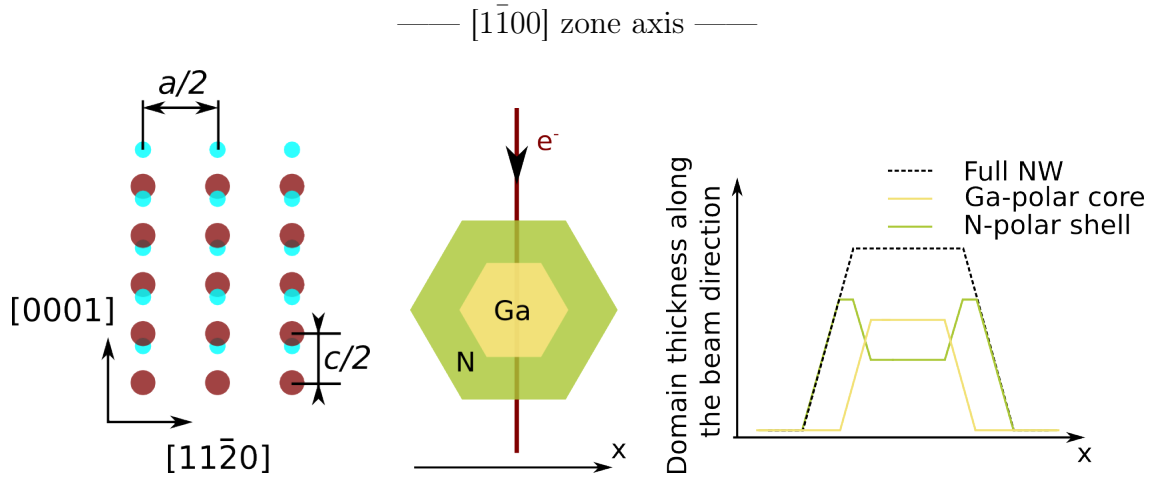

(d) Relative atomic columns positions – blue: N column, red: Ga column

(e) NW orientation versus e-beam

(f) Domain thickness crossed by the e-beam

Figure 4.1: Two different zone axis for STEM imaging of GaN NWs

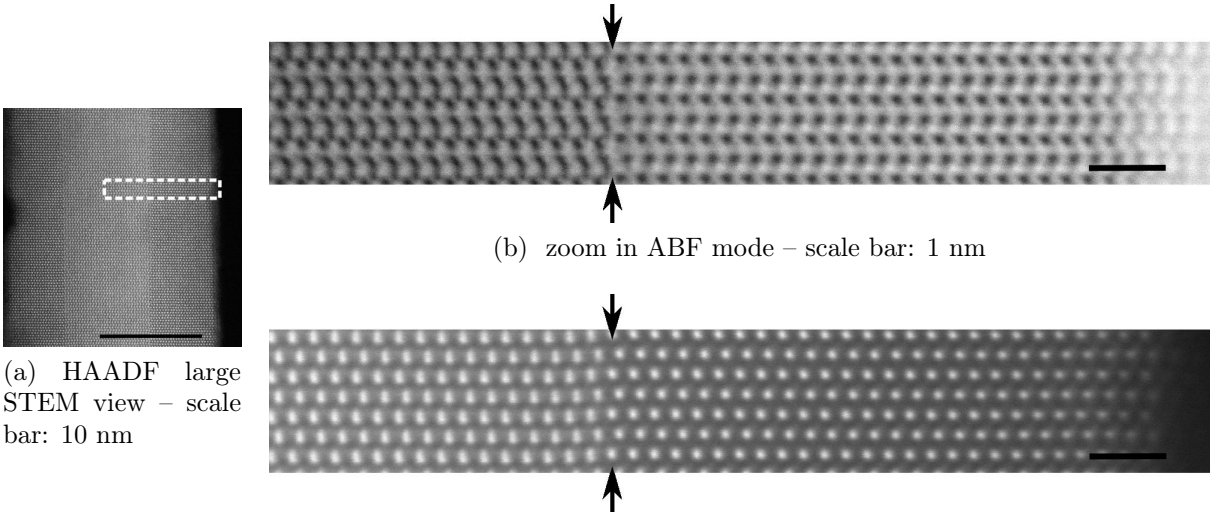

(a) HAADF large STEM view – scale bar: 10 nm

(b) zoom in ABF mode – scale bar: 1 nm

(c) zoom in HAADF mode – scale bar: 1 nm

Figure 4.2: STEM view in the [11$\bar{2}$0] zone axis of an IDB located in a Ga-polar core/N-polar shell NW – the IDB location is emphasized by the arrows; on the right is the shell only and on the left is the superposition of the core and the shell – the growth direction is toward the top – N2056

other along the vertical direction (*i.e.* the c axis) by $\sim \frac{c}{8}$. Therefore, it is assumed that the left side corresponds to the superposition of Ga-polar and N-polar domains, bond together by an IDB of the IDB* type (see farther for the atomic model and a description of this type of IDB).

This envisaged structure can be confirmed by taking advantage of the coherence of the ABF mode. In Figure 4.3, the ABF STEM image of an IDB in a NW is shown.

On both sides of the IDB, an average primitive lattice cell of the acquired pattern is performed, using a template matching routine [148]. On the right side, the average pattern is matching the simulated pattern of a fully N-polar GaN domain. On the left side, the average pattern is matching the simulated pattern of a Ga-polar domain sandwiched between to other N-polar domains. It is further confirmed by observing that the simulated pattern for a Ga-polar domain stacked (*i.e.* not sandwiched) with two other N-polar domains renders a fully different pattern. Therefore, the ABF mode observation confirms the initial assumption of the HAADF mode, *i.e.* the NW outer part correspond to N-polar GaN whereas the NW inner part corresponds to the superposition of N- and Ga-polar domains. Additionally, it evidences that the Ga-polar domain is sandwiched between the N-polar domains. This last observation is actually a general case. Indeed, for all the observed NWs, the Ga-polar ID was systematically observed to be confined in the core of the NW, leading to a polar core/shell structure[4].

Once the presence of IDBs in a NW is confirmed, the overall shape of the ID can be deduced from its specific contrast visible in large scale images. However, thickness

[4]see chapter 3, section 3.3.4, page 101 for a discussion about the growth mode of such polar core/shell structures

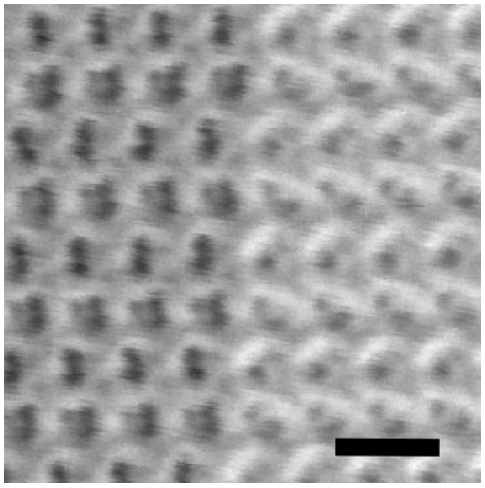

(a) STEM large view of an IDB – scale bar: 5 Å

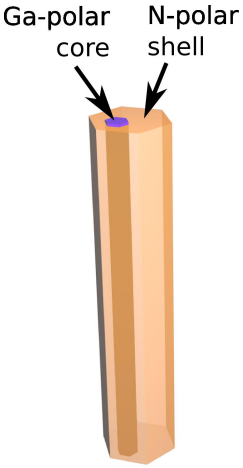

(b) Sketch of the polar core/shell structure

Left side

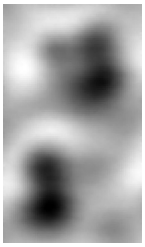

(c) Average experimental primitive lattice cell

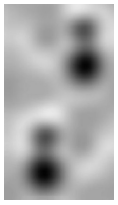

(d) Simulated primitive lattice cell

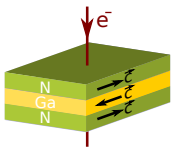

(e) Trial stacked structure

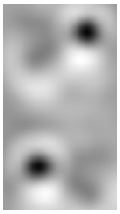

(f) Simulated primitive lattice cell

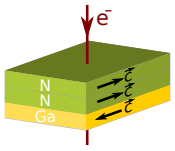

(g) Trial stacked structure

Right side

(h) Average experimental primitive lattice cell

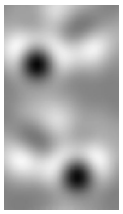

(i) Simulated primitive lattice cell

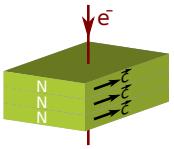

(j) Trial stacked structure

Figure 4.3: ABF STEM image in the $[11\bar{2}0]$ zone axis of an IDB found in a NW – the average experimental primitive lattice cell were obtained using a template matching routine [148] – N2183

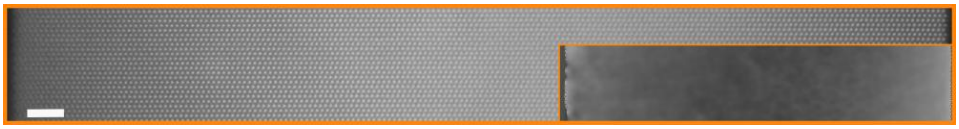

(a) NW free of ID

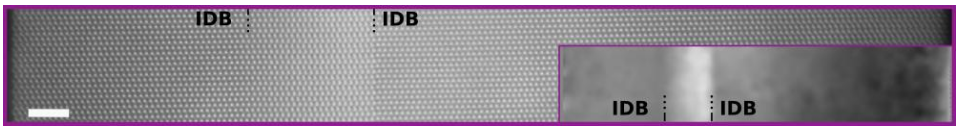

(b) NW hosting an ID

Figure 4.4: HAADF STEM images of two NWs – insets: displacement maps of the mass center of the bright spots in the HAADF STEM image, relatively to their expected position for a fully N-polar GaN NW – scale bar: 2 nm – N1111

variations might perturb the contrast as well, leading to a low visibility of the ID. In such a case, an additional numerical treatment on STEM images, as shown in the insets of Figure 4.4, might be used.

It requires an HAADF STEM picture where the acquisition drift was negligible (or has been corrected) and where the Ga atomic columns are well resolved. In such a case, the ID extent can be resolved by mapping the displacement of the mass center of the bright spots (which correspond to the Ga atomic columns) relatively to their theoretical position in the case of a unipolar material. Indeed, over the ID, the spots are asymmetrically elongated along the c axis (see Figure 4.2c and 4.6), which is clearly emphasized in the displacement map.

It is this method that has been primarily used in order to non-ambiguously hint the existence of IDs in the various samples discussed in this manuscript. Only as a second step, KPFM or KOH have been used to probe the presence of IDs, noticeably to get statistically relevant results.

4.2.3 Atomic structure of the prismatic inversion domain boundaries

m plane Two configurations for prismatic IDBs in the wurtzite $(1\bar{1}00)$ plane have been predicted and experimentally observed:

- the Holt type [181, 182], obtained by a simple switch between Ga and N atoms, in the ID
- the IDB* type [182, 177, 186] (see Figure 4.5), obtained first by switching Ga and N atoms in the ID and next by shifting the whole ID by a vector $\mathbf{R} = \frac{1}{2}[0001]$.

The energy formation of both have been *ab initio* calculated by Northrup *et al.* [151], resulting in 25 meV.Å^{-2} for the IDB* and 167 meV.Å^{-2} for the Holt type. Those values

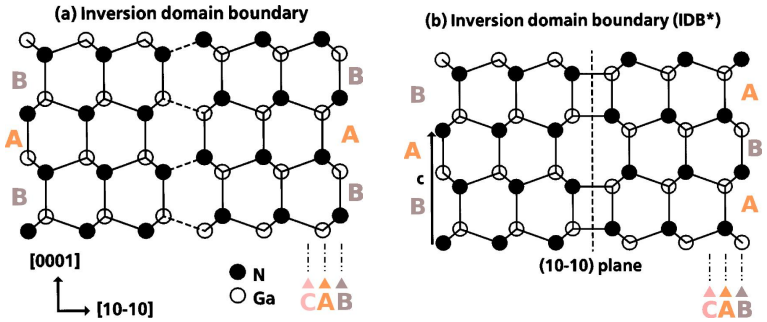

(a) Holt IDB (b) IDB*

Figure 4.5: Two atomic configurations for IDBs in the $(1\bar{1}00)$ plane, from [151] – based on the Ga-N vertical dumbbells positions within a c plane, two types of planes, denoted A and B, have been identified and labeled

can be compared with the calculated energy formations of two free $(1\bar{1}00)$ surfaces, which is 236 meV.Å^{-2}. Therefore, the formation of the IDB* appears to be energetically favored compared to the Holt IDB, but both are more stable than two m facets, thereby, the growth of the two types of IDB could be expected. For the two atomic configurations, both N and Ga atoms are tetragonally bonded but in the case of the Holt type, wrong bonds (*i.e.* $N-N$ and $Ga-Ga$ bonds) are formed. It is their poor stability that is expected to account for the highest formation energy of the Holt type IDB structure. The transition from an Holt IDB to an IDB* could be done by shifting one of the two unipolar domains by a value of $\frac{c}{2}$ along the c axis. It constitutes a large kinetic barrier, meaning that once formed, the transition from an Holt IDB toward and IDB* is unlikely.

Other means that direct observation of the IDB atomic configuration would be desirable in order to discriminate the Holt to the IDB* type. For the two IDBs, the shift along the c axis of mono-atomic planes crossing through the IDB is equal to $\sim c/8$. Hence, it cannot be used as a discrimination parameter. Conversely, the stacking sequence of c planes on each side of the IDB should be able to provide information on the IDB atomic configuration. Indeed, wurtzite structure is composed of the stacking along the c axis of A and B planes, which differ by the in plane position of the Ga-N dumbbells. As shown in Figure 4.5, a reference plane in the structure is first labeled A so that all the other planes could be identified as A or B, relatively to the reference plane. On one hand, it appears that an A plane is unchanged if crossing through the Holt IDB, *i.e.* one has a $..ABAB..//..ABAB..$ stacking sequence on both side of the IDB. On the other hand, an A plane is transformed into a B plane if crossing through an IDB*, *i.e.* one has a $..ABAB..//..BABA..$ stacking sequence on both side of the IDB. Therefore, by looking at the stacking sequence on both side of the IDB, one should be able to discriminate between an IDB* and an Holt IDB, without the need for a strong STEM spatial resolution.

Thereby, as for instance in Figure 4.6, the IDB* configuration has been always identified in NWs hosting an ID.

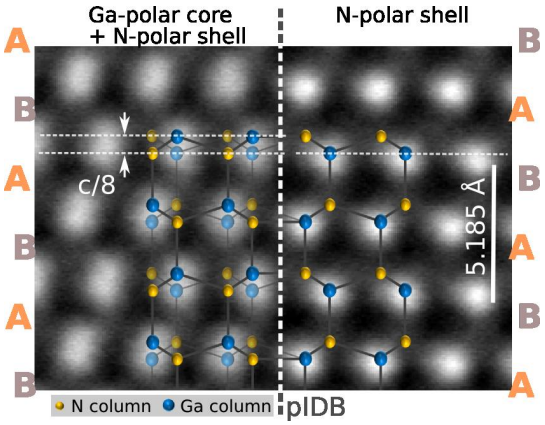

Figure 4.6: HAADF HR-STEM image of an IDB. An atomic model corresponding to the IDB* configuration is superimposed.

a plane GaN NWs side facets are *m* facets, whose surface energy is slightly lower than the one of *a* facets [187]. However, the corners of NW side facets are usually observed not to be sharp but slightly rounded, thereby, composed of a mixture between m and a facets. It can be assigned to a minimization of the corner energy, which should be a trade off between the Laplace pressure and the facets energies. The first is inversely proportional to the curvature radius of the corner, then increases for sharpened corners and the second one minimizes the formation of *a* facets, then decreases for sharpened corners. Similar mechanisms should prevail at the ID corners, thereby, implying the formation of IDBs parallel to the *a* plane.

As for the m plane case, different atomic configurations have been computed, but none has been yet experimentally observed. They are sketched in Figure 4.7.

The IDB-I configuration is obtained by shifting the two domains by a vector $\mathbf{R} = \frac{1}{2}[1\bar{1}00]$ and by switching Ga and N atoms in one domain. No wrong bonds are formed but the high amount of distorted bonds lead to a rather high energy of formation: 122 meV.Å^{-2} [183]. In contrast, the IDB*$_{(11\bar{2}0)}$ configuration, which is a derivative of the IDB*$_{(1\bar{1}00)}$, is obtained by shifting the two domains by a vector $\mathbf{R} = \frac{1}{2}[0001]$ and by switching Ga and N atoms in one domain. Its formation energy has been *ab initio* calculated to be 29 meV.Å^{-2} [184], which is lower than the IDB-I configuration and slightly higher than the IDB*$_{(1\bar{1}00)}$. It is assigned to different surface density of distorted bonds. Indeed, the surface density ratio of fourfold rings between IDB*$_{(11\bar{2}0)}$ and IDB*$_{(1\bar{1}00)}$ is 1.15, which is comparable to the formation energy ratio of the two atomic configurations: 1.16.

Atomic planes crossing the IDB* configuration are shifted along the *c* axis by $\sim \frac{c}{8}$, which is similar to the IDB*$_{(1\bar{1}00)}$ planes. Therefore, the coexistence of IDB*$_{(1\bar{1}00)}$ and IDB*$_{(11\bar{2}0)}$ should not imply the formation of extra defects, which makes the two configurations fully compatible. For the IDB-I configuration, atomic planes crossing the defect are shifted by $\sim \frac{c}{8}$ along the *c* axis but also by $a\frac{\sqrt{3}}{2}$ along the $[1\bar{1}00]$ direction. Hence, due to projection effect, the IDB* and IDB-I configurations cannot be differentiated from a HAADF STEM cross section along the $[1\bar{1}00]$ zone axis.

As a conclusion, the most probable atomic configuration for prismatic IDBs should still be the IDB* as it has the lower formation energy. However, for kinetic reasons, the

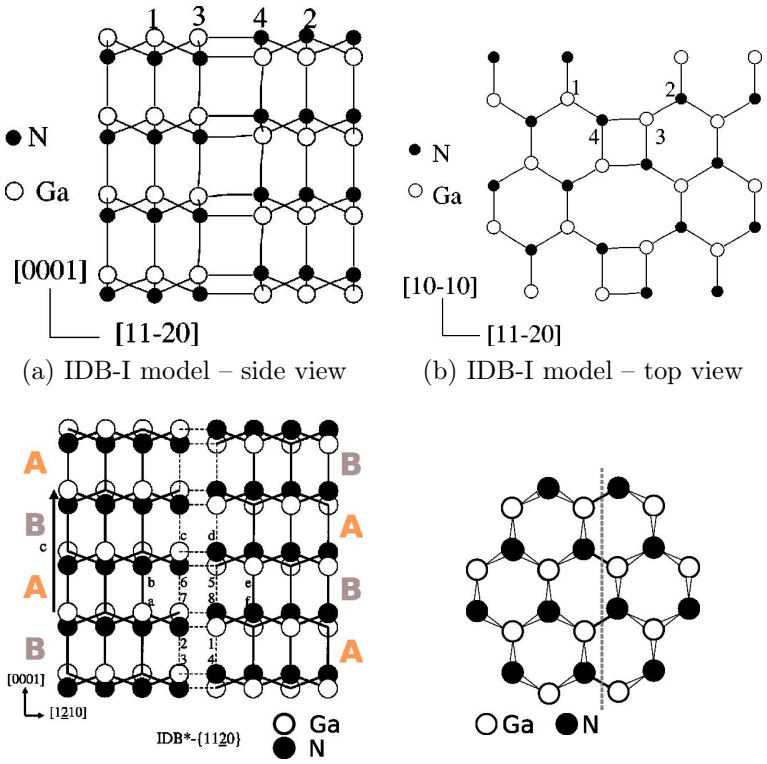

(a) IDB-I model – side view

(b) IDB-I model – top view

(c) IDB* – side view

(d) IDB* – top view – atoms on the sharp side of triangular bonds are at a lower altitude than atoms located on the other side of the bonds

Figure 4.7: Two atomic configurations for IDBs in the $(11\bar{2}0)$ plane. The IDB-I model is extracted from [183] and the IDB* from [184]

formation of Holt IDB or IDB-I cannot be ruled out.

4.3 Optical signature of inversion domain boundaries

4.3.1 Inversion domain boundaries photoluminescence

The *ab initio* calculations of the IDB* structures [184, 185] or of the IDB-I structure [183] have shown that prismatic IDBs are free of electronic states in the band gap, meaning that they are not constituting a channel for non-radiative recombinations. However, spatially resolved μ-PL and cathodo-luminescence (CL) studies of intentionally grown $IDB_{1\bar{1}00}$ in GaN thin films have revealed that IDBs actually exhibit an intense luminescence centered at 3.45 eV, stronger than for the neighboring "bulk" GaN [22, 23]. This sub-band gap bright PL suggests that IDBs are acting as localization centers for excitons, which was not expected from the *ab initio* calculations. This difference could be assigned to excitonic effects, which were not taken into accounts in the simulations [185],

or to inner defects within the IDB. For the latter case, Yan *et al.* [188] have calculated in ZnO that IDBs are gettering point defects such as Zn or O vacancies, interstitials or antisites by lowering their formation energy in their vicinity compared to the bulk ZnO. If charged, those defects would locally build up non-negligible electrical potentials. Therefore, the impact of IDBs over the optoelectronic properties of the crystal is not yet clear and requires further study.

4.3.2 The 3.45 eV band in GaN nanowires

Back to the case of PA-MBE GaN NWs, one of their specificity is a PL band centered at 3.45 eV, which has been almost systematically reported in their low temperature PL spectra. The intensity of this band is larger in NWs than in thin films grown on the same substrate, with the same temperature, hence primarily suggesting an implication of the surface [189].

Various attributions have been given to this band:

- a two electron satellites (TES) [146]
- a (sub-)surface point defect [112, 190]
- prismatic IDBs [191]

The two electron satellite A TES corresponds to the radiative recombination of an exciton bound on a donor, which is accompanied by the promotion of an electron of the donor to higher energy states. The emitted photon energy is slightly lower than for a simple excitonic recombination on the donor, as part of the recombination energy as been used to promote the electron. In bulk GaN, a TES recombination giving rise to a low intensity 3.45 eV luminescence has been non-ambiguously observed [192]. Hence, Corfdir *et al.* [146] have proposed that the 3.45 eV PL band of NWs is related to a TES, whose properties are tailored by the presence of the surface, in particular by increasing its relative intensity to the D_0^X by a factor ~ 100 compared to the bulk case.

The sub-surface point defect Both the N-rich conditions and the pinning of the Fermi level at the NW surface are prone to favor the incorporation of subsurface point defects, such as Ga-vacancies. Their density would be then increased in NWs, which are grown in N-rich conditions and are featuring a large amount of free surface, compared to thin films, which are grown in Ga-rich conditions. Therefore, the 3.45 eV band has been tentatively assigned by Furtmayr *et al.* [112] to excitonic recombinations on Ga-vacancies.

In addition, Brandt *et al.* [190] have attributed this defect to a surface point defect.

The work of Sam-Giao *et al.* Sam-Giao *et al.* [193] have performed additional spectroscopy measurements on the 3.45 eV band in order to challenge the proposed attributions. Noticeably, they have shown an absence of Zeeman splitting for the 3.45

eV band, which would have been expected for a bulk TES. In addition, they have shown that the dipole direction of the 3.45 eV band is mainly parallel to the NW axis, whereas the dipole direction of the D_0^X is mainly perpendicular to the NW axis. Therefore, the properties of the 3.45 eV PL band strongly differ from the properties of the D_0^X, which rules out the two previous attribution to the 3.45 eV band.

The prismatic inversion domains boundaries Based on the CL and μ-PL measurements carried on intentionally grown prismatic IDBs, Robins *et al.* [191] have suggested the presence of IDBs in NWs as responsible for the PL at 3.45 eV. However, this hypothesis has been discarded at that time because nobody was aware of the presence of IDs in NWs.

Now that the possible existence of IDs in plasma-assisted molecular beam epitaxy (PA-MBE) NWs has been demonstrated, it is is proposed that indeed, the specific 3.45 eV PL of NWs is related to IDBs. Such proposal will be under the scrutiny of this section.

Optical confinement In addition, a recent work dealing with the origin of the 3.45 eV line has been published [194]. It tentatively relates the 3.45 eV PL to the recombination of excitons in a strong radial confinement regime, which could be obtain, according to the authors, in the sharp corners of the NWs. However, this work is clearly missing a physical basis: they have no convincing experimental input, they have neglected the specific electronic structure of the free surface and they have not discussed the probable error bars of their calculations.

4.3.3 Correlation between inversion domain boundaries and 3.45 eV photoluminescence

In order to non-ambiguously assess the origin of the 3.45 eV PL in IDBs, correlated μ-PL measurements and HR-STEM characterizations on the same NW have been performed.

SiN grids Home-made free standing SiN membranes have been used to perform such experiment. They are made of a 50 nm thick Si_3N_4 film laying on a Si 100, in which 100×100 μm^2 windows have been opened. In addition, metal markers have been deposited on the film, in order to localize the NWs between different experiments. The fabrication procedure is described in the Ref [97] and an overview of the grid is shown in Figure 4.8.

Thin SiN films are transparent to electrons, which allows their use for STEM observation. In addition, they have no visible PL response in the energy range of interest and are smooth enough to see the NW by optical microscopy[5], which makes them also suitable for μ-PL observations.

[5] more exactly to see an optical interference related to the presence of a dispersed NW

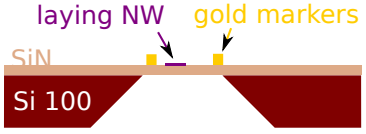

(a) Sketched side view of the SiN grids

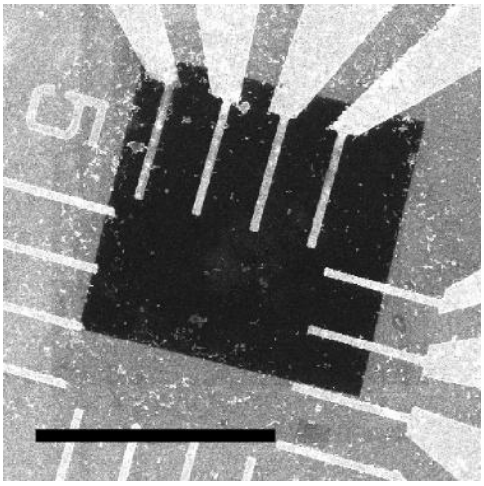

(b) scanning electron microscopy (SEM) top view of an SiN grid with dispersed NWs – scale bar: 100 μm

Figure 4.8: SiN grids

Nanowire growth NWs have been grown on Si with the help of an Al-first AlN buffer obtained by a series of four Al depositions of 3 ML_{AlN} followed by nitridation. The NWs have been grown along regular conditions for more than 10 hours, resulting in 2.3 μm long NWs with a density of 1.2×10^{10} NW.cm^{-2}. Long NWs were grown to ensure their easier localization by optical microscopy and to increase the amount of luminescent material once dispersed. A drawback is the quasi systematic coalescence of NWs with their neighbors.

Nanowire dispersion The mean diameter of the μ-PL beam is about 1 μm, which means that for acquiring the PL spectra of single NWs, they have to be spatially separated by more than 1 μm. It could be achieved by the use of dispersion techniques that transfer the NWs from their initial substrate (featuring high density of NWs) to another substrate with a much lower density.

In this case, a wet technique has been chosen to disperse the NWs on the SiN grid, in order to minimize the mechanical contacts with the SiN film, which would have likely damaged it. A piece of sample with as-grown NWs is dipped in an ethanol solution and sonicated for few minutes, thereby, NWs are broken from the substrate and put in suspension in the ethanol. Next a droplet of the ethanol solution is directly deposited on the SiN grid that has been heated to $\sim$ 60 °C. There, the droplet is almost instantaneously vaporized, which allows an homogeneous and low density dispersion of the NWs.

Using SEM observations, dispersed NWs could be classified in three types, which are exemplified in Figure 4.9:

- single NWs. They are the targeted system for this study but constitute a minority.

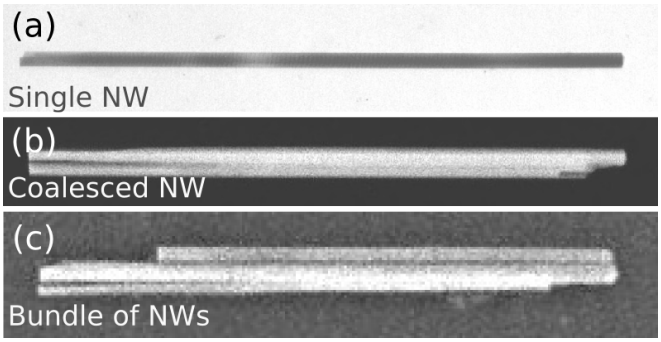

Figure 4.9: SEM images of (a) a single NW, (b) a coalesced NW, (c) a bundle of NWs

- coalesced NWs. They are single NWs that have agglomerated during the growth. They are the majority compared to single NWs and are less preferred for this study as they appeared on STEM images with multiple contrasts, due to the abrupt thickness variations stemming from the coalescence. It makes more complex the identification of IDs.
- bundle of NWs. They are indifferently constituted of single and coalesced NWs, which have aggregated during the dispersion process.

Electron damaging The irradiation of GaN, GaAs or ZnO materials by high energy e-beam ($E \sim MeV$) has been shown to generate point defects. Three different mechanisms can be envisaged:

- impinging electrons knock out an atom from its sub-lattice, move it to an interstitial site, which leaves a vacancy. This point defect is referred as a Frenkel pair [195].
- impinging electrons knock out local electrons, resulting in a positive charging of the sample
- impinging electrons break chemical bonds of organic residues located around the sample, creating radicals that will likely chemically react with the sample or accumulate on the sample surface (as for instance C deposition)

Such defects in GaN, especially the Frenkel pairs, are mobile at room temperature (RT), thereby, diffuse and recombine with other defects (other point defects, dopants, extended defects, surface, etc.) [196]. Annealing to higher temperatures is helping to heal the crystal but usually the GaN band edge PL intensity does not recover to its initial value measured before irradiation [197]. It means that for most of the cases, non-radiative defects are systematically included in the GaN matrix due to the irradiation. Although the STEM observation of GaN NWs requires electron irradiation with lower fluences and lower energy (200 $\sim$ 300 keV) than for the previously reported experiments, the formation of non-radiative defects might be still expected, especially the formation of N vacancies, as the Frenkel pair formation threshold for the N sub-lattice is 150 keV (and 500 keV for the Ga sub-lattice). The probability to generate defects is also dependent on

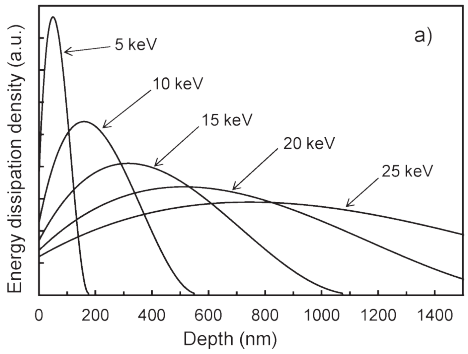

Figure 4.10: Electron energy dissipation depth profiles in GaN plotted for different acceleration voltage – from [199]

the beam fluence and, for instance, the PL intensity of non-intentionally n-doped GaN (as for our NWs) have been observed to be quenched for lower fluences than Mg p-doped GaN [198]. Therefore, the STEM observation of GaN NWs is expected to induce the formation of numerous non-radiative defects, leading to the full quenching of their PL. In our study, it means that μ-PL measurements have to be carried on prior to the STEM structural characterizations.

The nanometric size of the NWs prevents optical microscopy to differentiate the different types of dispersed NWs and to discriminate them from possible dust or roughness of the substrate. Hence, a prior SEM observation of the grid is unavoidable to locate single NWs.

The energy of the e-beam used for SEM imaging is ten times lower than for STEM imaging, but the fluence is between 10 to 10^3 times higher, which might have deleterious consequences as well. Indeed, CL quenching due to the irradiation of GaN or InGaN materials have been reported. Generation of Ga-vacancies [199], increased mobility of dislocations [200] or charging of the material under irradiation have been hypothesized to be responsible for the PL quenching [201]. In addition, as emphasized in Figure 4.10, decreasing the acceleration voltage down to 5 kV leads to a maximization of the electron energy dissipation in the subsurface region, accounting for a maximum of the transferred energy density well above the maximum obtained at higher acceleration voltages. This counter intuitive process emphasizes the need to keep acceleration voltage above 10 kV.

The prior observation of dispersed GaN NWs is done with an acceleration voltage of 10 kV, an estimated beam current of 30 nA and with a low spatial resolution. The dose received by each NW is estimated to be $\sim 10^{-10}$ C.NW^{-1}.

In order to qualitatively assess the effect of this observation on the PL properties of the dispersed NWs, μ-PL spectra were acquired on the same NW (1) after having received a small dose (*i.e.* $\sim 10^{-10}$ C.NW^{-1}, which is required to quickly locate single NWs) and (2) after having received a larger dose (*i.e.* $\sim 10^{-8}$ C.NW^{-1}, which is required to fully image a NW). Typical spectra are plotted in Figure 4.11.

Neither shift of the existing PL peaks, nor appearance of new peaks are observed due to the longer irradiation under the e-beam. The only consequence of the longer SEM observation is a decrease in intensity of both the 3.45 eV band and the band edge. Therefore, short SEM pre-observations of the NWs do not seems to be deleterious to the intended experiment.

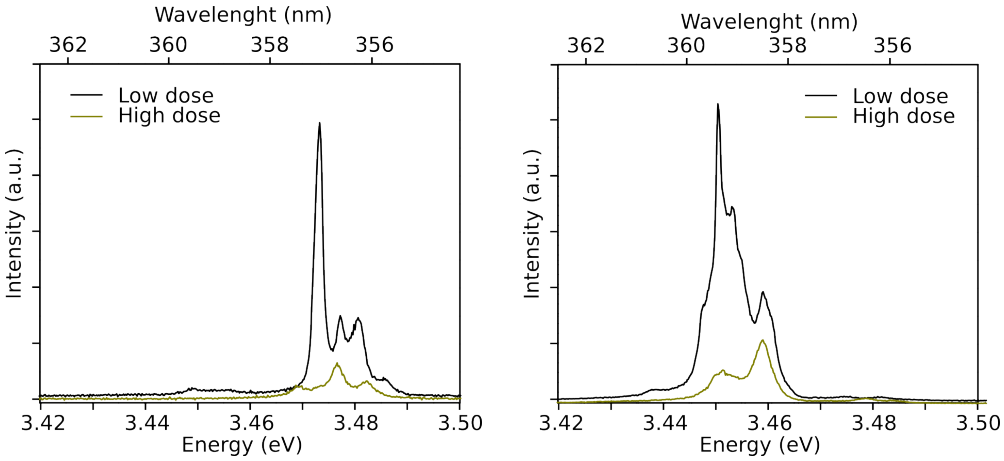

(a) 3.45 eV band (b) band edge

Figure 4.11: Comparative PL spectra acquired on the same NWs after receiving different doses of electron irradiations

Photoluminescence of dispersed nanowires Due to the small size and large surface over volume ratio of NWs, their PL properties are prone to be influenced by the NW environment. For instance, NWs deposited on a substrate with a different thermal expansion coefficient are expected to be strained while cooling down to 5 K, inducing a frequency shift of their band edge luminescence [202, 203]. Surface adsorbates such as oxygen are expected as well to disturb the sub-surface band structure of GaN NWs, as their presence results in an overall PL intensity decrease [204]. Actually, the PL band edge of NWs has been shown to be dominated by so-called surface excitons, which correspond to excitons bound to sub-surface donors [190]. Their recombination energy is expected to be dependent on the close environment of the donor, meaning that a fully relaxed single NW could still exhibit PL lines at various energies, depending on the donor distance to the surface and on the NW environment uniformity. Depending on the amount of non-intentionally incorporated impurities in assembly of as-grown NWs, the band edge PL line-width can vary from more than 20 meV to 0.5 meV. Therefore, additional energy broadening and shifting of the PL peaks have to be expected while probing dispersed NWs compared to as-grown ones.

In the case of the sample under scrutiny, the as-grown PL spectra acquired at 10 K, on $\sim 10^7$ NWs at the same time and with an excitation density of ~ 10 μW is shown in Figure 4.12.

The band edge PL is composed of the prominent donor bound exciton at 3.472 eV and a PL at 3.479 eV attributed to the free exciton A. The line-width of the donor bound exciton is about 2.5 meV, which suggests a rather homogeneous environment around the radiative centers (*i.e.* the donors) located in the NWs, thereby a low doping and strain. The PL band at 3.45 eV is clearly visible and well separated from the band edge contribution. It is composed of two lines at 3.450 and 3.457 eV with a respective line-width of 6.5 and 4.5 meV.

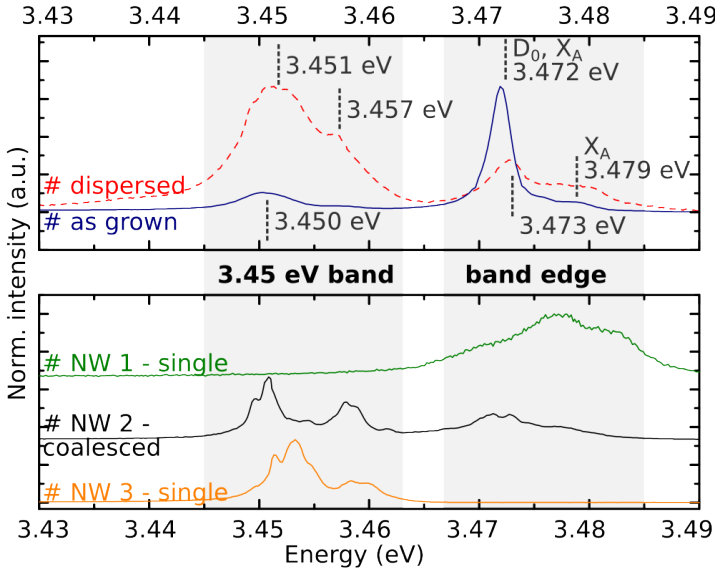

Figure 4.12: Acquired PL spectra at 10 K of as-grown NWs, dispersed NWs (single ones, a coalesced one and an average over all the dispersed NWs)

Once dispersed, the PL spectra of NWs, acquired at 10 K and with and excitation density of $\sim 10\ \mu$W, exhibit multiple peaks at energies that differ from what was observed on as-grown NWs. Three typical spectra are given in Figure 4.12. However, if averaging the acquired PL spectra of the ~ 70 probed objects (including single and coalesced NWs so as bundles), the usual features become visible again. A band at high energy with two contributions respectively at 3.473 and 3.48 eV is observable and is attributed to the band edge PL, *i.e.* surface excitons or free excitons whose recombination energies have been shifted compared to the case of as-grown NWs due to a change in the NW environment/strain/surface state caused by the dispersion itself. Another band at low energy with two contributions respectively at 3.451 and 3.457 eV is observable as well and is attributed to the 3.45 eV band.

The band edge PL intensity is observed to have an higher intensity compared to the 3.45 eV band PL in as-grown NWs, whereas it is the reverse for dispersed NWs. This difference is explained considering the collection efficiency of the experiment and the orthogonal direction of the two involved dipoles, as sketched in Figure 4.13. Indeed, the band edge PL has a dipole orientated perpendicular to the NW axis, whereas the 3.45 eV has a dipole mainly parallel to the NW axis [193], therefore the relative collection efficiency of the two radiations is inverted when NWs are laying on a substrate in comparison to standing as-grown NWs.

Compared to the as-grown case, the 3.45 eV band and the band edge band are spectrally broader but no significant overlapping between both is observed. As a consequence, while probing dispersed NWs, each PL peaks measured in the $3.445 - 3.463$ eV range will be attributed to the 3.45 eV band whereas each PL peaks measured in the $3.467 - 3.485$ eV range will be attributed to the band edge.

Full resolution SEM images of the probed dispersed NWs have been acquired after the μ-PL acquisition. It reveals that most of the dispersed NWs were actually coalesced or bundles so that only three single NWs were found. Interestingly, for those three single

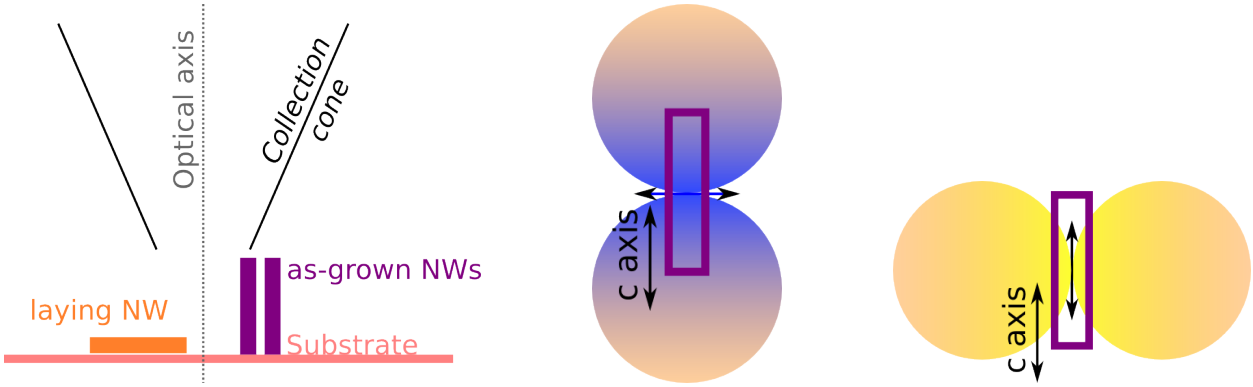

(a) μ-PL setup geometry

(b) Spatial emission of the band edge PL – the NW is vertical

(c) Spatial emission of the 3.45 eV band PL – the NW is vertical

Figure 4.13: Sketched of the 3.45 eV and D_o^x dipole direction compared to the collection cone of the μ-PL setup

NWs, their PL spectra were featuring peaks either in the 3.45 eV band or in the band edge but never in both.

Correlation study 5 dispersed NWs were next characterized by STEM. A non-ambiguous correlation between the existence of an IDs and a PL in the 3.45 eV band has been found. A similar experiment, carried on GaN NWs grown directly on Si (111) (*i.e.* without the help of an AlN buffer) has revealed a similar correlation (not shown here).

Therefore, the 3.45 eV PL band is attributed to the recombination of an exciton bound to an IDB. This is in agreement with the observed non-coexistence of PL lines both in the band edge and in the 3.45 eV band in single NWs. Indeed, IDs extend from the bottom to the NW top, meaning that any atoms of the NWs cannot be farther than $\sim$ 30 nm from an IDBs. Therefore, the capture volume of the IDB exceeds by far the NW volume, considering an exciton diffusion length as low as 70 nm (measured in the chapter 6).

The μ-PL spectra acquired on single NWs show that the 3.45 eV band is actually the addition of spectrally narrow lines (down to 1 meV large) with varying energies from NW to NW. This spectral diffusion should not be expected for prismatic IDBs, which constitute planar defects having atomically sharp interfaces and free of strain. This is very similar to the well known case of stacking faults (SFs) in GaN, for which various mechanisms have been proposed to account for the usual large line-width of their PL signature (see the topical review of Lähnemann *et al.* [18]):

- the screening of the electric field highly dependent on the local excitation density
- the weak confinement of the hole within the plane of the SF

- micro-strain fields
- interaction between neighboring basal SFs
- interaction with neighboring donors

In the case of prismatic IDBs, the absence of a spontaneous polarization perpendicular to the defect plane prevents the formation of inner electric fields, thereby, reduces the influence of the local excitation density on the PL energy. But the four others mechanisms could all account for the observed spectral diffusion. Especially, IDBs are expected to act as a getter for point defects [188], which should result in an increased local disorder.

Nevertheless, those mechanisms are expected to induce a Gaussian broadening of the 3.45 eV PL contribution, while probing a large number of NWs. Therefore, it cannot account for the observed doublet separated by 6 meV that is usually reported for the NW 3.45 eV band [189]. It differs also from the case of the basal SFs where interaction between two neighboring SFs could account for PL line shifting.

There is no direct evidence for the origin of the 3.45 eV doublet, therefore, only hypothesis are proposed:

- the corners of the IDs have a specific geometry, possibly with a facets that could exhibit different properties and so a different binding energy for the exciton compared to the m facets. Hence, the PL doublet could originate from the two binding sites for excitons.
- two types of point defects acting as localization centers for exciton could be trapped in the IDB vicinity, which would fit the observation of Pfüller *et al.* who observed as-grown single NWs and were unable to observe both doublet lines in a single NW.

Last but not least, a decrease of the 3.45 eV luminescence has been reported [112] while increasing the Mg doping. Again, there is no direct explanation for this fact, especially it is difficult to know if the Mg is preventing the nucleation of IDs (note that incorporation of Mg might favor the formation of basal IDB in GaN [152, 153]) or if Mg is quenching the PL of the IDBs itself (note that the incorporation of Mg is expected to lower the Fermi level energy, hence likely reducing the density of point defects[6], which were suggested as radiative centers in IDBs).

As a conclusion, the attribution of the 3.45 eV to excitonic recombinations on prismatic IDBs constitutes a first step, but there are still open questions emphasizing the need for further spectroscopic and theoretical work.

[6]Saarinen *et al.* [205], using positron annihilation techniques, have observed a decrease of the Ga vacancy concentration in Mg doped GaN compared to non-intentionally doped GaN. It was attributed to the increase of the Ga vacancy formation energy when decreasing the Fermi level energy [206]

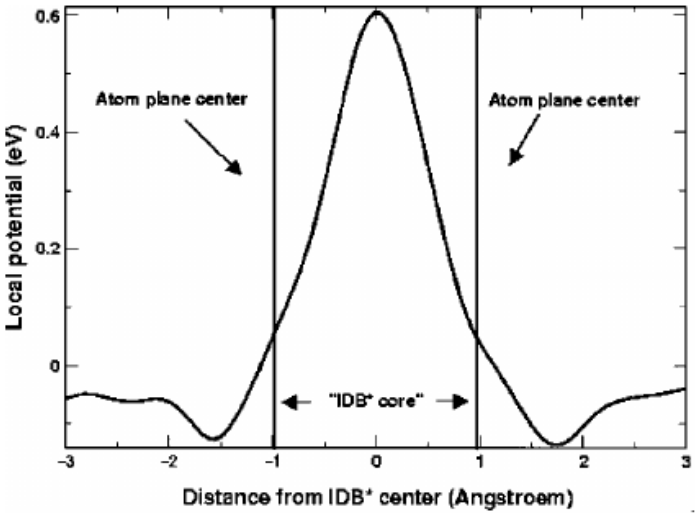

Figure 4.14: *ab initio* calculations of the IDB* electronic potential profile – from [185]

Electronic potential profile of IDB* The electronic potential profile generated by the IDB* has been *ab initio* calculated by Fiorentini [185] (see Figure 4.14). It exhibits two shallow dips and one high (but thin) peak in the core of the IDB. If not properly screened by free carriers in the structure, this potential profile might have consequences on the transport properties of the materials. Especially in NWs, it should be taken into account as the IDBs are organized as an hexagonal tube, which would isolate the core of the NW from the surface.

Photoluminescence as a probe for inversion domains The optical signature of IDBs at 3.45 eV should allow to use PL as a tool to track the presence of IDs in GaN structures. To do so, one has to be sure that no other radiative centers or recombination mechanisms (such as the TES) could generate a luminescence at the same energy and with the same intensity. Nevertheless, the intense 3.45 eV PL reported for GaN NWs grown on Si(100), on Si(111) and on sapphire [189, 146] strongly suggests the presence of IDs in those NW assemblies. By contrast, the absence of 3.45 eV PL reported in GaN NWs grown on diamond [52] suggests that such NWs are free of IDs.

Conversely, GaN microwires grown by CVD techniques have been reported for long to host IDs [37, 207, 9], but no link has been done yet with a 3.45 eV PL. This should be assigned to the large line-width of the band edge luminescence reported for NWs hosting IDs, which is masking a possible contribution at 3.45 eV.

Ratio of nanowires hosting inversion domains By looking at the probability for single NWs to exhibit a PL line in the 3.45 eV band, one can extract the nucleation probability of IDs. However, only three single NWs have been measured, which prevents a statistically significant study.

Nevertheless, assuming two things:

- the presence of an ID quenches the band edge PL in a single NW

- bundles of NWs and coalesced NWs are the addition of non-interacting single NWs (whose amount can be later estimated by SEM observations)

one can take advantage of the numerous PL spectra acquired on more than one single NWs at the same time. Indeed, if r is the probability for a single NW to nucleate with an ID, while acquiring the PL spectra of n single NWs at the same time, the probability P to measure PL peaks only in the 3.45 eV band should follow a binomial law, which is:

$$P_{\text{3.45 eV only}} = r^n \tag{4.1}$$

Similarly, the probability to measure PL peaks in the band edge only should be:

$$P_{\text{band edge only}} = (1-r)^n \tag{4.2}$$

and the probability to measure PL peaks both in the band edge and in the 3.45 eV band can be expressed as:

$$P_{\text{both bands}} = 1 - [r^n + (1-r)^n] \tag{4.3}$$

It is clear that for $n \to \infty$, $P_{\text{both bands}}$ will tend to the unity, which corroborates with the macro PL spectra of as-grown NWs (measuring $\sim 10^7$ NWs at the same time) as it features PL in both the 3.45 eV band and the band edge.

PL spectra of dispersed NWs including the same amount of single NWs were gathered in pools. The ratios of spectra having PL peaks in either of the two bands, or in both, have been extracted from each pools and plotted in Figure 4.15. The most statistically significant ratios are obtained for the pools including 2 or 3 single NWs.

The most satisfying fit of the experimental ratio is obtained for $r = 0.5$. It would infer that the probability for a single NW to nucleate with an ID was 50% for the sample under scrutiny. This probability still has to be considered as a raw estimation due to the crude initial assumptions, especially when concerning coalesced NWs as the sum of single and independent NWs. In addition, the nucleation mechanism for IDs is not yet fully clarified, meaning that this probability cannot be extended to all the NWs grown in other labs in different MBE and slightly different conditions. Nevertheless, the 3.45 eV is a common feature in PL spectra of GaN NWs, which strongly suggest the recurrent existence of IDs in self-organized NWs grown by PA-MBE.

4.4 Inversion domain boundaries crossing stacking faults

As detailed in the previous sections, prismatic IDBs are theoretically not expected to generate deep states in the gap and experimental optical characterizations have shown that a bright PL centered at 3.45 eV is originating from this defect. It should be attributed to the absence of dangling bonds or wrong bonds in the IDB atomic configuration.

However, a common defect in GaN NWs such as a basal SF crossing the IDB should highly perturb the boundary formation energy.

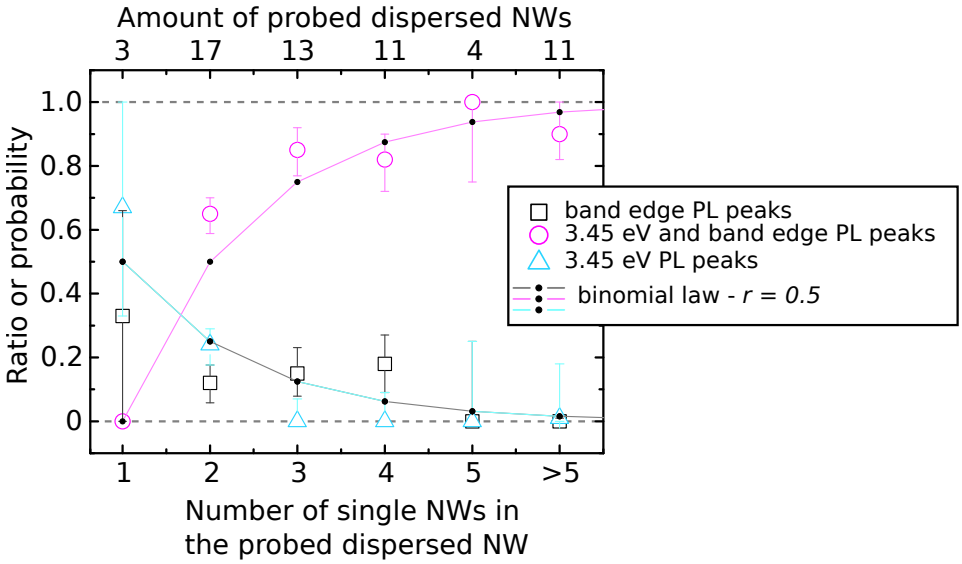

Figure 4.15: Ratio of PL spectra having PL peaks in the 3.45 eV band only or in the band edge only or in both bands, plotted for each pools of dispersed NWs including the same amount single NWs. The error bars indicates the ratio shift if one dispersed NW of the specified category would have been erroneously attributed (-1 spectra for the category) or forgotten (+1 spectra for the category). The expected ratio in each pools, for $r = 0.5$ have been superposed.

4.4.1 Theoretical structure

In Figure 4.16, tentative atomic models featuring IDBs after the crossing of a I_1 SF above a plane A or B are shown.

Despite the fact that those atomic models should be optimized by *ab initio* calculations in order to obtain the lower formation energy possible, the formation of wrong bonds or threefold coordinated atoms seems unavoidable. Hence, it highly suggests an high formation energy and the generation of deep levels in the gap.

4.4.2 Experimental reports

Experimental reports dealing with IDB interacting with SFs are scarce in the literature, most probably due to the almost random localization of the TEM observations.

Sanchez *et al.* [179] observed an I_1 SF that was terminated at the IDB location, suggesting a lower formation energy of this defect compared to the crossing of the IDB by the SF. They have hypothesized an atomic model shown in Figure 4.17, with the termination of the SF resulting in a so-called Shockley partial dislocation, which has the following Burger vector:

$$\frac{1}{6}\langle 02\bar{2}3\rangle = \frac{1}{3}[01\bar{1}0] + \frac{1}{2}[0001] \tag{4.4}$$

According to the authors, the $\frac{1}{2}[0001]$ component would be responsible for a switch of

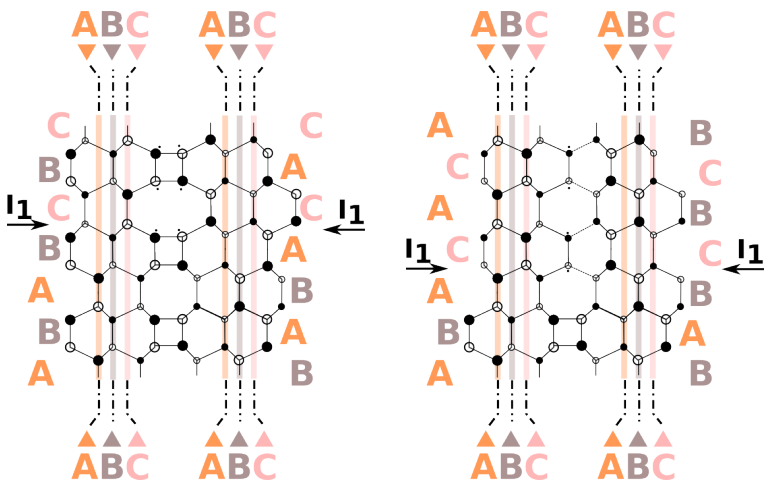

(a) $..BAB-CBC..//..ABA-CAC..$ (b) $..ABA-CAC..//..BAB-CBC..$

Figure 4.16: Tentative atomic model for an I_1 SF crossing a prismatic IDB* using the $[11\bar{2}0]$ zone axis – atoms represented with different sizes belong to different planes shifted each other by $\frac{a}{2}$ along the $[11\bar{2}0]$ zone axis, the atomic bonding between those planes are depicted by shorter bonds in the general case (*i.e.* out of the IDB)

the IDB structure from IDB* to the Holt type[7], thereby, accounting for the formation of the latter which has often been experimentally reported [181, 182, 178] although it has a much higher formation energy.

Tentative atomic models for an I_1 basal SF terminating at an IDB* are sketched in Figure 4.18. Accurate atomic bond lengths in bulk GaN and in the IDB* have been taken into account, as well as the different depths of the atoms along the $[11\bar{2}0]$ zone axis of the sketch. Depending on the position of the I_1 SF within the initial $..ABAB..//..BABA..$ stacking sequence, two stacking sequences can be formed above the SF: $..ABAB..//..BCBC..$ or $..ABAB..//..CACA...$ For each, two atomic configurations featuring either wrong bonds or threefold coordinated atoms have been found and displayed, as it is difficult without calculations to select the most stable out of the two[8]. The obtained structures slightly differ from the one hypothesized by Sanchez *et al.* and do not exactly fit the Holt type IDB. Indeed, the wrong bonds have inadequate

[7] as visible in Figure 4.5, the two IDB structures can be obtained from each other by a shift of $\frac{c}{2}$ along the c direction

[8] Both wrong bonds and threefold coordinated atoms are expected to have high formation energy. In order to compare the two, one can use the formation energy calculations performed by Northrup *et al.* [151] of the Holt type IDB (featuring wrong bonds and having a 165 meV.Å^{-2} formation energy) and of the stacking mismatch boundary (featuring threefold coordinated atoms and having a 105 meV.Å^{-2} formation energy). The lower formation energy of the stacking mismatch boundary has been assigned by the authors to a dimerization of the threefold coordinated atoms along the $[11\bar{2}0]$ direction, however such stabilization process is dependent of the steric environment of the threefold coordinated atoms, meaning that it has to be evaluated in each case. As a conclusion, it seems that wrong bonds and threefold coordinated atoms have similar formation energies so that none could be *a priori* rule out.

lengths and are not included in the same plane compared to the Holt type IDB but a relaxation toward this configuration, through elastic deformation, could be envisaged.

Iwamoto *et al.* [180] have also reported TEM images of interacting SFs with prismatic IDBs enclosing a columnar ID. In their case, they observed an I_1 SF that has crossed the prismatic IDBs with an additional I_1 SF confined in the ID and stacked on the other I_1 (*i.e.* forming an I_2 SF in the ID). Above the terminated SF, the IDB is bending toward semipolar planes, which results in the termination of the ID itself. Similarly to Sanchez *et al.* [179], they have argued that the termination of the SF should have resulted in to the formation of an Holt type IDB, which is weakly stable, so that the system has preferred to bend the IDB in order to reduce its total energy. However, in this case, the SFs growth have been intentionally stimulated by depositing In, meaning that In incorporation or surfactant effect could have also played a role for the IDB bending. Actually, the self annihilation of Ga-polar IDs in GaN has been reported as well if growing InN [178] but no tracking of SFs has been done in this study.

4.4.3 The nanowire case

The usual 3.42 eV contribution in the PL spectra of GaN NW, which is attributed to SF bound exciton luminescence, indicates that NW are hosting SFs. Therefore, the probability of having a SF crossing a IDB should not be negligible.

Among the pool of NWs which has been observed by STEM to host an ID, only one has been observed to include a SF. The STEM view is shown in Figure 4.19. In this case, it is remarkable that the I_1 SF included in the ID is observed to terminate at the IDB, but another I_1 SF is generated one atomic plane upper, in the shell.

A tentative atomic model for the structure is shown in Figure 4.20, with two stacking sequences that could be found in 60° off m planes around the c axis[9]. Although the exact configuration of the termination structure could be debated, it is clear that the growth of the second I_1 basal SF in the shell allows to switch the atomic configuration of the IDB back to the IDB* structure. Hence, this observed stacking sequence could be regarded as an efficient relaxation process for the IDB-SF interaction, which does not require any bending of the IDB. On a large scale, it only provokes a $\sim \frac{a}{n\sqrt{3}}$, with $n\epsilon(1,2)$, shift along the $[1\bar{1}00]$ direction of the IDB plane and a $\frac{a}{\sqrt{3}}$ shift of the SF along the c axis.

One can note that in this configuration, the I_1 basal SF has nucleated in the ID before to extend in the shell, thereby, suggesting that side facets are not, or not only, the driving force for SF nucleation. Impurities, Ga-polar surface, IDBs or kinetic phenomenon could be still incriminated.

4.4.4 Conclusion

SFs have been observed to interact with IDBs through different processes:

[9] a I_1 basal SF can be considered as a small cubic inclusion, meaning that it has a 3 fold symmetry around the c axis, whereas the wurtzite phase has a 6 fold symmetry around the c axis. Hence, two different configurations for the boundary have to be considered for a SF included in an ID having 6 facets

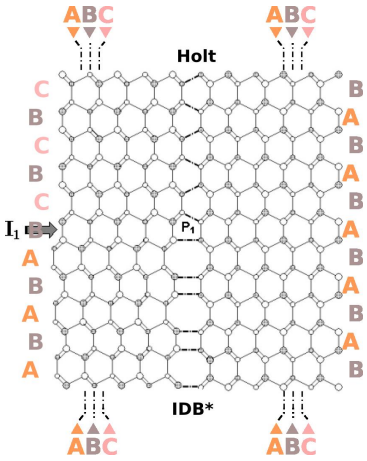

Figure 4.17: Atomic model of an I_1 basal SF terminating at a prismatic IDB according to [179]

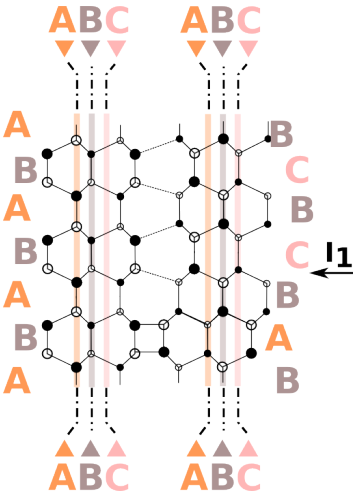

(a) $..ABA..//..BAB$ to $..ABA..//..BCB$ – configuration 1

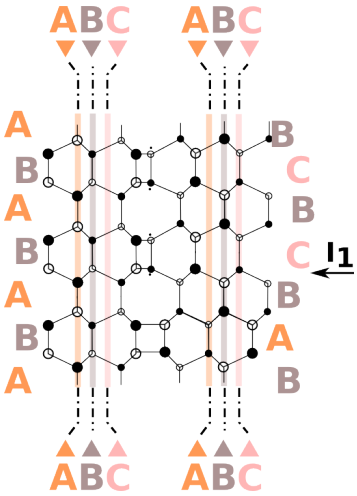

(b) $..ABA..//..BAB$ to $..ABA..//..BCB$ – configuration 2

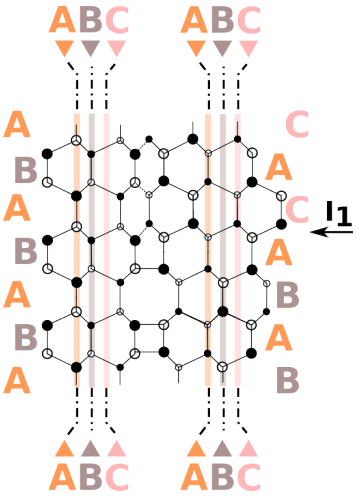

(c) $..ABA..//..BAB$ to $..ABA..//..CAC$ – configuration 1

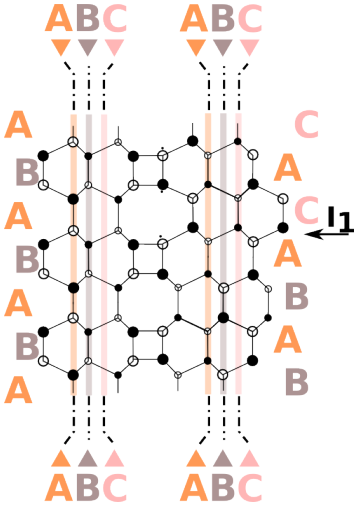

(d) $..ABA..//..BAB$ to $..ABA..//..CAC$ – configuration 2

Figure 4.18: Tentative atomic models for I_1 basal SF terminating at an IDB* – atomic configuration are shown from the $[11\bar{2}0]$ zone axis – atoms represented with different sizes belong to different planes shifted each other by $\frac{a}{2}$ along the $[11\bar{2}0]$ zone axis, the atomic bonding between those planes are depicted by shorter bonds in the general case

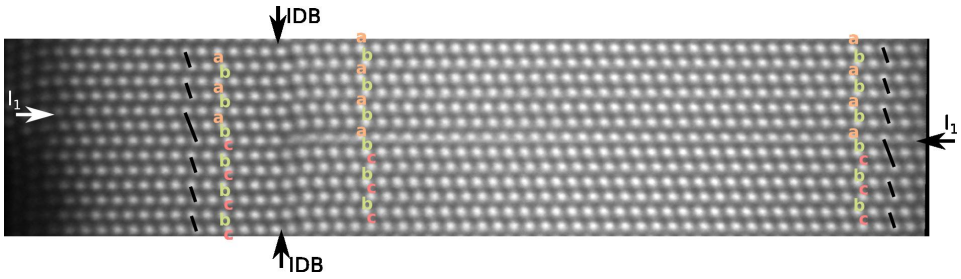

Figure 4.19: HAADF STEM view of an I_1 basal SF crossing an IDB – the letters a and b characterize the position of the plane, within the stacking sequence – dark lines are guides to the eyes in order to locate the I_1 basal SF

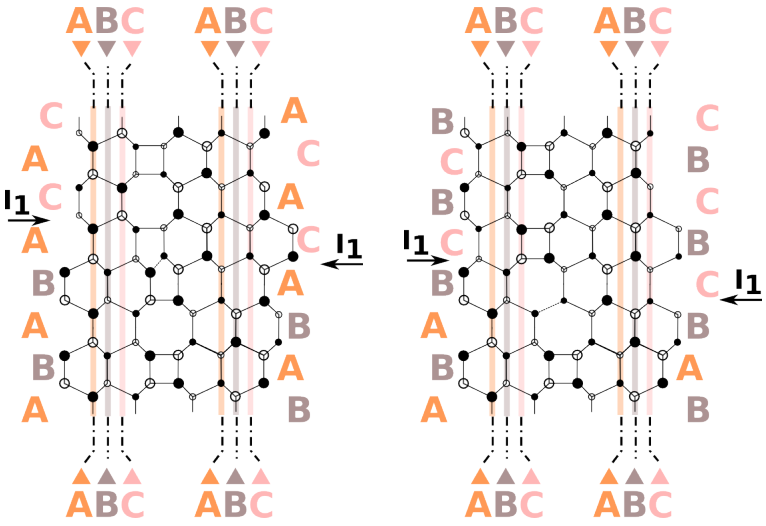

Figure 4.20: Tentative atomic models for the structure observed in Figure 4.19 – atomic configuration are shown from the $[11\bar{2}0]$ zone axis – Atoms represented with different sizes belong to different planes shifted each other by $\frac{a}{2}$ along the $[11\bar{2}0]$ zone axis, the atomic bonding between those planes are depicted by shorter bonds in the general case

- by terminating at the IDB
- by terminating and bending the IDB
- by forming a step

The exact atomic configurations at the intersection of IDBs and SFs are not yet fully determined, due to a lack of systematic STEM observation and the absence of *ab initio* calculations. Nevertheless, for all the configurations that can be hypothesized, partial dislocations including wrong bonds and threefold coordinated atoms could be found, suggesting the generation of deep states in the gap opening a non-radiative recombination channel. However, partial dislocations with similar Burgers vectors have been found at the boundaries of SFs in GaN[10] and CL studies have demonstrated the existence of a sub-band gap luminescence stemming from those defects [209, 208, 91]. It would demonstrate an unexpected radiative behavior, but the role of impurities likely decorating the dislocation has not yet been clarified [208]. Hence, the optoelectronic properties of those defects have still to be determined.

4.5 Conclusion and discussion

In this Chapter, the optical and structural characterization of prismatic IDBs included in GaN NWs has been addressed.

Guidelines for the identification of IDs in GaN NWs by STEM have been first introduced. The systematic observation by STEM of NWs hosting IDs has shown that the ID is always confined in the core, forming a polar core/shell structure.

For all the NWs, an IDB* atomic configuration has been found, which corresponds to the structure having the lower formation energy. It agrees with the observations done in GaN thin films and MOCVD pillars.

A fine optical characterization performed at the scale of the single NW has shown that IDBs are a shallow localization center for exciton, giving rise to the typical 3.45 eV PL of PA-MBE GaN NWs. It constitutes a decisive step on the topic of the 3.45 eV PL origin, which has been debated for few years now. In addition, the reciprocity between 3.45 eV PL and presence of IDBs in NW suggests that most of the PA-MBE GaN NWs are hosting IDs if grown on Si or sapphire substrates but none if grown on diamond.

At last, the interaction between the IDBs and SFs has been shown to result in the formation of a linear defect, which is a good candidate for being a non-radiative recombination center. It means that IDBs could be potentially deleterious to the overall optoelectronic properties of GaN NWs.

[10] Stair-rod like dislocations are found at the intersection between an I_1 basal SF and a prismatic SF [91] and a Frank-type partial dislocation ($\mathbf{b} = \frac{1}{6}[20\bar{2}3]$) could terminate an I_1 basal SF. [208]

Chapter 5

GaN/AlN quantum heterostructures

In order to push further their applicability, plasma-assisted molecular beam epitaxy (PA-MBE) GaN nanowires (NWs) could be functionalized with GaN/AlN quantum heterostructures aiming at confining charge carriers. It may be designed for creating convenient photon sources covering a wide range of emission energies. Although the proof of concept of such devices has been already reported [27], their performance are still limited by the unpredictability of their growth. Hence, the target of this chapter is to explore novel growth modes for GaN/AlN heterostructures, which would lead to the synthesis of a more robust light source.
First, the regular GaN/AlN NW heterostructures, referred as quantum disks (QDisks), will be in the scrutiny, with thorough optical and structural investigations. Such objects are observed to be very similar to 2D quantum wells (QWs) as concerns the correlation of their luminescence properties with their thickness.
Next, taking advantage of the observed "2D" growth mode of GaN on top of AlN NWs, exotic geometries for QDisks have been explored such as pyramidal QDisks. In this case, the luminescence properties were discussed in terms of polar orientation, thicknesses and polarity.
Finally, the ability to nucleate GaN quantum dots (QDs) on top of GaN/AlN NWs has been evidenced, paving the way for a novel type of GaN/AlN NWs heterostructure. Such "3D" growth mode change has been reached both by enlarging the AlN NWs in order to obtain atomically smooth and large NW top facets and by lowering the growth temperature. Preliminary optical investigations are suggesting a significant electron-hole (e-h) pair confinement up to room temperature (RT) in a few QDs, which is promising for a possible light source application.

Contents

Experimental data credits

High-resolution scanning transmission electron microscopy (HR-STEM) images in this chapter have been acquired by Benedikt Haas (CEA, Grenoble, France), Catherine Bougerol and Martien Den Hertog (Néel institute, Grenoble, France). Correlated STEM and cathodo-luminescence (CL) images have been acquired by Sophie Meuret, Luiz Tizei and Mathieu Kociak (LPS, Orsay, France).

5.1 Issues at stake

The self-organized growth of GaN quantum dots (QDs) on 2D AlN films has now been mastered for long [107], with successful photoluminescence (PL) emissions covering a broad range of energies (4 to 1.5 eV) [210, 211] and up to room temperature (RT) [212].

However, assemblies of self-organized GaN QDs on AlN obtained with a Stranski Krastanov (SK) growth mode usually exhibit a large density ($> 10^{10}$ cm^{-2} [213])[1], which might constitute a bottleneck[2] in order to individually address QDs. To overcome this experimental issue, QDs have been included in AlN or AlGaN nanowires (NWs), allowing their subsequent dispersion and individual addressing. In such a case, they are referred as quantum disks (QDisks) or nanodisks in relation to their structure, once inserted in a NW. At first sight, the reported optical properties of those disks seem very similar to the conventional SK QDs, as demonstrated by their excitonic behavior [216], their constant radiative lifetime up to RT [217, 27] and their ability to perform single photon emission [27]. However, a few studies have emphasized additional non-negligible differences with their 2D counterparts:

- the 3D strain relaxation at the NW free surface is responsible for building up radial electric fields [218, 219] even for a QDisk thickness lower than 2 nm. Those are decreasing the overlap between holes and electrons, leading to relatively long lifetimes [217].

- the concomitant growth of an AlN shell is generating an additional strain, which is shifting the QDisk emission energy [220, 219] and possibly leads to a plastic relaxation through the formation of misfit dislocations at the AlN/GaN QDisk interface [221, 222].

- the QDisk might be affected by surface states localized on the NW top and side facets [28], possibly leading for instance to a dependence on the amount of adsorbed O_2 [12].

[1] noticeably, the density of SK QDs has been partly related to the density of threading dislocations (TDs) which are acting as preferential nucleation sites [214, 215]. It means that reducing SK QDs density would require to reduce the TD density in the AlN substrate, which remains a challenge up to date

[2] Mesa etched by lithography techniques, CL on samples prepared in cross sections or laser resonant excitation [215] are a few examples of the techniques required to address single QDs

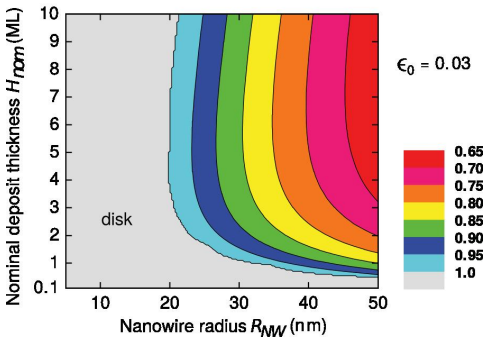

Figure 5.1: Expected morphology for a crystal of nominal thickness H_{nom}, epitaxially deposited on a NW with a diameter R_{NW} and with a lattice mismatch of 3% between both. In the colored area, islanding of the epitaxial crystal would be expected whereas a disk-like shape would be expected in the gray area. It results from the balance between strain energy and surface/interface energies – from [62]

Due to the limited control over the AlN shell thickness during growth and of the NW surface states, such dependencies are making QDisks a rather unpredictable radiative center. It emphasizes a need for a novel type of QDs inserted in NWs with an improved robustness against strain and surface inhomogeneities. For instance, Holmes *et al.* [223] have synthesized by MOCVD GaN QDs on top of pencil-like AlGaN microwires. Their structure has two strong assets: (1) the very low density of the microwires obtained thanks to the selective area growth (SAG) allows individual addressing of QDs by μ-PL without the requirement for NW dispersion and (2) their QDs could perform single photon emission up to RT, suggesting an efficient electronic confinement coupled to an excellent structural quality.

This chapter will be an exploratory work aiming at discovering novel growth modes for GaN on top of AlN NWs by plasma-assisted molecular beam epitaxy (PA-MBE), in order to synthesize improved QDisks or at least a heterostructure with a novel set of peculiarities. First, single QDisks having various geometries will be in the focus. Next, based on the theoretical prediction of Glas and Daudin [62], the growth of GaN QDs on top of AlN NWs will be intended by enlarging the AlN NW top diameter. Indeed, according to the two authors and as shown in Figure 5.1, there should be a critical NW diameter above which the growth mode of a mismatched material on top of a NW switch from 2D to 3D, *i.e.* from a QDisk-like structure to 3D island structure. The expectation is to synthesize a heterostructure combining the robustness of the well known GaN SK QDs with the practicality of the NWs.

In the general case, correlated structural and optical characterizations will be performed on the different heterostructures that have been synthesized, in order to assess their own set of peculiarities.

5.2 GaN quantum disks

GaN QDisks are the reference system for NW heterostructures, since their growth on a regular sized AlN NW seems spontaneous.

5.2.1 Growth

The growths have been carried on as follows:

1. GaN base: a "regular" GaN NW assembly is grown for few hours and is used as a quasi-substrate for the subsequent growth of the heterostructure. In this Chapter, no specific care has been dedicated to the AlN buffer polarity, meaning that the random nucleation of IDs in NWs is expected, with significant variations between samples (see the chapter 3).

2. AlN base (bottom barrier): AlN is grown for 30 $\sim$ 60 min, with a substrate temperature of 840 ℃ and a III/V ratio of 0.5 $\sim$ 0.6. The obtained AlN section is grown longer than 100 nm, which allows to obtain its full relaxation and the certainty that its growth has ended up while a steady state regime was reached. The AlN NWs diameters are in the 30 $\sim$ 60 nm range.

3. GaN QDisks: they are grown at a substrate temperature of 840 ℃ and with a III/V ratio of 0.6 $\sim$ 0.8, for 40 $\sim$ 80 s, which correspond to nominal thicknesses of 5 $\sim$ 15 ML_{GaN}. Prior and after the GaN insertion growth, NWs are exposed for 1 $\sim$ 2 min to the N flux only, in order to consume the possible residual amount of Al and Ga atoms residing on the NW side facets. Such process is expected to prevent further possible intermixing between GaN and AlN.

4. AlN capping (top barrier): AlN is further grown for capping the GaN QDisks, in similar conditions than for the former AlN section, with length in the 20 $\sim$ 50 nm range.

Four samples, labeled #A, #B, #C and #D, have been grown along this growth route, leading to heterostructures whose dimensions are gathered in Table 5.1. The sample #D slightly departs from the aforementioned growth route and will be discussed more precisely farther.

A scanning electron microscopy (SEM) side view of the NW assembly #A, which is representative of all the grown samples, is shown in Figure 5.2a. The NWs are observed to protrude over a thick 2D layer, which has mostly developed during the AlN growth step. The highly defective structure of this layer is expected to quench its PL, hence its contribution will be neglected in the PL spectra acquired on as-grown NWs. The observed dispersion in tilt, attributed to the asymmetric AlN shell, has prevented an *in situ* reflection high energy electron diffraction (RHEED) monitoring of the GaN QDisks nucleation, which is one weakness for such heterostructures.

To better resolve the GaN/AlN heterostructure, NWs have been mechanically dispersed on a holey carbon grid, to perform STEM observations on single NWs. Two prototypical examples, NW #A1 and #A2, are shown in Figure 5.2. The chemical contrast allows to differentiate the AlN from the GaN, which unveils an overview of the GaN/AlN heterostructure. NW #A1 exhibits an AlN base with a rather constant diameter, at least above the GaN base top facet. The GaN QDisk, visible in the NW top section, is highlighted by a dark arrow. In contrast, NW #A2 exhibits a perturbed AlN

Sample label	Sample ref.	AlN base		GaN QDisk		AlN capping
		Length (nm)	Diameter (nm)	Nom. thick. (ML_{GaN})	Temp. (℃)	Length (nm)
#A	N2042	120 ∼ 140	20 ∼ 40	7	840	45 ∼ 50
#B	N2041	120 ∼ 140	20 ∼ 40	15	840	20 ∼ 50
#C	N2020	180 ∼ 190	30 ∼ 40	5	840	40 ∼ 50
#D	N2178	20 ∼ 60	35 ∼ 75	7	860 ∼ 820	7 (nominal)

Table 5.1: Heterostructure dimensions of the various QDisks samples – measurements have done by STEM or estimated from the nominal values

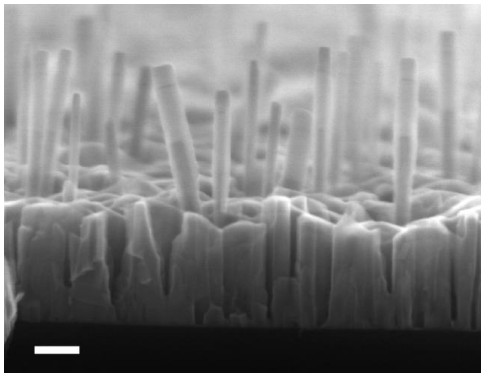

(a) SEM side view of as-grown NWs – scale bar: 100 nm

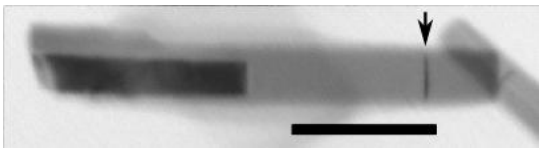

(b) Annular bright field (ABF) STEM – NW # A1 – scale bar: 100 nm

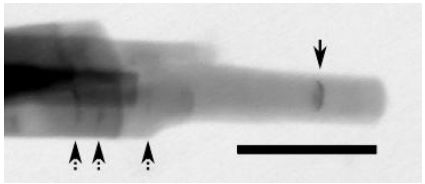

(c) ABF STEM – NW # A2 – scale bar: 100 nm

Figure 5.2: SEM and STEM images of sample #A – in the STEM images, darker contrast correspond to the GaN NW base and the GaN QDisk – acceleration voltage: 10 kV for SEM and 30 kV for STEM

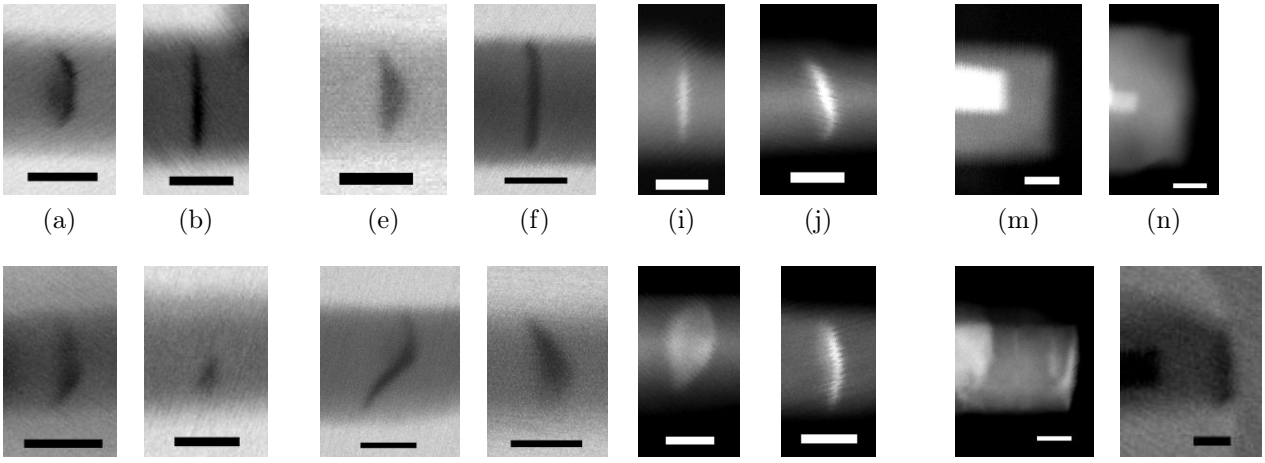

Figure 5.3: Dark or bright field STEM images of GaN QDisk inserted in AlN NWs, for various growth conditions – scale bar: 20 nm, acceleration voltage: 30 kV, QDisks nominal thickness: indicated below each image

base, which has numerous shoulders likely stemming from coalescence events. One GaN QDisk is visible in the NW top section and is pointed by a dark arrow, but additional dark features are visible in the bottom of the AlN base (pointed by dotted arrows), which suggests that GaN has also been grown on the AlN shoulders. Although such NWs are a minority, those multiple GaN inclusions should be taken into account to understand the PL properties of single NWs. For instance, similar inclusions, which were optically active, have been reported by Zagonel *et al.* [220] on a stack of GaN/AlN QDisks.

5.2.2 Structural investigation

Zoomed pictures of the typical obtained GaN QDisks in samples #A, #B, #C and #D are given in Figure 5.3.

In the majority of the cases, the GaN QDisk appears as a thin film-like section, having a rather constant thickness, but which are often distorted, *i.e.* not perfectly perpendicular to the NW axis. Such specific QDisk geometry is very similar to the usual topography of the AlN NW top facet, which probably stems from the small diffusion length of Al adatoms at 840 °C in N-rich conditions. Hence, it is deduced that the GaN QDisk growth corresponds to a conformal deposition on the AlN NW top facet, indicating a "2D" growth mode. It infers that for increasing the uniformity of the GaN QDisks within an assembly, one needs first to increase the uniformity of the AlN NWs geometry.

An attempt has been made with sample #D, where the AlN base has been grown at higher temperature (+20 °C) and with an higher III/V ratio (equal to 1) compared

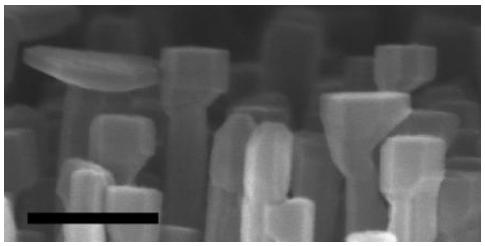

Figure 5.4: SEM side view of the top facet of sample #D – scale bar: 200 nm

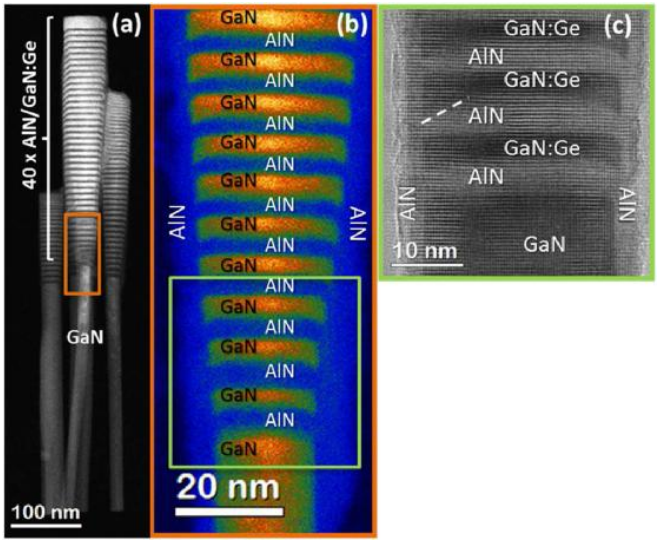

Figure 5.5: high angle annular dark field (HAADF) STEM images of GaN/AlN heterostructures from [217] – according to the authors, the full NWs have been grown at ∼ 790 °C

to other samples, with the aim of smoothing the NW top facet. The AlN capping has been done at lower temperature and kept short (2 min of growth, *i.e.* a nominal thickness of 7 nm, instead of the regular 50 nm). As exemplified in Figure 5.3 and 5.4, it has resulted in a shorter but larger AlN base, with an apparent smoother top surface. However, although the temperature has been lowered to 820 °C for GaN QDisk growth, their effective nucleation *ex situ* checked by STEM was seldom, with less than ∼ 10% of the NWs hosting a GaN QDisk. Such behavior is tentatively attributed to the existence of an incubation time for GaN nucleation on top of AlN NWs, which is significantly increased in the case of atomically flat AlN top facets. Such hypothesis will be further discussed throughout this chapter.

Within the model proposed by Glas and Daudin [62], the observed "2D" growth mode of the GaN QDisks, supported by the results published in the literature (see an example in Figure 5.5), indicates that the critical diameter above which the GaN would nucleate on the AlN NWs as an island rather than a disk, is above 60 nm. However, as emphasized in their model, this critical diameter is dependent on surface and interfaces energies. Therefore, an abrupt change of the critical diameter can be expected if switching the NW polarity, if a surfactant layer is stabilized [224] or even if the roughness of the GaN/AlN interface is different. For instance, the preliminary STEM results[3] shown in Figure 5.6, highlight a "3D" growth mode when the GaN has nucleated on top of an AlN NWs hosting and inversion domain (ID). In this case, the GaN island has a truncated pyramidal shape with $(1\bar{1}03)$ side facets and an aspect ratio of 5, which is similar to

[3]obtained by Benedikt Haas and Martien Den Hertog on a sample of Matthias Belleoeil (CEA, Grenoble, France

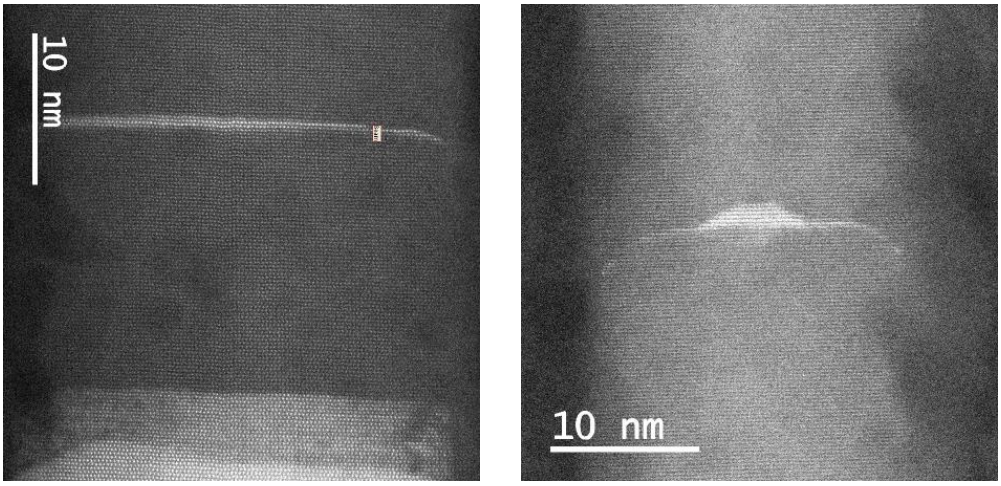

(a) N-polar AlN NWs (b) N-polar AlN NWs hosting an ID

Figure 5.6: HAADF STEM images of GaN QDisk grown on top of a fully N-polar NW or on top of a N-polar NW hosting an ID – the ID has been clearly identified in the GaN NW base, which is not visible here and is expected to be also present in the subsequent AlN section

the Ga-polar GaN SK QDs. It means that the lower bound of 60 nm, for the critical diameter, may not be straightforwardly generalized, and stands only for growth carried on at $\sim$ 840 ℃, in nominally N-rich conditions on an usually rough N-polar AlN top facet.

The structural investigation of GaN QDisks grown on top of AlN NWs has revealed in the general case a "2D" growth mode. A consequence is the high correlation between the QDisk geometry and the AlN NW top facet, meaning that size dispersion between both will be correlated as well. In addition, the tentative evidence of an incubation time for GaN on AlN NWs depending on the NW roughness can increase as well the geometry dispersion of QDisks. At last, preliminary results have shown that the GaN growth mode could be switched to "3D" in the presence of an ID. All those results predict a large dispersion in the QDisk luminescence properties in relation to their large geometry dispersion.

5.2.3 Optical investigation

The PL spectra acquired on as-grown NWs of sample #A, at different temperatures, is shown in Figure 5.7. It features a peak at $\sim$ 3.4 eV attributed to the PL of the GaN base, noticeably due to intensity drop with temperature starting at 50 K. Hence, the other contributions of the spectra are attributed to QDisks and/or to any other radiative centers present in the sample. However, the absence of clear peaks in this

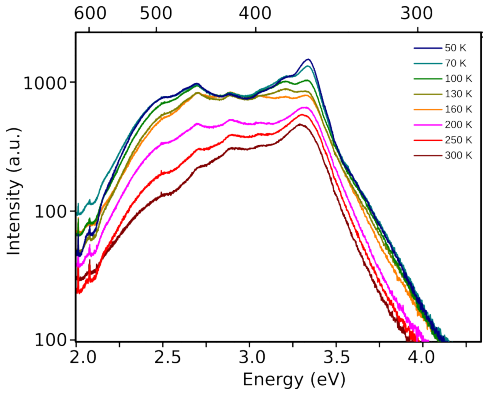

Figure 5.7: PL spectra of $\sim 10^7$ as-grown NWs of sample #A between 50 K and RT – incident power: 70 μW – note that the small peaks observed for $E < 3.4$ eV are attributed to Fabry-Perot oscillations

broad PL band[4] prevents to deconvolute the various contributions, *i.e.* impede further analysis. Such PL spectra is typical for the samples #A, #B, #C and #D. Hence, it obliges to perform the optical investigations at the scale of the single NW, in order to reduce the number of radiative centers probed at the same time, and to get rid of the possible parasitic signal stemming from the 2D layer.

Only sample #A and #B will be further investigated, especially because from the growth point of view, they only differ by the GaN QDisk thickness, which is nominally 2 times thicker in #B compared to #A. In the case of coupled CL-STEM measurements, NWs have been deposited on commercial SiN grids, whereas for PL measurements, acquisitions have been performed directly on the NW assembly, or on NWs dispersed on Si substrates. For the latter case, subsequent SEM observations have shown that on average 4 NWs are measured at the same time when acquiring a μ-PL spectra.

Radiative centers Due to its ability to spatially localize the radiative centers, CL is a convenient tool for the optical characterization of GaN QDisks in single NWs. A systematic analysis on samples #A and #B has been performed by the group of Matthieu Kociak (LPS, orsay, France) and emphasized the existence of several radiative centers within a single NW:

- the GaN base. In Figure 5.8, its CL contribution is at 3.6 eV, whereas the QDisk contribution is at 3.1 eV
- the QDisk.
- point-like defects, which are mostly found in sample #B. As shown in Figure 5.9, the radiative center is confined in a tiny volume, which is far from the QDisk or the GaN base. In this case, it has a luminescence energy at 5.2 eV.

The various CL contributions acquired on several NWs of samples #A and #B are reported on the graph of Figure 5.10a as function of their energy and full width half maximum (FWHM). For sample #A, the QDisks have luminescence energies in the range 3.6 ± 0.6 eV, with FWHMs of $40 \sim 250$ meV. In comparison, for sample

[4] the small peaks observed in the spectra are ascribed to Fabry-Perot oscillations

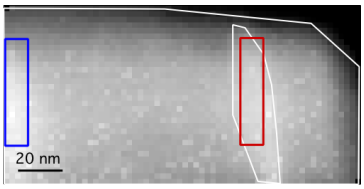

(a) HAADF STEM image of the NW – the GaN QDisk is outlined by the white line (right side)

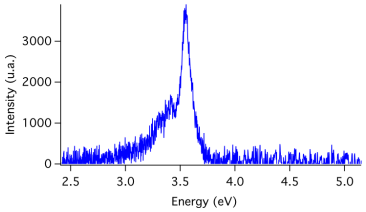

(b) CL signal stemming from the GaN base – blue rectangular on the STEM image

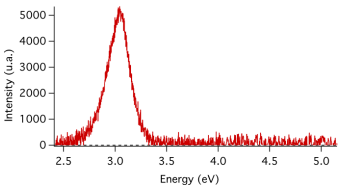

(c) CL signal stemming from the GaN QDisk – red rectangular on the STEM image

Figure 5.8: Spatial decorrelation between the luminescence stemming from the GaN base and from QDisk – CL acquired at 150 K, with an acceleration voltage of 60 kV – sample #B

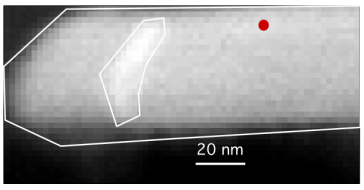

(a) HAADF STEM image of the NW – the GaN QDisk is outlined by the white line (left side) and the point-like defect is indicated by the red spot

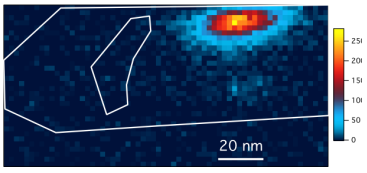

(b) CL intensity mapping of the signal at 5.2 eV

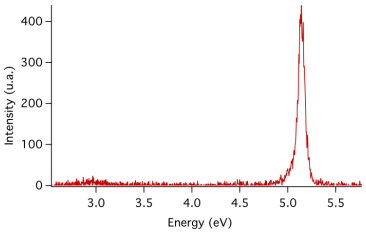

(c) CL spectra on a point-like defect

Figure 5.9: CL spatial localization of a point-like defect – CL acquired at 150 K, with an acceleration voltage of 60 kV – sample #B

#B, which features QDisks nominally thicker than in sample #A, the QDisks have lower luminescence energies, in the range 2.8 ± 0.4 eV, but larger FWHMs, in the range $180 \sim 450$ meV. It is attributed to the quantum confined Stark effect (QCSE), as detailed farther. For the point-like defects, their luminescence energies spread on several eV, with small FWHMs. Hence, they are attributed either to GaN QDs randomly grown on the AlN NW side facets during the QDisk growth and later encapsulated by the AlN shell, or to defects in the AlN. For the first hypothesis, it correlates well with their large energy dispersion, their systematic localization under the GaN QDisk and their larger frequency in NWs of sample #B, where the QDisk growth was longer than in sample #A. At last, the GaN base is observed to have a CL signature in the $3.0 \sim 3.6$ eV range, which spectrally overlaps the QDisks signals.

For comparison purpose, μ-PL spectra have been acquired at 10 K, on bunches of single NWs dispersed on a Si substrate. The energy of the various PL peaks measured on bunches of NWs is reported in the graph of Figure 5.10b. For sample #A, the NWs PL spreads on average from 3.3 to 4.4 eV, whereas for sample #B, the average NWs PL

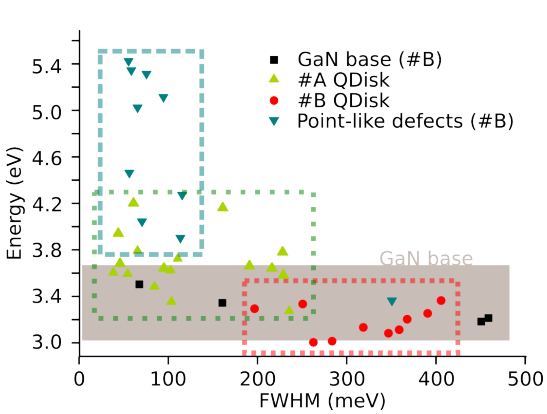

(a) Statistical graph of the various CL contributions observed in NWs of samples #A and #B – CL acquired at 150 K, with an acceleration voltage of 60 kV

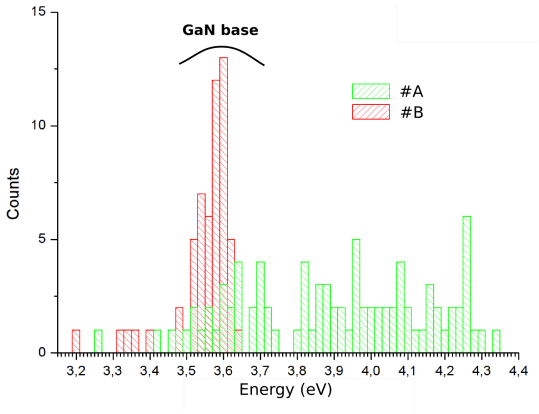

(b) Statistical graph of the various PL contributions observed in NWs of samples #A and #B – from the CL systematic analysis, the contribution at 3.6 eV in sample #B is tentatively attributed to the GaN base – PL acquired at 10 K

Figure 5.10: Statistical analysis of the CL and PL signatures of the NW radiative centers

spreads from 3.2 to 3.7 eV, which fully correlates with the results obtained from CL. However, PL is *a priori* unable to decorrelate the contributions of the GaN QDisk from the ones of the GaN base or point-like defects.

The average QDisk luminescence energy found for sample #A spreads on a larger energy range than for sample #B. Such broadening most probably stems from the geometry dispersion of QDisks within the assembly, although the growth were nominally performed in the same conditions. In addition, the CL of single QDisks usually gives large peaks, which partly stems from the existence of more than one localization center within the QDisk. A time resolved CL acquisition, displayed in Figure 5.11, even shows blinking on a timescale of few seconds of different CL peaks stemming from the same QDisk.

Quantum confined Stark effect Four contributions are usually invoked to account for the PL properties of a QDisk: (1) the electronic confinement, (2) the 3D strain field, (3) the Fermi level, possibly pinned at nearby facets and (4) the polarization induced surface charges. By modeling the three latter contributions by a single 3D electric field, one can retrieve the simple case of 2D quantum wells (QWs) or QDs, for which the luminescence properties are well explained by taking into account the QCSE. As depicted in Figure 5.12, the QCSE describes the spatial separation of electron and holes due to an electric field, which results in a reduced recombination energy and a larger lifetime for electron-hole (e-h) pairs compared to the fictive case where the built-in electric field would be absent. Assuming a constant electric field in a QW and neglecting the confinement contribution, an affine dependence between the QW luminescence energy

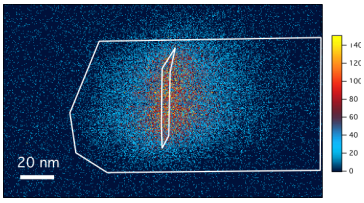

(a) CL intensity map – white lines outline the NW and the GaN QDisk

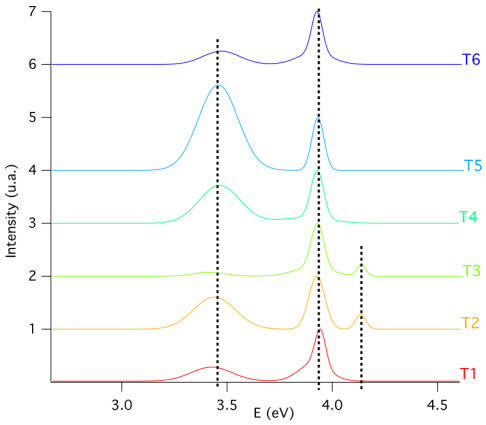

(b) CL spectra integrated for 3 s, at different times

Figure 5.11: Time-resolved CL spectra – acquisition performed at 60 kV, at 150 K

and its thickness is expected and can be expressed as [225]:

$$E = E_0 - \Delta x \times e \times F - R_y(F) \tag{5.1}$$

where E is the QW luminescence energy, E_0 is the QW gap for $F = 0$ (including the electrical confinement contribution), Δx is the thickness of the QW, e is the elementary charge, F is the amplitude of the electric field and $R_y(F)$ is the excitonic binding energy.

Such behavior has been confirmed by experimental reports on QWs or QDs embedded in AlN [226, 210], as well as by the tight binding calculations of Camacho [35]. They are summarized in Figure 5.13. In the specific case of QDisks, the results of Renard *et al.* [27] have also emphasized a dependence of the luminescence energy with the QDisk thickness, which has been attributed to a QCSE, although in their case the electric field amplitude decrease compared to the reference cases of QWs or QDs, for large thicknesses. It likely stems from the 3D strain relaxation effect and/or to the influence of the surface states in QDisks, in agreement with more advanced simulations [28, 218]. One has to note that the QDisks of Renard *et al.* have thinner AlN barriers ($\sim$ 10 nm) compared to the one of samples #A and #B ($>$ 50 nm), which must result in a different strain state between those quantum heterostructures.

A consequence of the QCSE is the ability to estimate the thickness of a quantum heterostructure based on its luminescence energy and on the knowledge of its built-in electric field amplitude. For QDisks of sample #A and #B, the built-in electric field will be assumed equal to the one of conventional QWs. Hence, based on the experimental results of Adelmann *et al.* [226] (already reported in Figure 5.13), the QDisks thicknesses would be $2 \sim 6$ ML_{GaN} in sample #A and $5 \sim 7$ ML_{GaN} in sample #B. For both cases, the obtained thicknesses are much smaller than the nominal values of deposited GaN, which suggests two explanations:

- the QDisk thickness is underestimated due to an overestimation of the built-in electric field amplitude. However, a comparison with the results of Renard *et al.* [27] suggests that such error should likely not exceed 1 ML_{GaN}.

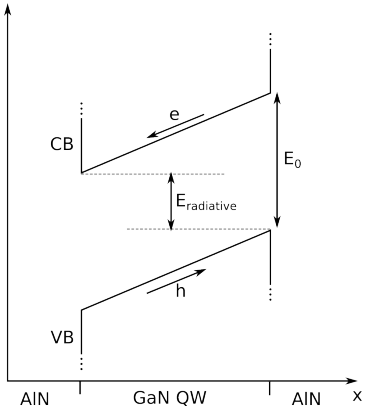

Figure 5.12: Sketch of the band diagram within a QW – due to the spatial separation of the electron and hole, their recombination energy $E_{radiative}$ is lower than E_0.

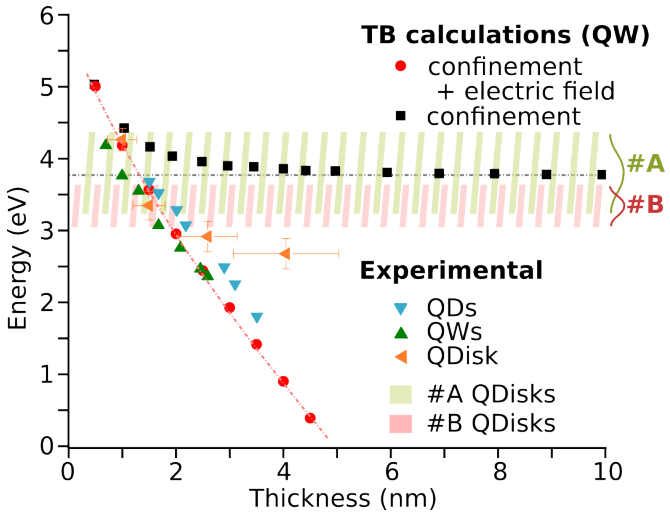

Figure 5.13: Experimental reported luminescence energy of GaN QWs [226], QDs [210] and QDisks [27] – tight binding (TB) calculations [35] of a GaN QW luminescence energy, including or not the built-in electric field contribution – note that the bulk GaN band gap value is overestimated in the calculation (+31 meV) likely due to the neglect of excitonic interactions – the luminescence energy ranges of the QDisks of samples #A and #B are indicated by colored rectangles

- a growth speed lower than the nominal values, due to the existence of an incubation time for GaN nucleation on top of the AlN NWs.

The existence of an incubation time would agree with the seldom nucleation of GaN QDisk for sample #D and experiments presented in the last section of this chapter will further corroborate this hypothesis.

A side effect of the presence of the QCSE is the possible partial screening of the built-in electric fields by free carriers, resulting in a luminescence blue-shift of the heterostructure, with an amplitude scaling with the excitation density [211]. As detailed in Figure 5.14, a similar behavior can be observed by CL. The QDisk under scrutiny is shown in Figure 5.14b; it exhibits three major CL peaks, labeled A, B and C, which are fitted by Gaussian curves. Their energy maxima and FWHM have been plotted in Figure 5.14c as function of the excitation distance from the QDisk itself. As expected, when reducing the distance between the electron beam (e-beam) probe and the QDisk, a larger amount of charge carriers are injected in the QDisk[5], resulting in an observed blue-shift of the CL. However, the blue-shift amplitude differs whether exciting from the AlN base or the AlN cap. Based on the results of the chapter 6, such difference could be attributed to a specific set of built-in electric fields, leading to an asymmetric injection

[5]see the chapter 6

efficiency of carriers in the QDisk. Indeed, if the QDisk CL peaks energies are plotted as function of the total CL intensity, *i.e.* as function of the amount of injected charge carriers, this asymmetry between the AlN base and cap fades out (see Figure 5.14e).

A linear dependence between the amount of injected charge carriers and the total QDisk CL intensity is assumed. Hence, Figure 5.14e suggests, within the explored range, a single logarithmic dependence between the QDisk energy and the amount of injected carriers. It slightly differs from the result of Kalliakos *et al.* [211] (see Figure 5.14f) who performed similar experiments with PL on assemblies of GaN QDs in AlN. In their work, one can observe two different regimes whether being at low or high excitation density, each regime likely corresponding to a logarithmic dependency[6]. As they are probing assemblies of QDs, the authors can probably reach lower excitation densities (and still collect a signal) compared to CL performed on a single NW. Therefore, it can be assumed that the measured characteristics on the QDisk correspond to the high excitation density regime reported by Kalliakos *et al.* [211].

Electric fields screening could be advantageously used when performing $\mu-$PL on single NWs, in order to decorrelate the luminescence contributions of QDisks and possibly point-like defects from the one of GaN base. An example is shown in Figure 5.15, where the $\mu-$ PL spectra acquired on few singles NWs exhibit two bands[7]. If increasing the incident laser power, one is shifting toward higher energy whereas the other not. Based on this observation, the first band is tentatively attributed to a QDisk signature and the other one to the GaN base signature. Point-like defects are ruled out in this case as their FWHM is usually lower than the 250 meV observed for this band. The energy dependence of the QDisk on the excitation density is hardly following the expected logarithmic dependence previously observed for CL and in the work of Kalliakos *et al.* [211]. It is tentatively ascribed to the fact that several QDisks are probed at the same time but individually received different excitation densities. Hence, it could account as well for the increase of the PL peak FWHM and the noisy data set.

Nevertheless, one can define $E = \alpha + \beta ln(P/P_o)$, with $\beta = 29$ meV in the case depicted in Figure 5.15. It indicates a significant variation of the carriers density in the QDisk along with excitation density. If considering only a radiative and a non-radiative recombination channel for *e-h* pairs in the QDisk, one can estimate their amount, n, in the QDisk :

$$\Phi = \frac{n}{\tau_r} + \frac{n}{\tau_{nr}} \quad \Leftrightarrow \quad n = \Phi\tau \quad with \quad \tau = \frac{\tau_r \tau_{nr}}{\tau_r + \tau_{nr}} \tag{5.2}$$

where, Φ is the incoming flux of *e-h* pairs in the QDisk, which scales linearly with the excitation density, and τ_r (τ_{nr}) is the radiative (non-radiative) lifetime of *e-h* pairs. One has to note that an increase of n implies a screening of the electric-field, which infers a decrease of τ_r [210]. Therefore, there is no proportionality between the incoming flux of *e-h* pairs and their density, as first suggested by the equation 5.2. With the

[6] for the QDs having a PL at 2.8 eV, which is close to the case of the NW under scrutiny, the low excitation density regime corresponds to a plateau rather than a logarithmic increase

[7] note that the laser energy is 5.09 eV which is beneath the value of the AlN gap (6.02 eV), meaning that the QDisk excitation occurs by generation of *e-h* pairs directly in the QDisk

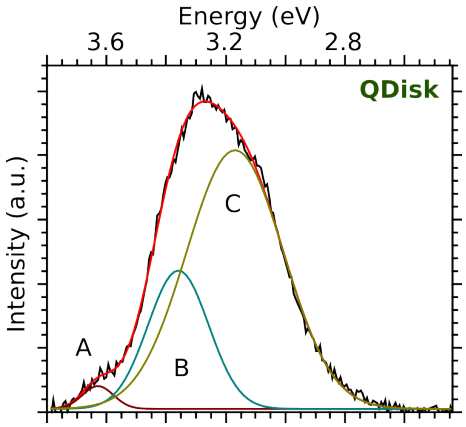

(a) CL spectra of the QDisk (acquired on the QDisk) – the spectra fitted by three Gaussian peaks

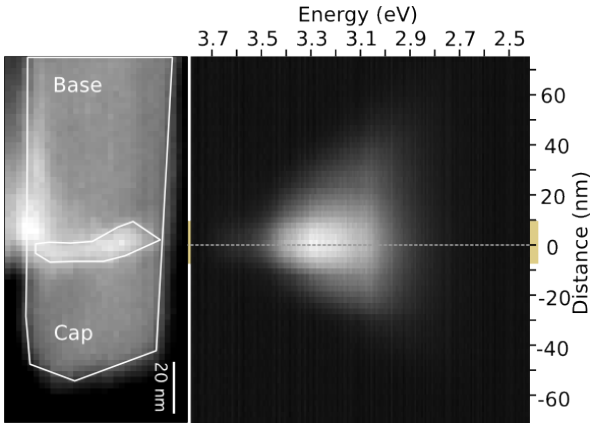

(b) Left: HAADF STEM image a QDisk NW – right: CL spectra of the QDisk as function of the excitation distance from the QDisk

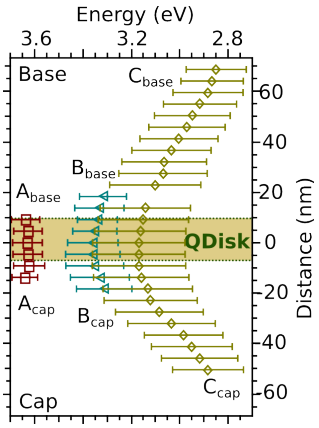

(c) Peaks energy (open symbols) and FWHM (bars) as function of the excitation distance from the QDisk

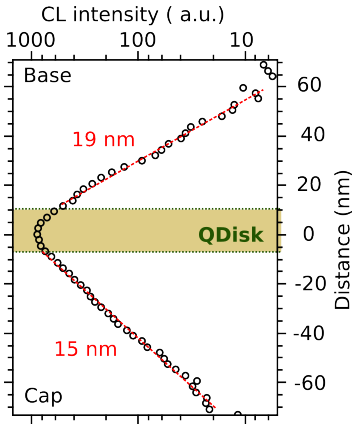

(d) QDisk CL intensity as function of the excitation distance from the QDisk – the intensity is in ln scale

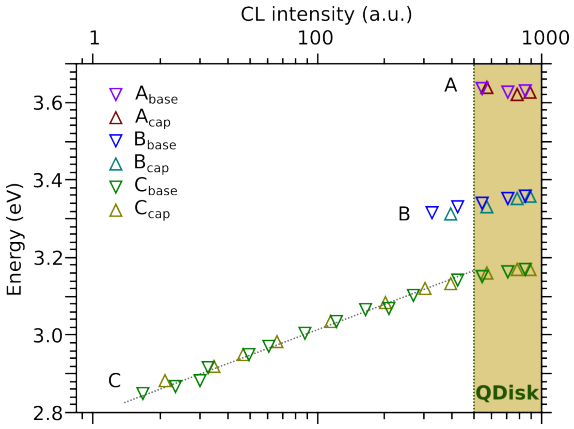

(e) Peaks energy as function of the total CL intensity

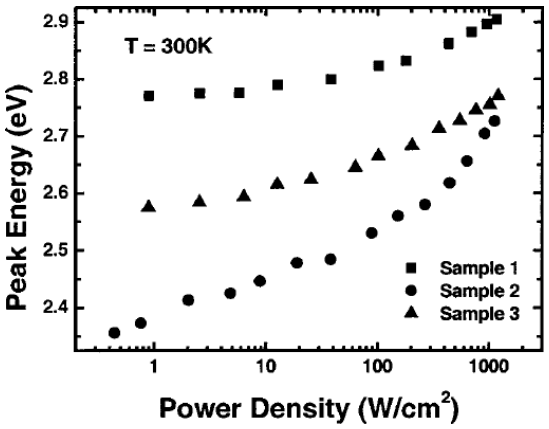

(f) PL energy versus excitation density of GaN QDs assemblies embedded in AlN – from [211]

Figure 5.14: Highlight of the QCSE in a GaN QDisk – CL acquired at 150 K, with an acceleration voltage of 60 kV – sample #B

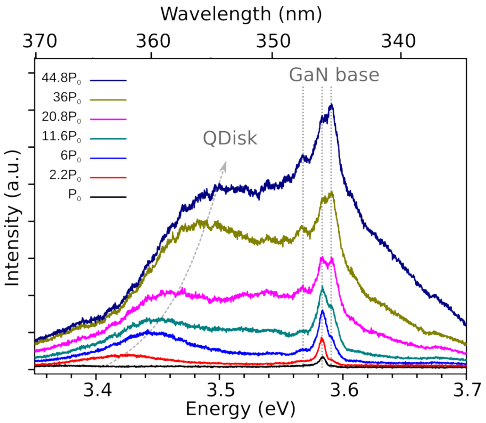

(a) μ−PL spectra of singles NWs acquired at 10 K, as function of the incident power

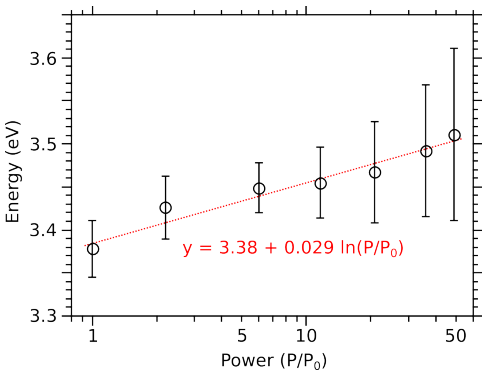

(b) Energy and FWHM of the PL peak associated to QDisk luminescence as function of the incident power – the red dotted line is a tentative logarithmic fit of the data set, using a logarithmic law

Figure 5.15: PL energy of single NWs as function of the incident power – laser energy: 5.09 eV, initial laser power measured before the waist: $P_0 = 2.5$ μW – sample #B

aim of identifying GaN QDisk PL The dependence of n over the lifetime has two main consequences:

- according to the abacus of Bretagnon *et al.* [210], there is an almost exponential decrease of the radiative lifetime versus luminescence energy. Therefore, based on the equation 5.2, β should also exponentially decrease with the luminescence energy and falls below the experimental resolution for QDisks having a PL larger than 4 eV.

- in the case of the presence of non-radiative defects in the QDisk, τ should drop compared to the previous case, leading to a decrease of β.

Therefore, the measurement of β on PL peaks lower than 4 eV could be tentatively used as a gauge to estimate the presence of non-radiative defects in QDisks or to identify the GaN base PL contribution. However, only relative values of β, acquired on the same excitation density range, should be considered, meaning that a calibration or a measure on a large pool of NWs has to be done. Unfortunately, such systematic analysis has not been tried yet so that this conclusion stands as a proposal only.

Lifetime The lifetime of carriers trapped in QDisks or point-like defects has been measured both by time correlated cathodo-luminescence (TC-CL) and time resolved photoluminescence (TR-PL) on single NWs of sample #A. They are plotted as function of the recombination energy in Figure 5.16a. An almost affine dependence between the lifetime and the related radiation energy is found, which is the signature of the aforementioned QCSE. For comparison purpose, data have been superimposed on the

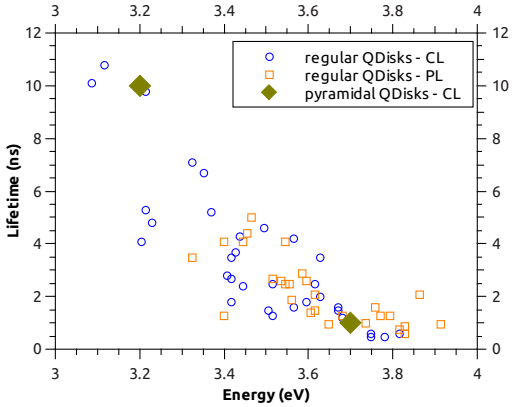

(a) Open symbols: lifetime of QDisks (and point-like centers) found in sample #A measured either by TC-CL (at 150 K) or TR-PL (at 10 K) – Green diamond: lifetimes measured on pyramidal QDisks (cf next section)

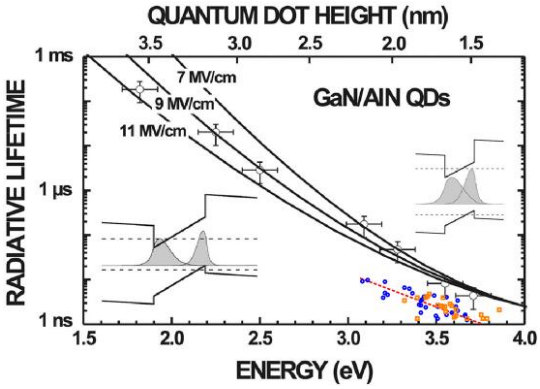

(b) Lifetime versus energy reported for the luminescence of GaN dots embedded in AlN – from Bretagnon *et al.* [210] – acquired lifetimes on NWs of sample #A have been superposed (orange squares and blue disks)

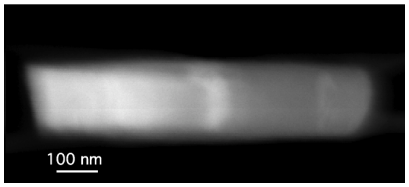

(c) HAADF STEM image of the NW

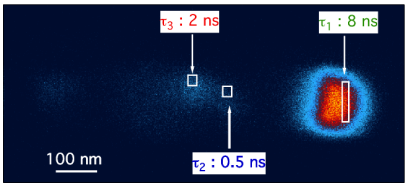

(d) CL intensity map on the above NW – acquisition performed at 60 kV, at 150 K – extracted lifetime from TC-CL have been labeled on each radiative centers

Figure 5.16: Radiative centers lifetime in sample #A

results experimentally obtained by Bretagnon *et al.* [210] on GaN QDs embedded in AlN, in Figure 5.16b[8]. It highlights a slightly shorter lifetime for QDisks compared to QDs having the same emission energy. Such disparity might stem from a different axial confinement in QDs and QWs of same thicknesses. Indeed, Widmann *et al.* [227] have theoretically shown that, neglecting electric fields, a truncated pyramidal QD of height h gives the same luminescence energy than a QW of height $0.72h$. It is in agreement with the +0.5 eV difference between the luminescence energy of QDs and QWs of similar thicknesses reported in Figure 5.13. Hence, using this correction in the abacus of Bretagnon *et al.* would shift the QDisk dataset almost exactly on the QDs characteristic curve. Such result evidences that the built-in electric field of the QDisks of sample #A and #B is, on average, similar to the one of QWs or QDs, *i.e.* in the order of ~ 10 MV.cm^{-1}.

TC-CL allows to spatially localize the radiative center whose lifetime is measured. Hence, point-like defects and QDisks could be fully differentiated. As expected, QDisks

[8] no similar data could be found with QWs

have a longer lifetime compared to the point-like defects, most likely due to their large size. In addition, the affine dependence between lifetime and the radiative energy is still observed for the point-like defects, which strengthens the hypothesis that they are actually small GaN inclusions rather than defects in the AlN.

The precise CL study of single NWs has shown the existence of several radiative centers: the QDisk itself (with multiple localization centers), the GaN base and point-like defects, tentatively attributed to small GaN dots non-intentionally grown on the AlN side facets and/or to defects in the AlN. It is the different nature of those radiative centers, coupled to strain and geometry variabilities from NWs to NWs which are considered responsible for the broad energy PL of a NW assembly. If now looking back to the PL spectra acquired on as-grown NWs of sample #A at different temperatures (Figure 5.7), a significant drop of the PL intensity along with temperature is observed for the contribution in the range 3.2 $\sim$ 4.4 eV. Such range should correspond to the QDisks PL, and would indicate their quenching at RT, most probably due to the presence of non-radiative defects in the QDisk or its close vicinity. Actually, a similar behavior has been reported for GaN/AlGaN NW heterostructures [228].

5.2.4 Conclusion and discussion

A main peculiarity for GaN QDisks is their "2D" growth mode, allowing the spontaneous growth of a QW-like heterostructure on top of NWs. Hence, similarly to the case of 2D QWs, their luminescence energy could be tuned in a broad range only by changing the QDisks thicknesses, in relation to the QCSE. Noticeably, a built-in electric field in the QDisk on the order of $\sim$ 10 MV.cm^{-1} has been inferred.

However, the growth of QDisks with a controlled thickness and strain state is difficult to obtain. A prototypical example is the growth of AlN/GaN QDisks stacks in NWs (see Figures 5.5 and 5.17), where the enlargement of the NW diameter along growth seems unavoidable, building up an inhomogeneous strain field in the QDisk stack, resulting in a broadening of the overall luminescence energy of a single stack. Such behavior has been clearly emphasized by Zagonel *et al.* [220] and is depicted in Figure 5.17. Therefore, it makes challenging the growth of heterostructure with a pre-selected narrow luminescence energy.

5.3 Pyramidal GaN quantum disks

A side effect of the growth of AlN NWs using grazing incident atomic fluxes is the formation of structurally complex top facets, noticeably exhibiting faceted pyramid-like structures. Therefore, taking advantage of the "2D" growth mode of GaN on AlN NWs, such pyramidal structure could be used to mold the QDisk, leading to a so-called pyramidal QDisk. It is this specific quantum heterostructure which is in the focus of this section.

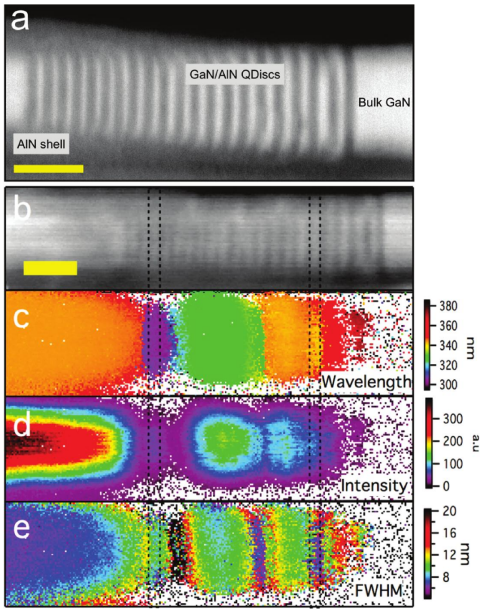

Figure 5.17: Map of the wavelength (c), intensity (d) and FWHM (e) of the CL signal stemming from a stack of GaN/AlN QDisks pictured by annular dark field (ADF) STEM in (a) and (b) – scale bar in (a) and (b) : 20 nm – from [220]

Sample label	Sample ref.	AlN base		GaN QDisk		AlN capping
		Length (nm)	Diameter (nm)	Nom. thick. (ML_{GaN})	Temp. (℃)	Length (nm)
#E	N1950	~ 600	$40 \sim 70$	7	840	$30 \sim 40$
#F	N1958	~ 900	$80 \sim 120$	7	840	$30 \sim 40$

Table 5.2: Heterostructure dimensions of the various samples – measurements have been done by STEM or estimated from nominal values

5.3.1 Growth

The growth follows the same steps described in the first section for regular GaN QDisks, except concerning the AlN base. During this step, the sample holder has been rotated so that the incident angle of the Al (N) atomic fluxes has been shifted from 28° (20°) to 40° (30°)[9]. Two samples have been grown along this route and differ only by the duration of the AlN base growth. A few of their dimensions are gathered in Table 5.2.

A SEM side view of the NWs of sample #F, which is representative of the two samples under scrutiny, is shown in Figure 5.18. As usual, NWs are observed to protrude over a thick 2D layer, mostly formed during the AlN growth steps. A tilt dispersion between NWs is observed as well, most likely stemming from the inhomogeneous strain induced by the AlN shell over the initial GaN NWs.

[9]The angle labeled $\theta_{substrate}$ is reported in the sketch of the MBE setup in Figure 1.1b, page 10 in the chapter 1 has been shift from 0 to 11°.

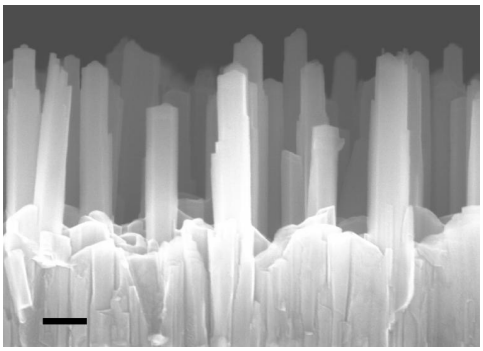

Figure 5.18: SEM side image of sample #F – scale bar: 200 nm

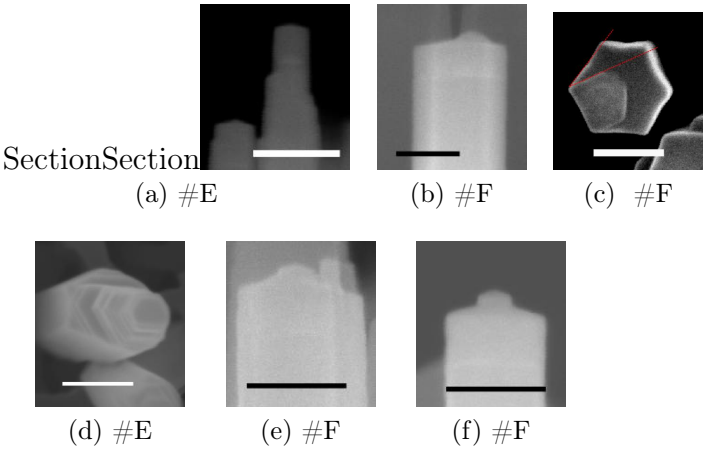

(a) #E (b) #F (c) #F

(d) #E (e) #F (f) #F

Figure 5.19: SEM images of the different NW top facets of sample #E and #F – scale bar: 100 nm

If zooming over the NW top facets, different geometries are observed, as displayed in Figure 5.19. For the majority of the NWs of sample #E, the top facet appears almost flat, but numerous shoulders are visible on the side facets few tenth of nm below the top one. By contrast, for the majority of the NWs of sample #F, their top facets appear perturbed, exhibiting pyramid-like structures or even small pedestals. Based on Figures 5.19c and 5.20a, the pyramids are inferred to exhibit $(11\bar{2}3)$ or $(11\bar{2}\bar{3})$ semi-polar facets. Their observation only in a fraction of NWs of the same assembly suggests that they are stemming from the presence of IDs.

5.3.2 Structural investigation

Nevertheless, the interest lies here in the specific geometries that can reach the heterostructure from the GaN conformal deposition on such AlN features. Especially, the focus will be brought on the GaN deposited on pyramid-like AlN structures, which are observed in up to 50% of the NWs of sample #F. STEM and electron energy loss spectroscopy (EELS) images of such pyramidal QDisks are shown in Figure 5.20. Its confirms the conformal deposition of the GaN so that three different regions could be identified within the QDisk: (1) the base and (2) the top part, which both correspond to polar QWs and (3) the pyramid facets where the GaN QW is on a $(11\bar{2}3)$ or $(11\bar{2}\bar{3})$ surface.

5.3.3 Optical investigation

In order to address directly pyramidal GaN QDisks, CL is preferred, noticeably in order to spatially decorrelate the radiative centers.

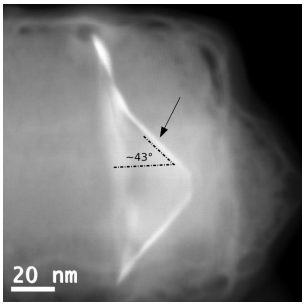

(a) HAADF STEM image

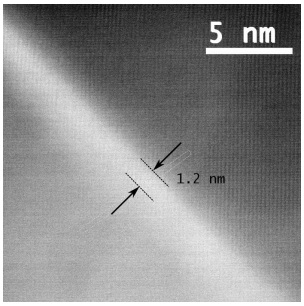

(b) HAADF-STEM – zoom over the area pointed by an arrow on the left image

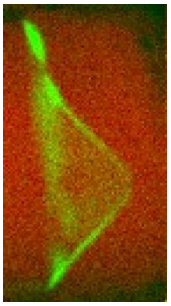

(c) Superposed intensity mapping of the Ga (green) and Al (red) signal acquired by EELS

Figure 5.20: STEM and EELS observations carried on a pyramidal QDisk – zone axis: $[1\bar{1}00]$

Radiative centers A typical example is shown in Figure 5.21, where three radiative centers are emphasized:

- the pyramid base, with a CL signal at 3.21 eV
- one of the pyramid facet, with a CL signal at 3.60 eV
- the top pyramid, with a CL signal at 3.75 eV

Considering the top and base parts of the pyramidal QDisk as small QWs with similar strain states, the abacus of Adelmann *et al.* [226] would give a base GaN QW which is thicker by 2 ML_{GaN} compared to the top GaN QW. It is tentatively attributed to different incubation times due to differences in roughness and/or surface polarity, but further investigation would be needed to confirm this hypothesis.

The bright CL emission stemming from the pyramid side facets, which is shown in Figure 5.21, has not been systematically observed in other pyramidal QDisks, suggesting the usual presence of non-radiative defects brought by plastic relaxation for instance. In addition, the amplitude of the luminescence red-shift related to the QCSE is smaller in semi-polar QWs compared to polar QWs of same thicknesses, due to a lower amplitude of the built-in electric field. For instance, Lahourcade *et al.* [229] have shown that a QW parallel to the (0001) plane and with a PL at 3.2 eV would have a PL at 3.7 eV if parallel to the $(11\bar{2}2)$ plane instead (see the abacus of Figure 5.22). Such +0.5 eV difference is in the same order of magnitude than the +0.4 eV observed between the semi-polar QW on the pyramid facets and the base QW[10]. Hence, it suggests that the base and semi-polar QWs have similar thicknesses, whereas the top QW is much thinner.

[10] although here it is a $(11\bar{2}3)$ or a $(11\bar{2}\bar{3})$ plane rather than a $(11\bar{2}2)$ plane

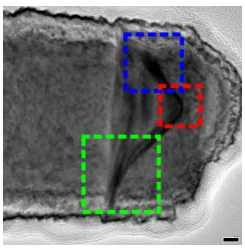

(a) BF STEM – all – 160 × 160 nm^2

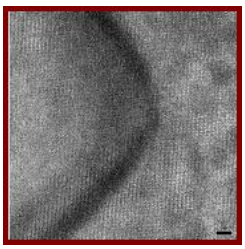

(b) BF STEM – top – 28 × 28 nm^2

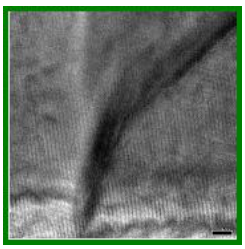

(c) BF STEM – base – 56 × 56 nm^2

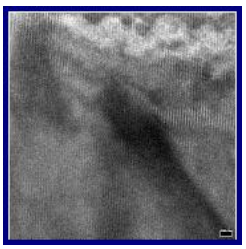

(d) BF STEM – facet – 38 × 38 nm^2

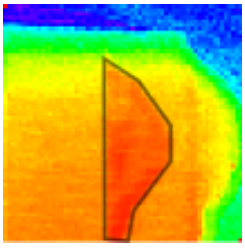

(e) BF STEM – 200 × 200 nm^2

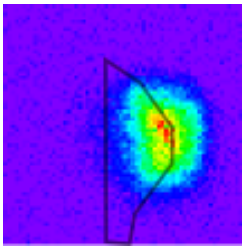

(f) 3.75 eV only – 200 × 200 nm^2

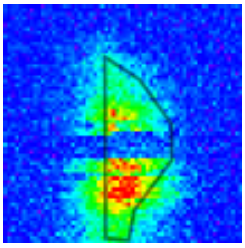

(g) 3.21 eV only – 200 × 200 nm^2

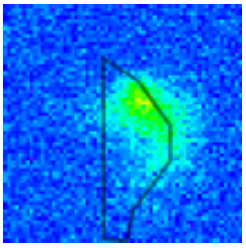

(h) 3.60 eV only – 200 × 200 nm^2

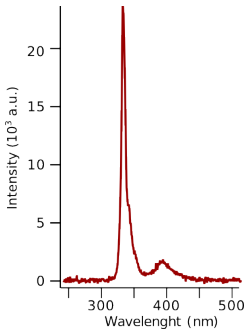

(i) CL spectra top

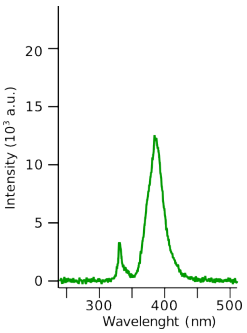

(j) CL spectra base

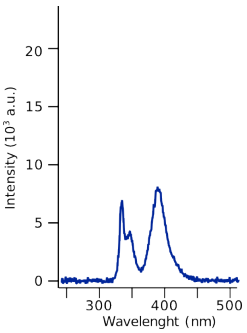

(k) CL spectra facet

Figure 5.21: CL intensity mapping filtered in energies and correlated to structural images at 150 K – sample #F

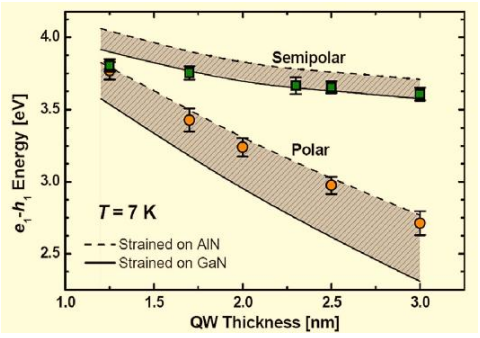

Figure 5.22: PL blue-shift of GaN-AlN QWs between (0001) and (11$\bar{2}$2) orientations – from [229]

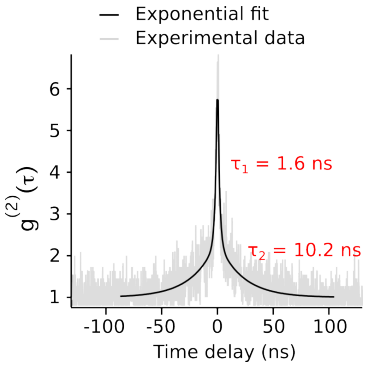

(a) Second order autocorrelation function of the full pyramid CL signal – no energy filtering

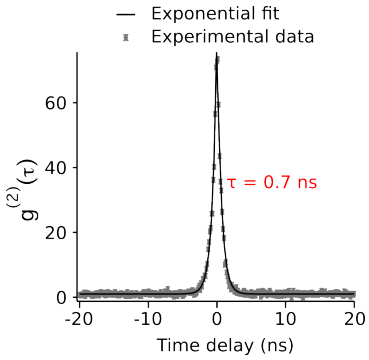

(b) Second order autocorrelation function of the pyramid top CL signal – $4.13 > E > 3.65$ eV

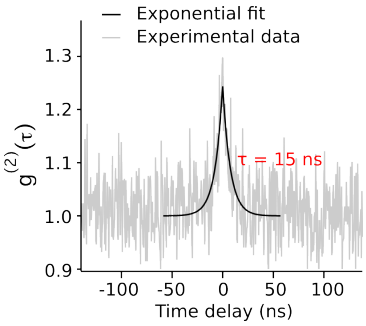

(c) Second order autocorrelation function of the pyramid base CL signal – $E < 3.5$ eV

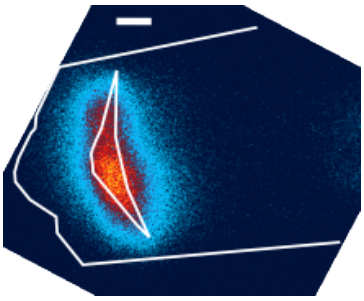

(d) CL intensity mapping – no energy filtering

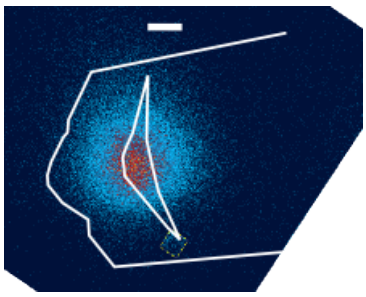

(e) CL intensity mapping – $4.13 > E > 3.65$ eV

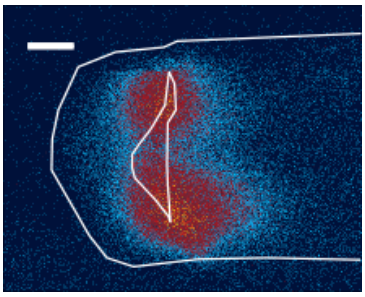

(f) CL intensity mapping – $E < 3.5$ eV

Figure 5.23: TC-CL lifetime measurement of the base and top of GaN pyramids – note that the acquisitions have been done on two different NWs

Lifetime For two different NWs, the lifetimes of the top and base QDisks have been measured, using TC-CL. The top QDisk emits light at 3.7 eV, whereas the base ones emit light at 3.2 eV, which follows the exact same trend discussed in the previous paragraph. Taking advantage of the different energies of the emission, spectral filters were used to select the signal stemming exclusively from the top or the base. The results of the lifetime measurements are shown in Figure 5.23. A lifetime of the order of 1 ns (10 ns) is found at the top (base) QWs. Those measurements, added on Figure 5.16a as green diamonds, are fully matching the typical trend between lifetime and radiative energy previously observed for regular QDisks. It suggests that the different emission energies between the top and the base of the pyramid only stems from thickness differences, rather than strain differences.

Photoluminescence on as-grown nanowires The 5 K and RT PL spectra acquired on as-grown NWs ($\sim 10^7$ NWs) and with a similar excitation density are shown in Figure 5.24. At 5 K, the PL maximum is at 3.4 eV and at 3.2 eV for the RT acquisition. This 200 meV difference is larger than the expected red-shift of ~ 60 meV observed for the GaN

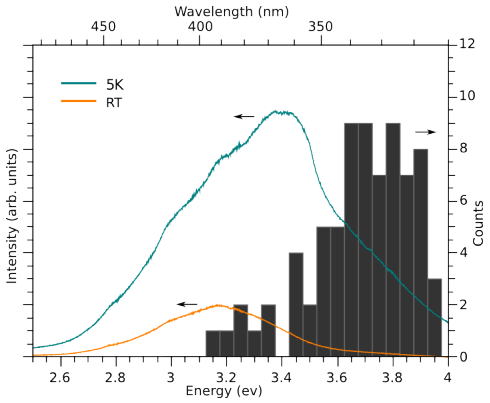

Figure 5.24: 5 K and RT PL spectra acquired on as-grown NWs of sample #F, with a constant excitation power – in the background, the energy distribution of PL peaks acquired on single NWs is displayed. Note that peaks lower than 3.1 eV were disregarded

NWs band edge between 5 K and RT, hence, the low temperature spectra is attributed to a convolution of the GaN base signal and to the QDisks signals, whereas the RT spectra is attributed to the QDisks only. Note, that the 3.2 eV signal has its intensity divided by only ~ 5 between 5 K and RT, whereas a division by ~ 40 is usually expected for pure GaN NWs on the same temperature range.

On the RT spectra, the three contributions observed by CL on a few pyramidal QDisks at 3.7, 3.6 and 3.2 eV are not resolved. It stands also for the μ-PL study performed on single NWs at 10 K, for which the measured PL peak distribution is plotted in the background of Figure 5.24 and does not exhibit the three specific contributions found by CL. Actually, on PL spectra of as-grown NWs, most of the luminescence is below 3.2 eV, which suggests as in the case of regular QDisks, the existence of other types of radiative centers in the NW assembly.

5.3.4 Conclusion

Pyramidal QDisks constitute a case study which has allowed us to improve our fine understanding of NW heterostructures. For instance, CL has shown the existence of several radiative centers within a single QDisk, which has been ascribed to different polar orientations and thicknesses of the QDisk. However, the weak control over the growth of such exotic heterostructures discourages their further development as a novel robust radiative center.

5.4 GaN quantum dots

In order to increase the robustness of GaN/AlN NW heterostructures, the purpose of this section is to synthesize SK QDs rather than QDisks on top of NWs. The expectation is to enhance the confinement of e-h pairs within the core of the NW thanks to the island shape of SK QDs, hence to reduce the impact of the radial fields.

To do so, AlN NWs with large diameters and atomically flat top facets should be required. However, as shown in the chapter 2 and briefly reminded in the previous sections, extensive growth of AlN is usually efficient to increase the NW diameter, but at the price of a rough top facet and to a significant tilt dispersion between NWs. To

overcome this issue, the chosen growth route is to enlarge first the GaN base and to subsequently grow the AlN.

5.4.1 "3D" growth mode for GaN on large AlN nanowires

To demonstrate a possible "3D" growth mode of GaN on large AlN NWs, one needs to check first if the initial AlN top facet is flat, especially free of the pyramidal features observed in the previous section. Therefore, a systematic atomic force microscopy (AFM) imaging of NWs top facets, at different stages of the growth, has been performed.

Growth A sample labeled #G[11] has been grown along the following steps:

1. GaN base: a "regular" GaN NW assembly has been grown for 4 hours and is used as a quasi-substrate
2. GaN enlarged: the NW diameter is enlarged by lowering the growth temperature to 750 ℃ and increasing the III/V ratio up to 1.46
3. AlN base (bottom barrier): AlN has been grown for 1 hour, at 860 ℃ and a flux ratio of 1 in order to mimic the growth of AlN thin films, so that a smooth top facet could be obtained.
4. GaN QDs: GaN is deposited at 760 ℃ with a III/V ratio of 0.6 an a nominal thickness of 9 ML_{GaN} for #G1 (and 4.5 ML_{GaN} for #G3). Next the GaN is exposed to the N flux for 30s
5. AlN capping (top barrier): AlN is grown for 6 min, at 750 ℃ with a III/V ratio of 0.3

The growth run has been initiated on three substrates at the same time, labeled #G1, #G2 and #G3, but #G1 and #G2 have been removed from the MBE chamber after specific growth steps. They are aimed at having an exact *ex situ* version of the sample under scrutiny at different time of the growth. The growth steps undergone by each substrates are summed-up in the next table:

	GaN base	*GaN enlarged*	*AlN base*	*GaN QDs*	*AlN capping*
#G1	✓	✓	✓		
#G2	✓	✓	✓	✓	
#G3	✓	✓	✓	✓	✓

One has to note that for removing a substrate, actually the whole substrate holder has to be temporally removed from the MBE chamber. Hence, a residual oxidation of the NWs

[11] sample N2142

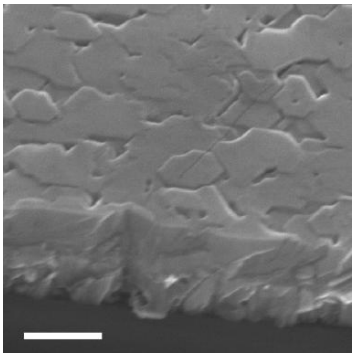

(a) Coalesced domain

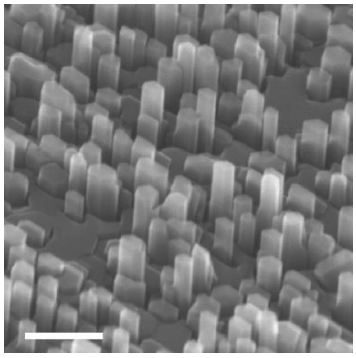

(b) Non-coalesced domain

Figure 5.25: SEM bird eye view of the sample #G1 – scale bar: 200 nm

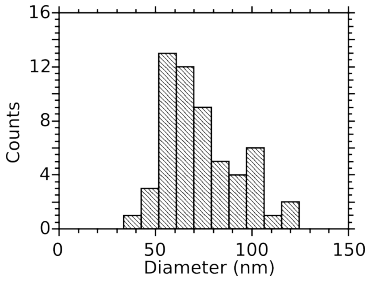

Figure 5.26: Distribution of NW diameter for sample #G – extracted from SEM images

has probably occurred, which could disturb the subsequent growth. In order to "clean" the NW top surface, AlN has been re-grown for 1 min at 750 ℃ after the removal step of #G1. Similarly, after the removal step of #G2, the GaN QDs have been thermally dissociated, AlN has been again re-grown for 1 min at 750 ℃, and new QDs have been grown (smaller than the previous ones).

As emphasized in Figure 5.25, SEM imaging of the sample #G1 has revealed the presence of two domains in each substrates, one with fully coalesced NWs resulting in a 2D layer and one with well separated and nicely hexagonal NWs. Their diameters cover the range $45 \sim 120$ nm, which is, on average, slightly smaller than for sample #F.

Atomic force microscopy investigation In order to observe the nucleation mode of the GaN, AFM measurements on the NW top facets have been done on the bare AlN NWs (#G1), on the non-capped GaN QDs (#G2) and on the capped QDs (#G3). Due to the high aspect ratio of the NWs, such measurements are delicate as the AFM tip needs to be able to "climb" up to the NWs top facets which are several hundreds nm high meanwhile being still able to probe the NW top facet with a sub-nanometer vertical accuracy. To do so, the AFM mapping has been performed in tapping mode, using low scanning speed ($\sim$ 0.5 μm.s^{-1}), and settings for the proportional-integral controller allowing the higher sensibility achievable, without entering in an instability regime[12]. The results are shown in Figure 5.27.

It is clearly emphasized that the AlN base top facets are initially atomically flat (#G1) and become covered by numerous small islands after the GaN deposition (#G2). Hence, it is deduced that the GaN has undergone a "3D" growth mode, so that the observed islands are actually GaN QDs[13]. They exhibit a $10 \sim 20$ nm diameter, a $1.5 \sim 2$ nm height, a density of $\sim 2.5 \times 10^{11}$ cm^{-2} and they are quasi-coalesced. From

[12] those settings are tip dependent

[13] Note here that the denomination "QD" refers yet only to structural properties and is used in opposition to QDisks

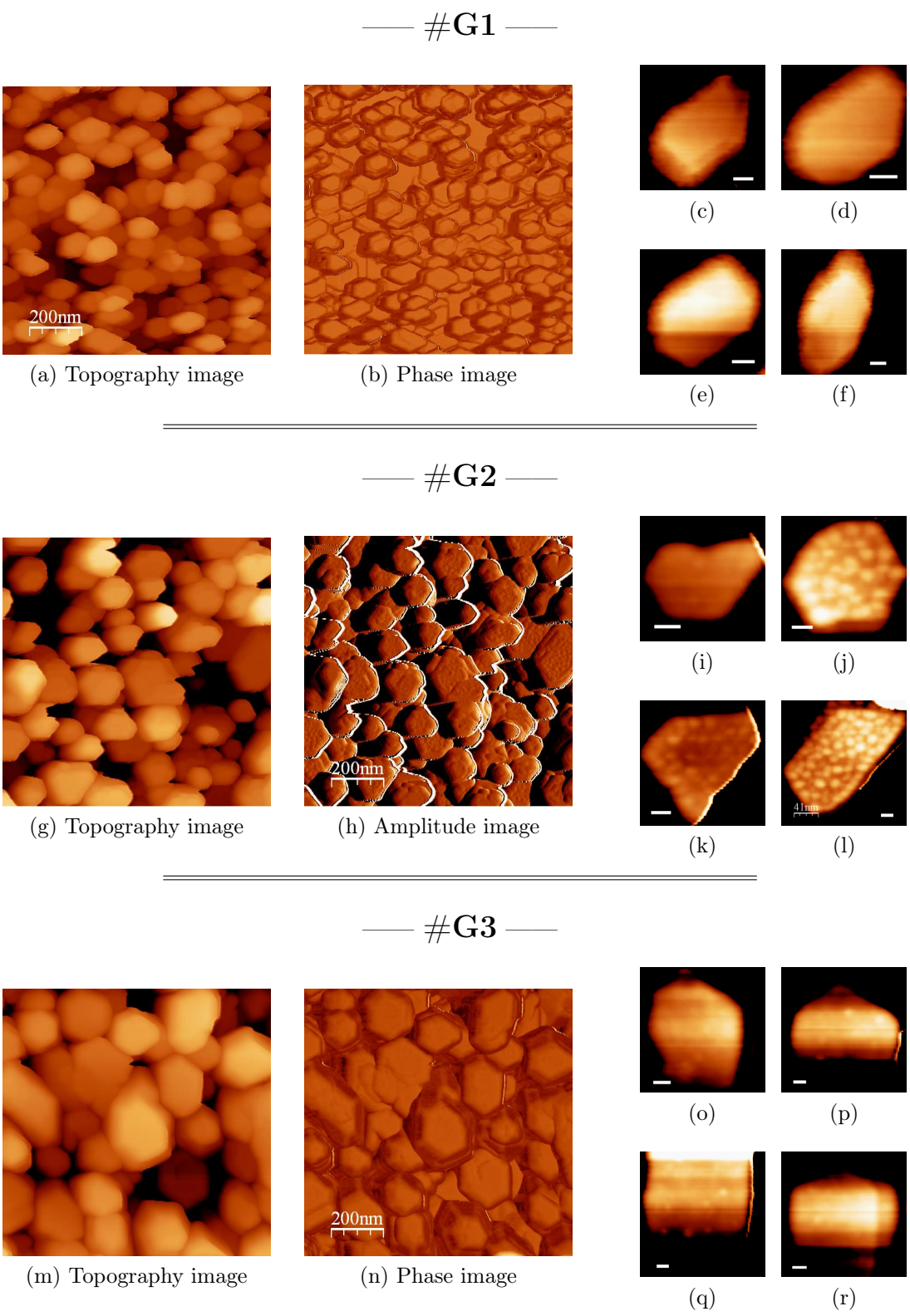

(a) Topography image (b) Phase image (c) (d) (e) (f)

(g) Topography image (h) Amplitude image (i) (j) (k) (l)

(m) Topography image (n) Phase image (o) (p) (q) (r)

Figure 5.27: AFM analysis of sample #G – AFM images of the left and middle columns are 1×1 μm^2 large, the color coded scale spans over 350 nm for topography images, 100° for phase images and 0.3 V for the amplitude image – AFM images of the right column are zoom over the several NW top facets, scale bar: 20 nm

the structural point of view and neglecting the issue of the wetting layer, those islands appear very similar to the usual GaN SK QDs grown on 2D AlN at low temperature ($\sim$ 700 ℃) and free of ripening [213].

Few NWs of #G2 are observed not to host QDs, but it does not reveal any correlation between NW diameter and QD nucleation. It would suggest that the critical diameter above which the island nucleation is expected from the model of Glas and Daudin [62] is beneath 40 nm, for nucleation at 760 ℃ on an atomically flat top facet. This value is already lower than the 60 nm reported as a lower bound for the critical diameter, in the case of nucleation at 840 ℃, on a rough AlN top facet. Such discrepancy highlights the significant contribution of surface and interface energies, compared to elastic strain energy, in the nucleation process.

At last, although the GaN has been re-grown thinner for #G3, the AlN capping is observed not to be fully smooth.

5.4.2 Nucleation dependence on III-V ratio

In sample #H[14], a stack of QDs has been grown with different III-V ratio on enlarged AlN NWs and their nucleation has been *in situ* monitored by RHEED, thanks to the absence of tilt dispersion within the NW assembly.

Growth The growth route is similar to that followed for sample #G concerning the GaN base, the enlarged GaN and the AlN base. Next, four GaN QDs planes have been grown at 780 ℃ for 40 s with increasing III/V ratio: 1, 1.2, 1.6 and 1.7 respectively, and with a constant N flux of $\sim$ 0.23 $ML_{GaN}.s^{-1}$. They are respectively labeled #H1, #H2, #H3 and #H4. The AlN spacers[15] between the QDs planes are respectively on the order of 37, 26, 20 and 147 nm. Note that the last QDs plane has not been capped.

SEM images of the sample are given in Figure 5.28. It shows that NWs are almost coalesced, implying a large dispersion in the NW top diameter, from 70 to 300 nm. In addition, the top GaN QDs are nicely visible.

Reflection high energy electron diffraction analysis In Figure 5.29, the typical RHEED images of the NW assembly before, during and after GaN QDs nucleation are given. Prior to GaN growth, the RHEED image displays rods and Bragg spots, which are typical for large AlN NWs with a flat top facet[16]. Next, during the GaN deposition, extra Bragg spots are observed to pop after a certain delay in addition to AlN Bragg spots. Those spots are attributed to the GaN QDs nucleation.

A systematic monitoring of the RHEED Bragg spots associated to GaN QDs have been done for the four planes of grown QDs, by recording their intensity and in-plane

[14] sample N2184

[15] measured thanks to SEM side view images of cleaved NWs at the substrate edge

[16] indeed, at a μm scale, the assembly of NWs constitutes a rough film accounting for the observed Bragg spots, but at the nm scale NWs can exhibit atomically flat facets leading to the observed RHEED rods.

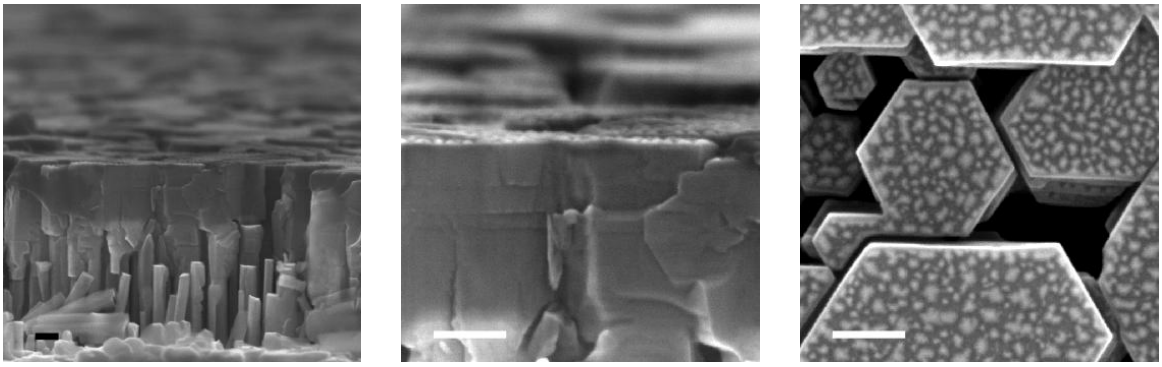

(a) side view (b) side view (c) top view

Figure 5.28: SEM images of sample #H – scale bar: 100 nm

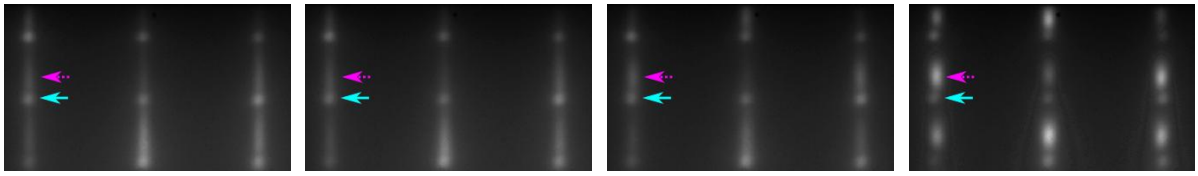

(a) 0 ML_{GaN} (b) 2 ML_{GaN} (c) 5 ML_{GaN} (d) 14 ML_{GaN} (end of growth)

Figure 5.29: RHEED images of the QDs nucleation for #H4 – the amount of grown GaN is deduced considering an N limited growth regime – blue plain (red dotted) arrows point toward the expected position for an AlN (GaN) Bragg spot

position. From the latter, using the AlN rods as a reference for relaxed AlN, the in-plane state of the grown GaN could be estimated. Data are reported in Figure 5.30.

For #H1, there is no large increase of the GaN related RHEED dots, neither a clear shift of the strain state. Therefore, it is deduced that the deposited GaN has either grown in a "2D" mode or not nucleated at all. In contrast, for #H2, #H3 and #H4, a large increase of the GaN Bragg spots is observed after a certain delay, in an almost close correlation with the in-plane relaxation of the GaN, which evidences a "3D" growth mode. One can notice that the nominal conditions are heavily Ga-rich, which, according to the case of 2D layers [224], should have hampered the formation of dots for #H3 and #H4 during the GaN growth step. At last, the strain state of the fully formed QDs is $\sim 1\%$, which is in agreement with the report of Daudin *et al.* [107] for SK QDs grown on 2D AlN.

Considering a N-limited regime, GaN QDs nucleation has occurred in #H3 and #H4 after the nominal growth of respectively 3.5 and 4.6 ML_{GaN}, whereas in the case of #H1, the nominal growth of 9.2 ML_{GaN} has been unable to trigger the "3D" growth mode. Two reasons could be invoked in order to account for this observation:

- there is a significant incubation time for GaN nucleation on top of the AlN NW

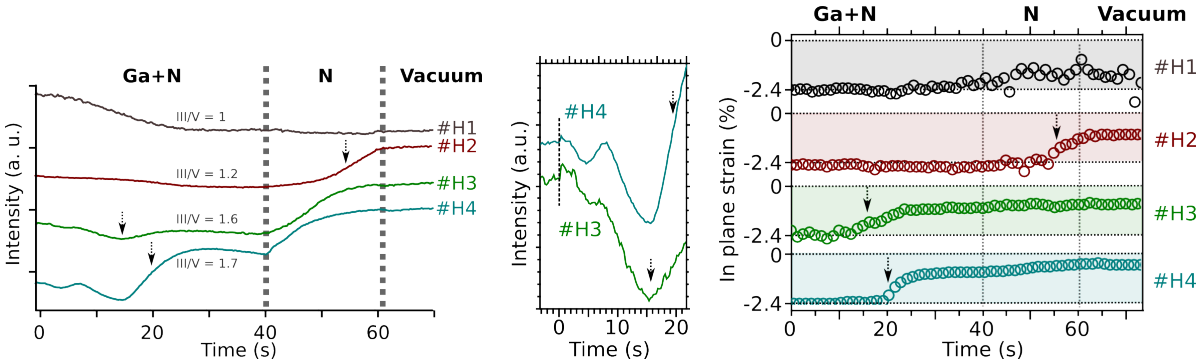

(a) Intensity of GaN QDs related signal on the RHEED image – N-flux: 0.23 $ML_{GaN}.s^{-1}$

(b) Zoom from left plot

(c) In-plane strain of GaN QDs – GaN is assumed fully strained on the AlN at $t = 0$ s, *i.e.* $(a - a_0)/a_0 = -2.4\%$, with a_0 the relaxed in-plane lattice parameter of GaN

Figure 5.30: RHEED monitoring of the GaN QDs nucleation on AlN NWs – sample #H – dark dotted arrows indicate the time when the GaN Bragg spot relaxation is occurring

top facet. Indeed, the latter is expected to be atomically flat and free of extrinsic defects, hence free of favorable adsorption sites for Ga adatoms and free of favorable nucleation sites for GaN [214].

- the NW side facets are initially free of adatoms, hence a fraction of the Ga adatoms deposited on the top facet are diffusing toward the side facets. In other words, Ga adatoms are initially wetting the sample surface. This transient phenomenon can induce a temporary decrease of the effective III/V ratio on the NW top facet, resulting in a drop of the growth speed and an increase of the incubation time.

If the QDs are nucleating along a SK growth mode, the observation of RHEED oscillations during the wetting layer growth could provide a direct measurement of the effective growth speed. Such measurement would be of great help in order to further discuss the previous hypothesis. Actually, as detailed in Figure 5.30b, oscillations of the GaN Bragg spots intensity are observed prior to the islanding of GaN for #H3 and #H4. Assuming that they are related to the growth of a wetting layer, it would indicate a growth speed of ~ 0.1 $ML_{GaN}.s^{-1}$ with a wetting layer thickness of $1 \sim 2$ ML_{GaN}, in rather good agreement with the case of GaN SK QDs nucleation on AlN 2D layer [107, 230].

Nevertheless, further experiments are needed in order to confirm those preliminary results.

5.4.3 Quantum dots geometry and spatial distribution

The former RHEED analysis of GaN QDs nucleation on top of the AlN NWs has emphasized a significant in-plane relaxation of the GaN once dots are formed. By comparison to the 2D case, it questions whether ripening of the QDs occurred or not.

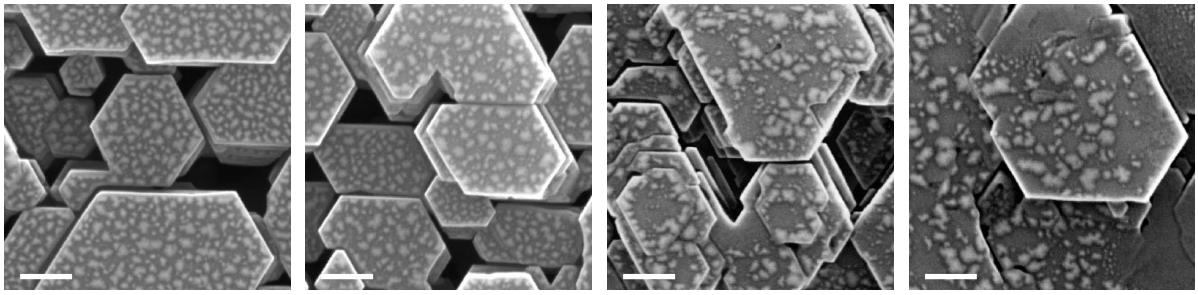

(a) $r = 0$ mm (b) $r = 10$ mm (c) $r = 20$ mm (d) $r = 24$ mm

Figure 5.31: SEM images of #H4 QDs acquired at a parametric distance r from the substrate center – scale bar: 100 nm

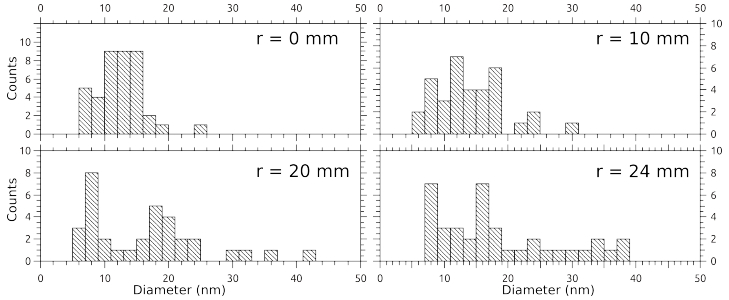

Figure 5.32: Diameter distribution of the QDs #H4, as function of the distance r from the substrate center – the QD diameter has been inferred by measuring the QD area and then by assuming it circular

Low growth temperature Taking advantage of the last plane of QDs, #H4, which has not been capped, a structural investigation by SEM has been performed on such QDs nucleated at 760 °C. SEM images acquired along a radius of the substrate are shown in Figure 5.31 and the related distribution of QDs diameter extracted from the SEM images is plotted in Figure 5.32.

QDs grown in the center of the substrate exhibit an homogeneous distribution and a small diameter dispersion: $5 \sim 20$ nm. In contrast, an inhomogeneous distribution of QDs is observed at the edge of the substrate, correlated with a larger diameter dispersion: $7 \sim 40$ nm. It highlights an enhanced ripening of the QDs on the substrate edge, where the growth temperature was the lower, which is very puzzling at that time.

High growth temperature In order to observe the influence of temperature over the geometry of GaN SK QDs on top of AlN NWs, another sample, labeled #I[17] has been grown. The growth was similar to that of samples #G and #H concerning the GaN base, the enlarged GaN and the AlN base. The obtained diameters for the AlN NW top facets were ranging between 50 and 200 nm. GaN SK QDs were nucleated at 840 °C, for 40 s and with a III/V ratio of 1.7 (with an N flux of 0.23 $ML_{GaN}.s^{-1}$), followed by an

[17] N2215

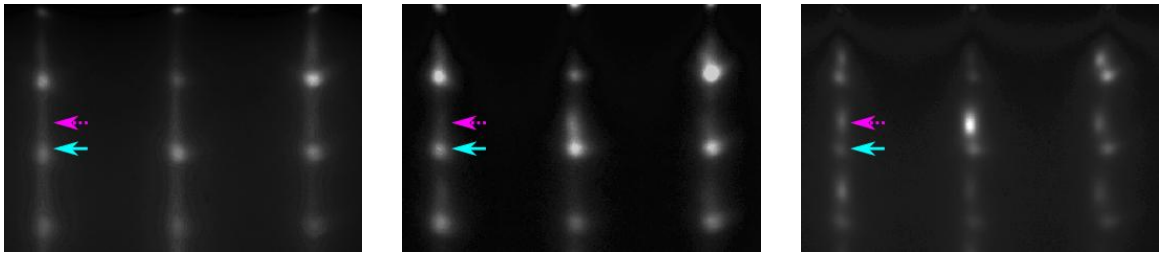

(a) AlN NWs – substrate center (b) GaN QDs – substrate center (c) GaN QDs – substrate edge

Figure 5.33: RHEED images of sample #I before and after GaN QDs nucleation – the RHEED spot can be moved on the substrate surface to probe predominantly the center or the edge – blue plain (red dotted) arrows point toward the expected position for an AlN (GaN) Bragg spot

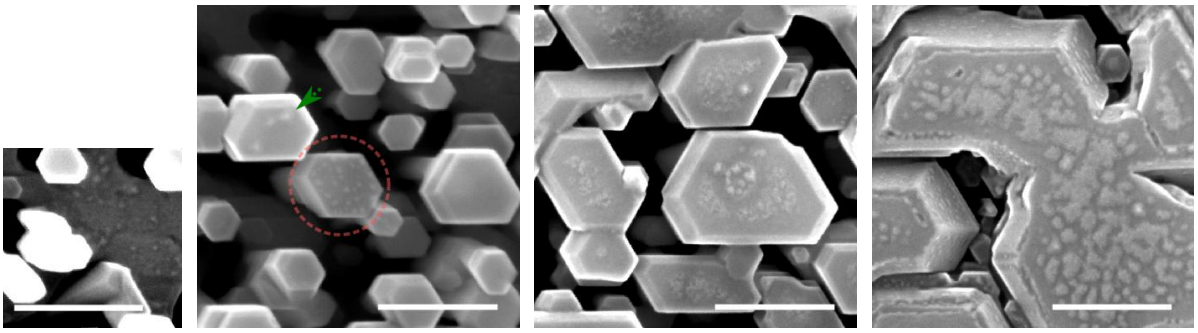

(a) $r = 0$ mm (zoom) (b) $r = 0$ mm (c) $r = 15$ mm (d) $r = 20$ mm

Figure 5.34: SEM top view image of the sample #I – images have been acquired at a parametric distance r from the substrate center– scale bar: 200 nm

exposure of 20 s under the N flux only. Therefore, apart the growth temperature, QDs have been grown in the exact same conditions than #H4.

The RHEED images of the sample after the QDs growth and acquired on the substrate center and periphery are shown in Figure 5.33. It emphasizes the absence of Bragg spots related to the GaN QDs in the substrate center[18], suggesting the absence of QDs nucleation.

A structural investigation of the grown GaN QDs has been done by SEM. Obtained pictures acquired at several locations of the sample are shown in Figure 5.34. In the substrate center (inset 5.34b), the majority of the NWs exhibit a top facet appearing very flat, hence free of GaN QDs, in agreement with the RHEED observation. However, for a minority of NWs (less than 1%), two specific features could be observed: (1) large pyramids (pointed by the dotted arrow) similar to the case of pyramidal QDisks, which

[18]the faint dots visible above the AlN Bragg spots are attributed to the GaN QDs localized on the substrate edge. Indeed, due to the grazing incidence of the electrons, it is difficult to shine only NWs in the substrate center

suggests that they are an AlN singularity rather than a GaN island and (2) assemblies of small pyramids, which are tentatively assessed as GaN QDs. The zoom of inset 5.34a reveals the existence of similar QDs all over the 2D layer in between the NWs. If moving along a substrate radius, the ratio of NWs hosting GaN QDs is rising from less than 1% to 100% while getting from $r = 13$ mm to $r = 20$ mm, with an observed preferential nucleation on NWs having a large diameter. AlN pyramids are still observed on a few NWs and, for $r = 20$ mm, QDs are even observed on the NW side facets.

The quasi-systematic absence of GaN QDs on top of NWs localized in the substrate center, whereas QDs are observed on the 2D layer, is remarkable and is attributed once again to a significant incubation time. The reasons would be the high temperature coupled to the atomically flat top facets, which would both enhance the adatom desorption and/or diffusion on the side facets. Surprisingly, close to the edge of the substrate, the GaN QDs nucleation is observed to favorably occurs in the center of the NW top facet rather than in the edges, which is in contrast to former observations on #H4.

Those preliminary results are still puzzling but already emphasize a strong temperature dependence of GaN nucleation on top of AlN NWs. The invoked reasons are the existence of an incubation time and the possible diffusion of adatoms toward the NW side facets.

5.4.4 Optical properties

Most of the samples grown for this study have been dedicated to the understanding of the QDs growth mode so that little optimization has been achieved for optical studies. Therefore, the results shown here are preliminary only and are tentatively displayed as a proof of concept.

Growth The main drawback of the NW enlargement process is the quasi systematic coalescence of the NW assembly, which would prevent the mechanical dispersion of NWs allowing to probe them by μ-PL one by one. Hence, a dedicated sample, labeled #J[19], has been grown along a growth route similar to the one used for the previous samples as concerns the GaN base, the GaN enlarged and the AlN base, except that the two last steps have been limited to 45 min instead of 1 h to reduce the extent of the enlargement. As shown in the SEM side view of the sample, displayed in Figure 5.35, it succeeds to prevent the NW coalescence, although the NW diameter range between 60 $\sim$ 120 nm. Next, 4 planes of GaN QDs have been grown on top of the AlN NW, with nominal thicknesses of, respectively 21, 18, 7 and 7 ML_{GaN}.

As shown in Figure 5.36, a structural investigation by STEM has confirmed the growth of QDs in the NWs. In order to probe the luminescence signal stemming from those QDs, PL spectra have been acquired on the as-grown NWs from 7 K to RT (see Figure 5.37). In the substrate edge, the large band at 2.4 eV whose intensity is only divided by $\sim$ 3 between 7 K and RT is attributed to the luminescence of a plane of

[19] N2191

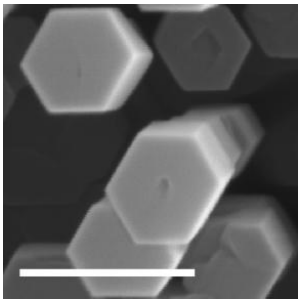

(a) Top view

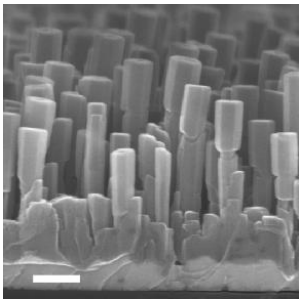

(b) Side view

Figure 5.35: SEM view of sample #J – scale bar: 200 nm

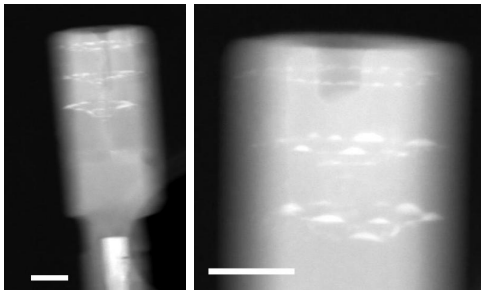

(a) (b)

Figure 5.36: STEM imaging of single NWs of sample #J – acceleration voltage: 200 kV, scale bar: 50 nm

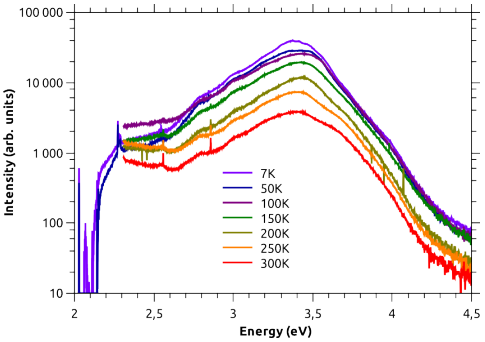

(a) Substrate center – excitation density: 100 μW

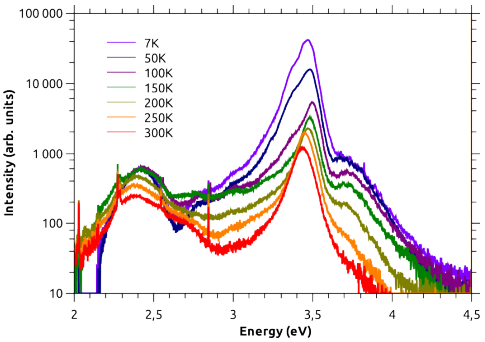

(b) Substrate edge – excitation density: 50 μW

Figure 5.37: PL spectra acquired on $\sim 10^7$ as-grown NWs of sample #J

GaN QDs. It suggests a significant *e-h* pair confinement up to RT. Other bands are also visible in the substrate center and edge, but their intensity seems to significantly drop with temperature, suggesting the presence of non-radiative recombination channels.

Those measurements are preliminary and further investigation would be needed, especially on single NWs, to confirm the efficient confinement potential of those GaN QDs up to RT.

5.4.5 Conclusion

In this study, the ability to grow GaN QDs on top of enlarged AlN NWs has been clearly demonstrated. From the structural point of view, those QDs exhibit very similar properties than the 2D GaN SK QDs, although their size and spatial distribution are not yet clearly correlated to the growth conditions. It has been tentatively attributed to the specificities of the NWs: (1) an atomically smooth top facet without extrinsic defects, (2) the presence of side facets toward which diffusion of adatoms might occurs and (3)

an enhanced strain relaxation through the elastic deformation of the free surfaces. Noticeably, the existence of a significant incubation time for GaN on AlN NWs is required to explain the observed low growth speed and further corroborate the observations concerning QDisks growth. At last, the preliminary PL study is giving encouraging results although further investigation would be need for more reliable conclusions.

5.5 General conclusion

In this Chapter, the growth of GaN/AlN quantum heterostructures in NWs has been investigated.

First, GaN QDisks were in the focus, with thorough structural and optical characterizations at the scale of the single NWs. It has shown that QDisks could be considered as small QWs with a large built-in electric field, resulting in luminescence energies closely related to their thicknesses. Therefore, due to the technical difficulty to synthesize exactly similar QDisk between NWs of the same assembly, a large dispersion in their optical properties is usually obtained. The dominance of non-radiative recombination channels at RT has been also reported.

Taking advantage of the "2D" growth mode of GaN QDisks, heterostructures such as pyramidal QDisks have been synthesized. It has allowed to explore the luminescence dependence of small QWs as function of their polar orientations and thicknesses, all in the same NW. However, such heterostructure is not well controlled, especially because the AlN pyramid is expected to stem from the presence of an ID, whose nucleation is not yet mastered. Hence, it prevents a reliable use of pyramidal QDisks.

Finally, the growth of the AlN NWs has been tuned so that large and atomically smooth top facets could be obtained. It has allowed to explore novel growth conditions, resulting in a switch of the GaN growth mode on top of the NWs from “2D” to “3D”. It paves the way for the growth of a new type of heterostructure by PA-MBE, possibly coupling the versatility of the NWs with the robustness of the GaN SK QDs.

Chapter 6

Charge carriers diffusion in nitride nanowires

This chapter focuses on the measurement of charge carriers diffusion length, with the purpose of unveiling the electronic potential landscape of nitride nanowires (NWs). Taking advantage of the quasi-cylindrical symmetry of the NWs, diffusion equations could be scaled down to a one dimensional problem, which eased their solving. In addition, the small diameter of NWs allows to generate charge carriers in a tiny volume using electron-beam excitation, thereby, observations of diffusion lengths as small as 15 nm could be performed.
Diffusion lengths of electron-hole pairs in GaN NWs have been extracted by taking advantage of the presence of I_1 basal stacking faults (SFs). The measured small diffusion lengths compared to the thin film case and its variability between and within NWs has been attributed to the presence of non-radiative centers and to a dependence on the NWs chemical environment.
Diffusion of charge carriers in AlN NWs has been probed with the help of a GaN quantum disk (QDisk). A strong asymmetry of the cathodoluminescence (CL) signal stemming from the GaN QDisk has been observed whether generating charge carriers above or below the disk, which has been related to the existence of large built-in electric fields in the vicinity of the QDisk. In addition, it has highlighted a dependence of charge carriers diffusion on the polarity of the heterostructure.
The knowledge of the diffusion lengths of charge carriers is a key parameter, which can be use to discuss and improve our understanding of the optoelectronic properties of nitride NWs.

Contents

Experimental data credits

In the first section of this chapter, scanning transmission electron microscopy (STEM) images have been acquired by Martien Den Hertog and cathodo-luminescence (CL) data by Gilles Nogues (Néel Institute, Grenoble, France). Both have also prepared the substrates used for nanowire (NW) dispersion. In the second section of this chapter, coupled STEM and CL images have been acquired by Sophie Meuret, Luiz Tizei and Mathieu Kociak, working at the LPS (Orsay, France).

Related publications

Most of the work presented in the first part of the chapter has been published by Nogues *et al.* [231]. Most of the work presented in the second part of the work has been published by Tizei *et al.* [232].

6.1 Issues at stake

Accessing the diffusion length of charge carriers allows to get an insight into the electronic potential landscape of a material. For instance, the surprisingly large internal quantum efficiency (IQE) of InGaN QWs, considering the high density of surrounding extended defects, has been partly attributed to internal disorder [233, 234] and quantum well (QW) thickness fluctuations [235], which correlates with the rather small diffusion lengths of carriers measured even up to room temperature (RT) in this system [236, 237]. In addition, the measurement of the diffusion length of carriers can be used to hint the presence of non-radiative defects such as dislocations [238, 236] or surface defects in NWs [239].

Thanks to their large aspect ratio and constant diameter, NWs are a convenient system in order to scale down diffusion equations to only one dimension. Therefore, NWs have been already used to measure diffusion length of charge carriers [240, 239, 241, 242], but also of adatoms on their side facets [243, 84].

In a basic scheme, a diffusion experiment requires the existence of particle source and sink spatially separated each other by a parametric distance. Charge carriers diffusion experiments in NWs are greatly eased by the ability to generate charge carriers on demand and with a spatial resolution down to ~ 1 nm, if performing electron beam (e-beam) excitation in a STEM setup for instance. The diffusion and relaxation of charge carriers in sinks can be next probed by monitoring radiative recombinations in the sink, which corresponds to the regular use of a CL setup.

In this chapter, the focus is brought on the diffusion of charge carriers generated by electron beams in GaN and AlN NWs. Two types of sinks are used: an I_1 basal stacking fault (SF) in GaN NWs[1] and a GaN quantum disk (QDisk) in AlN NWs[2]. The

[1] see Figure 1.5, page 17 in the chapter 1 for the atomic configuration of this defect
[2] see the chapter 5 for growth details

extracted diffusion length will be used to establish the presence of non-radiative channels and built-in electric fields.

6.2 Basic principle

6.2.1 Charge carriers generation - the source

The following experiments are carried on in CL setups, meaning that the charge carriers are locally generated by focusing an e-beam on a NW. The spatial resolution of the excitation is directly dependent on the interaction volume of the electrons going through the NW, which depends, for a given NW, on the e-beam size and on the impinging electron energy. Two types of e-beam have been used in those experiments:

- a FEI scanning electron microscopy (SEM) beam, operated between 5 and 25 kV with a $\sim$ 30 pA current. It will be observed to generate charge carriers with a maximal spatial resolution of $\sim$ 30 nm. The setup can be cooled down to 5 K and a secondary electron detector allows structural imaging.

- a VG HB 501 SEM beam, operated at 60 kV with a 50 pA current. It has a maximum spatial resolution of 1 nm. The setup can be cooled down to 150 K and a STEM detector allows a precise structural imaging.

Despite the use of different apparatus for the experiments, the mechanisms leading to the carrier generation should be similar and have been outlined by Meuret *et al.* [61]. These authors have inferred the following steps in the excitation process[3]:

1. the creation of few bulk plasmons for electrons crossing the material. Each plasmon has a high energy (several tenth of eV) and decays in few femto seconds into *e-h* pairs.

2. the diffusion of the *e-h* pairs into the material

3. the recombination of *e-h* pairs. In case of radiative recombination, a part of the generated photons can be collected and contributes to the CL signal

A noticeable point in their mechanism is the demonstration that one impinging electron can generate more than one *e-h* pair through the decay of the bulk plasmon, thereby, accounting for a possible photon bunching in a low excitation regime. It is in contrast to regular photoluminescence (PL) experiments for which each absorbed photon generates a single *e-h* pair with an energy slightly above the material band gap, which usually prevents its decay into more than one *e-h* pair.

At last, built-in electric fields and phonon interaction might break the diffusing *e-h* pair into a free electron and a free hole [244]. It means that the diffusing flux of charge

[3] their conclusions are based on the observation of a photon bunching by low current CL excitation of NV centers in diamond crystallites

carriers contributing to the CL signal can include either *e-h* pairs or free holes/electrons. In the latter case, the particles have a non-zero electrical charge, meaning that a drift contribution due to built-in electric fields should be added to the diffusion process.

6.2.2 Charge carriers relaxation - the sink

Once a charge carrier has reached a sink, its relaxation will be either radiative or non-radiative.

In the case of a radiative recombination, the gain in the emitted light intensity while approaching the charge carriers source to the sink is directly related to the amount of charge carriers effectively reaching the sink by diffusion and/or drift. A proportionality should be obtained for steady state measurements and in the absence of saturation, *i.e.* for low excitation densities. In addition, energy filtering of the emitted light can be used to selectively probe radiative centers in case several are in competition, which increases the practicality of the technique. In this study, two types of radiative recombination centers have been used:

- I_1 basal SFs in GaN NWs
- GaN QDisks in AlN NWs

In the case of a non-radiative recombination, the loss in the emitted light intensity while approaching the charge carriers source to the sink is directly related to the amount of charge carriers effectively reaching the sink by diffusion and/or drift. This scheme has been noticeably used to infer the diffusion length of *e-h* pairs in GaN thick films, in the vicinity of dislocations acting as non-radiative centers [238].

6.3 Diffusion in GaN nanowires

I_1 basal SFs have been used as a charge carrier sink, in order to probe their diffusion along GaN NWs *c* axis. The advantage of such defect is the absence of strain due to its incorporation, its planar geometry crossing the whole NW section and an intense sub-band gap luminescence at 3.42 eV [245, 92].

6.3.1 Growth

An assembly of GaN NWs[4] has been grown on Si, using an Al-first AlN buffer, a III/V ratio of 0.3 and $T_{substrate} = 840$ °C. The growth was 18 hours long so that NWs 3.2 μm long with a $\sim$ 110 nm diameter were obtained. A side view SEM picture is shown in Figure 6.1.

A peculiarity of the NWs is that each will be observed to host between 0 and 4 I_1 basal SFs. As detailed farther, SFs can be precisely localized within the NWs thanks to their CL signature. Hence, the distance between successive SFs within a NW and the

[4] sample N1954

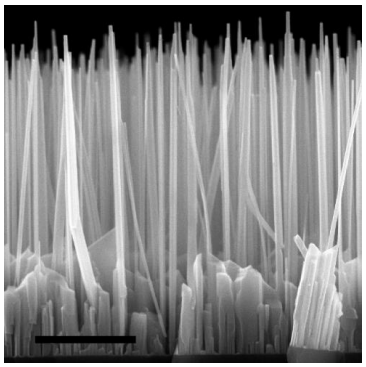

Figure 6.1: NW assembly SEM side view – scale bar: 1 μm

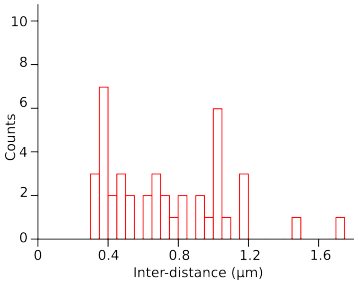

(a) Distribution of the distance between successive SFs in a NW

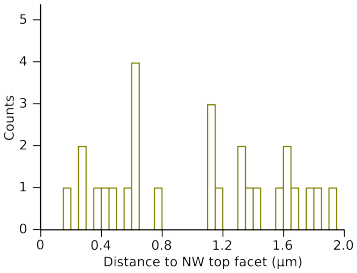

(b) Distribution of the extracted distances between SFs and NWs top facet

Figure 6.2: Distribution of the SFs inter distance and distance to NW top facet

distance between a SF and the NW top facet have been both measured on several NWs belonging to the same sample. Those distances are reported in Figure 6.2 and exhibit a rather flat distribution. Assuming a similar growth speed for all the NWs, it means that SFs growth is not correlated between NWs, *i.e.* not induced by a specific event that occurred in the molecular beam epitaxy (MBE) chamber.

Nevertheless, the large distance between successive SFs is adequate to observe by CL the diffusion of charge carriers.

6.3.2 Cathodoluminescence signature

In order to observe single NWs by CL, GaN NWs have been mechanically[5] dispersed on a Si substrate. Prior to the dispersion, the Si substrate has been patterned by standard lithography techniques to create markers allowing to retrieve the same NWs between experiments. In addition, a 100 nm thick Al film has been sputtered on its surface, followed by a 20 nm thick SiO_2 film. Those films are expected to reflect upward the light emitted by the NW in the direction of the substrate, in order to enhance the collection efficiency of the CL setup.

CL spectra acquired on single NWs at 5 K, with the FEI microscope are shown in Figure 6.3.

It exhibits similar features than the μ-PL spectra on single NWs:

- a peak at 3.48 eV attributed to exciton bound to donors (D^oX)
- a peak at 3.42 eV, whose intensity is spatially localized (SFX)
- a peak at 3.28 eV with replica at lower energies, attributed to donor-acceptor pair (DAP) recombinations, with phonon replica (DAP)

[5]NWs have been first transfered to a "clean-room" paper by scratching it on the sample surface and then transfered to the Si substrate by scratching the "clean-room" paper on its surface

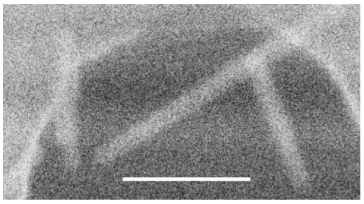

(a) SEM view of dispersed NWs – scale bar: 500 nm

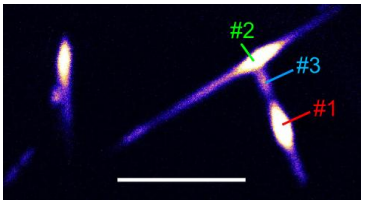

(b) CL intensity map, filtered between 3.40 and 3.50 eV – scale bar: 500 nm

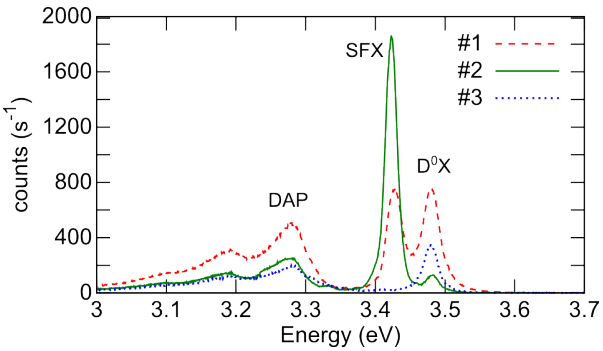

(c) CL spectra of the spots #1 to #3

Figure 6.3: CL spectra acquired at 5 K on dispersed NWs

The DAP CL intensity is rather homogeneous over the length and diameter of the NWs, suggesting an homogeneous distribution of dopants[6]. By contrast, the 3.42 eV CL is very localized, stemming from point like areas. In order to assess the origin of this CL signal, NWs from the same sample have been mechanically dispersed on a SiN grid[7] allowing to perform successive CL and STEM characterization of the same NW. A typical example is shown in Figure 6.4.

An I_1 basal SF has been systematically observed by STEM whenever the 3.42 eV CL signal is reaching a maximum, thereby, this signal is attributed to the recombination of an exciton bound to a SF (SFX), which was already expected from previous reports [245, 92].

For two typical NWs, the intensities of the D^oX and SFX CL signals, averaged along the NW radius, are plotted versus the coordinates of the NW along its length in Figure 6.5.

Although the atomic thickness of a SF along the NW length is about a few Å[8] and the exciton Bohr radius is lower than 3 nm [247][9], a non-negligible CL signal at 3.42 eV is still observed while focusing the e-beam a few tenth of nm away from a SF. It is attributed both to the large excitation volume of the e-beam and to the effective

[6]Those dopants have been non-intentionally incorporated during the growth and likely stems from residual pollution in the MBE chamber (0_2, CO_2, H_2O, organic compounds, etc). Such residues used to be present in the MBE chamber within the few weeks following a maintenance for which pumping of the chamber has been stopped.

[7]a description of the grid can be found in the chapter 4, page 120 – NW dispersion on such grid has been done by mechanical friction between the grid and the substrate with as-grown NWs

[8]from the electronic point of view, the thickness of an I_1 basal SF has been estimated to be 0.85 ML_{GaN} [246]

[9]only excitons are considered here as charge carriers

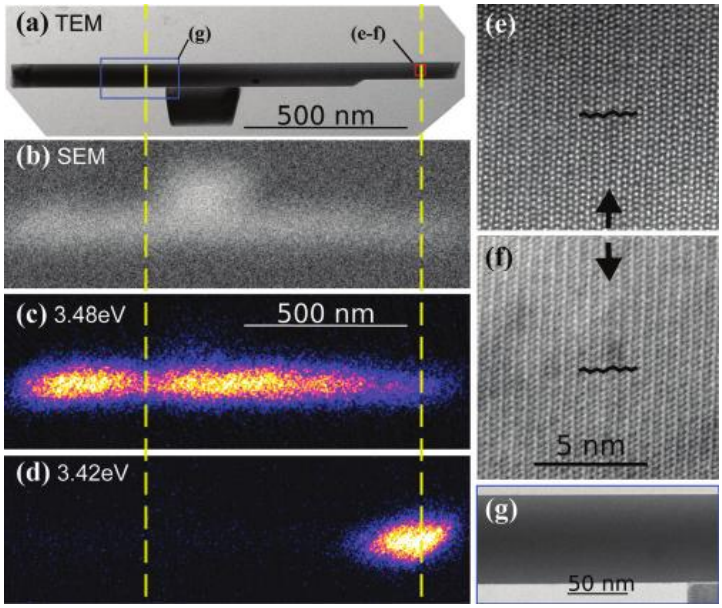

Figure 6.4: Correlated (a, e-g) STEM, (b) SEM and (c-d) CL characterization on the same NW. (c-d) are CL intensity map filtered at, respectively, 3.48 (D^oX) and 3.42 eV (SFX). (e-f) are, respectively, high angle annular dark field (HAADF) and annular bright field (ABF) images in the [11$\bar{2}$0] zone axis of a SF located where the 3.42 eV CL signal reaches it maximum. (g) is a large HAADF view of the area where the CL signal at 3.48 eV exhibits a minimum (the left one)

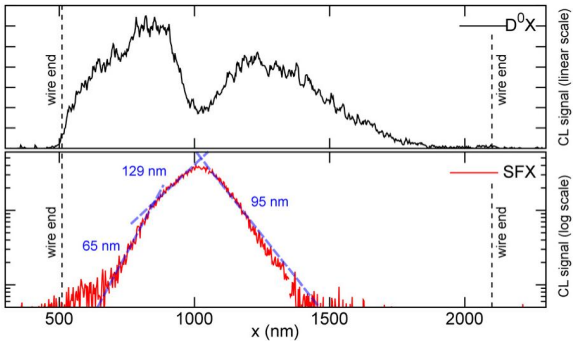

(a) NW #A

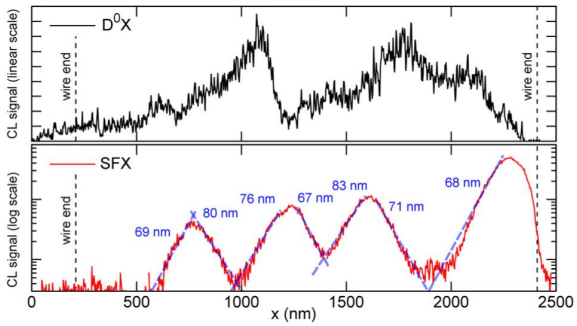

(b) NW #B

Figure 6.5: Plot of the D^oX and SFX CL signal acquired at 5 K along the NW axis – a log scale is used for the SFX signal – the dashed lines emphasize the exponential decay of the SFX signal apart each SFs.

collection of charge carriers diffusing toward the SF plane. More precisely, the intensity profile of the SFX signal on both side of the SF is observed to exhibit an exponentially modified Gaussian like shape, *i.e.* the convolution of a Gaussian by an exponential decay. Hence, the Gaussian contribution is attributed to the e-beam excitation profile, which is characterized by its full width half maximum (FWHM), w, and the exponential decay is attributed to the diffusion of the charge carriers toward the SF, which is characterized by a diffusion length, L. As the experiment is performed at 5 K, and assuming an absence of strong built-in electric fields, the charge carriers diffusion toward the SF will be considered as excitons only, meaning that L corresponds to an ambipolar diffusion length.

w and L values have been extracted from CL profiles acquired on various SFs, belonging to different NWs and with different acceleration voltages. Data are recorded in

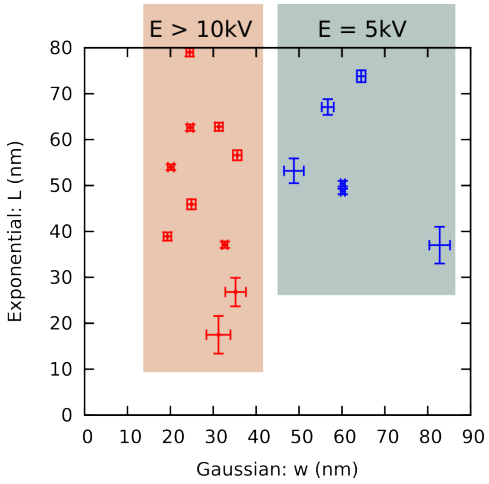

Figure 6.6: Gaussian width and exponential characteristic length extracted on different NWs and for different acceleration voltage, labeled $E - E > 10$ V for red crosses and $E = 5$ kV for blue crosses

Figure 6.6.

The width, w, of the e-beam excitation area is ~ 30 nm independently of the probed NWs but noticeably degrades to 60 nm if the acceleration voltage is lowered down to 5 kV. It is assigned to the scattering of the impinging electrons toward larger angles when the impinging electron velocity is decreased, *i.e.* the overlap between the NW and the electronic interaction peer is increased. Hence, the acceleration voltage has been usually set to 10 kV, which provides a maximum spatial resolution and minimizes the apparent aging of the NWs, *i.e.* a loss of the CL intensity through time[10].

The extracted diffusion lengths, L, are ranging from 20 to 80 nm. In addition, the asymmetric CL signal around a SF is remarkable. It emphasizes different diffusion lengths whether the *e-h* pair was coming from one side or the other of a same SF (see Figure 6.5).

In addition, in Figure 6.5, the intensity maxima of the SFX CL signal are observed to be systematically correlated to local minima of the D^oX luminescence. It is attributed to the preferential relaxation of the *e-h* pairs into the SF rather than in neutral donors. Such anticorrelation has not been observed by the CL study of Corfdir *et al.* [17] on SFs, however, the geometry of their experiment suggests that more than one NW could be probed at the same time with their e-beam. At last, the D^oX CL is also observed to be quenched in random point-like areas free of SFs (see Figure 6.4), and sometimes in the vicinity of the NW boundary (see the two NWs of Figure 6.5). It suggests the existence of non-radiative defects, that thorough STEM observations were unable to resolved.

***e-h* pair diffusion toward the stacking faults** The extracted average diffusion length of *e-h* pairs (~ 70 nm) in NWs is smaller than values reported in GaN thin films (80 nm [248] and 200 nm [238]) and also in NWs made of other III/V materials such as InP NWs (500 nm [241]) or GaAs/AlGaAs cores/shell NWs (700 nm [239]).

It suggests the existence of surface states on NW side facets acting as non-radiative recombination channels, *i.e.* bringing an additional competing sink for *e-h* pairs. Such

[10]likely stemming from carbon deposition due to the decomposition of surrounding organic compounds

defects have been already hinted in GaAs NWs, where the *e-h* pair diffusion length has been reported to be divided by 7 if the NW surface is not passivated by an AlGaAs shell [239], or in MgZnO NWs, where a dependence of the *e-h* pair diffusion length to the NW diameter has been reported [240], both at 10 K.

In the case of PA-MBE GaN NWs, the existence of surface defects has been demonstrated as well by time resolved photoluminescence (TR-PL) experiments, which have exhibited a decrease of the D^oX lifetime for NWs with smaller diameters [203].

In order to better estimate the contribution of surface states over the diffusion of *e-h* pairs, a diffusion model is proposed. The radial symmetry of the NW in the vicinity of the SFs allows to scale down the diffusion to one dimension, *i.e.* along the NW axis. In the model, the diffusing *e-h* pairs are assumed to be free excitons (FX), which have a probability to relax in any of the following recombination channels: neutral donors, DAP, SFs and surface states. Hence, one can define $n_{FX}(x,t)$ (respectively $n_{D^oX}(x,t)$, $n_{DAP}(x,t)$ and $n_{SFX}(x,t)$) the linear density of FX (respectively neutral donor, DAP and SF bound excitons) between x and $x+dx$, which are coordinates along the NW axis.

At (t,x), neglecting other non-radiative centers than the NW surface, one has:

$$\begin{aligned}\frac{\partial n_{FX}}{\partial t} = D\frac{\partial^2 n_{FX}}{\partial x^2} + p(x) - \left(\frac{1}{\tau_{r,FX}} + \frac{4s}{d}\right) n_{FX} \\ - \left[\frac{1}{\tau_{FX\to D^oX}} + \frac{1}{\tau_{FX\to DAP}} + \gamma_{FX\to SFX}(x)\right] n_{FX}\end{aligned} \tag{6.1}$$

where

- D is the diffusion coefficient of the FX along the axis of the NW.
- $p(x)$ the incoming flux of FX generated by the e-beam. As a first approximation, it will be considered point-like, meaning that when focusing the e-beam at $x = x_o$, one has $p(x) = p_o\delta(x - x_o)$.
- $\tau_{r,FX}$ is the radiative recombination lifetime of the FX.
- $4s/d$ is a first order expression to account for the capture rate of FX by non-radiative surface states on NW side facets. d is the NW diameter and s is the surface recombination velocity.
- $\tau_{FX\to D^oX}$ and $\tau_{FX\to DAP}$ are the decay times of the FX into, respectively, the neutral donors and the DAP.
- $\gamma_{FX\to SFX}$ is the trapping rate of the FX into the I_1 basal SF. This trapping rate is non-zero only in the vicinity of the SF.

In addition, neglecting detrapping processes of the FX bound to neutral donors, DAP or SFs, one should have:

$$\begin{aligned}\frac{\partial n_{D^oX}}{\partial t} &= \frac{n_{FX}}{\tau_{FX\rightarrow D^oX}} - \frac{n_{D^oX}}{\tau_{r,D^oX}} \\ \frac{\partial n_{DAP}}{\partial t} &= \frac{n_{FX}}{\tau_{FX\rightarrow DAP}} - \frac{n_{DAP}}{\tau_{r,DAP}} \\ \frac{\partial n_{SFX}}{\partial t} &= \gamma_{FX\rightarrow SFX} - \frac{n_{SFX}}{\tau_{r,SFX}}\end{aligned} \tag{6.2}$$

where τ_{r,D^oX}, $\tau_{r,DAP}$ and $\tau_{r,SFX}$ are the radiative lifetime of the FX bound to, respectively, the donors, the DAP and the SFs. It means that in the steady state regime, every FX captured by one of those defects will result in an emitted photon. One has to note that at 5 K, neglecting detrapping processes seems to be a crude approximation concerning the DoX as emphasized by its non-single exponential decay time reported in high quality bulk GaN [249], which has been attributed to an interplay between the D^oX and FX states [250]. By contrast, neglecting detrapping of excitons bound to DAP or basal SFs is rather safe, due to the large e-h pair binding energy for DAP [251] and a reported thermal escape for SFs in GaN NWs occurring only above 40 K [17].

If neglecting SFs, one has in the steady state regime:

$$n_{FX} = p_o e^{-|x-x_o|/\sqrt{D\tau_{eff}}} \tag{6.3}$$

with,

$$\frac{1}{\tau_{eff}} = \frac{1}{\tau_{r,FX}} + \frac{4s}{d} + \frac{1}{\tau_{FX\rightarrow D^oX}} + \frac{1}{\tau_{FX\rightarrow DAP}} \tag{6.4}$$

In order to discuss the relative amplitudes of each terms in the equation 6.4, one can use the TR-PL results acquired by Corfdir *et al.* [17] on a similar NW assembly. First, the PL band edge is observed to be dominated by the D^oX signal rather than the FX, suggesting that $\tau_{FX\rightarrow D^oX} \ll \tau_{r,FX}$, with $\tau_{r,FX}$ measured to be $\sim$ 200 ps. Hence, the radiative recombination of FX could be further neglected in equation 6.4. In addition, the authors have measured τ_{r,D^oX} of the order of 200 ps, which is well below the $\sim$ 1 ns measured for high quality bulk GaN [249], emphasizing the relaxation of FX into non-radiative channels, likely on the NW side facets. Different values for the surface recombination velocity have been reported for PA-MBE GaN NWs and cover 2 orders of magnitude ($s = 2 \times 10^2$ [17], 6×10^3 [252], 9×10^3 [203] and 2.7×10^4 cm.s^{-1} [253]). Considering that the extreme ones are indirect estimates, thereby, using $s = 9 \times 10^3$ cm.s^{-1}, one should have with $d = 110 \pm 10$ nm, $d/4s = 300$ ps. Hence, the carrier relaxation into surface states would have a similar probability than relaxation into the neutral donors.

If now considering a basal SF in the close vicinity, $\gamma_{FX\rightarrow SFX}$ would become prominent over $1/\tau_{FX\rightarrow D^oX}$, as revealed by the observed anti-correlated intensity of the SFX and D^oX CL signal. Hence, one can assume that every FX crossing the SF plane are captured by the defect and later radiatively recombine at 3.42 eV, as sketched in Figure

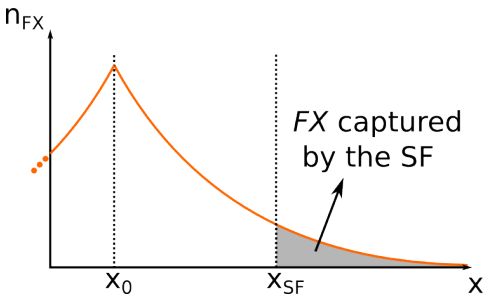

Figure 6.7: Sketch of the n_{FX} distribution along a NW length. In the case of the presence of a SF at the coordinate $x = x_{SF}$, the FX belonging to the gray area are assumed to be trapped by the SF.

6.7. Then, the intensity of the 3.42 eV signal, for a SF localized at $x = x_{SF}$ (with $x_{SF} > x_o$) is:

$$\begin{aligned} I_{3.42eV} &\propto \int_{x_{SF}}^{+\infty} p_0 e^{-(x-x_o)\sqrt{D\tau_{eff}}} \mathrm{d}x \\ &\propto \frac{p_0}{\sqrt{D\tau_{eff}}} e^{-(x_{SF}-x_o)\sqrt{D\tau_{eff}}} \end{aligned} \tag{6.5}$$

Hence, the L value, *i.e.* the charge carriers diffusion length extracted from the fit of the 3.42 eV CL profile (Figure 6.5), should be equal to:

$$L = \sqrt{D\tau_{eff}} \tag{6.6}$$

with τ_{eff} defined in equation 6.4. From this equation, the dependence between the trapping rate of the different recombination channels and the *e-h* pairs diffusion length is straightforward.

6.3.3 Diffusion length variability

Taking into consideration the former equations, one can discuss the origin in the variability of the measured diffusion lengths between NWs and within a single NW (cf Figure 6.6). Various contributions can be suggested: (1) different diameters, (2) fluctuations in neutral donor/acceptor density, (3) variation in surface recombination velocity, or (4) the presence of additional point-like non-radiative defects.

Dependence on the diameter According to the equations 6.6 and 6.4, the dependence of the charge carriers diffusion length (L) to the NW diameter (d) should be:

$$\frac{1}{L^2} = A + \frac{B}{d} \tag{6.7}$$

where A and B are constants. A plot of $1/L^2$ as function of $1/d$ is shown in Figure 6.8. The large uncertainty in the diameter measurement is due to the low resolution of the obtained SEM images. No affine dependence is observed, probably because (1) the explored range of diameter is too small, (2) NWs are not perfect cylinders, especially if coalescence events occurred during growth [254] and (3) the surface recombination s might not be constant. Nevertheless, dispersion in NW diameter cannot account by itself for the diffusion length variability.

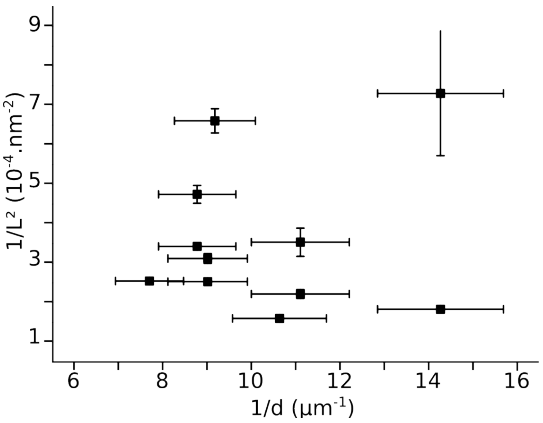

Figure 6.8: Plot of the $1/L^2$ versus $1/d$ with L, the charge carriers diffusion length and d the NW diameter

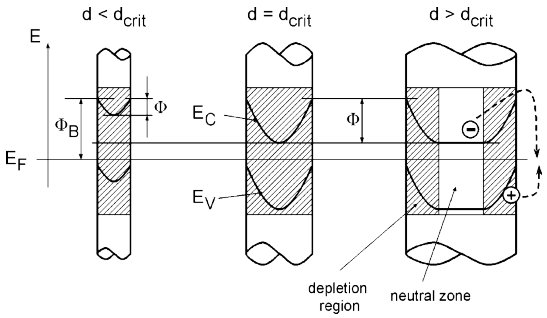

Figure 6.9: Sketch of the band bending presumed by Calarco *et al.* in GaN NWs as function of their diameter – from [255] – according to the authors, $d_{crit} = 2r_{depl} \simeq 100$ nm

Dependence on the doping level A dependence of the diffusion length with dopant density has been already reported in GaN films [238, 248]. Increasing the dopant concentration by $10 \sim 100$ leads to an average increase of the charge carriers diffusion length of only $10 \sim 20\%$[11]. Hence, in order to account for the different diffusion lengths measured in a single NW, a dopant concentration variation by, at least, one order of magnitude should be expected, which seems not reasonable. In addition, based on the observed large DAP signal, the estimated average density of non-intentional dopants incorporated in those NWs is not smaller than 10^{17} cm^{-3}, which corresponds to a linear density, along a NW length, higher than 1 dopant per nm. Such density is too large to be able to resolve by CL the individual contributions of each dopant. Hence, the variation in dopant density should not account for the observed large diffusion length dispersion.

Dependence on the surface states As sketched in Figure 6.9, Calarco *et al.* [255] have experimentally inferred the presence of an upward bending of the conduction band (CB) and valence band (VB) in the vicinity of the NW side facets, resulting from a surface pinning of the Fermi level. The expected consequences of this band bending are many fold:

- it locally ionizes donors, hence, generating a depleted volume penetrating the NW with a depth r_{depl} from the surface.

    1. according to Corfdir *et al.* [256], no luminescence related to the donors should be expected anymore from this depleted volume, as the binding of the FX on the ionized donors is not stable,

[11] one has to note that charge carriers diffusion lengths in GaN thin films used to be measured around threading dislocations (TDs). As segregation of impurities around TD is usually presumed, the dependence between the local dopant density and the applied extrinsic growth conditions might not be straightforward.

2. the ionization of donors in the depleted volume should alter the photo-conductivity of NWs [255, 97, 257].

- it repulses electron away from the surface but attract holes on the surface,
- above a certain value ($\sim 10^5$ V.cm^{-1} [244]), the band bending might ionize the FX, leading to the drift of the electrons in the NW core and the drift of the hole at the NW surface.

However, there are still uncertainties in the extent and amplitude of this band bending, especially due to its dependence on environmental factors. Textbook formula applied to a cylinder geometry would give a depleted volume depth [257]:

$$r_{depl} = \sqrt{\frac{16\epsilon\epsilon_0\Phi}{e^2 N_d}} \tag{6.8}$$

where Φ is the surface potential, ϵ_0 is the vacuum permittivity, ϵ is the relative permittivity, e the electron charge and N_d the doping density. If assuming a non-intentional doping of $10^{17} \sim 10^{18}$ cm^{-3} for the NWs under scrutiny and $0.3 < \Phi < 0.6$ eV, one has $r_{depl} = 50 \sim 200$ nm, which would agree with the $r_{depl} \simeq 50$ nm measured by Calarco *et al.* [255]. However, it would mean that NWs with a diameter lower than $d_{crit} = 2r_{depl} \simeq 100$ nm should be fully depleted, hence free of D^oX PL according to the proposition of Corfdir *et al.* [256], which does not fit the experiments. This incoherence might stem from the dependence of the Fermi level pinning position on the chemical environment of the surface. For instance, O_2 photo-desorption has been reported to drastically influence the NW photo-conductance [97, 257] so as its band-edge luminescence intensity [258, 204, 12]. Although the mechanism is not clear, it is generally accepted that the O_2 ionosorption leads to a decrease of the non-radiative lifetime of e-h pairs. However, such environmental dependence might be reduced thanks to surface passivation by SiO_2 or SiN [259], which, thereby, questions the influence of the contact between the NW side facets and the substrate over the band bending of a dispersed NW.

Those reports suggest a certain variability in the surface band bending, which can be translated in a non-constant value for the surface recombination velocity in our diffusion model. Therefore, it would be the addition of NW diameter, doping and surface chemical environment fluctuations which would infer significant variations in surface recombination velocity, thereby, accounting for a part of the observed diffusion length variability.

Existence of additional non-radiative defects At last, the incorporation of non-radiative defects other than the surface states should not be disregarded. For instance, the quenching of the D^oX CL signal, in the left side of the NW shown in Figure 6.4, highly suggests the presence of an additional non-radiative defect. Hauswald *et al.* [250] have listed surface states and coalescence induced defects as evident non-radiative channels. However, they have observed a lack of correlation between radiative decay times and coalescence degree or surface-to-volume ratio, which have led them to the

conclusion that additional non-radiative channels must exist within the NWs. Such conclusion would corroborate our results.

The analysis of the CL signal of GaN NWs has allowed to extract charge carrier diffusion length and to outline the existence of non-radiative channels. The observed variability in the measured diffusion length has been tentatively attributed to fluctuations in the surface band bending, as well as to the presence of unidentified non-radiative defects.

6.4 Diffusion in AlN nanowires

6.4.1 GaN quantum disks in AlN

A GaN QDisk inserted in an AlN NW has been used as a sink for charge carriers. It forms a AlN/GaN/AlN heterostructure along the c axis, with a quasi- cylindrical symmetry. In comparison to I_1 basal SFs in NWs, GaN QDisks are intentionally grown, meaning that their vertical position along the AlN NW can be fully controlled. In addition, the band alignment with the AlN is of type I, allowing an efficient trapping and confinement of the charge carriers. However, as depicted in the chapter 5, the GaN QDisk shape is missing uniformity from NW to NW, which, in addition to the related strain field generated by the GaN QDisk, particularizes each NW and prevents straightforward comparisons between each.

6.4.2 Growth

First, a regular GaN NW assembly was grown on Si (111), using an Al-first AlN buffer, in order to obtain NWs $\sim$ 300 nm long. Next, the growth was switched to AlN, using the same substrate temperature and a III/V flux ratio of 1. The length of the obtained AlN section is $\sim$ 100 nm. Nominally, 4 ML_{GaN} of GaN have been deposited on top of the AlN NW, which were next capped by $\sim$ 40 nm of AlN[12]. It results in a GaN QDisk sandwiched between two AlN sections. In the following, only one NW will be in the focus of the study (labeled NW #A), but the conclusions which will be drawn from this single NW have been qualitatively validated on others.

The NW under scrutiny is shown in Figure 6.10, it hosts a GaN QDisk $\sim$ 4 ML thick inserted in an AlN NW having a 100 nm diameter. The contrast grading visible from AlN to GaN, in the HR-STEM image of Figure 6.10d, could be attributed to a roughness of the QDisk. EELS mapping of the Ga and Al related signals confirms the absence of a large intermixing between between Al and Ga atoms, in contrast to what can be observed while growing AlGaN disks instead of GaN ones [228].

In addition, CBED images acquired on the same NW confirm the full N-polarity of the NW.

[12] sample N1772

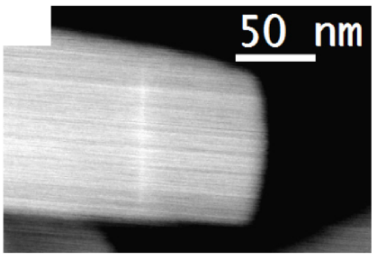

(a) HAADF STEM image of the NW #A – scale bar: 50 nm

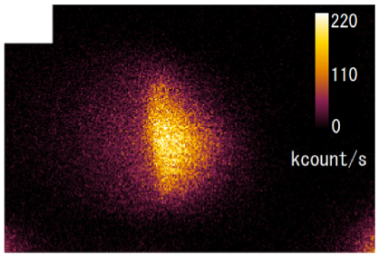

(b) CL intensity mapping of the NW #A acquired simultaneously to the HAADF STEM image at 100 K

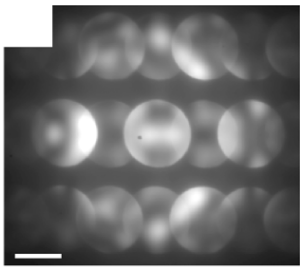

(e) Experimental convergent beam electron diffraction (CBED) pattern – scale bar: 2 nm^{-1}

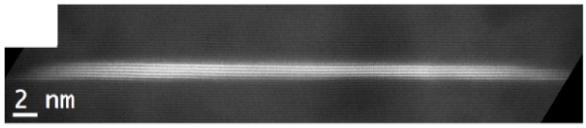

(c) HAADF HR-STEM image of the GaN QDisk – scale bar: 2 nm

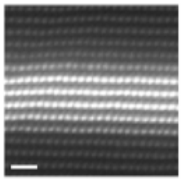

(d) HAADF HR-STEM image of the GaN QDisk – scale bar: 5 Å

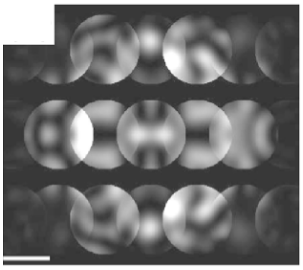

(f) Simulated CBED pattern for an N-polar AlN – scale bar: 2 nm^{-1}

Figure 6.10: Structural characterization of a typical GaN QDisk embedded in an AlN NW

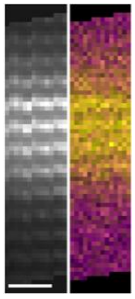

(a) Ga and Al electron energy loss spectroscopy (EELS) intensity signals mapped over the GaN QDisk – scale bar: 5 Å

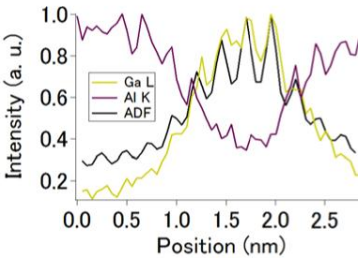

(b) EELS line scan of the Ga and Al signals across the GaN QDisk

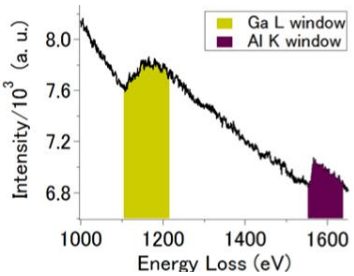

(c) EELS spectra showing integration energies for the Ga-L and Al-K edges

Figure 6.11: Chemical mapping of a typical GaN QDisk – Ga-L and Al-K edges intensities are respectively represented in yellow and green

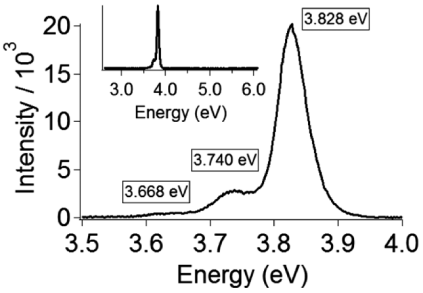

Figure 6.12: Average CL spectra acquired at 100 K on all the NW – the inset is showing the same spectra on a larger energy range

6.4.3 Cathodoluminescence signature

The average CL spectra acquired at 150 K over the whole NW is shown in Figure 6.12. It features a peak at 3.828 eV with two replica at lower energies, respectively, 3.740 and 3.668 eV, which are attributed to longitudinal optical (LO) phonon replica[13]. The CL spatial mapping shown in Figure 6.10b indicates that the luminescence is coming exclusively from the GaN QDisk, so that the luminescence contribution stemming from the AlN and GaN NWs will be further neglected.

6.4.4 Asymmetric cathodoluminescence profile

As shown in Figure 6.13b and 6.14a, the asymmetric profile of the CL on both side of the GaN QDisk is remarkable. The CL is ~ 2 times more intense on the right side (*i.e.* above the QDisk) than on the left side (*i.e.* below the QDisk). Knowing that the AlN sections above and below the QDisk have been grown in the exact same conditions, *i.e.* should exhibit the same properties, and ruling out Ga and Al intermixing, it suggests an asymmetry in the injection efficiency of the charge carriers into the QDisk. In addition, as exhibited in Figure 6.14, exciting above rather than below the QDisk implies a ~ 10 meV redshift and a narrowing of the zero phonon line CL of the GaN QDisk. It is the presence of strong built-in electric fields within the NW, which will be argued as responsible for this CL asymmetry.

A qualitative description of built-in electric fields along the NW axis can be obtained based on the knowledge of the spontaneous polarization of GaN and AlN. Indeed, one has:

$$div(\vec{P}) = -\rho \tag{6.9}$$

where ρ are bonded charges and $\vec{P}$ is the sum of the spontaneous and piezoelectric polarizations. Neglecting the latter, one has $\vec{P} = P(x)\vec{c}$, with $P(x)$ equal to -0.029 and -0.081 C.m^{-2} respectively for GaN and AlN [16] and with $\vec{c}$ pointing toward the (0001) direction. Due to the discontinuities of the function $P(x)$ at the interface between two materials, the bonded charge expected from the equation 6.9 are actually surface charge. Hence, considering an N-polar NW, the bottom AlN/GaN interface should host positive surface charges whereas the upper interface should host negative surface charges. Next, the electric field variations can be inferred using $div(\vec{E}) = \rho/\epsilon$, or directly,

[13]The LO phonon energy in AlN estimated to be 80 meV [260]

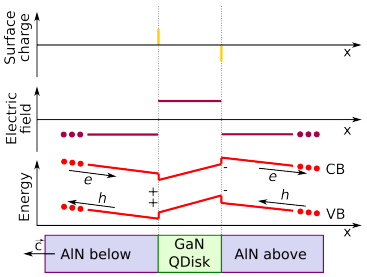

(a) Sketch of the surface charges, electric fields and band diagram in the environment of a N-polar GaN QDisk

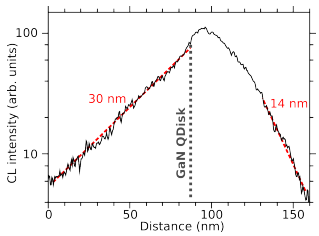

(b) CL intensity profile of NW #A along the $-c$ axis and average along its section

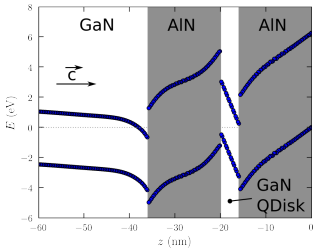

(c) Band diagram of a GaN/AlN/GaN/AlN NW heterosructure calculated by [28] – note that their NW is Ga-polar

Figure 6.13: Asymmetric CL profile along the NW axis correlated to asymmetric built-in electric fields

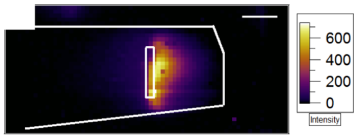

(a) Intensity spatial mapping

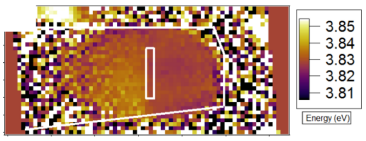

(b) Energy spatial mapping

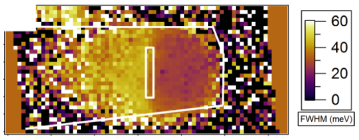

(c) FWHM spatial mapping

Figure 6.14: Spatial mapping on the NW #A of the QDisk CL intensity, energy and FWHM of its zero phonon line – the NW geometry and the position of the QDisk is recalled by the white lines – scale bar: 42 nm

$div(\vec{P} + \epsilon\vec{E}) = 0$. A qualitative sketch of the surface charges, built-in electric fields and band profile is given in Figure 6.13a. One has to note that the sign of the built-in electric field is dependent on the sign of the spontaneous polarization, hence on the polarity of the heterostructure.

At this stage, the screening of the built-in electric fields by free carriers has been neglected, which is a crude approximation. Noticeably, in the AlN sections, the amplitude of the electric field has to drop to zero far from AlN/GaN interfaces [20], therefore, the spatial extent of the proposed qualitative band diagram should be limited to the close vicinity of the GaN QDisk. By comparison to the tight binding calculations of Camacho and Niquet [28] performed on GaN/AlN NW heterostructures (see Figure 6.13c), the maximal amplitude of the built-in electric field in the AlN sections can be estimated to be up to ~ 1 MV.cm^{-1}. It means that every e-h pairs generated by the e-beam in the AlN should be ionized, hence, a charge carriers current of independent free electrons and holes instead of e-h pairs must be considered.

The free charge diffusion along the c axis of an AlN NW can be described by a similar equation than for e-h pairs (Equation 6.1), if adding a drift term accounting for the electric field dependence. One can define $n_q(x,t)$, the linear density of the free electrons ($q = e$) or free holes ($q = h$) between x and $x + dx$, which are coordinates along the NW axis.

At (t, x), neglecting other non-radiative centers than the NW surface, one has:

$$\begin{aligned}\frac{\partial n_q}{\partial t} = D_q \frac{\partial^2 n_q}{\partial x^2} + p(x) - \left(\frac{1}{\tau_{r,q}} + \frac{4 s_q(E_\perp)}{d}\right) n_q \\ - \gamma_{q \to disk}(x) n_q - q\mu_q E_\parallel(x) \frac{\partial n_q}{\partial x}\end{aligned} \tag{6.10}$$

where:

- D_q is the diffusion coefficient of the free charge.
- $p(x)$ is the incoming flux of free charges generated by the e-beam. Again, it will be considered point-like, meaning that when focusing the e-beam at $x = x_o$, one has $p(x) = p_o \delta(x - x_o)$.
- $1/\tau_{r,q}$ is the radiative recombination rate of the free charge in the AlN. In this case, as no CL signal stemming from the AlN is observed, $1/\tau_{r,q}$ can be considered negligible.
- $4 s_q(E_\perp)/d$ is the capture rate of the free carrier by the surface, with s_q the surface recombination velocity and d the NW diameter. s_q depends on the band bending at the NW side facets, *i.e.* an upward band bending would increase the capture rate of holes compared to electrons and a downward band bending would lead to the reverse. Hence, s_q is a function of the equivalent electric field $E_\perp$, which accounts for the band bending at the side facets.
- $\gamma_{q \to disk}$ is the capture rate of the GaN QDisk.
- $-q\mu_q E_\parallel(x) \frac{\partial n_q}{\partial x}$ is the drift contribution related to the built-in electric field, $\vec{E_\parallel}$, which has been previously shown to stem from the surface charges. q is the electrical charge of the carrier and μ_q its mobility.

If neglecting the presence of the QDisk and with $E_\parallel$ constant along x, the solution of the equation 6.10 in the steady state regime is:

$$\begin{aligned} & n_q = p_0 e^{-|x - x_0|\Delta_q} \\ & \text{with, for } x \geq x_0 \quad \Delta_q = \frac{-q\mu_q E_\parallel + \sqrt{(q\mu_q E_\parallel)^2 + 4D_q + (\frac{1}{\tau_{r,q}} + \frac{4 s_q(E_\perp)}{d})}}{2D_q} \\ & \text{with, for } x \leq x_0 \quad \Delta_q = \frac{-q\mu_q E_\parallel - \sqrt{(q\mu_q E_\parallel)^2 + 4D_q + (\frac{1}{\tau_{r,q}} + \frac{4 s_q(E_\perp)}{d})}}{2D_q} \end{aligned} \tag{6.11}$$

Neglecting the differences in the values μ_q, D_q and s_q between an electron and a hole, the main asymmetry between the two types of carriers thus lies in the sign of their electric charge q. Indeed, in the case of $E_\parallel > 0$, one has $\Delta_e < \Delta_h$ for $x \geq x_0$ but $\Delta_e > \Delta_h$ for $x \leq x_0$, which infers asymmetric diffusion lengths for electron and holes apart the

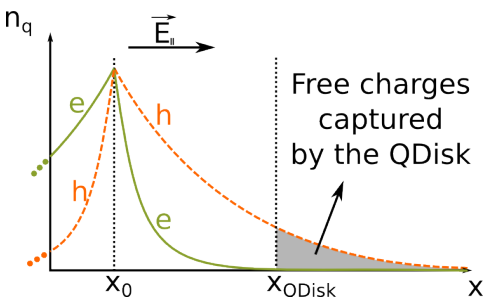

Figure 6.15: Sketch of the n_q distribution along a NW length, either considering holes or electrons. In the case of the presence of a QDisk at the coordinate $x = x_{QDisk}$, the charge carriers belonging to the gray area are assumed to be trapped by the QDisk.

excitation beam, as depicted in Figure 6.15. In other words, within an electric field, electrons and holes drift in opposite directions, which would lead in the geometry of the NW in scrutiny, to a selective injection of holes or electrons in the QDisk, whether the e-beam is pointing above or below the QDisk. However, such behavior should be a transient phenomenon as the generated free charges might imply a screening of the built-in electric field. Nevertheless, in the following development, the band profile will be assumed unperturbed by those free charges.

Considering a point-like QDisk at $x = x_{disk}$, it gives a QDisk trapping rate $\gamma_{q\rightarrow disk} = \gamma_0\delta(x - x_{disk})$. As sketched in Figure 6.15, every charge carriers crossing the QDisk will be assumed to be captured. Hence, in a similar manner than for the FX captured by I_1 basal SFs, the incoming flux of charge carriers into the QDisk is:

$$\Phi_q = \frac{p_0}{\Delta_q} e^{-|x_{QDisk}-x_0|\Delta_q} \tag{6.12}$$

In the steady state regime, and considering a non-radiative recombination channel in the QDisk, one has:

$$\Phi_q = \frac{n_{q,disk}}{\tau_{r,q,disk}} + \frac{n_{q,disk}}{\tau_{nr,q,disk}} \quad \Leftrightarrow \quad n_{q,disk} = \frac{\Phi_q}{1 + \tau_{r,q,disk}/\tau_{nr,q,disk}} \tag{6.13}$$

where $\tau_{r,q,disk}$ and $\tau_{nr,q,disk}$ are respectively the radiative and non-radiative lifetimes of the charge carriers trapped in the QDisk and $n_{q,disk}$ the density of carriers trapped in the QDisk. Therefore, the CL intensity stemming from the QDisk should be:

$$\begin{aligned} I_{q,QDisk}(x_0) &\propto \frac{n_{q,disk}}{\tau_{r,q,disk}} \\ &\propto \frac{\Phi_q}{1 + \tau_{r,q,disk}/\tau_{nr,q,disk}} \\ &\propto \frac{p_0 e^{-|x_{QDisk}-x_0|\Delta_q}}{\Delta_q(1 + \tau_{r,q,disk}/\tau_{nr,q,disk})} \end{aligned} \tag{6.14}$$

Due to the usual non-intentional n-doping of AlN NWs [55], holes are minority carriers, leading to $\tau_{r,e,disk} \gg \tau_{r,h,disk}$. Assuming $\tau_{nr,e,disk} \simeq \tau_{nr,h,disk}$, it means that for a similar amount of injected holes or electrons, *i.e.* $\Phi_h = \Phi_e$, one has $I_{h,QDisk} \gg I_{e,QDisk}$ and $n_{h,disk} \ll n_{e,disk}$. Therefore, in this model, the large CL intensity of the QDisk when

generating *e-h* pairs above the QDisk should directly relate (1) to the favorable diffusion of holes toward the QDisk in relation with the built-in electric fields and (2) to the short radiative lifetime of holes. By contrast, if generating *e-h* pairs below the QDisk, only electrons should reach the QDisk, giving rise to a tiny CL intensity, due to their large lifetime. In addition, due to $n_{h,disk} \ll n_{e,disk}$, the screening of the built-in electric field, implying a decrease of the quantum confined Stark effect (QCSE) in the GaN QDisk, should be stronger when injecting electrons compared to holes, which fits the experimental observation of a blue-shift and a broadening of the QDisk signature if pointing the e-beam below rather than above the QDisk.

However, this model suffers from two inconsistencies. First, the QCSE in very thin QDisks is expected to be negligible, which would rule out its contribution in the CL blue-shift observed while exciting below rather than above the QDisk[14]. But more importantly and as already mentioned, this model is based on a static band diagram, which does not take into consideration the presence of free carriers. Therefore, it fully neglects the static screening of the built-in electric fields by the free carriers stemming from the residual doping and it neglects the dynamic screening provided by free carriers generated by the e-beam itself. It means that a more precise picture of the system would need an improved estimation of the built-in electric fields with static and dynamic contributions. It also suggests that probing the heterostructure by e-beam is likely perturbing the system.

As a conclusion, the strong asymmetry of the CL signature of a GaN QDisk inserted in an AlN NW has been related to the existence of built-in electric fields within the NW. A model has been proposed where such fields, stemming from the large spontaneous polarization discontinuity in nitride materials, lead first to the ionization of the majority of diffusing *e-h* pairs and then imply an anisotropic drift of carriers having opposite electronic charges. Hence, a majority of electrons or holes would be injected in the QDisk, whether exciting below or above the QDisk. However, this model would need further refinement by taking into consideration the possible screening effect of the free carriers generated by the e-beam itself.

Interestingly, the drift direction for a defined charge carrier is dependent on the heterostructure polarity, which further questions the case of NWs hosting inversion domains (IDs), as shown in chapter 4.

6.5 Conclusion

In this Chapter, the focus has been brought to the diffusion of charge carriers in NWs. Taking advantage of the quasi-cylindrical symmetry of the NWs, the understanding of the diffusion mechanisms can be eased by scaling the problem down to one dimension. The local generation of carriers has been done by e-beam excitation and their relaxation has been monitored through their radiative recombinations in specific sinks.

[14] this conclusion is supported by recent CL results acquired on GaN QDisk in the group of Matthieu Kociak

In GaN NWs, I_1 basal SFs have been used as a sink for the diffusing e-h pairs. A diffusion length of ~ 70 nm has been measured for the FX, with large variations between NWs and even between SFs included in the same NW. Based on the diffusion equations, such low diffusion length compared to the thin film case has been attributed to the presence of non-radiative channels, mostly localized on the side facets. In addition, the dispersion of the diffusion length is attributed to local fluctuations in the surface band bending, which would stem, for instance, from a point-like contact of the NW with the substrate.

In AlN NWs, a GaN QDisk has been used as a sink for the diffusing charge carriers. A strong asymmetry of the CL signal stemming from the GaN QDisk has been observed whether generating charge carriers above or below the disk. A model has been proposed where the CL asymmetry is attributed to the presence of large built-in electric fields in the vicinity of the QDisk. It has noticeably highlighted a dependence of the CL signal on the polarity of the heterostructure.

Conclusion and prospects

GaN nanowire nucleation on AlN buffers In order to answer the question of GaN nanowire (NW) nucleation, the idea has been to focus first on the AlN buffer. Hence, the experiments depicted in the chapter 3 have revealed two different growth modes for the AlN buffer on Si, whether N or Al atoms are provided first. For both cases, the systematic nucleation of singularities in the AlN buffer has been emphasized and explained through a growth model relying on the high reactivity of Al and N species with silicon substrate, a point that is not often considered in literature reports. Those singularities were next observed to interfere in the GaN NW self-organized nucleation process, by usually acting as preferential nucleation sites.

On the other hand, a systematic polarity analysis of the NWs has demonstrated their N-polarity. Hence, it has been deduced that the N-polarity is required for the self-organized nucleation of NWs, in agreement with recent literature reports. Therefore, the observed preferential nucleation of GaN NWs on AlN singularities has been related to the ability for GaN to nucleate with the N polarity on such features. It means that the polarity pattern of the AlN buffer is a key point if one want to reproducibly control NW nucleation, especially in terms of NW density. According to reports on thick AlN films and in agreement with preliminary results shown in this chapter, the polarity of AlN seems hardly predictable and rather inhomogeneous over the whole film. Therefore, a future prospect would be to tackle the issue of AlN buffer polarity and noticeably to check the role of residual Si which has been presumed to favor the formation of basal inversion domain boundarys (IDBs).

At last, the systematic polarity analysis of the NWs has revealed the unexpected existence of inversion domains (IDs) in a significant ratio of NWs. It means that two populations of NWs, likely with different properties, could be now differentiated in a single assembly. Such observation is of prime importance in order to asses the stemming of the usual dispersion in the properties of NWs belonging to the same assembly. In addition, it questions the former polarity measurements published in the literature with tools not able to resolve such IDs.

Inversion domains The presence of IDs in self-organized plasma-assisted molecular beam epitaxy (PA-MBE) NWs has allowed a thorough optical and structural characterization of prismatic IDBs, benefiting from the advantageous geometry of the NWs. The results are presented in the chapter 4. Not surprisingly, this extended defect has been systematically observed in the most stable atomic configuration, even upon interaction

with other defects such as stacking faults (SFs). A noticeable output is the observation of an optical signature of IDBs at 3.45 eV, which has brought a decisive answer in the debated origin of the 3.45 eV PL specifically observed in NWs. Such optical signature has even allowed to infer the presence of IDBs in the majority of the NW samples grown in other laboratories, meaning that the discovered IDs are not a singularity but a general feature for self-organized PA-MBE GaN NWs. However, reported *ab initio* calculations, although neglecting electron-hole (*e-h*) interactions, do not predict the luminescence of IDBs at 3.45 eV. Such inconsistency could either stem from the lack of accuracy of the calculations or from the fact that inner defects localized in the IDB could act as radiative centers. Hence, a future prospect would be to perform additional spectroscopic work of the 3.45 eV line and/or to refine the *ab initio* calculations.

GaN nucleation on top of an AlN nanowire As the picture of GaN nucleation on 2D AlN is getting clearer, one might wonder if the same growth modes could be observed on top of AlN NWs. However, in this case, and as depicted in the chapter 5, the interest lies in the growth of robust GaN/AlN heterostructures in order to confine *e-h* pairs.

First, a "2D" growth mode for GaN on top of AlN NWs has been evidenced, leading to so-called quantum disks (QDisks). Correlated structural and optical investigations of such disks have shown a close similarity of those objects with conventional quantum wells (QWs). In agreement with previous literature reports, the QDisks luminescence has been shown to depend on built-in electric fields, strain and geometrical factors. Due to the difficulty to grow such heterostructures with a similar geometry and strain state for all the NWs of an assembly, the luminescence properties of single NWs are hardly predictable.

In order to synthesize GaN/AlN heterostructure more robust than QDisks, a "3D" growth mode of GaN on top of AlN NWs has been intended. It has been successfully reached by enlarging the AlN NW top diameter, using a growth route previously developed in the chapter 2, and by decreasing the growth temperature. An *in situ* characterization has evidenced the nucleation of GaN islands with a significant delay, suggesting the existence of a non-negligible incubation time. Therefore, a future prospect would be to quantify this incubation time as function of the growth temperature and the impinging atomic fluxes.

At last, preliminary results have suggested a significant confinement of *e-h* pairs up to room temperature. Hence, a future prospect would be to push further the optical investigation of such heterostructures in order to confirm their quantum dot-like behavior.

Diffusion of carriers Taking advantage of the one dimensional geometry of the NWs and the ability to grow GaN QDisks in AlN, NWs have been used in order to measure charge carrier diffusion both in AlN and GaN, as depicted in chapter the 6.

In GaN NWs, a diffusion length of several tenth of nm has been measured for *e-h* pairs in the vicinity of SFs. Such low value compared to previous results measured in 2D layers has been assigned to non-radiative defects, likely localized on the NW side

facets. However, the dispersion in the diffusion lengths obtained in different NWs or at different locations within a NW has suggested fluctuations in the surface states density, or the existence of additional non-radiative recombination channels within the NW. Hence, a future prospect would be to closely characterize the role of surface states in the optoelectronic properties of GaN NWs, although there is no evident experiments that would straightforwardly answer this need.

At last, in the vicinity of a GaN QDisk in an AlN NW, the diffusion of charge carriers has been evidenced to strongly depend on local built-in electric fields. Noticeably, it generates a significant asymmetry in the excitation efficiency of the GaN QDisk by cathodoluminescence, which is polarity dependent.

[214]

Résumé en français

Des nitrures aux nanofils de GaN

Depuis le milieu du XX^{me} siècle, la communauté scientifique s'intéresse aux semiconducteurs à grand gap comme le GaN. 50 ans de recherche ont permis d'approfondir la connaissance de ce matériau et de développer des méthodes de synthèse sous forme de couche minces en limitant le nombre de défauts cristallins et en autorisant le dopage. Pour l'exemple, on peut citer la publication d'Amano *et al.* [1], faite en 1986, qui expose pour la première fois les avantages à utiliser une couche mince d'AlN entre le GaN et son substrat pour minimiser la formation de défauts étendus aux interfaces. En 1989 le même groupe de recherche a démontré la capacité de doper p le GaN en incorporant des atomes de magnésium (Amano *et al.* [2]). Ces deux découvertes ont donné l'impulsion pour utiliser les matériaux nitrures (GaN, AlN, InN et les alliages ternaires dérivés) dans la confection de diodes à électroluminescence (DELs). Ainsi, Akasaki *et al.* [4] en 1992 et Nakamura *et al.* [5] en 1994 ont rapporté la synthèse des premières DELs bleues qui ont permis de mettre au point quelques années plus tard la technologie *Blu-ray-disk*. Aujourd'hui, en cette fin d'année 2015, des DELs blanches basées sur les matériaux nitrures et visant à remplacer les lampes fluorescentes compactes sont disponibles sur le marché grand public, ce qui donne un indice de la maturité du matériau. Sans oublier qu'Akasaki, Nakamura et Amano ont tous les trois reçu le prix Nobel de physique 2014 pour féliciter leurs travaux recherches qui ont été décisifs dans les développements successifs des nitrures.

Les nanofils sont apparus comme un sous-produit des recherches visant à optimiser les couches minces de GaN. En 1997 and 1998, deux groupes de recherche concurrents, respectivement dirigés par Kishino au Japon [6] et Calleja en Espagne [7], ont rapporté la croissance spontanée de nanocolonnes de GaN lors de l'utilisation de conditions de croissance spécifiques en épitaxie par jets moléculaires (EJM). L'intérêt pour ces nanostructures, obtenues par croissance dite *bottom-up*, est (1) la quasi-systématique absence de défauts étendus, même lors de croissance sur des substrats présentant un large désaccord de maille et (2) la robustesse du processus de nucléation auto-organisé qui permet notemment la croissance de nanofils sur des substrats silicium. Un marqueur de l'intérêt porté par cette géométrie spécifique du GaN est la mise au point de méthodes de croissance de nanofils utilisant l'épitaxie par phase vapeur [9, 10] plus adéquate pour une hypothétique production à grand échelle.

Du point de vue des applications, les nanofils nitrures se classent déjà au rang de

concurrents des couches minces classiques avec l'espoir d'augmenter l'efficacité des DELs et/ou de réduire les coûts de production en utilisant des substrats silicium. Un exemple est la start-up grenobloise Aledia [11] qui a pour ambition de produire sur silicium des DELs nitrures blanches à haut rendement, et ce grâce à une technologie intégrant des microfils de GaN. D'autres utilisations des fils de GaN sont déjà imaginées mais nécessitent encore des développements sur le long terme. On peut citer pour l'exemple les transducteurs opto-chimiques [12] ou les générateurs piezo-électroniques [13].

Motivations du travail de thèse

Au vu de l'histoire des nitrures, il apparaît qu'une partie significative de la communauté scientifique réussit avec succès une recherche appliquée, visant à la mise au point de dispositifs. Cette activité est sous-tendue par un autre type de recherche, à caractère plus fondamental, et dont l'objectif majeur consiste à étendre les connaissances sur les propriétés élémentaires des matériaux nitrures. C'est justement le but de l'équipe de chercheurs, menée par Bruno Daudin et Bruno Gayral, dans laquelle ma thèse s'est déroulée.

De ce fait, il n'est pas surprenant que mon travail expérimental a été initié uniquement sur la base de deux questions très spécifiques:

- quel est le mécanisme de nucléation des nanofils de GaN sur une couche mince d'AlN ?
- quel est le mode de croissance du GaN au sommet d'un nanofil d'AlN ?

D'un point de vue pratique, donner réponse à ces deux questions permet (1) d'améliorer la reproductibilité des nucléations de nanofils de GaN sur AlN et (2) de réussir la synthèse d'hétérostructures filaires AlN/GaN optimisées pour l'émission de lumière à température ambiante.

De plus, l'expérience gagnée dans la croissance de nanofils m'a amené à produire des échantillons destinés à alimenter diverses collaborations scientifiques. Parmi ces études, uniquement les résultats obtenus en lien avec les propriétés fondamentales des nitrures sont exposés dans ce manuscrit de thèse. Ils comprennent (1) la caractérisation détaillée des parois d'inversion de domaine et (2) l'étude de la diffusion des porteurs de charge dans les nanofils.

Collaborations

Les deux compétences principales de l'équipe de recherche sont la croissance par EJM de nitrures et la caractérisation optique par photoluminescence. Pour approfondir la caractérisation des échantillons ou bien créer de nouvelles expériences, des collaborations ont été mises en place et ont notamment impliquées:

- Jean-Luc Rouvière et Benedikt Haas pour des observations par microscopie électronique en transmission (CEA Grenoble, France)

- Catherine Bougerol et Martien den Hertog pour des observations par microscopie électronique en transmission et la synthèse de substrats spécifiques (Institut Néel, Grenoble, France)

- Gilles Nogues pour des observations par cathodoluminescence et la synthèse de substrats spécifiques (Institut Néel, Grenoble, France)

- Mathieu Kociak, Luiz Tizei et Sophie Meuret pour les observations en nano-cathodoluminescence résolue en temps (LPS, Orsay, France)

- Ana Cros et Albert Minj pour les observations de sonde Kelvin en microscopie à force atomique (Institute of material science, Valencia, Espagne)

- Katharina Lorenz pour l'implantation de terres rares dans les nanofils (IPFN, Lisbonne, Portugal)

- Xavier Biquard, François Rieutord et Samuel Tardiff pour les analyses en rayons X faites à l'ESRF (CEA, Grenoble, France)

Organisation du manuscrit

Chapitre 1 Une brève présentation des outils expérimentaux utilisés dans les diverses expériences présentées dans ce manuscrit de thèse est donnée dans ce chapitre :

- L'EJM et ses principaux composants sont décrits, avec en particulier les méthodes misent au point pour mesurer la température du substrat et pour estimer les flux atomiques générés par les cellules.

- Quelques propriétés fondamentales des matériaux nitrures sont données, telle que la structure cristalline qui est le plus souvent wurtzite, l'existence d'une polarisation spontanée et piézoélectrique ainsi que le concept de polarité qui différencie les surfaces $hkil$ de leur symétrique $hki\bar{l}$.

- Due à la profusion de synthèse d'objets "nano", une définition spécifique et propre au manuscrit de thèse de l'objet "nanofil" est proposée. Le diagramme de croissance par EJM de ces nanofils, mise au point par Fernandez-Garrido *et al.* [39], est donné.

- Les méthodes de caractérisation utilisées dans les différentes études relatées dans le manuscrit de thèse sont décrites, à savoir la diffraction d'électron à haute énergie en incidence rasante, la photoluminescence, la microscopie électronique, la microscopie à force atomique, la gravure chimique et la cathodoluminescence.

Chapitre 2 Les nanofils de caractérisent pas une croissance axiale (*i.e.* dans l'axe du fil) supérieure à la croissance radiale (*i.e.* perpendiculairement à l'axe du nanofils). Dans le cas du GaN, cette asymétrie de croissance donne lieu à des objets ayant un diamètre d'environ 50 nm pour une longueur de 1 μm, soit un rapport d'aspect d'environ 20. Plusieurs facteurs ont été étudiés dans la littérature pour expliquer ce phénomène :

- différents énergies de facette [76]
- différentes barrière à la diffusion entre les facettes radiales et axiales [25, 78]
- la géométrie des flux atomiques incidents sur les nanofils [82, 83]

Une étude de cas sur la croissance d'InN au sommet de fils de GaN est faite pour illustrer ces différents mécanismes.

Comme l'état de contrainte d'une hétérostructure déposée au sommet d'un nanofil dépend du diamètre même du nanofils, il peut être intéressant de pouvoir contrôler le diamètre des nanofils nitrures. Divers procédés pour arriver à ce but sont présentés :

1. croissances en conditions riche Ga et à basse température pour augmenter le diamètre des nanofils
2. croissance d'AlN avec la possibilité de changer la dispositions des flux atomiques par rapport au substrat pour augmenter le diamètre des nanofils
3. recuit à haute température pour diminuer le diamètre des nanofils

Les meilleurs résultats ont été obtenus en utilisant la croissance riche Ga à basse température. Cette technique sera utilisée pour la synthèse d'échantillons spécifiques dans les chapitres 3 et 5.

Chapitre 3 En octobre 2012, au début de ma thèse, il n'y avait pas de consensus dans la littérature sur le mécanisme de nucléation auto-organisé des nanofils de GaN sur couche mince d'AlN déposée sur silicium. Plus précisément, des résultats expérimentaux ont suggéré l'importance de la polarité du nucleus de GaN : seul les cristaux de polarité N pouvant évoluer sous forme de nanofils [51]. A l'inverse, d'autres résultats expérimentaux ont suggéré l'importance de nano-structures dans la couche mince d'AlN agissant comme centre de nucléations pour nanofils [114, 31].

Une première partie de mon travail a été de développer des mécanismes de croissance pour expliquer et prévoir l'apparition de ces nano-structures dans l'AlN. Pour ce faire, des couches minces d'AlN, qualifiées de *Al-first*, ont été produites en déposant au préalable l'aluminium sur le substrat de silicium puis, dans un second temps, en nitrurant cet aluminium par exposition au flux d'azote. D'autres couches d'AlN, qualifiées de *N-first*, ont été produites en nitrurant au préalable la surface du silicium par exposition au flux d'azote puis, dans un second temps, en exposant ce nitrure de silicium au flux d'aluminium provoquant ainsi la réduction du silicium et la formation d'AlN. Indépendamment du processus de croissance utilisé, des nano-structures au sein de la couche

d'AlN ont été observées avec des densités de l'ordre de $10^8 \sim 10^9$ cm^{-2}. A l'appuie de diverses expériences, des mécanismes de croissances sont proposés. Ils résultent tous de la forte réactivité de l'aluminium avec le silicium et le nitrure de silicium.

Cette étude systématique a permis de mettre en évidence des conditions de croissance faisant varier la densité des nano-structures par un facteur 10. Ceci m'a permis d'étudier l'influence de la densité des nano-structures sur la nucléation des nanofils de GaN. Mais bien que ces nano-structures aient été clairement identifiées comme centre de nucléation pour les nanofils de GaN, aucune corrélation n'a été trouvée entre la densité des nanofils et la densité des nano-structures. Ceci suggère l'existence d'autres centres de nucléation pour nanofils au sein des couches minces d'AlN.

En parallèle, une étude approfondie de la polarité des nanofils de GaN a systématiquement confirmé leur polarité N alors que la couche 2D de GaN résidant entre les nanofils est de polarité Ga. Ces observations ont définitivement mis en évidence le rôle primordial de la polarité dans le processus de nucléation des nanofils, ce qui peut se traduire par la nécessité d'une hiérarchie spécifique entre les énergies de facettes polaires, semi-polaires et apolaires du nucleus initial de GaN pour autoriser sa croissance sous forme filaire. Ce ce fait, la capacité des nano-structures d'AlN a jouer le rôle de centre de nucléation a été uniquement rattaché à leur capacité à induire la nucléation de GaN de polarité N.

L'étude systématique de la polarité des nanofils a par ailleurs amené à la découverte de l'existence de domaines d'inversion de domaine, *i.e.* de domaine de polarité Ga au coeur des fils de polarité N, dans une ratio significatif de nanofils. La possible existence de ces inversions de domaine au sein des nanofils de GaN rend critique la mesure de leur polarité ce qui peut expliquer les observations antagonistes dans la littérature à propos de la polarité des nanofils de GaN.

Chapitre 4 La paroi d'inversion de domaine (PID), séparant un domaine de polarité Ga de celui de polarité N, constitue un défaut étendu dont la caractérisation structurale et optique fait l'objet de ce chapitre.

Une analyse structurale poussée réalisée par microscopie électronique en transmission a montré que la PID présente une structure atomique de type IDB* qui a été calculée comme la plus stable par Northrup *et al.* [151]. Cependant, la structure de la PID peut être perturbée par l'intersection avec une faute d'empilement basale, donnant lieu à un défaut linéaire.

Pour évaluer une éventuelle signature optique de la PID, une expérience corrélant des mesures de micro-photoluminescence sur fils uniques et une caractérisation structurale par microscopie électronique en transmission des mêmes fils a été tentée. Une corrélation entre la PID et l'existence d'une bande de luminescence centrée à 3.45 eV a été démontrée. Cette découverte a permis de préciser l'origine de la bande à 3.45 eV dont l'existence a été rapportée depuis la croissance des premiers échantillons de nanofils de GaN [115] mais dont l'origine a fait débat.

Chapitre 5 Pour fonctionnaliser les nanofils de GaN, des hétérostructures d'AlN/GaN peuvent être crûe à leur sommet. Elles visent à confiner des paires électrons-trous et ainsi pouvoir contrôler leur recombinaison radiative en changeant quelques paramètres structuraux de l'hétérostructure.

Des disques de GaN ont été introduits entre deux sections filaires d'AlN. Les propriétés optiques de ces objets, observées par photoluminescence et nano-cathodoluminescence résolue en temps, sont apparues très similaires au puits quantiques 2D d'AlN/GaN. En effet, il existe aussi au sein des disques de GaN un champ électrique interne lié aux discontinuités de polarisation à l'interface AlN/GaN qui affecte le temps de vie des paires électrons-trous et leur énergie de recombinaison (*i.e.* l'effet Stark confiné quantiquement [226, 210]). L'obtention d'une assemblée d'hétérostructures filaires GaN/AlN qui luminesceraient à la même énergie implique donc la croissance de disques avec une faible dispersion d'épaisseur d'un fil à l'autre, ce qui constitue une contrainte forte en terme de croissance.

Les tentatives d'élargissement des fils d'AlN ont parfois donné lieu à des structures pyramidales au sommet du fil. Des sections fines de GaN ont donc été déposées de manière conforme sur ces pyramides, donnant lieu à des petits puits quantiques d'orientation semi-polaires et polaires au sein d'un même fil. Leur caractérisation par nano-cathodoluminescence résolue en temps a validé l'existence d'une champ électrique interne.

Pour augmenter le confinement radial des paires électrons-trous au sein des hétérostructures AlN/GaN filaires, les conditions de croissance ont été intentionnellement changées pour synthétiser des boîtes quantiques de GaN pyramidales, similaires au boîtes quantiques de GaN obtenues sur AlN 2D avec un mode de croissance de type Stranski-Krastranov [213]. Ce changement de mode de croissance a été obtenus en réduisant la température de croissance et en augmentant la diamètre de la section filaire d'AlN.

Chapitre 6 En tirant partie de la structure unidimensionnel des nanofils, la mesure de la longueur de diffusion de porteurs de charge le long de l'axe axial des nanofils a pu être mesurée.

Dans le cas des fils de GaN, une longueur de diffusion de l'exciton de l'ordre de 75 nm à 10 K a été mesurée. Les excitons ont été générés localement avec un faisceau d'électron et leur recombinaison radiative a été mesurée dans une faute d'empilement basale.

Dans le cas des fils d'AlN, la longueur de diffusion des porteurs de charge s'est vue dépendre des champs électrique internes. Les excitons ont été générés localement avec un faisceau d'électron et leur recombinaison radiative a été mesurée dans un disque de GaN.

Bibliography

[1] H. Amano, N. Sawaki, I. Akasaki, and Y. Toyoda. Metalorganic vapor phase epitaxial growth of a high quality GaN film using an AlN buffer layer. Applied Physics Letters, 48(5):353–355, 1986. 5, 199

[2] Hiroshi Amano, Masahiro Kito, Kazumasa Hiramatsu, and Isamu Akasaki. P-type conduction in Mg-doped GaN treated with low-energy electron beam irradiation (leebi). Japanese Journal of Applied Physics, 28(12A):L2112, 1989. 5, 199

[3] S. Nakamura and M.R. Krames. History of gallium nitride-based light-emitting diodes for illumination. Proceedings of the IEEE, 101(10):2211–2220, Oct 2013. 5

[4] I. Akasaki, H. Amano, K. Itoh, N. Koide, and K. Manabe. Gan-based ultraviolet/blue light emitting devices. Inst. Phys. Conf. Ser., 129(851), 1992. 5, 199

[5] Shuji Nakamura, Takashi Mukai, and Masayuki Senoh. Candela-class high-brightness InGaN/AlGaN double-heterostructure blue-light-emittign diodes. Applied Physics Letters, 64(13):1687–1689, 1994. 5, 199

[6] Masaki Yoshizawa, Akihiko Kikuchi, Masashi Mori, Nobuhiko Fujita, and Katsumi Kishino. Growth of self-organized GaN nanostructures on Al2O3 (0001) by rf-radical source molecular beam epitaxy. Japanese Journal of Applied Physics, 36(4B):L459, 1997. 5, 20, 27, 199

[7] M.A. Sanchez-Garcia, E. Calleja, E. Monroy, F.J. Sanchez, F. Calle, E. Muñoz, and R. Beresford. The effect of the III/V ratio and substrate temperature on the morphology and properties of GaN- and AlN-layers grown by molecular beam epitaxy on Si(1 1 1). Journal of Crystal Growth, 183(1–2):23 – 30, 1998. 5, 20, 27, 199

[8] Wei Lu and Charles M Lieber. Semiconductor nanowires. Journal of Physics D: Applied Physics, 39(21):R387, 2006. 5

[9] X. J. Chen, G. Perillat-Merceroz, D. Sam-Giao, C. Durand, and J. Eymery. Homoepitaxial growth of catalyst-free GaN wires on N-polar substrates. Applied Physics Letters, 97(15):151909, 2010. 5, 128, 199

[10] Geoffrey Avit, Kaddour Lekhal, Yamina André, Catherine Bougerol, François Réveret, Joël Leymarie, Evelyne Gil, Guillaume Monier, Dominique Castelluci,

and Agnès Trassoudaine. Ultralong and defect-free GaN nanowires grown by the hvpe process. Nano Letters, 14(2):559–562, 2014. PMID: 24393103. 5, 14, 199

[11] Official website of aledia. http://www.aledia.com/en/. Accessed: 2015-10-11. 6, 200

[12] J Teubert, P Becker, F Furtmayr, and M Eickhoff. GaN nanodiscs embedded in nanowires as optochemical transducers. Nanotechnology, 22(27):275505, 2011. 6, 139, 186, 200

[13] Noelle Gogneau, Pascal Chrétien, Elisabeth Galopin, Stephane Guilet, Laurent Travers, Jean-Christophe Harmand, and Frédéric Houzé. GaN nanowires for piezoelectric generators. physica status solidi (RRL) – Rapid Research Letters, 8(5):414–419, 2014. 6, 200

[14] O. Landré, R. Songmuang, J. Renard, E. Bellet-Amalric, H. Renevier, and B. Daudin. Plasma-assisted molecular beam epitaxy growth of GaN nanowires using indium-enhanced diffusion. Applied Physics Letters, 93(18):183109, 2008. 12

[15] B.A. Joyce, P.J. Dobson, J.H. Neave, K. Woodbridge, Jing Zhang, P.K. Larsen, and B. Bôlger. Rheed studies of heterojunction and quantum well formation during mbe growth — from multiple scattering to band offsets. Surface Science, 168(1):423 – 438, 1986. 12

[16] Fabio Bernardini, Vincenzo Fiorentini, and David Vanderbilt. Spontaneous polarization and piezoelectric constants of III-V nitrides. Phys. Rev. B, 56:R10024–R10027, Oct 1997. 15, 92, 189

[17] P. Corfdir, C. Hauswald, J. K. Zettler, T. Flissikowski, J. Lähnemann, S. Fernández-Garrido, L. Geelhaar, H. T. Grahn, and O. Brandt. Stacking faults as quantum wells in nanowires: Density of states, oscillator strength, and radiative efficiency. Phys. Rev. B, 90:195309, Nov 2014. 17, 181, 183

[18] Jonas Lähnemann, Uwe Jahn, Oliver Brandt, Timur Flissikowski, Pinar Dogan, and Holger T Grahn. Luminescence associated with stacking faults in GaN. Journal of Physics D: Applied Physics, 47(42):423001, 2014. 17, 41, 126

[19] Raffaele Resta. Electrical polarization and orbital magnetization: the modern theories. Journal of Physics: Condensed Matter, 22(12):123201, 2010. 17

[20] Vincenzo Fiorentini, Fabio Bernardini, Fabio Della Sala, Aldo Di Carlo, and Paolo Lugli. Effects of macroscopic polarization in iii-v nitride multiple quantum wells. Phys. Rev. B, 60:8849–8858, Sep 1999. 17, 190

[21] Andrew Ian Duff, Liverios Lymperakis, and Jörg Neugebauer. Understanding and controlling indium incorporation and surface segregation on InGaN surfaces: An ab initio approach. Phys. Rev. B, 89:085307, Feb 2014. 17

[22] P. J. Schuck, M. D. Mason, R. D. Grober, O. Ambacher, A. P. Lima, C. Miskys, R. Dimitrov, and M. Stutzmann. Spatially resolved photoluminescence of inversion domain boundaries in GaN-based lateral polarity heterostructures. Applied Physics Letters, 79(7):952–954, 2001. 17, 109, 118

[23] Ronny Kirste, Ramón Collazo, Gordon Callsen, Markus R. Wagner, Thomas Kure, Juan Sebastian Reparaz, Seji Mita, Jinqiao Xie, Anthony Rice, James Tweedie, Zlatko Sitar, and Axel Hoffmann. Temperature dependent photoluminescence of lateral polarity junctions of metal organic chemical vapor deposition grown GaN. Journal of Applied Physics, 110(9):093503, 2011. 17, 109, 118

[24] P. M. Coulon, M. Mexis, M. Teisseire, M. Jublot, P. Vennéguès, M. Leroux, and J. Zuniga-Perez. Dual-polarity GaN micropillars grown by metalorganic vapour phase epitaxy: Cross-correlation between structural and optical properties. Journal of Applied Physics, 115(15):153504, 2014. 17

[25] Tosja Zywietz, Jörg Neugebauer, and Matthias Scheffler. Adatom diffusion at GaN (0001) and (0001-bar) surfaces. Applied Physics Letters, 73(4):487–489, 1998. 17, 29, 30, 202

[26] Santino D. Carnevale, Thomas F. Kent, Patrick J. Phillips, A. T. M. G. Sarwar, Camelia Selcu, Robert F. Klie, and Roberto C. Myers. Mixed polarity in polarization-induced p–n junction nanowire light-emitting diodes. Nano Letters, 13(7):3029–3035, 2013. 17, 56

[27] J. Renard, R. Songmuang, G. Tourbot, C. Bougerol, B. Daudin, and B. Gayral. Evidence for quantum-confined stark effect in GaN/AlN quantum dots in nanowires. Phys. Rev. B, 80:121305, Sep 2009. 17, 137, 139, 149, 150

[28] D. Camacho Mojica and Yann-Michel Niquet. Stark effect in GaN/AlN nanowire heterostructures: Influence of strain relaxation and surface states. Phys. Rev. B, 81:195313, May 2010. 17, 139, 149, 190

[29] Karine Hestroffer, Cédric Leclere, Catherine Bougerol, Hubert Renevier, and Bruno Daudin. Polarity of GaN nanowires grown by plasma-assisted molecular beam epitaxy on Si(111). Phys. Rev. B, 84:245302, Dec 2011. 17, 18, 56

[30] A. Minj, A. Cros, N. Garro, J. Colchero, T. Auzelle, and B. Daudin. Assessment of polarity in GaN self-assembled nanowires by electrical force microscopy. Nano Letters, 15(10):6770–6776, 2015. PMID: 26380860. 18, 53, 81

[31] Ludovic Largeau, Elisabeth Galopin, Noelle Gogneau, Laurent Travers, Frank Glas, and Jean-Christophe Harmand. N-polar GaN nanowires seeded by al droplets on Si(111). Crystal Growth & and Design, 12(6):2724–2729, 2012. 18, 55, 56, 58, 59, 67, 88, 99, 202

[32] O. Romanyuk, S. Fernández-Garrido, P. Jiříček, I. Bartoš, L. Geelhaar, O. Brandt, and T. Paskova. Non-destructive assessment of the polarity of GaN nanowire ensembles using low-energy electron diffraction and x-ray photoelectron diffraction. Applied Physics Letters, 106(2):021602, 2015. 18, 56

[33] X Kong, J Ristić, M A Sanchez-Garcia, E Calleja, and A Trampert. Polarity determination by electron energy-loss spectroscopy: application to ultra-small iii-nitride semiconductor nanocolumns. Nanotechnology, 22(41):415701, 2011. 18, 56

[34] O. Romanyuk, P. Jiříček, T. Paskova, I. Bieloshapka, and I. Bartoš. GaN polarity determination by photoelectron diffraction. Applied Physics Letters, 103(9):091601, 2013. 18

[35] Carolina Camacho Mojica, Dulce. Modeling of the structural, electronic and optical properties Theses, Université de Grenoble, May 2010. 18, 27, 149, 150

[36] A Urban, J Malindretos, J-H Klein-Wiele, P Simon, and A Rizzi. Ga-polar GaN nanocolumn arrays with semipolar faceted tips. New Journal of Physics, 15(5):053045, 2013. 19, 20, 97, 101

[37] B. Alloing, S. Vézian, O. Tottereau, P. Vennéguès, E. Beraudo, and J. Zuniga-Pérez. On the polarity of GaN micro- and nanowires epitaxially grown on sapphire (0001) and Si(111) substrates by metal organic vapor phase epitaxy and ammonia-molecular beam epitaxy. Applied Physics Letters, 98(1):011914, 2011. 19, 56, 128

[38] S. Fernández-Garrido, G. Koblmüller, E. Calleja, and J. S. Speck. In situ GaN decomposition analysis by quadrupole mass spectrometry and reflection high-energy electron diffraction. Journal of Applied Physics, 104(3):033541, 2008. 18, 29, 46

[39] S. Fernández-Garrido, J. Grandal, E. Calleja, M. A. Sánchez-García, and D. López-Romero. A growth diagram for plasma-assisted molecular beam epitaxy of GaN nanocolumns on Si(111). Journal of Applied Physics, 106(12):126102, 2009. 18, 19, 201

[40] Johannes K. Zettler, Christian Hauswald, Pierre Corfdir, Mattia Musolino, Lutz Geelhaar, Henning Riechert, Oliver Brandt, and Sergio Fernández-Garrido. High-temperature growth of GaN nanowires by molecular beam epitaxy: Toward the material quality of bulk GaN. Crystal Growth & Design, 0(0):null, 0. 19, 20, 41

[41] Sergio Fernández-Garrido, Johannes K. Zettler, Lutz Geelhaar, and Oliver Brandt. Monitoring the formation of nanowires by line-of-sight quadrupole mass spectrometry: A comprehensive description of the temporal evolution of GaN nanowire ensembles. Nano Letters, 15(3):1930–1937, 2015. PMID: 25671678. 19, 45

[42] † Raffaella Calarco, *, † Ralph J. Meijers, † Ratan K. Debnath, † Toma Stoica, ‡ Eli Sutter, , and Hans. Lüth†. Nucleation and growth of GaN nanowires on Si(111)

performed by molecular beam epitaxy. Nano Letters, 7(8):2248–2251, 2007. PMID: 17602537. 19

[43] Rafael Mata, Karine Hestroffer, Jorge Budagosky, Ana Cros, Catherine Bougerol, Hubert Renevier, and Bruno Daudin. Nucleation of GaN nanowires grown by plasma-assisted molecular beam epitaxy: The effect of temperature. Journal of Crystal Growth, 334(1):177 – 180, 2011. 19, 33, 45

[44] Hiroto Sekiguchi, Takuya Nakazato, Akihiko Kikuchi, and Katsumi Kishino. Structural and optical properties of GaN nanocolumns grown on (0001) sapphire substrates by rf-plasma-assisted molecular-beam epitaxy. Journal of Crystal Growth, 300(1):259 – 262, 2007. 20, 57

[45] Olivier Landré. Study of nucleation and growth of GaN and AlN nanowires like structures. Theses, Université Joseph-Fourier - Grenoble I, June 2010. 20, 57

[46] Elif Ertekin, P. A. Greaney, D. C. Chrzan, and Timothy D. Sands. Equilibrium limits of coherency in strained nanowire heterostructures. Journal of Applied Physics, 97(11):114325, 2005. 20, 27

[47] Frank Glas. Critical dimensions for the plastic relaxation of strained axial heterostructures in free-standing nanowires. Phys. Rev. B, 74:121302, Sep 2006. 20, 27

[48] Xu Zhang, Vladimir G. Dubrovskii, Nickolay V. Sibirev, and Xiaomin Ren. Analytical study of elastic relaxation and plastic deformation in nanostructures on lattice mismatched substrates. Crystal Growth & Design, 11(12):5441–5448, 2011. 20

[49] E. Calleja, J. Ristić, S. Fernández-Garrido, L. Cerutti, M. A. Sánchez-García, J. Grandal, A. Trampert, U. Jahn, G. Sánchez, A. Griol, and B. Sánchez. Growth, morphology, and structural properties of group-iii-nitride nanocolumns and nanodisks. physica status solidi (b), 244(8):2816–2837, 2007. 20

[50] Toma Stoica, Eli Sutter, Ralph J. Meijers, Ratan K. Debnath, Raffaella Calarco, Hans Lüth, and Detlev Grützmacher. Interface and wetting layer effect on the catalyst-free nucleation and growth of GaN nanowires. Small, 4(6):751–754, 2008. 20

[51] Sergio Fernández-Garrido, Xiang Kong, Tobias Gotschke, Raffaella Calarco, Lutz Geelhaar, Achim Trampert, and Oliver Brandt. Spontaneous nucleation and growth of GaN nanowires: The fundamental role of crystal polarity. Nano Letters, 12(12):6119–6125, 2012. 20, 55, 56, 102, 202

[52] Fabian Schuster, Florian Furtmayr, Reza Zamani, Cesar Magén, Joan R. Morante, Jordi Arbiol, Jose A. Garrido, and Martin Stutzmann. Self-assembled GaN nanowires on diamond. Nano Letters, 12(5):2199–2204, 2012. PMID: 22506554. 20, 128

[53] Shinta Nakagawa, Takuya Tabata, Yoshio Honda, Masahito Yamaguchi, and Hiroshi Amano. GaN nanowires grown on a graphite substrate by radio frequency molecular beam epitaxy. Japanese Journal of Applied Physics, 52(8S):08JE07, 2013. 20

[54] † Toma Stoica, *, † Ralph J. Meijers, † Raffaella Calarco, † Thomas Richter, ‡ Eli Sutter, , and Hans Lüth†. Photoluminescence and intrinsic properties of mbe-grown InN nanowires. Nano Letters, 6(7):1541–1547, 2006. PMID: 16834446. 20

[55] O. Landré, V. Fellmann, P. Jaffrennou, C. Bougerol, H. Renevier, A. Cros, and B. Daudin. Molecular beam epitaxy growth and optical properties of AlN nanowires. Applied Physics Letters, 96(6):061912, 2010. 20, 192

[56] T Palacios, F Calle, M Varela, C Ballesteros, E Monroy, F B Naranjo, M A Sánchez-García, E Calleja, and E Muñoz. Wet etching of GaN grown by molecular beam epitaxy on Si(111). Semiconductor Science and Technology, 15(10):996, 2000. 22

[57] W. Guo, J. Xie, C. Akouala, S. Mita, A. Rice, J. Tweedie, I. Bryan, R. Collazo, and Z. Sitar. Comparative study of etching high crystalline quality AlN and GaN. Journal of Crystal Growth, 366(0):20 – 25, 2013. 22, 23

[58] Hong-Yeol Kim, Younghun Jung, Sung Hyun Kim, Jaehui Ahn, Michael A. Mastro, Jennifer K. Hite, Charles R. Eddy Jr., and Jihyun Kim. Wet etching of nonpolar gallium nitride light-emitting diode structure for enhanced light extraction. Journal of Crystal Growth, 326(1):65 – 68, 2011. 22

[59] L. Lu, Z. Y. Gao, B. Shen, F. J. Xu, S. Huang, Z. L. Miao, Y. Hao, Z. J. Yang, G. Y. Zhang, X. P. Zhang, J. Xu, and D. P. Yu. Microstructure and origin of dislocation etch pits in GaN epilayers grown by metal organic chemical vapor deposition. Journal of Applied Physics, 104(12):123525, 2008. 22, 97

[60] Dongsheng Li, M. Sumiya, S. Fuke, Deren Yang, Duanlin Que, Y. Suzuki, and Y. Fukuda. Selective etching of GaN polar surface in potassium hydroxide solution studied by x-ray photoelectron spectroscopy. Journal of Applied Physics, 90(8):4219–4223, 2001. 22

[61] S. Meuret, L. H. G. Tizei, T. Cazimajou, R. Bourrellier, H. C. Chang, F. Treussart, and M. Kociak. Photon bunching in cathodoluminescence. Phys. Rev. Lett., 114:197401, May 2015. 23, 176

[62] Frank Glas and Bruno Daudin. Stress-driven island growth on top of nanowires. Phys. Rev. B, 86:174112, Nov 2012. 27, 140, 144, 165

[63] Xiaobin Niu, Gerald B. Stringfellow, Young-Ju Lee, and Feng Liu. Simulation of self-assembled compositional core-shell structures in InGaN nanowires. Phys. Rev. B, 85:165316, Apr 2012. 27

[64] C. Leclere, N. A. Katcho, G. Tourbot, B. Daudin, M. G. Proietti, and H. Renevier. Anisotropic In distribution in InGaN core-shell nanowires. Journal of Applied Physics, 116(1):013517, 2014. 27

[65] G Tourbot, C Bougerol, A Grenier, M Den Hertog, D Sam-Giao, D Cooper, P Gilet, B Gayral, and B Daudin. Structural and optical properties of InGaN/GaN nanowire heterostructures grown by pa-mbe. Nanotechnology, 22(7):075601, 2011. 27

[66] Hiroto Sekiguchi, Katsumi Kishino, and Akihiko Kikuchi. Emission color control from blue to red with nanocolumn diameter of InGaN/GaN nanocolumn arrays grown on same substrate. Applied Physics Letters, 96(23):231104, 2010. 27

[67] T Schumann, T Gotschke, F Limbach, T Stoica, and R Calarco. Selective-area catalyst-free mbe growth of GaN nanowires using a patterned oxide layer. Nanotechnology, 22(9):095603, 2011. 27

[68] V. Consonni, M. Knelangen, U. Jahn, A. Trampert, L. Geelhaar, and H. Riechert. Effects of nanowire coalescence on their structural and optical properties on a local scale. Applied Physics Letters, 95(24):241910, 2009. 27

[69] K.A. Grossklaus, A. Banerjee, S. Jahangir, P. Bhattacharya, and J.M. Millunchick. Misorientation defects in coalesced self-catalyzed GaN nanowires. Journal of Crystal Growth, 371(0):142 – 147, 2013. 27

[70] Caroline Chèze, Lutz Geelhaar, Olivier Brandt, Walter M. Weber, Henning Riechert, Steffen Münch, Ralph Rothemund, Stephan Reitzenstein, Alfred Forchel, Thomas Kehagias, Philomela Komninou, Georges Dimitrakopulos, and Theodoros Karakostas. Direct comparison of catalyst-free and catalyst-induced GaN nanowires. Nano Research, 3:528–536, 2010. 27

[71] Jelena Ristić, Enrique Calleja, Sergio Fernández-Garrido, Laurent Cerutti, Achim Trampert, Uwe Jahn, and Klaus H. Ploog. On the mechanisms of spontaneous growth of iii-nitride nanocolumns by plasma-assisted molecular beam epitaxy. Journal of Crystal Growth, 310(18):4035 – 4045, 2008. 27, 70

[72] L Largeau, D L Dheeraj, M Tchernycheva, G E Cirlin, and J C Harmand. Facet and in-plane crystallographic orientations of GaN nanowires grown on Si(111). Nanotechnology, 19(15):155704, 2008. 28

[73] Benjamin N. Bryant, Asako Hirai, Erin C. Young, Shuji Nakamura, and James S. Speck. Quasi-equilibrium crystal shapes and kinetic wulff plots for gallium nitride grown by hydride vapor phase epitaxy. Journal of Crystal Growth, 369(0):14 – 20, 2013. 28, 101

[74] Qian Sun, Christopher D. Yerino, Tsung Shine Ko, Yong Suk Cho, In-Hwan Lee, Jung Han, and Michael E. Coltrin. Understanding nonpolar GaN growth through kinetic wulff plots. Journal of Applied Physics, 104(9):093523, 2008. 28, 101

[75] Qian Sun, Christopher D. Yerino, Benjamin Leung, Jung Han, and Michael E. Coltrin. Understanding and controlling heteroepitaxy with the kinetic wulff plot: A case study with GaN. Journal of Applied Physics, 110(5):053517, 2011. 28, 101

[76] Hong Li, Lutz Geelhaar, Henning Riechert, and Claudia Draxl. Computing equilibrium shapes of wurtzite crystals: The example of GaN. Phys. Rev. Lett., 115:085503, Aug 2015. 28, 29, 37, 44, 101, 202

[77] W. A. Harris. Electronic structure and properties of solids. Dover, 1980. 29

[78] Liverios Lymperakis and Jörg Neugebauer. Large anisotropic adatom kinetics on nonpolar GaN surfaces: Consequences for surface morphologies and nanowire growth. Phys. Rev. B, 79:241308, Jun 2009. 29, 31, 202

[79] Xiaojing Gong, Pinar Dogan, Xiaoliang Zhang, Uwe Jahn, Ke Xu, Lifeng Bian, and Hui Yang. Atomic-scale behavior of adatoms in axial and radial growth of GaN nanowires: Molecular dynamics simulations. Japanese Journal of Applied Physics, 53(8):085601, 2014. 30

[80] K. K. Sabelfeld, V. M. Kaganer, F. Limbach, P. Dogan, O. Brandt, L. Geelhaar, and H. Riechert. Height self-equilibration during the growth of dense nanowire ensembles: Order emerging from disorder. Applied Physics Letters, 103(13):133105, 2013. 31

[81] R Songmuang, T Ben, B Daudin, D González, and E Monroy. Identification of iii–n nanowire growth kinetics via a marker technique. Nanotechnology, 21(29):295605, 2010. 31

[82] C.T. Foxon, S.V. Novikov, J.L. Hall, R.P. Campion, D. Cherns, I. Griffiths, and S. Khongphetsak. A complementary geometric model for the growth of GaN nanocolumns prepared by plasma-assisted molecular beam epitaxy. Journal of Crystal Growth, 311(13):3423 – 3427, 2009. 31, 202

[83] Karine Hestroffer and Bruno Daudin. A geometrical model for the description of the AlN shell morphology in GaN-AlN core-shell nanowires. Journal of Applied Physics, 114(24):244305, 2013. 31, 42, 44, 202

[84] E Galopin, L Largeau, G Patriarche, L Travers, F Glas, and J C Harmand. Morphology of self-catalyzed GaN nanowires and chronology of their formation by molecular beam epitaxy. Nanotechnology, 22(24):245606, 2011. 32, 175

[85] Sergio Fernández-Garrido, Vladimir M. Kaganer, Karl K. Sabelfeld, Tobias Gotschke, Javier Grandal, Enrique Calleja, Lutz Geelhaar, and Oliver Brandt. Self-regulated radius of spontaneously formed GaN nanowires in molecular beam epitaxy. Nano Letters, 13(7):3274–3280, 2013. 34, 37, 103

[86] Jörg Neugebauer, Tosja K. Zywietz, Matthias Scheffler, John E. Northrup, Huajie Chen, and R. M. Feenstra. Adatom kinetics on and below the surface: The existence of a new diffusion channel. Phys. Rev. Lett., 90:056101, Feb 2003. 37, 40

[87] N. Gogneau, E. Monroy, F. Fossard, B. Gayral, S. Monnoye, H. Mank, and B. Daudin. Properties of self-assembled Ga-polar and N-polar GaN/AlN quantum dots. physica status solidi (c), 1(10):2504–2507, 2004. 38, 39

[88] Christoph Adelmann, Julien Brault, Guido Mula, Bruno Daudin, Liverios Lymperakis, and Jörg Neugebauer. Gallium adsorption on (0001) GaN surfaces. Phys. Rev. B, 67:165419, Apr 2003. 38

[89] Pinar Dogan, Oliver Brandt, Carsten Pfüller, Jonas Lähnemann, Uwe Jahn, Claudia Roder, Achim Trampert, Lutz Geelhaar, and Henning Riechert. Formation of high-quality GaN microcrystals by pendeoepitaxial overgrowth of GaN nanowires on Si(111) by molecular beam epitaxy. Crystal Growth & Design, 11(10):4257–4260, 2011. 40

[90] D. Cherns, L. Meshi, I. Griffiths, S. Khongphetsak, S. V. Novikov, N. Farley, R. P. Campion, and C. T. Foxon. Defect reduction in GaN/(0001)sapphire films grown by molecular beam epitaxy using nanocolumn intermediate layers. Applied Physics Letters, 92(12):121902, 2008. 40

[91] J. Mei, S. Srinivasan, R. Liu, F. A. Ponce, Y. Narukawa, and T. Mukai. Prismatic stacking faults in epitaxially laterally overgrown GaN. Applied Physics Letters, 88(14):141912, 2006. 41, 135

[92] P. Corfdir, P. Lefebvre, J. Levrat, A. Dussaigne, J.-D. Ganière, D Martin, J. Ristić, T. Zhu, N. Grandjean, and B. Deveaud-Plédran. Exciton localization on basal stacking faults in a-plane epitaxial lateral overgrown GaN grown by hydride vapor phase epitaxy. Journal of Applied Physics, 105(4):043102, 2009. 41, 177, 179

[93] J. A. Chisholm and P. D. Bristowe. Stacking fault energies in Si doped GaN: A first principles study. Applied Physics Letters, 77(4):534–536, 2000. 41

[94] J A Chisholm and P D Bristowe. A first principles investigation of stacking fault energies and bonding in wurtzite materials. Journal of Physics: Condensed Matter, 11(26):5057, 1999. 41

[95] Jafar Safarian, Leiv Kolbeinsen, and Merete Tangstad. Liquidus of silicon binary systems. Metallurgical and Materials Transactions B, 42(4):852–874, 2011. 41, 65, 66, 67

[96] Tetsuya Kouno and Katsumi Kishino. Well-arranged novel InGaN hexagonal nanoplates at the tops of nitrogen-polarity GaN nanocolumn arrays. AIP Advances, 2(012140), 2012. 42

[97] M. I. den Hertog, F. González-Posada, R. Songmuang, J. L. Rouviere, T. Fournier, B. Fernandez, and E. Monroy. Correlation of polarity and crystal structure with optoelectronic and transport properties of GaN/AlN/GaN nanowire sensors. Nano Letters, 12(11):5691–5696, 2012. PMID: 23030278. 42, 120, 186

[98] N. Gogneau, D. Jalabert, E. Monroy, E. Sarigiannidou, J. L. Rouvière, T. Shibata, M. Tanaka, J. M. Gerard, and B. Daudin. Influence of AlN overgrowth on structural properties of GaN quantum wells and quantum dots grown by plasma-assisted molecular beam epitaxy. Journal of Applied Physics, 96(2):1104–1110, 2004. 42

[99] R. Groh, G. Gerey, L. Bartha, and J. I. Pankove. On the thermal decomposition of GaN in vacuum. physica status solidi (a), 26(1):353–357, 1974. 46

[100] M. E. Lin, B. N. Sverdlov, and H. Morkoç. Thermal stability of GaN investigated by low-temperature photoluminescence spectroscopy. Applied Physics Letters, 63(26):3625–3627, 1993. 46

[101] M. Kuball, F. Demangeot, J. Frandon, M. A. Renucci, J. Massies, N. Grandjean, R. L. Aulombard, and O. Briot. Thermal stability of GaN investigated by raman scattering. Applied Physics Letters, 73(7):960–962, 1998. 46

[102] C. B. Vartuli, S. J. Pearton, C. R. Abernathy, J. D. MacKenzie, E. S. Lambers, and J. C. Zolper. High temperature surface degradation of III-V nitrides. Journal of Vacuum Science & Technology B, 14(6):3523–3531, 1996. 46

[103] M.A. Mastro, O.M. Kryliouk, T.J. Anderson, A. Davydov, and A. Shapiro. Influence of polarity on GaN thermal stability. Journal of Crystal Growth, 274(1–2):38 – 46, 2005. 47, 48

[104] Thomas Auzelle, Benedikt Haas, Albert Minj, Catherine Bougerol, Jean-Luc Rouvière, Ana Cros, Jaime Colchero, and Bruno Daudin. The influence of AlN buffer over the polarity and the nucleation of self-organized GaN nanowires. Journal of Applied Physics, 117(24):245303, 2015. 53

[105] V. Consonni, M. Hanke, M. Knelangen, L. Geelhaar, A. Trampert, and H. Riechert. Nucleation mechanisms of self-induced GaN nanowires grown on an amorphous interlayer. Phys. Rev. B, 83:035310, Jan 2011. 53

[106] C. Q. Chen, Y. Shi, Y. S. Zhang, J. Zhu, and Y. J. Yan. Size dependence of young's modulus in ZnO nanowires. Phys. Rev. Lett., 96:075505, Feb 2006. 53

[107] B. Daudin, F. Widmann, G. Feuillet, Y. Samson, M. Arlery, and J. L. Rouvière. Stranski-krastanov growth mode during the molecular beam epitaxy of highly strained GaN. Phys. Rev. B, 56:R7069–R7072, Sep 1997. 53, 139, 166, 167

[108] O Landré, C Bougerol, H Renevier, and B Daudin. Nucleation mechanism of GaN nanowires grown on (111) Si by molecular beam epitaxy. Nanotechnology, 20(41):415602, 2009. 54

[109] V. Consonni, M. Knelangen, L. Geelhaar, A. Trampert, and H. Riechert. Nucleation mechanisms of epitaxial GaN nanowires: Origin of their self-induced formation and initial radius. Phys. Rev. B, 81:085310, Feb 2010. 54, 101, 103

[110] M Knelangen, V Consonni, A Trampert, and H Riechert. In situ analysis of strain relaxation during catalyst-free nucleation and growth of GaN nanowires. Nanotechnology, 21(24):245705, 2010. 55, 103

[111] Vladimir G. Dubrovskii, Vincent Consonni, Achim Trampert, Lutz Geelhaar, and Henning Riechert. Scaling thermodynamic model for the self-induced nucleation of GaN nanowires. Phys. Rev. B, 85:165317, Apr 2012. 55, 103

[112] Florian Furtmayr, Martin Vielemeyer, Martin Stutzmann, Jordi Arbiol, Sònia Estradé, Francesca Peirò, Joan Ramon Morante, and Martin Eickhoff. Nucleation and growth of GaN nanorods on Si (111) surfaces by plasma-assisted molecular beam epitaxy - the influence of Si- and Mg-doping. Journal of Applied Physics, 104(3):034309, 2008. 56, 70, 119, 127

[113] R Armitage and K Tsubaki. Multicolour luminescence from InGaN quantum wells grown over GaN nanowire arrays by molecular-beam epitaxy. Nanotechnology, 21(19):195202, 2010. 56

[114] Matt D. Brubaker, Igor Levin, Albert V. Davydov, Devin M. Rourke, Norman A. Sanford, Victor M. Bright, and Kris A. Bertness. Effect of AlN buffer layer properties on the morphology and polarity of GaN nanowires grown by molecular beam epitaxy. Journal of Applied Physics, 110(5):053506, 2011. 55, 56, 88, 202

[115] E Calleja, M.A Sànchez-García, F.J Sánchez, F Calle, F.B Naranjo, E Muñoz, S.I Molina, A.M Sánchez, F.J Pacheco, and R García. Growth of iii-nitrides on Si(111) by molecular beam epitaxy doping, optical, and electrical properties. Journal of Crystal Growth, 201–202(0):296 – 317, 1999. 56, 70, 97, 203

[116] Sang-Tae Lee, Byung-Guon Park, Moon-Deock Kim, Jae-Eung Oh, Song-Gang Kim, Young-Heon Kim, and Woo-Chul Yang. Control of polarity and defects in the growth of AlN films on Si (111) surfaces by inserting an Al interlayer. Current Applied Physics, 12(2):385 – 388, 2012. 56, 57, 80, 93

[117] Sansaptak Dasgupta, F. Wu, J. S. Speck, and U. K. Mishra. Growth of high quality N-polar AlN(000[overline 1]) on Si(111) by plasma assisted molecular beam epitaxy. Applied Physics Letters, 94(15):151906, 2009. 56

[118] S. A. Nikishin, V. G. Antipov, S. Francoeur, N. N. Faleev, G. A. Seryogin, V. A. Elyukhin, H. Temkin, T. I. Prokofyeva, M. Holtz, A. Konkar, and S. Zollner.

High-quality AlN grown on Si(111) by gas-source molecular-beam epitaxy with ammonia. Applied Physics Letters, 75(4):484–486, 1999. 56, 70

[119] F. Semond, B. Damilano, S. Vézian, N. Grandjean, M. Leroux, and J. Massies. GaN grown on Si(111) substrate: From two-dimensional growth to quantum well assessment. Applied Physics Letters, 75(1):82–84, 1999. 56

[120] S Karmann, H.P.D Schenk, U Kaiser, A Fissel, and Wo Richter. Growth of columnar aluminum nitride layers on Si(111) by molecular beam epitaxy. Materials Science and Engineering: B, 50(1–3):228 – 232, 1997. 56, 82

[121] K. Yasutake, A. Takeuchi, H. Kakiuchi, and K. Yoshii. Molecular beam epitaxial growth of AlN single crystalline films on Si (111) using radio-frequency plasma assisted nitrogen radical source. Journal of Vacuum Science and Technology A: Vacuum, Surfaces, and Films, 16(4):2140–2147, 1998. 56

[122] A. Le Louarn, S. Vézian, F. Semond, and J. Massies. AlN buffer layer growth for GaN epitaxy on (111) Si: Al or N first? Journal of Crystal Growth, 311(12):3278 – 3284, 2009. 57, 68

[123] Jiannan Hu, Zhibiao Hao, Lang Niu, Yanxiong E, Lai Wang, and Yi Luo. Atomically smooth and homogeneously N-polar AlN film grown on silicon by alumination of si3n4. Applied Physics Letters, 102(14):141913, 2013. 57, 68

[124] E. Calleja, M. A. Sanchez-Garcia, E. Monroy, F. J. Sanchez, E. Munoz, A. Sanz-Hervas, C. Villar, and M. Aguilar. Growth kinetics and morphology of high quality AlN grown on Si(111) by plasma-assisted molecular beam epitaxy. Journal of Applied Physics, 82(9):4681–4683, 1997. 57, 58

[125] A. Bourret, A. Barski, J. L. Rouvière, G. Renaud, and A. Barbier. Growth of aluminum nitride on (111) silicon: Microstructure and interface structure. Journal of Applied Physics, 83(4):2003–2009, 1998. 57, 72, 87, 94

[126] M Musolino, A Tahraoui, S Fernández-Garrido, O Brandt, A Trampert, L Geelhaar, and H Riechert. Compatibility of the selective area growth of GaN nanowires on AlN-buffered Si substrates with the operation of light emitting diodes. Nanotechnology, 26(8):085605, 2015. 57, 82, 86

[127] A.A. Saranin, V.G. Kotlyar, A.V. Zotov, T.V. Kasyanova, M.A. Cherevik, and V.G. Lifshits. Structure of domain walls in Al/Si(111) γ-phase. Surface Science, 517(1–3):151 – 156, 2002. 61, 63, 65

[128] Thomas Michely, Mark C. Reuter, and Ruud M. Tromp. Al on Si(111): Phase diagram and atomic mechanisms. Phys. Rev. B, 53:4105–4108, Feb 1996. 61

[129] A.V. Zotov, E.A. Khramtsova, S.V. Ryzhkov, A.A. Saranin, A.B. Chub, and V.G. Lifshits. Leed-aes reexamination of the Al/Si(111) "γ-phase". Surface Science, 316(1–2):L1034 – L1038, 1994. 62, 82

[130] Luo and Yu-Ran. 63

[131] Nicola Ferralis, Farid El Gabaly, Andreas K. Schmid, Roya Maboudian, and Carlo Carraro. Real-time observation of reactive spreading of gold on silicon. Phys. Rev. Lett., 103:256102, Dec 2009. 66

[132] Nicola Ferralis, Roya Maboudian, and Carlo Carraro. Temperature-induced self-pinning and nanolayering of AuSi eutectic droplets. Journal of the American Chemical Society, 130(8):2681–2685, 2008. 66

[133] Renaud Vaysset Geaymond Pasturel Schulli, Daudin. Substrate-enhanced supercooling in AuSi eutecticdroplets. Nature, 464:1174, April 2010. 66

[134] S. H. Oh, Y. Kauffmann, C. Scheu, W. D. Kaplan, and M. Rühle. Ordered liquid aluminum at the interface with sapphire. Science, 310(5748):661–663, 2005. 66

[135] A. Pélisson, M. Parlinska-Wojtan, H.J. Hug, and J. Patscheider. Microstructure and mechanical properties of Al–Si–N transparent hard coatings deposited by magnetron sputtering. Surface and Coatings Technology, 202(4–7):884 – 889, 2007. 67, 74

[136] Aude Pélisson-Schecker, Hans Josef Hug, and Jörg Patscheider. Complex phase compositions in nanostructured coatings as evidenced by photoelectron spectroscopy: The case of Al–Si–N hard coatings. Journal of Applied Physics, 108(2):023508, 2010. 67, 74

[137] M. Hermann, F. Furtmayr, F. M. Morales, O. Ambacher, M. Stutzmann, and M. Eickhoff. Impact of silicon incorporation on the formation of structural defects in AlN. Journal of Applied Physics, 100(11):113531, 2006. 67

[138] M. Hermann, F. Furtmayr, A. Bergmaier, G. Dollinger, M. Stutzmann, and M. Eickhoff. Highly Si-doped AlN grown by plasma-assisted molecular-beam epitaxy. Applied Physics Letters, 86(19):192108, 2005. 67

[139] V. Lebedev, F. M. Morales, H. Romanus, S. Krischok, G. Ecke, V. Cimalla, M. Himmerlich, T. Stauden, D. Cengher, and O. Ambacher. The role of Si as surfactant and donor in molecular-beam epitaxy of AlN. Journal of Applied Physics, 98(9):093508, 2005. 67, 80, 94

[140] S.H. Sheng, R.F. Zhang, and S. Vepřek. Decomposition mechanism of Al1-xSixNy solid solution and possible mechanism of the formation of covalent nanocrystalline AlN/Si3N4 nanocomposites. Acta Materialia, 61(11):4226 – 4236, 2013. 67

[141] Liu Chen-hui, Luo Qing-zhou, Luo Xiang-dong, and Liu Pei-sheng. Mixed phases at the bottom interface of Si-doped AlGaN epilayrs of optoelectronic devices. Journal of nanomaterials, 2014(729041). 67

[142] K.H. Jack. Sialons and related nitrogen ceramics. Journal of Materials Science, 11(6):1135–1158, 1976. 67

[143] J. H. Harris, R. A. Youngman, and R. G. Teller. On the nature of the oxygen-related defect in aluminum nitride. Journal of Materials Research, 5:1763–1773, 1990. 67, 93

[144] Alistair D. Westwood, Robert A. Youngman, Martha R. McCartney, Alasiair N. Cormack, and Michael R. Notis. Oxygen incorporation in aluminum nitride via extended defects: Part iii. reevaluation of the polytypoid structure in the aluminum nitride-aluminum oxide binary system. Journal of Materials Research, 10:2573–2585, 1995. 67, 93

[145] K. Hestroffer, C. Leclere, V. Cantelli, C. Bougerol, H. Renevier, and B. Daudin. In situ study of self-assembled GaN nanowires nucleation on Si(111) by plasma-assisted molecular beam epitaxy. Applied Physics Letters, 100(21):212107, 2012. 68

[146] P. Corfdir, P. Lefebvre, J. Ristić, P. Valvin, E. Calleja, A. Trampert, J.-D. Ganière, and B. Deveaud-Plédran. Time-resolved spectroscopy on GaN nanocolumns grown by plasma assisted molecular beam epitaxy on Si substrates. Journal of Applied Physics, 105(1):013113, 2009. 70, 119, 128

[147] C.-L. Wu, J.-L. Hsieh, H.-D. Hsueh, and S. Gwo. Thermal nitridation of the Si(111)-(7×7) surface studied by scanning tunneling microscopy and spectroscopy. Phys. Rev. B, 65:045309, Jan 2002. 70

[148] Jian-Min Zuo, Amish B. Shah, Honggyu Kim, Yifei Meng, Wenpei Gao, and Jean-Luc Rouviére. Lattice and strain analysis of atomic resolution z-contrast images based on template matching. Ultramicroscopy, 136(0):50 – 60, 2014. 80, 110, 113, 114

[149] E. Calleja, M. A. Sánchez-García, E. Monroy, F. J. Sánchez, E. Mu noz, A. Sanz-Hervás, C. Villar, and M. Aguilar. Growth kinetics and morphology of high quality AlN grown on Si(111) by plasma-assisted molecular beam epitaxy. Journal of Applied Physics, 82(9):4681–4683, 1997. 84

[150] T. Gotschke, T. Schumann, F. Limbach, T. Stoica, and R. Calarco. Influence of the adatom diffusion on selective growth of GaN nanowire regular arrays. Applied Physics Letters, 98(10):103102, 2011. 86

[151] John E. Northrup, Jörg Neugebauer, and L. T. Romano. Inversion domain and stacking mismatch boundaries in GaN. Phys. Rev. Lett., 77:103–106, Jul 1996. 92, 109, 115, 116, 131, 203

[152] S. Pezzagna, P. Vennéguès, N. Grandjean, and J. Massies. Polarity inversion of GaN(0001) by a high Mg doping. Journal of Crystal Growth, 269(2–4):249 – 256, 2004. 93, 127

[153] L. T. Romano, J. E. Northrup, A. J. Ptak, and T. H. Myers. Faceted inversion domain boundary in GaN films doped with Mg. Applied Physics Letters, 77(16):2479–2481, 2000. 93, 127

[154] V. Ramachandran, R. M. Feenstra, W. L. Sarney, L. Salamanca-Riba, J. E. Northrup, L. T. Romano, and D. W. Greve. Inversion of wurtzite GaN(0001) by exposure to magnesium. Applied Physics Letters, 75(6):808–810, 1999. 93

[155] A.L. Rosa and J. Neugebauer. Polarity inversion of GaN(0001) surfaces induced by Si adsorption. Surface Science, 600(2):335 – 339, 2006. 93

[156] Zhun Liu, Ru-Zhi Wang, Li-Min Liu, Hui Yan, and Woon-Ming Lau. Si doping at GaN inversion domain boundaries: an interfacial polar field for electron and hole separation. J. Mater. Chem. A, 2:9744–9750, 2014. 93

[157] T. Markurt, L. Lymperakis, J. Neugebauer, P. Drechsel, P. Stauss, T. Schulz, T. Remmele, V. Grillo, E. Rotunno, and M. Albrecht. Blocking growth by an electrically active subsurface layer: The effect of Si as an antisurfactant in the growth of GaN. Phys. Rev. Lett., 110:036103, Jan 2013. 93

[158] D Wang, S Yoshida, and M Ichikawa. Effect of Si doping on the growth and microstructure of GaN grown on Si(1111) using SiC as a buffer layer. Journal of Crystal Growth, 242(1–2):20 – 28, 2002. 93

[159] Jennifer K. Hite, Nelson Y. Garces, Ramasis Goswami, Michael A. Mastro, Fritz J. Kub, and Charles R. Eddy Jr. Selective switching of GaN polarity on Ga-polar GaN using atomic layer deposited Al2O3. Applied Physics Express, 7(2):025502, 2014. 93, 109

[160] T. Nakayama and J. Mikami. Ultrathin metal layers to convert surface polarity of nitride semiconductors. physica status solidi (b), 242(6):1209–1213, 2005. 93

[161] J. P. Michel, I. Masson, S. Choux, and A. George. Inversion domain boundaries and dislocations observed by tem in deformed aluminium nitride. physica status solidi (a), 146(1):97–108, 1994. 93

[162] Alistair D. Westwood, Robert A. Youngman, Martha R. McCartney, Alastair N. Cormack, and Michael R. Notis. Oxygen incorporation in aluminum nitride via extended defects: Part i. refinement of the structural model for the planar inversion domain boundary. Journal of Materials Research, 10:1270–1286, 5 1995. 93

[163] Alistair D. Westwood, Robert A. Youngman, Martha R. McCartney, Alastair N. Cormack, and Michael R. Notis. Oxygen incorporation in aluminum nitride via extended defects: Part ii. structure of curved inversion domain boundaries and defect formation. Journal of Materials Research, 10:1287–1300, 1995. 93

[164] Aleksander Rečnik, Nina Daneu, and Slavko Bernik. Nucleation and growth of basal-plane inversion boundaries in ZnO. Journal of the European Ceramic Society, 27(4):1999 – 2008, 2007. 93

[165] Andrew B. Yankovich, Brian Puchala, Fei Wang, Jung-Hun Seo, Dane Morgan, Xudong Wang, Zhenqiang Ma, Alex V. Kvit, and Paul M. Voyles. Stable p-type conduction from sb-decorated head-to-head basal plane inversion domain boundaries in ZnO nanowires. Nano Letters, 12(3):1311–1316, 2012. PMID: 22268642. 93

[166] D. Huang, P. Visconti, K. M. Jones, M. A. Reshchikov, F. Yun, A. A. Baski, T. King, and H. Morkoç. Dependence of GaN polarity on the parameters of the buffer layer grown by molecular beam epitaxy. Applied Physics Letters, 78(26):4145–4147, 2001. 94

[167] D. Litvinov, D. Gerthsen, R. Vöhringer, D.Z. Hu, and D.M. Schaadt. Transmission electron microscopy investigation of AlN growth on Si(111). Journal of Crystal Growth, 338(1):283 – 290, 2012. 94

[168] A.M. Sanchez, P. Ruterana, S.I. Molina, F.J. Pacheco, and R. Garcia. Origin of inversion domains in GaN/AlN/Si(111) heterostructures grown by molecular beam epitaxy. physica status solidi (b), 234(3):935–938, 2002. 94

[169] B.J Rodriguez, A Gruverman, A.I Kingon, and R.J Nemanich. Piezoresponse force microscopy for piezoelectric measurements of iii-nitride materials. Journal of Crystal Growth, 246(3–4):252 – 258, 2002. Proceedings of the International Workshop on Bulk Nitride Semicon ductors. 94

[170] A. M. Sánchez, P. Ruterana, M. Benamara, and H. P. Strunk. Inversion domains and pinholes in GaN grown over Si(111). Applied Physics Letters, 82(25):4471–4473, 2003. 94

[171] G. P. Dimitrakopulos, A. M. Sanchez, Ph. Komninou, Th. Kehagias, Th. Karakostas, G. Nouet, and P. Ruterana. Interfacial steps, dislocations, and inversion domain boundaries in the GaN/AlN/Si (0001)/(111) epitaxial system. physica status solidi (b), 242(8):1617–1627, 2005. 94

[172] L. T. Romano, J. E. Northrup, and M. A. O'Keefe. Inversion domains in GaN grown on sapphire. Applied Physics Letters, 69(16):2394–2396, 1996. 94

[173] F. Widmann, G. Feuillet, B. Daudin, and J. L. Rouvière. Low temperature sapphire nitridation: A clue to optimize GaN layers grown by molecular beam epitaxy. Journal of Applied Physics, 85(3):1550–1555, 1999. 102

[174] S. Mikroulis, A. Georgakilas, A. Kostopoulos, V. Cimalla, E. Dimakis, and Ph. Komninou. Control of the polarity of molecular-beam-epitaxy-grown GaN thin films by the surface nitridation of Al2O3 (0001) substrates. Applied Physics Letters, 80(16):2886–2888, 2002. 102

[175] Z. T. Wang, Y. Yamada-Takamura, Y. Fujikawa, T. Sakurai, and Q. K. Xue. Atomistic study of GaN surface grown on Si(111). Applied Physics Letters, 87(3):032110, 2005. 104

[176] Thomas Auzelle, Benedikt Haas, Martien Den Hertog, Jean-Luc Rouvière, Bruno Daudin, and Bruno Gayral. Attribution of the 3.45 ev GaN nanowires luminescence to inversion domain boundaries. 109

[177] J.L. Rouviere, M. Arlery, B. Daudin, G. Feuillet, and O. Briot. Transmission electron microscopy structural characterisation of GaN layers grown on (0001) sapphire. Materials Science and Engineering: B, 50(1–3):61 – 71, 1997. 109, 115

[178] T. Koukoula, J. Kioseoglou, Th. Kehagias, A. O. Ajagunna, Ph. Komninou, and A. Georgakilas. Self-annihilation of inversion domains by high energy defects in iii-nitrides. Applied Physics Letters, 104(14):141914, 2014. 109, 131, 132

[179] A. M. Sanchez, G. Nouet, P. Ruterana, F. J. Pacheco, S. I. Molina, and R. Garcia. A mechanism for the multiple atomic configurations of inversion domain boundaries in GaN layers grown on Si(111). Applied Physics Letters, 79(22):3588–3590, 2001. 109, 130, 132, 133

[180] C. Iwamoto, X. Q. Shen, H. Okumura, H. Matsuhata, and Y. Ikuhara. Termination mechanism of inversion domains by stacking faults in GaN. Journal of Applied Physics, 93(6):3264–3269, 2003. 109, 132

[181] V. Potin, G. Nouet, and P. Ruterana. Evidence for multiple atomic structure for the 10-10 inversion domain boundaries in GaN layers. Applied Physics Letters, 74(7):947–949, 1999. 109, 115, 131

[182] V. Potin, P. Ruterana, and G. Nouet. The atomic structure of 10-10 inversion domain boundaries in GaN/sapphire layers. Journal of Applied Physics, 82(5):2176–2183, 1997. 109, 115, 131

[183] J. Elsner, M. Kaukonen, M. I. Heggie, M. Haugk, Th. Frauenheim, and R. Jones. Domain boundaries on 11-20 planes in GaN: A theoretical study. Phys. Rev. B, 58:15347–15350, Dec 1998. 109, 117, 118

[184] John E. Northrup. Structure of the 11-20 inversion domain boundary in GaN. Physica B: Condensed Matter, 273–274(0):130 – 133, 1999. 109, 117, 118

[185] Vincenzo Fiorentini. Origin of the efficient light emission from inversion domain boundaries in GaN. Applied Physics Letters, 82(8):1182–1184, 2003. 109, 118, 128

[186] Fude Liu, Ramon Collazo, Seiji Mita, Zlatko Sitar, Stephen J. Pennycook, and Gerd Duscher. Direct observation of inversion domain boundaries of GaN on c-sapphire at sub-ångstrom resolution. Advanced Materials, 20(11):2162–2165, 2008. 115

[187] John E. Northrup and J. Neugebauer. Theory of GaN($10\bar{1}0$) and ($11\bar{2}0$) surfaces. Phys. Rev. B, 53:R10477–R10480, Apr 1996. 117

[188] Yanfa Yan and M. M. Al-Jassim. Inversion domain boundaries in ZnO: First-principles total-energy calculations. Phys. Rev. B, 69:085204, Feb 2004. 119, 127

[189] E. Calleja, M. A. Sánchez-García, F. J. Sánchez, F. Calle, F. B. Naranjo, E. Muñoz, U. Jahn, and K. Ploog. Luminescence properties and defects in GaN nanocolumns grown by molecular beam epitaxy. Phys. Rev. B, 62:16826–16834, Dec 2000. 119, 127, 128

[190] Oliver Brandt, Carsten Pfüller, Caroline Chèze, Lutz Geelhaar, and Henning Riechert. Sub-mev linewidth of excitonic luminescence in single GaN nanowires: Direct evidence for surface excitons. Phys. Rev. B, 81:045302, Jan 2010. 119, 124

[191] Lawrence H. Robins, Kris A. Bertness, Joy M. Barker, Norman A. Sanford, and John B. Schlager. Optical and structural study of GaN nanowires grown by catalyst-free molecular beam epitaxy. i. near-band-edge luminescence and strain effects. Journal of Applied Physics, 101(11):113505, 2007. 119, 120

[192] A. Fiorek, J.M. Baranowski, A. Wysmołek, K. Pakuła, M. Wojdak, I. Grzegory, and S. Porowski. Two-electron transition in homoepitaxial GaN layers. Acta Physica Polonica A, 92(4):742–744, Oct 1997. 119

[193] D. Sam-Giao, R. Mata, G. Tourbot, J. Renard, A. Wysmolek, B. Daudin, and B. Gayral. Fine optical spectroscopy of the 3.45 ev emission line in GaN nanowires. Journal of Applied Physics, 113(4):043102, 2013. 119, 125

[194] Pu Huang, Hua Zong, Jun jie Shi, Min Zhang, Xin he Jiang, Hong xia Zhong, Yi min Ding, Ying ping He, Jing Lu, and Xiao dong Hu. Origin of 3.45 ev emission line and yellow luminescence band in GaN nanowires: Surface microwire and defect. ACS Nano, 0(0):null, 0. PMID: 26301765. 120

[195] D.C. Look. Recent advances in ZnO materials and devices. Materials Science and Engineering: B, 80(1–3):383 – 387, 2001. 122

[196] K. H. Chow, G. D. Watkins, Akira Usui, and M. Mizuta. Detection of interstitial Ga in GaN. Phys. Rev. Lett., 85:2761–2764, Sep 2000. 122

[197] L. S. Vlasenko, C. Bozdog, G. D. Watkins, F. Shahedipour, and B. W. Wessels. Defects observed by optical detection of electron paramagnetic resonance in electron-irradiated p -type GaN. Phys. Rev. B, 65:205202, Apr 2002. 122

[198] D. C. Look, D. C. Reynolds, J. W. Hemsky, J. R. Sizelove, R. L. Jones, and R. J. Molnar. Defect donor and acceptor in GaN. Phys. Rev. Lett., 79:2273–2276, Sep 1997. 123

[199] S. Suihkonen, H. Nykänen, T. Tanikawa, M. Yamaguchi, Y. Honda, and H. Amano. Effects of low energy e-beam irradiation on cathodoluminescence from GaN. physica status solidi (a), 210(2):383–385, 2013. 123

[200] H. Nykänen, P. Mattila, S. Suihkonen, J. Riikonen, E. Quillet, E. Homeyer, J. Bellessa, and M. Sopanen. Low energy electron beam induced damage on InGaN/GaN quantum well structure. Journal of Applied Physics, 109(8):083105, 2011. 123

[201] Lawrence H. Robins, Kris A. Bertness, Joy M. Barker, Norman A. Sanford, and John B. Schlager. Optical and structural study of GaN nanowires grown by catalyst-free molecular beam epitaxy. ii. sub-band-gap luminescence and electron irradiation effects. Journal of Applied Physics, 101(11):113506, 2007. 123

[202] Roman Anufriev, Nicolas Chauvin, Hammadi Khmissi, Khalid Naji, Michel Gendry, and Catherine Bru-Chevallier. Impact of substrate-induced strain and surface effects on the optical properties of inp nanowires. Applied Physics Letters, 101(7):072101, 2012. 124

[203] John B. Schlager, Kris A. Bertness, Paul T. Blanchard, Lawrence H. Robins, Alexana Roshko, and Norman A. Sanford. Steady-state and time-resolved photoluminescence from relaxed and strained GaN nanowires grown by catalyst-free molecular-beam epitaxy. Journal of Applied Physics, 103(12):124309, 2008. 124, 182, 183

[204] P. Lefebvre, S. Albert, J. Ristić, S. Fernández-Garrido, J. Grandal, M.-A. Sánchez-García, and E. Calleja. Oxygen photo-adsorption related quenching of photoluminescence in group-iii nitride nanocolumns. Superlattices and Microstructures, 52(2):165 – 171, 2012. 124, 186

[205] K. Saarinen, J. Nissilä, P. Hautojärvi, J. Likonen, T. Suski, I. Grzegory, B. Lucznik, and S. Porowski. The influence of Mg doping on the formation of Ga vacancies and negative ions in GaN bulk crystals. Applied Physics Letters, 75(16):2441–2443, 1999. 127

[206] Michael A. Reshchikov and Hadis Morkoç. Luminescence properties of defects in GaN. Journal of Applied Physics, 97(6):061301, 2005. 127

[207] C. Tessarek, M. Bashouti, M. Heilmann, C. Dieker, I. Knoke, E. Spiecker, and S. Christiansen. Controlling morphology and optical properties of self-catalyzed, mask-free GaN rods and nanorods by metal-organic vapor phase epitaxy. Journal of Applied Physics, 114(14):144304, 2013. 128

[208] R. Liu, A. Bell, F. A. Ponce, C. Q. Chen, J. W. Yang, and M. A. Khan. Luminescence from stacking faults in gallium nitride. Applied Physics Letters, 86(2):021908, 2005. 135

[209] J. Bai, M. Dudley, L. Chen, B. J. Skromme, B. Wagner, R. F. Davis, U. Chowdhury, and R. D. Dupuis. Structural defects and luminescence features in heteroepitaxial GaN grown on on-axis and misoriented substrates. Journal of Applied Physics, 97(11):116101, 2005. 135

[210] T. Bretagnon, P. Lefebvre, P. Valvin, R. Bardoux, T. Guillet, T. Taliercio, B. Gil, N. Grandjean, F. Semond, B. Damilano, A. Dussaigne, and J. Massies. Radiative lifetime of a single electron-hole pair in GaN/AlN quantum dots. Phys. Rev. B, 73:113304, Mar 2006. 139, 149, 150, 151, 153, 154, 204

[211] S. Kalliakos, T. Bretagnon, P. Lefebvre, T. Taliercio, B. Gil, N. Grandjean, B. Damilano, A. Dussaigne, and J. Massies. Photoluminescence energy and linewidth in GaN/AlN stackings of quantum dot planes. Journal of Applied Physics, 96(1):180–185, 2004. 139, 150, 151, 152

[212] B. Damilano, N. Grandjean, F. Semond, J. Massies, and M. Leroux. From visible to white light emission by GaN quantum dots on Si(111) substrate. Applied Physics Letters, 75(7):962–964, 1999. 139

[213] F. Widmann, B. Daudin, G. Feuillet, Y. Samson, J. L. Rouvière, and N. Pelekanos. Growth kinetics and optical properties of self-organized GaN quantum dots. Journal of Applied Physics, 83(12):7618–7624, 1998. 139, 165, 204

[214] J. L. Rouvière, J. Simon, N. Pelekanos, B. Daudin, and G. Feuillet. Preferential nucleation of GaN quantum dots at the edge of AlN threading dislocations. Applied Physics Letters, 75(17):2632–2634, 1999. 139, 167, 197

[215] Gordon Schmidt, Christoph Berger, Peter Veit, Sebastian Metzner, Frank Bertram, Jürgen Bläsing, Armin Dadgar, André Strittmatter, Jürgen Christen, Gordon Callsen, Stefan Kalinowski, and Axel Hoffmann. Direct evidence of single quantum dot emission from GaN islands formed at threading dislocations using nanoscale cathodoluminescence: A source of single photons in the ultraviolet. Applied Physics Letters, 106(25):252101, 2015. 139

[216] Julien Renard, Rudeesun Songmuang, Catherine Bougerol, Bruno Daudin, and Bruno Gayral. Exciton and biexciton luminescence from single GaN/AlN quantum dots in nanowires. Nano Letters, 8(7):2092–2096, 2008. 139

[217] M. Beeler, C. B. Lim, P. Hille, J. Bleuse, J. Schörmann, M. de la Mata, J. Arbiol, M. Eickhoff, and E. Monroy. Long-lived excitons in GaN/AlN nanowire heterostructures. Phys. Rev. B, 91:205440, May 2015. 139, 144

[218] C. Rivera, U. Jahn, T. Flissikowski, J. L. Pau, E. Muñoz, and H. T. Grahn. Strain-confinement mechanism in mesoscopic quantum disks based on piezoelectric materials. Phys. Rev. B, 75:045316, Jan 2007. 139, 149

[219] Jelena Ristić, Carlos Rivera, Enrique Calleja, Sergio Fernández-Garrido, Michael Povoloskyi, and Aldo Di Carlo. Carrier-confinement effects in nanocolumnar GaN/al$_x$ga$_{1-x}$N quantum disks grown by molecular-beam epitaxy. Phys. Rev. B, 72:085330, Aug 2005. 139

[220] Luiz Fernando Zagonel, Stefano Mazzucco, Marcel Tencé, Katia March, Romain Bernard, Benoît Laslier, Gwénolé Jacopin, Maria Tchernycheva, Lorenzo Rigutti, Francois H. Julien, Rudeesun Songmuang, and Mathieu Kociak. Nanometer scale spectral imaging of quantum emitters in nanowires and its correlation to their atomically resolved structure. Nano Letters, 11(2):568–573, 2011. PMID: 21182283. 139, 143, 155, 156

[221] Florian Furtmayr, Jörg Teubert, Pascal Becker, Sonia Conesa-Boj, Joan Ramon Morante, Alexey Chernikov, Sören Schäfer, Sangam Chatterjee, Jordi Arbiol, and Martin Eickhoff. Carrier confinement in GaN/al$_x$ga$_{1-x}$N nanowire heterostructures ($0 < x \leq 1$). Phys. Rev. B, 84:205303, Nov 2011. 139

[222] C Bougerol, R Songmuang, D Camacho, Y M Niquet, R Mata, A Cros, and B Daudin. The structural properties of GaN insertions in GaN/AlN nanocolumn heterostructures. Nanotechnology, 20(29):295706, 2009. 139

[223] Mark J. Holmes, Kihyun Choi, Satoshi Kako, Munetaka Arita, and Yasuhiko Arakawa. Room-temperature triggered single photon emission from a iii-nitride site-controlled nanowire quantum dot. Nano Letters, 14(2):982–986, 2014. 140

[224] Guido Mula, C. Adelmann, S. Moehl, J. Oullier, and B. Daudin. Surfactant effect of gallium during molecular-beam epitaxy of GaN on AlN (0001). Phys. Rev. B, 64:195406, Oct 2001. 144, 166

[225] M. Leroux, J. Brault, A. Kahouli, D. Maghraoui, B. Damilano, P. de Mierry, M. Korytov, Je-Hyung Kim, and Yong-Hoon Cho. Stark effect in ensembles of polar (0001) Al0.5Ga0.5N/GaN quantum dots and comparison with semipolar (11-22) ones. Journal of Applied Physics, 116(3), 2014. 149

[226] C. Adelmann, E. Sarigiannidou, D. Jalabert, Y. Hori, J.-L. Rouvière, B. Daudin, S. Fanget, C. Bru-Chevallier, T. Shibata, and M. Tanaka. Growth and optical properties of GaN/AlN quantum wells. Applied Physics Letters, 82(23):4154–4156, 2003. 149, 150, 158, 204

[227] F. Widmann, J. Simon, B. Daudin, G. Feuillet, J. L. Rouvière, N. T. Pelekanos, and G. Fishman. Blue-light emission from GaN self-assembled quantum dots due to giant piezoelectric effect. Phys. Rev. B, 58:R15989–R15992, Dec 1998. 154

[228] C. Himwas, M. den Hertog, Le Si Dang, E. Monroy, and R. Songmuang. Alloy inhomogeneity and carrier localization in AlGaN section and AlGaN/AlN nanodisks in naniwires with 240 - 350 nm emission. Applied Physics Letters, 105(24):241908, 2014. 155, 187

[229] L. Lahourcade, J. Renard, B. Gayral, E. Monroy, M. P. Chauvat, and P. Ruterana. Ga kinetics in plasma-assisted molecular-beam epitaxy of GaN(112¯2): Effect on the structural and optical properties. Journal of Applied Physics, 103(9):093514, 2008. 158, 159

[230] Noëlle Gogneau. Croissance de boîtes quantiques GaN/AlN auto-organisées par épitaxie par jets moléculaires assistée par plasma. Theses, Université Joseph-Fourier - Grenoble I, 2004. 167

[231] Gilles Nogues, Thomas Auzelle, Martien Den Hertog, Bruno Gayral, and Bruno Daudin. Cathodoluminescence of stacking fault bound excitons for local probing of the exciton diffusion length in single GaN nanowires. Applied Physics Letters, 104(10):102102, 2014. 175

[232] L. H. G. Tizei, S. Meuret, K. March, K. Hestroffer, T. Auzelle, B. Daudin, and M. Kociak. A polarity-driven nanometric luminescence asymmetry in AlN/GaN heterostructures. Applied Physics Letters, 105(14):143106, 2014. 175

[233] Shigefusa Chichibu, Kazumi Wada, and Shuji Nakamura. Spatially resolved cathodoluminescence spectra of InGaN quantum wells. Applied Physics Letters, 71(16):2346–2348, 1997. 175

[234] Stefan Schulz, Miguel A. Caro, Conor Coughlan, and Eoin P. O'Reilly. Atomistic analysis of the impact of alloy and well-width fluctuations on the electronic and optical properties of InGaN/GaN quantum wells. Phys. Rev. B, 91:035439, Jan 2015. 175

[235] Vytautas Liuolia, Saulius Marcinkevičius, You-Da Lin, Hiroaki Ohta, Steven P. DenBaars, and Shuji Nakamura. Dynamics of polarized photoluminescence in m-plane InGaN/GaN quantum wells. Journal of Applied Physics, 108(2):023101, 2010. 175

[236] D. Cherns, S. J. Henley, and F. A. Ponce. Edge and screw dislocations as nonradiative centers in InGaN/GaN quantum well luminescence. Applied Physics Letters, 78(18):2691–2693, 2001. 175

[237] S. J. Rosner, G. Girolami, H. Marchand, P. T. Fini, J. P. Ibbetson, L. Zhao, S. Keller, U. K. Mishra, S. P. DenBaars, and J. S. Speck. Cathodoluminescence mapping of epitaxial lateral overgrowth in gallium nitride. Applied Physics Letters, 74(14):2035–2037, 1999. 175

[238] Naoyuki Ino and Naoki Yamamoto. Low temperature diffusion length of excitons in gallium nitride measured by cathodoluminescence technique. Applied Physics Letters, 93(23):232103, 2008. 175, 177, 181, 185

[239] Anders Gustafsson, Jessica Bolinsson, Niklas Sköld, and Lars Samuelson. Determination of diffusion lengths in nanowires using cathodoluminescence. Applied Physics Letters, 97(7):072114, 2010. 175, 181, 182

[240] Jinkyoung Yoo, Gyu-Chul Yi, and Le Si Dang. Probing exciton diffusion in semiconductors using semiconductor-nanorod quantum structures. Small, 4(4):467–470, 2008. 175, 182

[241] S. Naureen, N. Shahid, A. Gustafsson, V. Liuolia, S. Marcinkevičius, and S. Anand. Carrier dynamics in inp nanopillar arrays fabricated by low-damage etching. Applied Physics Letters, 102(21):212106, 2013. 175, 181

[242] Jun-Seok Hwang, Fabrice Donatini, Julien Pernot, Robin Thierry, Pierre Ferret, and Le Si Dang. Carrier depletion and exciton diffusion in a single ZnO nanowire. Nanotechnology, 22(47):475704, 2011. 175

[243] V. Consonni, V. G. Dubrovskii, A. Trampert, L. Geelhaar, and H. Riechert. Quantitative description for the growth rate of self-induced GaN nanowires. Phys. Rev. B, 85:155313, Apr 2012. 175

[244] Daniel F. Blossey. Wannier exciton in an electric field. i. optical absorption by bound and continuum states. Phys. Rev. B, 2:3976–3990, Nov 1970. 176, 186

[245] G. Salviati, M. Albrecht, C. Zanotti-Fregonara, N. Armani, M. Mayer, Y. Shreter, M. Guzzi, Yu. V. Melnik, K. Vassilevski, V. A. Dmitriev, and H. P. Strunk. Cathodoluminescence and transmission electron microscopy study of the influence of crystal defects on optical transitions in GaN. physica status solidi (a), 171(1):325–339, 1999. 177, 179

[246] Jonas Lähnemann, Oliver Brandt, Uwe Jahn, Carsten Pfüller, Claudia Roder, Pinar Dogan, Frank Grosse, Abderrezak Belabbes, Friedhelm Bechstedt, Achim Trampert, and Lutz Geelhaar. Direct experimental determination of the spontaneous polarization of GaN. Phys. Rev. B, 86:081302, Aug 2012. 179

[247] Peter Ramvall, Satoru Tanaka, Shintaro Nomura, Philippe Riblet, and Yoshinobu Aoyagi. Observation of confinement-dependent exciton binding energy of GaN quantum dots. Applied Physics Letters, 73(8):1104–1106, 1998. 179

[248] N. Pauc, M. R. Phillips, V. Aimez, and D. Drouin. Carrier recombination near threading dislocations in GaN epilayers by low voltage cathodoluminescence. Applied Physics Letters, 89(16):161905, 2006. 181, 185

[249] B. Monemar, P. P. Paskov, J. P. Bergman, G. Pozina, A. A. Toropov, T. V. Shubina, T. Malinauskas, and A. Usui. Transient photoluminescence of shallow donor bound excitons in GaN. Phys. Rev. B, 82:235202, Dec 2010. 183

[250] Christian Hauswald, Pierre Corfdir, Johannes K. Zettler, Vladimir M. Kaganer, Karl K. Sabelfeld, Sergio Fernández-Garrido, Timur Flissikowski, Vincent Consonni, Tobias Gotschke, Holger T. Grahn, Lutz Geelhaar, and Oliver Brandt. Origin of the nonradiative decay of bound excitons in GaN nanowires. Phys. Rev. B, 90:165304, Oct 2014. 183, 186

[251] R. Dingle and M. Ilegems. Donor-acceptor pair recombination in GaN. Solid State Communications, 9(3):175 – 180, 1971. 183

[252] A. Gorgis, T. Flissikowski, O. Brandt, C. Chèze, L. Geelhaar, H. Riechert, and H. T. Grahn. Time-resolved photoluminescence spectroscopy of individual GaN nanowires. Phys. Rev. B, 86:041302, Jul 2012. 183

[253] Park Young S, Holmes Mark J, Shon Y, Yoon Im Taek, Im Hyunsik, and Taylor Robert A. GaN nanorods grown on Si (111) substrates and exciton localization. Nanoscale Research Letters. 183

[254] Oliver Brandt, Sergio Fernández-Garrido, Johannes K. Zettler, Esperanza Luna, Uwe Jahn, Caroline Chèze, and Vladimir M. Kaganer. Statistical analysis of the shape of one-dimensional nanostructures: Determining the coalescence degree of spontaneously formed GaN nanowires. Crystal Growth & Design, 14(5):2246–2253, 2014. 184

[255] Raffaella Calarco, Michel Marso, Thomas Richter, Ali I. Aykanat, Ralph Meijers, André v.d. Hart, Toma Stoica, , and Hans Lüth. Size-dependent photoconductivity in mbe - grown GaN nanowires. Nano Letters, 5(5):981 – 984, 2005. PMID: 15884906. 185, 186

[256] Pierre Corfdir, Johannes K. Zettler, Christian Hauswald, Sergio Fernández-Garrido, Oliver Brandt, and Pierre Lefebvre. Sub-mev linewidth in GaN nanowire ensembles: Absence of surface excitons due to the field ionization of donors. Phys. Rev. B, 90:205301, Nov 2014. 185, 186

[257] F. González-Posada, R. Songmuang, M. Den Hertog, and E. Monroy. Environmental sensitivity of n-i-n and undoped single GaN nanowire photodetectors. Applied Physics Letters, 102(21):213113, 2013. 186

[258] Carsten Pfüller, Oliver Brandt, Frank Grosse, Timur Flissikowski, Caroline Chèze, Vincent Consonni, Lutz Geelhaar, Holger T. Grahn, and Henning Riechert. Unpinning the fermi level of GaN nanowires by ultraviolet radiation. Phys. Rev. B, 82:045320, Jul 2010. 186

[259] S. A. Chevtchenko, M. A. Reshchikov, Q. Fan, X. Ni, Y. T. Moon, A. A. Baski, and H. Morkoç. Study of SiNx and SiO2 passivation of GaN surfaces. Journal of Applied Physics, 101(11):113709, 2007. 186

[260] J. Li, K. B. Nam, M. L. Nakarmi, J. Y. Lin, H. X. Jiang, Pierre Carrier, and Su-Huai Wei. Band structure and fundamental optical transitions in wurtzite AlN. Applied Physics Letters, 83(25):5163–5165, 2003. 189